Understanding exoplanets with radial velocity observations

Hannah Laura May Osborne

A dissertation submitted in partial fulfillment of the requirements for the degree of

Doctor of Philosophy

of

University College London.

Department of Space and Climate Physics
University College London

September 4, 2025

I, Hannah Laura May Osborne, confirm that the work presented in this thesis is my own. Where information has been derived from other sources, I confirm that this has been indicated in the work.

Abstract

For the past 30 years the field of exoplanet science has grown rapidly; from the first detection of a planet around a main sequence star in 1995 to now over 5800 confirmed detections. One particularly interesting finding from these many discoveries is that our own Solar system does not seem to be the blueprint of all planetary systems; rather the diversity in exoplanets observed so far have challenged most planet formation models.

While many efforts remain to try and detect planets in different regions of parameter space, much of the focus has now shifted to characterizing planets in more detail. One way that we try to understand planets is by categorizing them based on their compositions. Whilst planet radii are now fairly-routinely found from transit observations, we still lack mass measurements for many planets. Finding the masses of exoplanets in specific regions of parameter space can help to inform our models of planet formation and evolution. The planet masses which we do have are primarily from radial velocity (RV) observations. But even where we have these follow-up RV observations there remain many open questions about the best ways to model these data and how we can use it to learn about the demographics of exoplanet populations.

In this thesis I focus on using RV observations to understand exoplanets. In Chapter 3 I use new observations to characterise a new planet, TOI-544b, and confirm the discovery of a second planet in the same system. TOI-544b has an unusual composition, a possible water-world, and is a top candidate for future atmospheric studies. In Chapter 4 I use archival data of a sample of known small planets to test how modelling choices impact the planet masses we find. For each

Abstract 4

planet I complete a homogeneous analysis with a variety of modelling choices, from this I find that just one change in model choice can impact planet mass up to a factor of 4 even for identical data sets. In Chapter 5 I use these new homogeneously-derived planet masses to show that the inferred compositions are consistent with predictions and propose the top candidates for future study. And finally, in Chapter 6 I use my own RV observations to search for previously-unknown planets which could be causing the migration of gas giants into unusual orbits, finding that some of my sample have potential companions.

Abstract 5

Impact Statement

Just a few decades ago it seemed impossible that the alien planets popular in science fiction could be anything other than just that; fiction. Now though, the study of exoplanets has enabled us to detect a wide diversity in planets in unusual systems across our galaxy. This area of research has opened up many new questions in how these planets come to be and how similar, or different, are they from our own Earth. By detecting and characterising exoplanets we can contribute to many areas of science: the study of star and planet formation; Earth and planetary science/geosciences; astrobiology and the search for life; and even solar physics. The interdisciplinary nature of this field allows for significant impact on the wider scientific community.

In this thesis I contribute directly to the scholarly research in exoplanets: Chapters 3 and 4 are both peer-reviewed works published in academic journals. Chapters 5 and 6 will also be submitted for publication soon. Chapter 3 presents a new planet which I characterised with ground-based observations. This unique planet has the potential to help answer questions on the types of planets we find outside of our solar system. Additionally, future observations of this planet may reveal it to harbour a large ocean, something which is an attractive candidate in searches for life. This search for potentially-habitable conditions would be of both scientific and public interest. In Chapters 4 and 5 I demonstrate the importance of homogeneity in our analysis of observations to find exoplanet masses. This is the first time such a large-scale homogeneous analysis of archival data has been completed for exoplanet masses. Finally, in Chapter 6 I present new observation data of a sample of giant planets in unusual orbits. These new data are now publicly available and so can be used by the community for many different scientific projects going forward.

More widely, the study of planets outside out Solar system is one of great public interest, with stories of strange new planets often being highlighted in national news. By continuing to contribute to this fascinating area of research I also contribute to the wider public understanding of these planets and, in turn, our understanding of our home planet.

Acknowledgements

There are many people to thank for contributing to my PhD journey. Firstly, to my supervisors: Vincent, for giving me this opportunity in the first place (even after I said no to a Masters project with you), and Louise, for teaching me so many things and helping me find joy in science again. And to both of you: thank you for believing in me even when I didn't believe in myself.

Thank you also to my friends at MSSL – especially to Nabil for teaching me to code properly. Thank you to the students at the P&A office in London for making me feel so welcome at a difficult time: in particular to Alex for our coffee chats and Sushuang for giving the best hugs. I owe a huge amount of my success in my PhD to Will and the entire Orbyts team – working with you has been an amazing experience and has inspired me to always strive to do better.

A special thanks goes to the wonderful people of ESO Garching, the student community there is second-to-none and it was a pleasure and privilege to be part of it for over a year. Thank you especially to Giulia and Tommy for our support group during postdoc applications, to Amedeo for being the most entertaining office mate I've ever had, to Tine for always encouraging me, and to David for making me feel at home in Munich. Thanks also to Calum for listening and supporting me and reminding me to rest.

To Caoimhe, thank you so much for always looking after me and having my back, for making me laugh and encouraging me to get out the house when things got tough, for introducing me to the joys of video games and being my personal DJ/librarian/hair stylist. I am so incredibly proud of you and I know you will achieve such great things, I can't wait to see them.

Finally, a thank you to my family for supporting me to pursue my passions (even when it means changing career and becoming a student again). Thank you to Pip for providing unending entertainment during the writing of this thesis – I know you don't understand this so I will make sure you get plenty of carrots as a thank you. Finally, I dedicate this thesis to Ruby and Mason; I hope you look up at the stars and know that your dreams are possible.

Contents

1	Intr	oductio	n to Exoplanets	35
	1.1	Small	exoplanets	36
		1.1.1	Mass-radius relations	38
		1.1.2	The radius valley	41
		1.1.3	What about the water worlds?	44
		1.1.4	The path forward	46
	1.2	Giant 6	exoplanets	47
		1.2.1	The problem with warm Jupiters	50
2	Met	hods		52
	2.1	How to	o characterise an exoplanet	52
		2.1.1	Transits	53
		2.1.2	Radial velocity	53
	2.2	RV ins	struments	54
	2.3	Masses	s from RVs	56
	2.4	Source	es of uncertainty	58
		2.4.1	Stellar activity	59
		2.4.2	Mitigating stellar activity	60
		2.4.3	Gaussian Processes	62
	2.5	Structu	are of this thesis	63
3	TOI	-544 b:	a potential water-world inside the radius valley in a two-	
	plan	et syste	m	66

	3.1	Abstra	ct
	3.2	Introdu	uction
	3.3	Observ	vations
		3.3.1	Space-based Photometry
		3.3.2	Ground-based photometry
		3.3.3	High-resolution HARPS and HARPS-N spectroscopy 72
	3.4	Stellar	Parameters
	3.5	Analys	sis and Results
		3.5.1	Transit model
		3.5.2	Frequency analysis of HARPS data
		3.5.3	Radial velocity analysis
	3.6	Discus	ssion
		3.6.1	Composition of TOI-544 b
		3.6.2	Location in relation to the radius valley
		3.6.3	Planet c
		3.6.4	Potential atmospheric studies of TOI-544 b 95
	3.7	Conclu	usions
4		Ü	ous planet masses I: Reanalysis of archival HARPS radial
		cities	99
	4.1		ct
			uction
	4.3		e selection
	4.4	HARP	S observations
	4.5	Autom	nating the process
	4.6	Radial	velocity modelling choices
	4.7	Result	s and discussion
		4.7.1	Impact of long-term trends
		4.7.2	Impact of eccentricity
		4.7.3	Impact of GP dimension
		4.7.4	Model comparison

		4.7.5 TIC 98720809: A representative example	
	4.8	Caveats and recommendations	
	4.9	Conclusions	1
5	Hon	nogeneous planet masses II: Small planet demographics 133	
	5.1	Introduction	
	5.2	Stellar Parameters	
	5.3	A new sample of homogeneous planet masses	
	5.4	The radius valley	
		5.4.1 Below the valley	
		5.4.2 Above the valley	
		5.4.3 Inside the valley	
	5.5	The potential for atmospheric follow-up	1
	5.6	Conclusions	
6	A Se	earch for warm Jupiter companions to test formation pathways 153	
	6.1	Introduction	
	6.2	Target Selection	
	6.3	RV observations	
	6.4	RV analysis and modelling	
	6.5	Results	
		6.5.1 HD 167768	1
		6.5.2 HD 203949	
		6.5.3 HD 206255	
		6.5.4 HD 207229	
		6.5.5 HD 13445	
	6.6	Discussion	
	6.7	Conclusion	
7	Con	clusions 171	
	7.1	Small planet compositions	
	7.2	The importance of consistency	

nts	11
nts	11

	7.3	When RVs alone are insufficient	176
	7.4	Looking to the future of exoplanet characterisation	177
Ap	pend	ices	180
A	App	endix material for Chapter 3	180
В	App	endix material for Chapter 4	196
	B.1	Individual systems	196
		B.1.1 Removal of RV data	196
		B.1.2 Defining priors	197
	B.2	Stellar IDs observation summary	197
C	App	endix material for Chapter 6	203
Bil	bliogr	aphy	230

List of Figures

1.1	The measured mass and orbital period for all confirmed exoplanets	
	which have mass and radius measurements (as of 20/03/2025 ac-	
	cording to the NASA Exoplanet Archive, planets with only a mass	
	limit are excluded). The different colours represent common group-	
	ings of exoplanet categories. Orange shows the hot Jupiter planets	
	(orbital periods less than 10 days and radii greater than 10 R_{\oplus}),	
	yellow the warm Jupiters (same radii but orbital periods between	
	10 and 200 days), and blue for the cold Jupiters (same radii but	
	orbital periods greater than 200 days). The purple colour shows the	
	population of small planets (radii less than 4 $R_{\oplus})$ and pink is for	
	intermediate between small and giant (radii between 4 and 10 R_{\oplus}).	
	The grey squares show the positions of solar system planets. Note	
	that error bars are not included on this plot. The sparsity of planets	
	of short period and intermediate mass is visible in the left of the plot.	
	This under-density in detections is often referred to as the Neptune	
	desert	37
1.0	Descripted from Man Federal (2010). Dedicate of fourtiers of	
1.2	Reprinted from Van Eylen et al. (2018). Radius as a function of	
	orbital period. In grey, data points and uncertainties by Fulton et al.	
	(2017) are shown, while the sample described in Van Eylen et al.	
	(2018) is shown in red. In many cases, the uncertainties are smaller	
	than the symbol size. The bottom plot highlights the part of the	
	sample where the radius gap occurs, around 2 R_{\oplus}	43

1.3	Reprinted from Fortney et al. (2021). Origins hypotheses for hot	
	Jupiters: in-situ formation, disk migration, and high eccentricity	
	tidal migration.	49

2.2 Reprinted from Perryman (2018). An elliptical orbit in three dimensions. The reference plane is tangent to the celestial sphere, *i* is the inclination of the orbit plane, and the nodes define the intersection of the orbit and reference planes. Ω is the longitude of the ascending (receding) node, measured in the reference plane. ω is the fixed angle defining the object's argument of pericentre relative to the ascending node. The true anomaly, ν(t), is the time-dependent angle characterising the object's position along the orbit. The right-handed x y z coordinate system has x towards east (increasing α), y towards north (increasing δ), and z away from the observer. The reference axis, y, contrasts with the use of x, the vernal equinox, as adopted for the solar system.

2.3	Reprinted from Rajpaul et al. (2015). GP model fit to SOAP 2.0	
	data, based on a simulation of four rotating spots (each with radius	
	5% of the stellar radius) at latitudes $\phi = 0^{\circ}$, 30°, 45°,6 0°, equally	
	spaced in longitude, with time sampling and noise levels taken from	
	one season of a real HARPS dataset, plus an injected Keplerian	
	signal. Here the injected signal has an amplitude comparable to, but	
	period different from, the rotationally-modulated activity signals.	
	The top panel shows the model fit to the ΔRV time series, including	
	residuals - the total combined GP and Keplerian fit (black line)	
	with $1-\sigma$ uncertainty shown in grey; the bottom panel shows the	
	Keplerian component of the fit	64
3.1	TESS light curves from Sector 6 (left) and 32 (right). SPOC light	
	curves are shown in the upper panel, with a full transit and noise	
	model (see Section 3.5.1) shown in blue. In the middle panel, TESS	
	light curves are shown after subtracting the best-fit GP model, and	
	residuals are shown in the bottom row	70
3.2	Generalised Lomb-Scargle Periodograms of the WASP-South data	
	for TOI-544. The horizontal line is the estimated 1% false-alarm	
	probability, data after phase 0.5 are in grey. The right-hand panels	
	show the data folded on the 20-d rotational period	71
	•	
3.3	Phase-folded TESS photometry from Sector 6 (top) and Sector 32	
	(bottom), with the best-fit transit model in blue, the lower panel of	
	each shows the residuals to the best fit model. The larger black	
	points show the data binned by a factor of 30	78

85

Generalised Lomb-Scargle periodograms of the SERVAL RV measurements and activity indicators of TOI-544. The right and left columns cover two frequency ranges encompassing the orbital frequency of TOI-544 c, the stellar rotation frequency and its first two harmonics (left panels), and the orbital frequency of TOI-544 b (right panels). The Doppler signals from the two planets are marked as vertical red dashed lines at $f_c \approx 0.02 \, d^{-1}$ (TOI-544 c) and $f_b \approx 0.646 \,d^{-1}$ (TOI-544b). Vertical, blue dashed lines indicate the stellar rotation frequency $(f_{rot} \approx 0.051 \ d^{-1})$ and its first two harmonics (2 $f_{rot} \approx 0.102\,d^{-1}$ and 3 $f_{rot} \approx 0.153\,d^{-1}).$ The horizontal red dashed line mark the 0.1% false alarm probability. The shaded yellow band highlights the frequency range encompassing the long-period activity signals that we significantly detected in the the FWHM, contrast, dLW, $H\alpha$, and Na D1, and that are likely related to spot evolution, along with their 1-year aliases (Sect. 3.5.2), last paragraph. From top to bottom: the SERVAL RV measurements; RV residuals following the subtraction of the Doppler reflex motion induced by TOI-544 c; RV residuals after subtracting the signals of the star rotation, its first two harmonics, and TOI-544 c; FWHM; BIS; contrast; dLW; CRX; S-index; H α ; Na D1; Na D2.

3.6	The phase-folded RV data from HARPS (orange circles) and
	HARPS-N (blue diamonds) alongside the best-fit planet model for
	TOI-544 b. The effect of TOI-544 c and the GP model have been
	subtracted. The lower part shows the residuals from the fit. There
	appears to be no trends visible in the residuals

 3.8 Mass-radius diagram showing confirmed planets with mass uncertainties < 20% in grey circles, with TOI-544 b shown as the black circle. Left: the coloured tracks show different potential planet compositions from Zeng et al. (2019), assuming a planetary equilibrium temperature of 1000 K. The dashed lines show compositions of an Earth-like rocky core surrounded by a layer of H-He in varying percentages by mass, the solid lines show water world compositions with varying water mass fractions, the dotted lines show rocky and Earth-like rocky compositions. TOI-544 b is closest to the tracks with 100% H₂O and 50% H₂O with 50% rock. Right: the same as the left panel but the dashed lines show compositions of an Earth-like rocky core surrounded by a layer of H-He in varying percentages by mass from Lopez and Fortney (2014) using the models for a 10Gyr planet, with solar metalicity and flux of $10F_{\oplus}$, the solid lines show compositions from Aguichine et al. (2021) of irradiated ocean worlds with varying water mass fractions, and the dotted lines show the same rocky and Earth-like rocky compositions from Zeng et al. (2019). TOI-544 b is closest to models with either 30% water mass fraction, or a rocky core with a Hydrogen envelope of between 0.5 - 1%. The data is downloaded from the NASA Exoplanet Archive. 89

 3.10 Top panel: The transmission spectroscopy metric (TSM) against equilibrium temperature of all small (R $< 4R_{\oplus}$) confirmed planets with a mass measurement, blue dots. The threshold given in Kempton et al. (2018) is shown by the solid line. TOI-544 b is shown in the black circle, it is within the top 15 planets for TSM value. Bottom Panel: Same as above but for the emission spectroscopy metric (ESM). TOI-544 b is within the top 10 planets for ESM value. The data is downloaded from the NASA Exoplanet Archive.

- 4.1 Histograms showing the properties of the stars and planets in our sample: (a) Stellar mass. (b) Stellar effective temperature. (c) Planet orbital period. (d) Planet radius. (e) Multiplicity (number of planets per star). (f) Number of RV observations per system. 105
- 4.2 Impact of long-term trends. Panel (a): Comparison of the RV amplitude found for each target for three different models, (a), (b), and (c). Error bars show the 1σ uncertainty from the MCMC posteriors. Target names are given as TIC IDs with the letter of the planet. Panel (b): Histogram showing the root-mean-squared error of the residuals to the fit. Panel (c): Histogram showing the RV amplitude found compared to model (a). Panel (d): Histogram showing the amplitude of the trend found (for the linear trend in m s⁻¹ days⁻¹, for the quadratic trend in $m s^{-1} days^{-2}$). The asterisk marks cases where the value for the quadratic trend amplitude has been multiplied by 1000 to plot on the same axes. Panel (e): Histogram showing the 1σ uncertainty in the RV amplitude found for the different models. . 116

4.3	Impact of orbital eccentricity. Panel (a): Comparison of the RV
	amplitude found for each target for three different models, (a), (d),
	and (e). Error bars show the 1σ uncertainty from the MCMC
	posteriors. Target names are given as TIC IDs with the letter of
	the planet. Panel (b): Histogram showing the RMS error of the
	residuals to the fit. Panel (c): Histogram showing the RV amplitude
	found compared to model (a). Panel (d): Histogram showing the
	value of eccentricity found. Panel (e): Histogram showing the 1σ
	uncertainty in the RV amplitude found for the different models 120

- 4.4 Impact of GP dimension. Panel (a): Comparison of the RV amplitude found for each target for four different models, (a), (f), (h), and (k). Error bars show the 1σ uncertainty from the MCMC posteriors. Target names are given as TIC IDs with the letter of the planet. Panel (b): Histogram showing the RMS error of the residuals to the fit. Panel (c): Histogram showing the RV amplitude found compared to model (a). Panel (d): Histogram showing the RV amplitude found for models (h) and (k) compared to model (f). Panel (e): Histogram showing the 1σ uncertainty in the RV amplitude found for the different models.

4.6	Best-fitting two-planet orbital model for TIC 9870809. HARPS
	data shown by blue circles as a function of time. The best-fitting
	model for the planet signals is shown in red, the 3D GP model in
	blue, and the combined planets and GP shown in black. The dark
	and light shaded areas show the 1σ and 2σ credible intervals of the
	corresponding GP model, respectively
4.7	Phase-folded RV data from HARPS (blue circles) alongside the
	best-fitting planet model for TIC 9870809 b (with the effect of the
	other planet and the GP model subtracted). The lower part shows
	the residuals from the fit. There appears to be no trends visible in
	the residuals
4.8	Phase-folded RV data from HARPS (blue circles) alongside the
	best-fitting planet model for TIC 9870809 c (with the effect of the
	other planet and the GP model subtracted). The lower part shows
	the residuals from the fit. There appears to be no trends visible in
	the residuals
4.9	Planet model with no GP beta distribution on eccentricity for TIC
	9870809. HARPS data shown by blue circles as a function of time.
	The best-fitting model for the planet signals is shown in black. The
	model does not fit the data well
4.10	Phase-folded RV data from HARPS (blue circles) alongside the
	planet model with no GP beta distribution on eccentricity for TIC
	9870809 b (with the effect of the other planet subtracted). The planet
	signal is hardly visible
4.11	Phase-folded RV data from HARPS (blue circles) alongside the
	planet model with no GP beta distribution on eccentricity for TIC
	9870809 c (with the effect of the other planet subtracted). The lower
	part shows the residuals from the fit. The planet signal is hardly
	visible 129

5.1	Planets in our sample which orbit M dwarf stars. Left: planet radius
	versus orbital period. The yellow solid lines show the upper and
	lower boundaries of the radius valley (calculated for the median
	stellar mass of the sample). The planets are colour coded by their
	location relative to the radius valley, calculated for their specific
	stellar mass. Right: the same sample of planets with the same
	colour coding, this time in mass-radius space. The coloured lines
	show theoretical composition tracks: pink lines from Lopez and
	Fortney (2014), purple lines from Aguichine et al. (2021), and green
	from Zeng et al. (2019)

5.3 Left: Planets in our sample which orbit M dwarf stars and are below the radius valley. Planet mass versus radius for the planets which are below the radius valley shown in Figure 5.1. Right: Planets in our sample which orbit FGK stars. Planet mass versus radius for the planets which are below the radius valley shown in Figure 5.2. Lines show theoretical composition tracks for solid planet scenarios. 145

5.4	Planets in our sample which orbit M dwarf stars and are above the
	radius valley. Planet mass versus radius for the planets which are
	above the radius valley shown in Figure 5.1. Left: pink lines show
	Earth-like rocky core surrounded by a layer of H-He in varying per-
	centages by mass from Lopez and Fortney (2014) using the models
	for a 10 Gyr planet, with solar metallicity and flux of 10 $F_{\oplus}.$ Right:
	purple lines show compositions from Aguichine et al. (2021) of ir-
	radiated ocean worlds with varying water mass fractions. In both
	panels: green lines show Earth-like rocky composition from Zeng
	et al. (2019)
5.5	Planets in our sample which orbit FGK stars and are above the radius
	valley. Planet mass versus radius for the planets which are above the
	radius valley shown in Figure 5.2. Left: pink lines show Earth-like
	rocky core surrounded by a layer of H-He in varying percentages by
	mass from Lopez and Fortney (2014) using the models for a 10 Gyr
	planet, with solar metallicity and flux of 10 $F_{\oplus}.$ Right: purple lines
	show compositions from Aguichine et al. (2021) of irradiated ocean
	worlds with varying water mass fractions. In both panels: green
	lines show Earth-like rocky composition from Zeng et al. (2019) 147
5.6	Planets in our sample which orbit M dwarf stars and are inside the
	radius valley. Planet mass versus radius for the planets which are
	inside the radius valley shown in Figure 5.1. Left: pink lines show
	Earth-like rocky core surrounded by a layer of H-He in varying per-
	centages by mass from Lopez and Fortney (2014) using the models
	for a 10 Gyr planet, with solar metallicity and flux of 10 $F_{\oplus}.$ Right:
	purple lines show compositions from Aguichine et al. (2021) of ir-
	radiated ocean worlds with varying water mass fractions. In both
	panels: green lines show Earth-like rocky composition from Zeng
	et al. (2019)

5.7	Planets in our sample which orbit FGK stars and are inside the radius
	valley. Planet mass versus radius for the planets which are inside the
	radius valley shown in Figure 5.2.Left: pink lines show Earth-like
	rocky core surrounded by a layer of H-He in varying percentages by
	mass from Lopez and Fortney (2014) using the models for a 10 Gyr
	planet, with solar metallicity and flux of 10 F_{\oplus} . Right: purple lines
	show compositions from Aguichine et al. (2021) of irradiated ocean
	worlds with varying water mass fractions. In both panels: green
	lines show Earth-like rocky composition from Zeng et al. (2019) 149
6.1	Planet model with a long-term quadratic trend included for HD
	167768. HARPS data shown by blue circles, the data from the
	HIDES instrument are modelled as 3 separate instruments due to
	alterations in the instrument at different times. All as a function of
	time. The best-fitting model for the planet signals is shown in black.
	The overall quadratic trend is visible
6.2	Phase-folded RV data from HARPS (blue circles), and HIDES
	alongside the planet model for HD 167768 b (with the effect of
	the quadratic trend subtracted)
6.3	Planet model with a long-term linear trend included for HD 203949.
	HARPS data shown by blue circles, FEROS data in orange dia-
	monds, and CHIRON data in green squares. All as a function of
	time. The best-fitting model for the planet signals is shown in black.
	The overall linear trend is visible
6.4	Phase-folded RV data from HARPS (blue circles), FEROS (or-
	ange diamonds), and CHIRON (green squares), alongside the planet
	model for HD 203949 b (with the effect of the linear trend subtracted). 163
6.5	Planet model without a long-term trend included for HD 206255.
	HARPS data shown by blue circles, and PFS data in orange dia-
	monds. All as a function of time. The best-fitting model for the
	planet signals is shown in black

6.6	Phase-folded RV data from HARPS (blue circles), and PFS (orange
	diamonds), alongside the planet model for HD 206255 b 164
6.7	Planet model with a long-term linear trend included for HD 207229.
	HARPS data shown by blue circles, CHIRON data in orange dia-
	monds, and FEROS in green squares. All as a function of time.
	The best-fitting model for the planet signals is shown in black. The
	overall linear trend is visible
6.8	Phase-folded RV data from HARPS (blue circles), CHIRON (orange
	diamonds), and FEROS (green squares), alongside the planet model
	for HD 207229 b (with the effect of the linear trend subtracted) 165
6.9	Planet model with a long-term linear trend included for HD 13445.
	HARPS data shown by blue circles, CORALIE as orange diamonds
	and UCLES as green squares. All as a function of time. The best-
	fitting model for the planet signals is shown in black. The short
	orbital period and long observing baseline mean it is difficult to see
	orbital motion, but the overall trend is clear
6.10	Phase-folded RV data from HARPS (blue circles), CORALIE (or-
	ange diamonds) and UCLES (green squares) alongside the planet
	model for HD 13445 b (with the effect of the linear trend subtracted). 167
B.1	Full posterior distribution of fitted parameters for TIC 98720809
	with the 3D GP beta distribution model
B.2	Full posterior distribution of fitted parameters for TIC 98720809
	with the no GP beta distribution model

List of Tables

3.1	Stellar parameters for TOI-544, modelled with SpecMatch-Emp
	and SME, and BASTA and astroARIADNE
3.2	Results of the transit and RV fit for TOI-544, showing the median
	value and 68 % credible interval for each parameter 87
4.1	Overview of the 12 models applied to RVs and activity indicators in
	this study
4.2	Priors used for all parameters in all models
5.1	Stellar parameters used for the stars in our sample, from Sousa et al.
	(2021). The name of the star, mass in solar masses, mass uncertainty,
	magnitude in V band, and effective temperature in K, are all given 135
5.2	The masses found for each planet in our sample. Also included
	are the planet radii, orbital period and eccentricity from the NASA
	Exoplanet Archive. Plus and minus 1σ uncertainties are included
	for each parameter
5.3	The planets in our sample split into three radius bins, then ordered
	in terms of highest TSM
6.1	The targets observed in the 109.233Q and 113.26DF observing pro-
	grammes. Columns show the main ID, additional names, the right
	ascension and declination, the magnitude in V-band and the expo-
	sure time of observations. Stellar data all from the NASA Exoplanet
	Archive

6.2	Number of observations of each of the 5 targets analysed in this
	work. The first column shows observations as part of our HARPS
	programme, the following column shows publicly available observa-
	tions which were included in our analysis. These are from the HIgh
	Dispersion Echelle Spectrograph, (HIDES, Izumiura, 1999), the
	Fiber-fed Extended Range Optical Spectrograph, (FEROS, Kaufer
	and Pasquini, 1998), CHIRON (Schwab et al., 2012), the Planet
	Finder Spectrograph (PFS, Crane et al., 2010), CORALIE (Queloz
	et al., 2000), and the University College London Echelle Spectro-
	graph (UCLES Diego et al., 1990)
6.3	AIC for each model of each target, as well as the amplitude of trend
	found for those models which include long term trend parameters 159
A.1	Absolute radial velocities and spectral activity indicators measured
	from the HARPS spectra with the DRS
A.2	Relative radial velocities and spectral activity indicators measured
	from the HARPS spectra with SERVAL and TERRA 185
A.3	Absolute radial velocities and spectral activity indicators measured
	from the HARPS-N spectra with the DRS
Λ 1	Relative radial velocities and spectral activity indicators measured
Λ.4	from the HARPS-N spectra with SERVAL and TERRA 193
	-
A.5	
	1-sigma
A.6	Priors used for the RV fitting for each parameter. $\mathcal{U}[a,b]$ refers to
	uniform priors in the range $a - b$, $\mathcal{N}[a,b]$ refers to a Gaussian prior
	with mean a and width b, and $\mathcal{F}[a,b]$ is a fixed parameter at value a. 195
A.7	Priors used for the transit fitting for each parameter. $\mathcal{U}[a,b]$ refers to
	uniform priors in the range $a-b$, $\mathcal{N}[a,b]$ refers to a Gaussian prior
	with mean a and width b, and $\mathcal{F}[a,b]$ is a fixed parameter at value a. 195

B.1	The T_c values added manually for targets where the NASA Exoplanet
	Archive does not provide these
B.2	Priors used for the 3D GP model with beta distribution on eccen-
	tricity for TIC 9870809
B.3	Fitted and derived parameters for the 2-planet system TIC 9870809. 201
B.3	The different identifiers of all stars in our sample
C .1	RV data used for modelling of HD 13445
C.2	RV data used for modelling of HD 167768
C.3	RV data used for modelling of HD 203949
C.4	RV data used for modelling of HD 206255
C 5	RV data used for modelling of HD 207229

UCL Research Paper Declaration Form: referencing the doctoral candidate's own published work(s)

- 1. **1. For a research manuscript that has already been published** (if not yet published, please skip to section 2):
 - (a) What is the title of the manuscript? TOI-544 b: a potential waterworld inside the radius valley in a two-planet system
 - (b) Please include a link to or doi for the work: https://doi.org/ 10.1093/mnras/stad3837
 - (c) Where was the work published? Monthly Notices of the Royal Astronomical Society
 - (d) Who published the work? Oxford University Press
 - (e) When was the work published? 13 December 2023
 - (f) List the manuscript's authors in the order they appear on the publication: H L M Osborne, V Van Eylen, E Goffo, D Gandolfi, G Nowak, C M Persson, J Livingston, A Weeks, E Pallé, R Luque, C Hellier, I Carleo, S Redfield, T Hirano, M Garbaccio Gili, J Alarcon, O Barragán, N Casasayas-Barris, M R Díaz, M Esposito, E Knudstrup, J S Jenkins, F Murgas, J Orell-Miquel, F Rodler, L Serrano, M Stangret, S H Albrecht, A Alqasim, W D Cochran, H J Deeg, M Fridlund, A P Hatzes, J Korth, K W F Lam
 - (g) Was the work peer reviewed? Yes
 - (h) Have you retained the copyright? Yes
 - (i) Was an earlier form of the manuscript uploaded to a preprint server (e.g. medRxiv)? If 'Yes', please give a link or doi Yes, https://doi.org/10.48550/arXiv.2310.14908
 - If 'No', please seek permission from the relevant publisher and check the box next to the below statement:
 - □ I acknowledge permission of the publisher named under 1d to include in this thesis portions of the publication named as included in

List of Tables

29

1c.

2. For a research manuscript prepared for publication but that has not yet

been published (if already published, please skip to section 3):

(a) What is the current title of the manuscript?

(b) Has the manuscript been uploaded to a preprint server 'e.g.

medRxiv'?

If 'Yes', please give a link or doi:

(c) Where is the work intended to be published?

(d) List the manuscript's authors in the intended authorship order:

(e) Stage of publication:

3. For multi-authored work, please give a statement of contribution covering

all authors (if single-author, please skip to section 4): I led the analysis

and writing of the paper. VVE contributed to writing the manuscript. EG

contributed to RV analysis. DG, GN, EP, RL and CH contributed observation

data. CP, JL, TH and AW contributed to the stellar modelling. IC and

SR contributed to the atmospheric modelling discussion. Observations were

made possible by MGG, JA, OB, NC-B, MD, ME, EK, JJ, FM, JO-M, FR,

LS and MS. KESPRINT consortium members who contributed to observing

proposals and the writing of the paper are SA, AA, WC, HD, MF, APH, JK

and KWFL.

4. In which chapter(s) of your thesis can this material be found? Chapter 3

e-Signatures confirming that the information above is accurate (this form

should be co-signed by the supervisor/ senior author unless this is not appropriate,

e.g. if the paper was a single-author work):

Candidate: Hannah Osborne

Date: 21/4/25

Supervisor/Senior Author signature (where appropriate): Vincent Van Eylen

Date: 21/04/25

UCL Research Paper Declaration Form: referencing the doctoral candidate's own published work(s)

- 1. **1. For a research manuscript that has already been published** (if not yet published, please skip to section 2):
 - (a) What is the title of the manuscript? Homogeneous planet masses I: Reanalysis of archival HARPS radial velocities
 - (b) Please include a link to or doi for the work: https://doi.org/ 10.1051/0004-6361/202452127
 - (c) Where was the work published? Astronomy & Astrophysics
 - (d) Who published the work? EDP Sciences
 - (e) When was the work published? 23 December 2024
 - (f) List the manuscript's authors in the order they appear on the publication: H L M Osborne, L D Nielsen, V Van Eylen and O Barragán
 - (g) Was the work peer reviewed? Yes
 - (h) Have you retained the copyright? Yes
 - (i) Was an earlier form of the manuscript uploaded to a preprint server (e.g. medRxiv)? If 'Yes', please give a link or doi Yes, https://doi.org/10.48550/arXiv.2411.12723
 - If 'No', please seek permission from the relevant publisher and check the box next to the below statement:
 - □ I acknowledge permission of the publisher named under 1d to include in this thesis portions of the publication named as included in 1c.
- 2. For a research manuscript prepared for publication but that has not yet been published (if already published, please skip to section 3):
 - (a) What is the current title of the manuscript?
 - (b) Has the manuscript been uploaded to a preprint server 'e.g.

List of Tables

32

medRxiv'?

If 'Yes', please give a link or doi:

(c) Where is the work intended to be published?

(d) List the manuscript's authors in the intended authorship order:

(e) Stage of publication:

3. For multi-authored work, please give a statement of contribution covering

all authors (if single-author, please skip to section 4): I led the analysis and

the writing of the paper. LN and VVE contributed to project design and

writing of the paper. OB contributed to the discussion on GPs and stellar

activity.

4. In which chapter(s) of your thesis can this material be found? Chapter 4

e-Signatures confirming that the information above is accurate (this form

should be co-signed by the supervisor/ senior author unless this is not appropriate,

e.g. if the paper was a single-author work):

Candidate: Hannah Osborne

Date: 21/04/25

Supervisor/Senior Author signature (where appropriate): Vincent Van Eylen

Date: 21/04/25

UCL Research Paper Declaration Form: referencing the doctoral candidate's own published work(s)

- 1. **1. For a research manuscript that has already been published** (if not yet published, please skip to section 2):
 - (a) What is the title of the manuscript?
 - (b) Please include a link to or doi for the work:
 - (c) Where was the work published?
 - (d) Who published the work?
 - (e) When was the work published?
 - (f) List the manuscript's authors in the order they appear on the publication:
 - (g) Was the work peer reviewed?
 - (h) Have you retained the copyright?
 - (i) Was an earlier form of the manuscript uploaded to a preprint server (e.g. medRxiv)? If 'Yes', please give a link or doi
 - If 'No', please seek permission from the relevant publisher and check the box next to the below statement:
 - □ I acknowledge permission of the publisher named under 1d to include in this thesis portions of the publication named as included in 1c.
- 2. For a research manuscript prepared for publication but that has not yet been published (if already published, please skip to section 3):
 - (a) What is the current title of the manuscript? Homogeneous planet masses II: Small planet demographics
 - (b) Has the manuscript been uploaded to a preprint server 'e.g. medRxiv'?
 - If 'Yes', please give a link or doi: No

List of Tables

34

(c) Where is the work intended to be published? Astronomy & Astro-

physics

(d) List the manuscript's authors in the intended authorship order: H

L M Osborne, A Weeks, M-L Steinmeyer, L D Nielsen, V Van Eylen,

and C Dorn

(e) Stage of publication: In prep.

3. For multi-authored work, please give a statement of contribution covering

all authors (if single-author, please skip to section 4): I led the analysis and

writing of the paper. AW provided the stellar parameters. M-LS provided

the theoretical composition tracks. LN and VVE contributed to the creation

of the project and writing the paper. CD contributed to discussion on planet

compositions.

4. In which chapter(s) of your thesis can this material be found? Chapter 5

e-Signatures confirming that the information above is accurate (this form

should be co-signed by the supervisor/ senior author unless this is not appropriate,

e.g. if the paper was a single-author work):

Candidate: Hannah Osborne

Date: 21/04/25

Supervisor/Senior Author signature (where appropriate): Vincent Van Eylen

Date: 21/04/25

Chapter 1

Introduction to Exoplanets

Exoplanet studies have fundamentally changed our view of our own solar system. With over 5800 confirmed detections of planets orbiting other stars¹ it has become increasingly clear that the blueprint of our solar system is not standard across the galaxy. In fact, the very first exoplanet detected around a Sun-like star, 30 years ago now (Mayor and Queloz, 1995), was of a type not seen at all in our solar system. By continuing to discover new exoplanets in exciting parameter space regimes we can begin to build up a picture of how unique our Earth really is – how different can these alien worlds be from our home planet? Simultaneously, increasing work on the characterisation of these systems, particularly at a population level, is starting to allow for greater understanding of how planetary systems might be formed and evolve over time. But there are still many unanswered and emerging questions in this relatively-young area of research.

While stars have spectral types and galaxies can be classified into types, exoplanets lack such comprehensive definitions. Within our solar system there are 3 general categories we might place each planet into: rocky planets (also called terrestrial planets), ice giants, and gas giants (Winn and Fabrycky, 2015). Of course there are also a host of dwarf planets, asteroids, trans-Neptunian objects etc. but here we focus on just the planets. Based on the physical characteristics of each planet – such as mass, radius and density – we can neatly fit every planet into a category with no ambiguity. Additionally, the location of the different types of planets with respect

https://exoplanetarchive.ipac.caltech.edu/

to the Sun also point to a formation mechanism that preferentially produces small planets close to their star with giant planets further out (Mizuno, 1980; Pollack et al., 1996). So we might think that other stellar systems will have a similar make up in terms of the types and locations of planets. However, this has not been the case for any currently detected exoplanet systems (Winn and Fabrycky, 2015; Zhu and Dong, 2021). Figure 1.1 shows the distribution in mass and orbital period of all confirmed exoplanets which have measured masses and radii. There is a huge variety in these parameters – the masses vary by 5 orders of magnitude and the orbital periods by 6. Also shown are the solar system planets. The addition of these data points shows two things: the exoplanets detected do not occupy the same parameter space as those in our solar system; and there are many planets in between the typical groupings of solar system planets.

1.1 Small exoplanets

Of the 5856 confirmed exoplanet detections to date² about 4400 of these have a radius measurement. Of these confirmed planets with measured radii, around 75% of them are what we might consider small planets – with radii less than 4 Earth radii, or, in other terms, smaller than Neptune, and around 16% of these could be called giant planets – roughly 10 times the size of the Earth and larger (i.e., around Jupiter or bigger). The remaining 9% comprise intermediate size planets. Population studies have shown that small planets are numerous across the galaxy (e.g. Winn and Fabrycky, 2015; Zhu and Dong, 2021), but their nature remains somewhat of a mystery. In fact, of the detected small planets, only 516 have a measured mass – that's only 9% of the total confirmed exoplanets. In order to find the bulk density and thereby begin to estimate planet compositions, it is essential to have a mass measurement. So if we want to do demographics studies we need more measurements of small planet masses. In addition to this, the mass measurements we do have come from a wide range of sources: including different methods of deriving masses e.g. from radial velocity observations, transit-timing

²As of 20/03/25

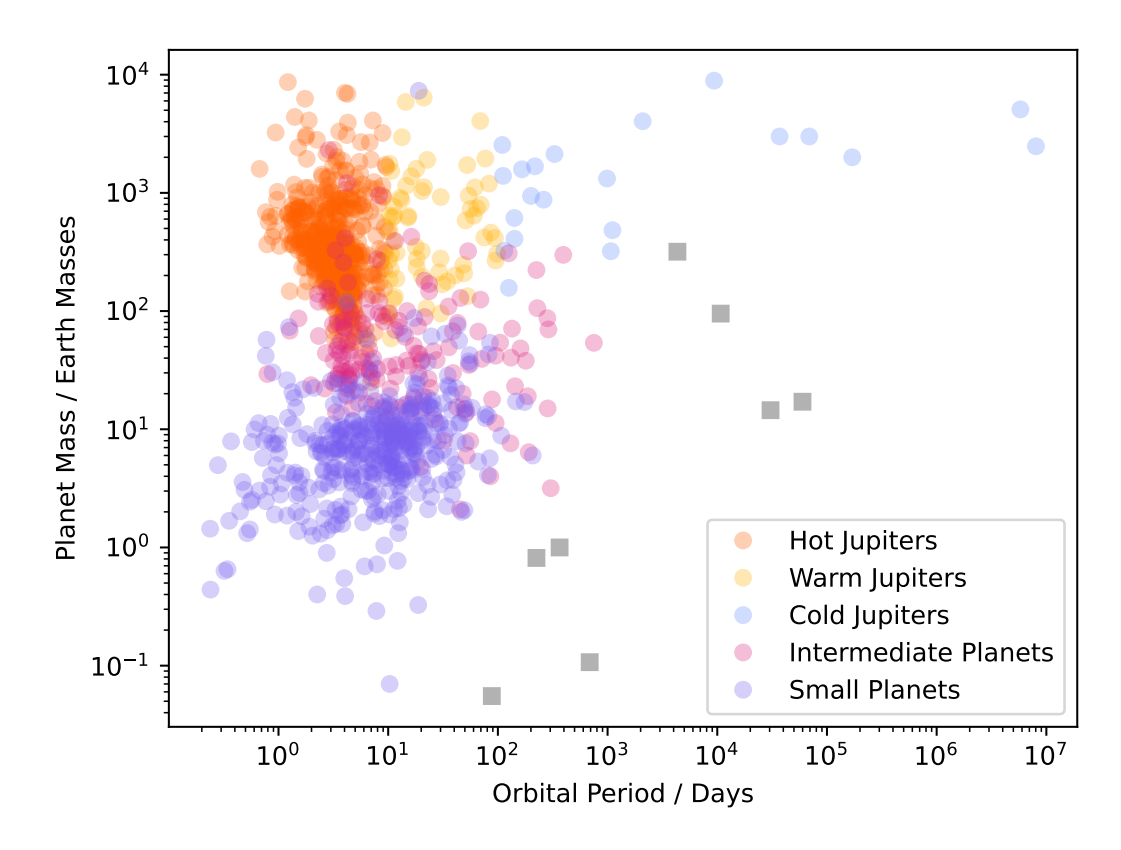


Figure 1.1: The measured mass and orbital period for all confirmed exoplanets which have mass and radius measurements (as of 20/03/2025 according to the NASA Exoplanet Archive, planets with only a mass limit are excluded). The different colours represent common groupings of exoplanet categories. Orange shows the hot Jupiter planets (orbital periods less than 10 days and radii greater than $10\,R_\oplus$), yellow the warm Jupiters (same radii but orbital periods between 10 and 200 days), and blue for the cold Jupiters (same radii but orbital periods greater than 200 days). The purple colour shows the population of small planets (radii less than $4\,R_\oplus$) and pink is for intermediate between small and giant (radii between 4 and $10\,R_\oplus$). The grey squares show the positions of solar system planets. Note that error bars are not included on this plot. The sparsity of planets of short period and intermediate mass is visible in the left of the plot. This under-density in detections is often referred to as the Neptune desert.

variations, and astrometry (Perryman, 2011). Each research group may use different telescopes, different choices and assumptions in modelling, and different statistical techniques to derive an actual planet mass. This can lead to the problem of a single planet having multiple published mass measurements – sometimes with significant differences between them. So not only do we need more measurements of planet masses, we also need to ensure that the masses we already have are consistent with one-another if we want to do statistics at a population level.

Putting aside the problems for a moment, what do we already know about the nature of small exoplanets from theory and observations?

1.1.1 Mass-radius relations

To try and understand the compositions and characteristics of small planets, we can place planets on a mass-radius diagram. This allows us to both look at the population as a whole and compare it to planets in the solar system. As the detections of small exoplanet masses and radii increased, teams began to investigate the mass-radius relationship for small exoplanets. This is to try and answer the question of what can we learn about a planets' composition from its mass and radius? If all small planets follow a single relation then it should be relatively easy to extrapolate what mass we expect for a planet of specific radius and vice versa. If the planets follow multiple, fairly well-defined, relations then we can use these as a way to categorise planets into types.

An early attempt to construct this mass-radius relationship was presented in Seager et al. (2007). Here they constructed a theoretical mass-radius relation for solid exoplanets using interior models of cold planets which they assumed are made primarily of iron, silicates, water and carbon compounds. They found several key results. Firstly, that planets are not likely to be formed of anything more dense than iron and the smallest planets theoretically possible have radii corresponding to a pure iron composition. Secondly, they found that several different populations of planets could occupy this 'small'-planet parameter space. There could be super-Earths (Earth-like rocky cores without significant atmospheres), sub-Neptunes (Earth-like rocky cores with hydrogen-helium, H-He, envelopes), water worlds (made of a

significant portion of water ices), and potentially carbon planets. However, Seager et al. (2007) suggest that it is only possible to distinguish between planets with significant H-He envelopes and those without. They say that there are significant degeneracies in the theoretical compositions of planets and so from mass and radius alone it would be challenging to tell the actual composition of planets with different mass fractions of materials. Swift et al. (2012) then provided an update to this work by deriving mass-radius relations for different materials using equations of state which account for the pressures likely experienced within planets.

Some other works have focused on finding an empirical mass-radius relationship, rather than theoretical ones. Weiss et al. (2013) analysed the mass, radius and incident flux of 138 exoplanets and found a breakpoint in the mass-radius relation at 150 M_{\oplus} . For planets above their 150 M_{\oplus} breakpoint they note that increasing incident flux also increases the planet radius – these larger planets become inflated at higher temperatures. In fact, they find that for these larger mass planets, the incident flux is more important for predicting a planet's radius than the mass (Weiss et al., 2013). Conversely, the lower mass planets below 150 M_{\oplus} show the opposite effect: the radii decrease on average as incident flux increases. Therefore, for these planets, the mass is more important for predicting the radius of the planet. However, it is noted that the 150 M_{\oplus} was chosen by-eye from plotting the mass-radius diagrams for their sample, rather than for a physically-motivated reason.

Looking specifically at the mass-radius relation for small planets, Weiss and Marcy (2014) aimed to find the mass-radius relation for 65 exoplanets below 4 R_{\oplus} . To do this they found the weighted mean densities of planets in bins of 0.5 R_{\oplus} . They found that at 1.4 R_{\oplus} there was a maximum in density of 7.6 g cm⁻³ (for reference the Earth has density 5.51 g cm⁻³) and that, on average, the density of planets increases with increasing radius up to 1.5 R_{\oplus} . The suggested reason for this is because rock is slightly compressible and so accreting additional material will cause the density to also increase. However, between 1.5 - 4 R_{\oplus} the density of planets actually tends to decrease with increasing radius – this can only be sufficiently explained with the addition of volatile materials. Adding a small percentage by mass of hydrogen

and helium can significantly increase the size of a planet without increasing its mass (thereby reducing the density). The mass-radius relations in Weiss and Marcy (2014) are consistent with the theoretical prediction of Seager et al. (2007), however there is a very large reduced χ^2 value, potentially indicating a large scatter in planet compositions at a given radius.

In order to select the planet sample the only selection criteria used by Weiss and Marcy (2014) was that $R_p < 4$ R_{\oplus} and the planets must have a marginal mass, a mass upper-limit or a mass determination. However at the time this work was done there were very few mass measurements of exoplanets less than 4 R_{\oplus} and even fewer for less than 1.5 R_{\oplus} . To overcome this they chose to also include solar system planets within their analysis, however it is noted that the equivalent-size solar system planets are on much wider orbital separations than the exoplanets within the sample (typically 100s of days compared to 10s of days).

A slightly different approach was taken by Hatzes and Rauer (2015) who investigated the mass-density relationship for planets, rather than the mass-radius. Their results suggested that the boundaries between objects should be set at: < 95 M_{\oplus} for low mass planets, giant planets at masses greater than this but < 60 $M_{Jupiter}$, and stellar objects at above 60 $M_{Jupiter}$ (Hatzes and Rauer, 2015).

Following this, Bashi et al. (2017) re-investigated the empirical mass-radius relationship, similar to the methodology in Weiss et al. (2013). They found that the transition between large and small planets occurs at a mass of $124 \pm 7 \, M_{\oplus}$ or radius of $12.1 \pm 0.5 \, R_{\oplus}$. Similarly to Weiss et al. (2013), Bashi et al. (2017) found that for low mass planets the radius increases as a function of mass but for higher mass planets there is a very weak relation between mass and radius.

Chen and Kipping (2017) created a publicly available tool to calculate a planet's mass (or radius) given its radius (or mass). They used a probabilistic relation conditioned on 316 objects which spanned a range of masses and radii, from the smallest planets up to stellar-type objects. The tool also enabled them to categories planets into 4 types based on the breakpoints in their relation: the Terran worlds, Neptunian worlds, Jovian worlds, and stellar worlds. The transition from Terran to

Neptunian worlds is found to be around 2 M_{\oplus} , which is lower but consistent with previous theory works such as Lopez and Fortney (2014).

More recent works have made use of the increasing number of detected exoplanets with both mass and radius measurements. Some works have focused on the possibility of using machine learning methods to categorise exoplanets into types based on a mass-radius relation e.g. Ulmer-Moll et al. (2019); Mousavi-Sadr et al. (2023). Some look to Bayesian mixture models and probabilistic mass-radius or mass-density-radius relations (Neil and Rogers, 2020; Parviainen et al., 2024). Others have focused on collating databases of exoplanet mass and radius measurements which are reliable and up-to-date, enabling reanalysis of previous mass-radius relations. Some of these are described in Otegi et al. (2020) and Sousa et al. (2024).

Many of the works mentioned above have results which are compatible with each other, but not exactly the same. There are several possible ways to make progress in finding a specific mass-radius relation for exoplanets. First, greater understanding from the theoretical side is required: the analysis of materials at high temperatures and pressures is crucial for the calculations of planet compositions and interiors (Swift et al., 2012). More detections of planet mass and radii are also required at a range of parameter space regimes: how does orbital period impact the possible planet compositions? Can we directly compare solar system and exoplanet mass-radius relations? Finally, as more observations of small exoplanets are made possible, we need to ensure that the parameters we derive are both precise and accurate to ensure the demographic relations found are not being biased (Sousa et al., 2024; Otegi et al., 2020).

1.1.2 The radius valley

Another factor which must be accounted for when attempting to categorise planets into types is the detection of the small planet radius valley. This significant discovery came following the NASA Kepler mission (Borucki et al., 2010) which detected thousands of small exoplanets. For the first time it was possible to look at exoplanet demographics (in radius space), and when doing so, an interesting pattern emerged: there is a distinct bi-modality in the distribution of small planet radii. This small

planet radius valley describes the region in the size distribution of exoplanets where few planets exist, specifically between approximately 1.5 and 2.5 R_{\oplus} (Fulton et al., 2017; Van Eylen et al., 2018). This lack of detections in the valley cannot be due to observation bias and so must have some physical origin. This is because we can detect planets both above and below the valley – if it were simply a result of not being able to detect smaller planets then we wouldn't see the lower peak of detections below the valley. Figure 1.2 shows the radius versus orbital period of the planets detected by Kepler. The grey points show the data and uncertainties calculated in Fulton et al. (2017) and the red data points and uncertainties show the sample analysed in Van Eylen et al. (2018). The analysis in Van Eylen et al. (2018) uses a smaller but more precise set of planet radii and orbital periods then those used in Fulton et al. (2017). These more precise parameters are found by making use of asteroseismology to find the stellar parameters, see Van Eylen et al. (2018) for details. Looking at the lower plot, which focuses on the specific region where the valley is located, the gap in detections is clear – especially for the more precise sample shown in red. It is also clear that there is a dependence on orbital period for the location of the valley: there is a downward slope towards longer orbital periods.

A variety of theories have been proposed to explain the radius valley, including photo-evaporation (Lopez and Fortney, 2013; Owen and Wu, 2013; Owen and Wu, 2017), and core-powered mass loss (Collier Cameron and Jardine, 2018; Gupta and Schlichting, 2019, 2021). Both theories predict that planets form as a rocky core surrounded by a layer of atmospheric hydrogen and helium, typically referred to as sub-Neptune planets, and located above the valley in period-radius space. The volatile layers are then removed from the planet, leaving behind a bare rocky core – known as super-Earth planets which are located below the valley in period-radius space. In the photo-evaporation case it is the X-ray and extreme ultraviolet radiation from the star which causes this atmospheric loss. In the core-powered mass-loss case the suggestion is that the leftover internal heat from the planet formation causes the outgassing of the atmosphere from the planet itself. The photo-evaporation model is consistent with the observation that the location of the valley moves downward (in

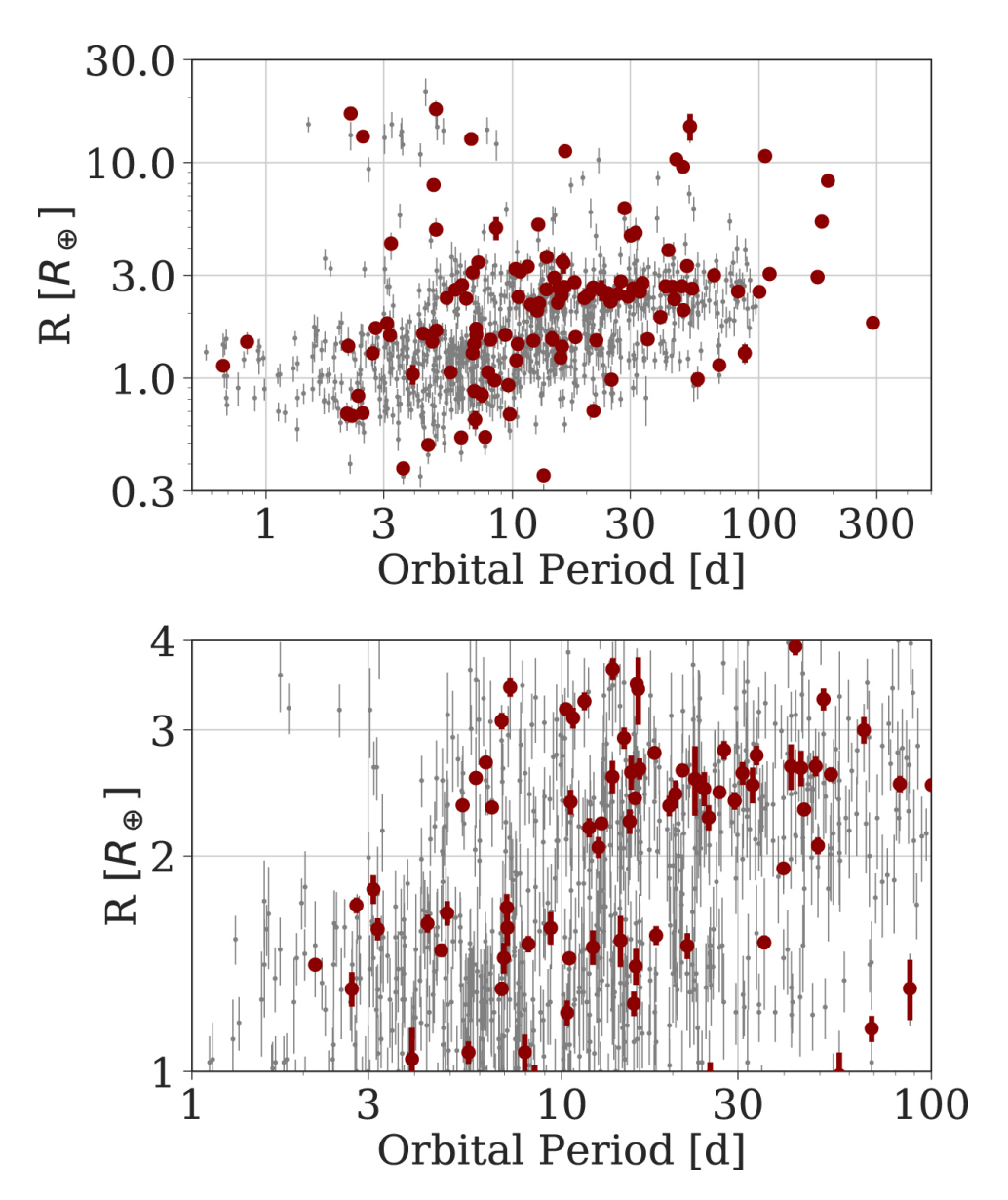


Figure 1.2: Reprinted from Van Eylen et al. (2018). Radius as a function of orbital period. In grey, data points and uncertainties by Fulton et al. (2017) are shown, while the sample described in Van Eylen et al. (2018) is shown in red. In many cases, the uncertainties are smaller than the symbol size. The bottom plot highlights the part of the sample where the radius gap occurs, around $2\,R_\oplus$.

radius) at longer orbital periods, this would mean that larger planets can be stripped of their atmospheres closer to the host star as they are receiving a higher level of incident-flux. Additionally, the location of the valley is found to shift to a larger radius for more massive host stars, (Ho and Van Eylen, 2023). This is in agreement with both the photo-evaporation and core-powered mass-loss models. It is very possible that the radius valley forms as a combination of both mechanisms, though in a comparison done by Rogers et al. (2021), it seems that the photo-evaporation case may be the dominant mechanism in shaping the valley.

Whichever mechanism is dominant in causing the radius valley, both agree that there seems to be two categories of small planets: those above and below the valley. These have been to referred to as sub-Neptunes and super-Earths, respectively (Bean et al., 2020). This agrees with many of the mass-radius relations discussed in Section 1.1.1 which separate small planets into groups based on mass-radius, mass-density, or mass-radius-density. The work of Seager et al. (2007) (ten years before the observation of the radius valley) suggested the existence of a population of super-Earth like planets which were distinct from those harbouring volatile layers. Weiss and Marcy (2014) put the turning point in their mass-radius relation at around 1.5 R_{\oplus} , just at the location of the lower boundary of the radius valley. These consistencies may seem very promising in our search of a way to categorise exoplanets. However, there is an important additional possibility which we have yet to include, the existence of water worlds.

1.1.3 What about the water worlds?

Planets with large amounts of water/ice have been predicted by theorists as a common outcome of planet formation models (Kuchner, 2003; Léger et al., 2004; Bitsch et al., 2019) but for many years the detection capabilities were not able to search for direct observational evidence of them. Now though, multiple groups have reported that the densities of some small planets are consistent with a composition containing a large (>10% by mass) fraction of water (e.g. Piaulet et al., 2022; Cadieux et al., 2022; Diamond-Lowe et al., 2022). This would be an interesting result as detecting a close-in planet with a large fraction of water would suggest that it formed further out in

the disk (beyond the snow line, the minimum distance from the star at which water could condense) and then migrated inwards (Seager et al., 2007). Additionally, the detection of a water world for studies of astrobiology and potential searches for life on exoplanets is very appealing (Madhusudhan et al., 2023; Mitchell and Madhusudhan, 2025).

Zeng et al. (2019) demonstrated that, at a theoretical level, the building blocks of planet materials in planet-forming disks could produce water worlds. They also show that the radius valley can be produced by having populations of rocky planets and water worlds – rather than being due to atmospheric escape. However, one complication is that the theoretical models predict mass-radius relations to be very similar for a variety of compositions i.e. there is a large degeneracy in the interpretation of planet compositions. For example, the mass and radius expected for a rocky planet with a thin atmosphere of H-He is almost identical to one composed of a rocky core with a large layer of water. Aguichine et al. (2021) provided an updated set of mass-radius relations for theoretical water world compositions which included the effects of the high irradiation many observed exoplanets experience. Luo et al. (2024) demonstrated that the water contained within a planet may not be on the surface, but rather can be mixed within the mantle and even core. This would imply at the predicted radius of water world planets of a certain mass could be overestimated (Luo et al., 2024).

The idea of water worlds in the observation community gained further attention after Luque and Pallé (2022) showed that for a sample of small exoplanets orbiting M dwarf stars, the mass and radius align exactly with the theoretical composition track for a planet made of 50% rock and 50% water. However, later work by Rogers et al. (2023) suggested that the composition track used was not suitable for this case and that the population could alternatively be explained by atmospheric boil-off processes. An investigation by Chakrabarty and Mulders (2024) then used simulations of planet evolution to show that > 20% of planets without H-He atmospheres around M dwarf stars could be water rich. But following this, the works of Parviainen et al. (2024); Parc et al. (2024) both found no statistical evidence for a third population

of small planets. Most recently, Dainese and Albrecht (2025) used several statistical methods (including a Gaussian mixture model, and a machine-learning based approach to finding planet composition) to investigate whether small planets can be clumped into two or three groups. For all their methods, a two group scenario was preferred over a three-group scenario, suggesting no robust evidence for a separate population of water worlds around M dwarf stars (Dainese and Albrecht, 2025).

The uncertainty on whether water worlds really exist, and if so, are they only found around M dwarf stars, has led to many researchers questioning: where are the water worlds? See Kempton et al. (2023); Chakrabarty and Mulders (2024) for discussions on this topic. Currently, the era of exoplanet atmospheric characterisation is upon us, with observations from telescopes like JWST providing possible water world candidates (e.g. Damiano et al., 2025). As these observations continue we may be able to begin answering these questions on the existence of water worlds.

1.1.4 The path forward

So the questions remain: what different categories of compositions exist for planets between the sizes of Earth and Neptune? Does this vary for different stellar types (specifically M dwarf stars)? And how do these compositions play into the existence of the radius valley? To answer these questions there are several approaches that one could take.

Firstly, detecting and characterising planets which could have unusual compositions (including potential water worlds) and/or planets inside or close to the edges of the radius valley can allow for additional constraints on explanations of small planet compositions. The unambiguous confirmation of a planet with a water-rich composition, particularly if it orbits an M dwarf star, would be strong evidence for the existence of a population of water worlds. Alternatively, detecting signs of atmospheric escape from a planet inside the radius valley could point towards the atmospheric loss scenario, suggesting that small planets fit into two categories rather than three. Either way, studying small planets in and around the radius valley, especially across a range of stellar types and ages, can help inform models of small planet formation and evolution.

Secondly, an important area of focus is in ensuring the observational data we already have is both precise and accurate. The methods used to find planet radii are generally consistent between groups, especially for large survey missions to detect exoplanets such as Kepler or the transitting exoplanet survey satellite (TESS, Ricker et al., 2014). However, the same is not true for the observational techniques used to find exoplanet masses. Even in cases where the same method of observations is used, there are many ways to model the data to actually measure a planet mass. This results in there being multiple published masses for a single detected planet. For population studies this is a major problem: how do you choose which planet mass to use? And is it statistically valid to use multiple methods of analysis in a single demographics study? An understanding of how impactful the homogeneity (or inhomogeneity) of exoplanet mass measurements is on population level statistics is becoming increasingly important as we detect more and more planets.

Some works have already attempted to tackle this problem of inhomogeneity. Dai et al. (2019) performed a homogeneous analysis of the masses (and compositions) of 11 hot-Earth planets using archival data. Many small planets have since been observed and characterised and so this sample could be expanded upon. Some recent surveys have chosen to tackle this issue as new data comes in, such as Polanski et al. (2024) who have a custom analysis pipeline which is followed for all new data. Others have been by designing their survey in a more unbiased way, as presented by Teske et al. (2021). However, there remains a wealth of archival data which has not been analysed in a homogeneous way. A reanalysis of archival data of exoplanet masses done in a consistent would be hugely beneficial for demographics studies. In addition, this would allow for better understanding of just how big an issue this is: how much do planet masses change based on modelling choices?

1.2 Giant exoplanets

Improvements in instrumentation have allowed for increasingly lower mass planets to be discovered and characterised, yet there is still much to learn from giant planets. By observing the physical properties of giant planets we can test whether they match

the predictions of planet formation theory (Fortney et al., 2021). Additionally, these planets are key targets for atmospheric characterisation studies with both ground-and space-based telescopes (e.g. Seidel et al., 2023; Balmer et al., 2025).

Prior to the detection of exoplanets, theories of planet formation focused on the solar system as the expected outcome. It was thought that planets formed from a cloud of gas and dust which then collapsed into a disk. In the outer parts of the disk, beyond the snow lines, more icy materials would be available and so larger planets would grow (Dawson and Johnson, 2018). Whereas in the inner disk, fewer materials would be available for planetary growth and so smaller planets would form (Dawson and Johnson, 2018). The discovery of hot Jupiter planets – giant planets close to their host star – then challenged these theories of planet formation.

There are several suggested origins for hot Jupiter planets. The first being in situ formation, where these giant planets form at their present close-in locations (Dawson and Johnson, 2018; Fortney et al., 2021). This formation could be as a result of either core accretion or gravitational instability. Core accretion models suggest that a rocky proto-planetary core accretes material from the surrounding proto-planetary disk, allowing it to gain a large amount of mass (Pollack et al., 1996; Chabrier et al., 2014). Alternatively, gravitational instability would suggest that the proto-planetary disk made of gas and dust fragments into clumps of bound material which form protoplanets (Boss, 1997; Durisen et al., 2007). Both of these theories have issues at such close locations to the host star though. For core accretion, it would be very challenging to build up large enough cores to trigger the massive growth of these giant planets with limited material available (Fortney et al., 2021). For the case of gravitational instability, the close proximity of the host star means that the conditions of the gas in this region would prevent such formation mechanisms from occurring (Rafikov, 2005). So although in situ formation is a possible formation mechanism, it is not regarded as the most likely (Fortney et al., 2021).

It seems likely then that giant planets form further out in the protoplanetary disk, beyond the snow line (Pollack et al., 1996; Alibert et al., 2005). The observed population of hot Jupiters must then have migrated inwards through their lifetime.

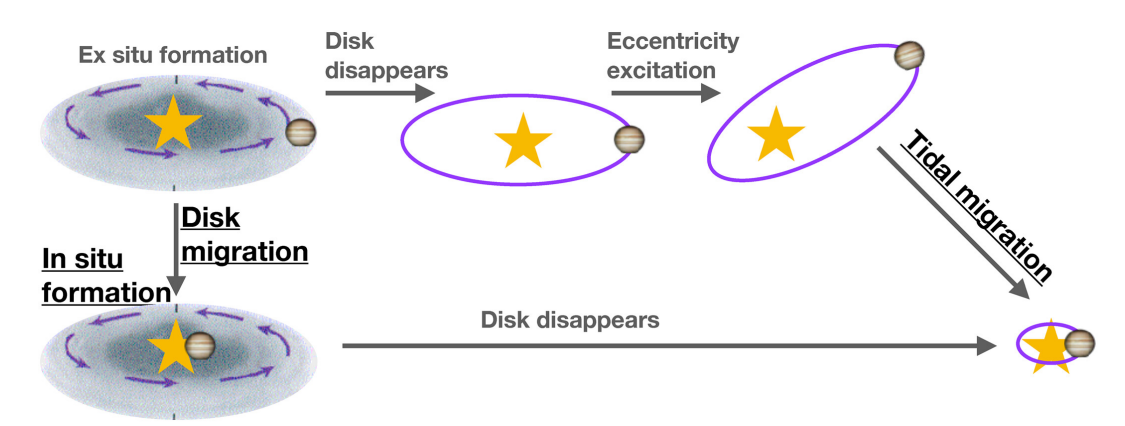


Figure 1.3: Reprinted from Fortney et al. (2021). Origins hypotheses for hot Jupiters: insitu formation, disk migration, and high eccentricity tidal migration.

There are two main mechanisms proposed for this migration: disk-driven migration, and high-eccentricity migration. In disk-driven migration, the planet smoothly migrates inwards by exchanging angular momentum with the surrounding protoplanetary disk (see e.g. Goldreich and Tremaine, 1980; Lin and Papaloizou, 1986). In high-eccentricity migration, the planet first attains a very high eccentricity through a mechanism such as planet-planet scattering (Rasio and Ford, 1996) or secular chaos (Takarada et al., 2020). This means that the periastron distance will now be very short and so when the planet reaches this close point to the star it will be effected by the tidal dissipation forces. This will cause the planet orbit to circularise at this much closer orbital distance (Rasio and Ford, 1996; Wu and Murray, 2003). The two scenarios are shown graphically in Figure 1.3.

Thankfully, these two different migration mechanisms have differing predictions on the properties of giant planets you would expect to observe. This means that by detecting and characterising the properties of hot Jupiter planets we can investigate which migration scenario is more likely. So far, observations of some hot Jupiters point to the high eccentricity migration case, but others point to disk driven migration. To make progress in understanding which mechanism is dominant requires further observations of giant planets close to their host stars.

1.2.1 The problem with warm Jupiters

While some progress has been made in understanding the formation and migration pathways of hot Jupiter planets, it is the warm Jupiters (giant planets with orbital periods between 10 and 200 days) which pose the biggest challenge to our understanding (Dawson and Johnson, 2018). If warm Jupiters form beyond the snow line and migrate inwards then it is likely they follow one of the proposed migration pathways for hot Jupiter planets. However, neither disk driven migration no high eccentricity migration can account for the properties of observed warm Jupiters (Petrovich and Tremaine, 2016).

Disk migration predicts the planets to have low eccentricities after migration, but this appears to be in contrast with observations of highly eccentric warm Jupiters (Jackson et al., 2021). Some planets may have increased their eccentricities through scattering events *after* their disk migration was complete, but even such a scenario cannot generally explain the higher end of observed warm Jupiter eccentricities (Petrovich, 2015).

The high-eccentricity migration model suffers from the opposite challenge as disk migration models: the observed warm Jupiter eccentricities are generally too *low* to get close enough to their star to further shrink their orbits (Jackson et al., 2021).

Nevertheless, high-eccentricity migration models can be 'rescued' by invoking Kozai-Lidov oscillations (Takeda and Rasio, 2005; Dong et al., 2013). Here, a planet's orbital eccentricity and inclination changes (oscillates) due to interactions with a perturber. This implies that a planet can periodically reach a high eccentricity (facilitating orbital shrinking) while being at a moderate or low eccentricity most of the time (matching the observed eccentricity distribution of warm Jupiters).

If warm Jupiters are the result of Kozai-Lidov interactions, these planets must have companions acting as a perturber. Furthermore, these companions need to be massive enough and nearby enough to result in perturber-coupled high-eccentricity migration (Dong et al., 2013). Therefore, detecting or ruling out the presence of such companions for warm Jupiter planets is a direct test of this origin scenario. Jackson

et al. (2021) completed detailed simulations to show that a well-designed ground-based survey of known warm Jupiters could detect 77% of perturbing companions, if they exist. One way forward in trying to understand the origins of warm Jupiter planets would be to perform such a survey to see if warm Jupiters do have companions capable of perturbations: if none are found then it would be a strong indication that this is not a dominant evolutionary pathway for warm Jupiters.

Chapter 2

Methods

2.1 How to characterise an exoplanet

To work towards answering the outstanding questions in exoplanet science we need a variety of observational methods to enable planet characterisation. In Chapter 1, I introduced the importance of exoplanet mass measurements in understanding the demographics of small planets. Additionally, the combination of mass and radius measurements allows for planet bulk densities to be calculated and therefore potential compositions to be estimated. It is important to note that the way we typically find exoplanet masses and radii are from separate methods – planet radii from the transit method (explained in Section 2.1.1), and planet masses from the RV method (explained in Section 2.1.2). In this thesis I focus primarily on the use of the RV method to better understand the nature of exoplanets, for further information on other detection methods see e.g. Kaushik et al. (2024).

In brief, other predominant methods of exoplanet detection and characterisation include astrometry and direct imaging (now more-commonly referred to as high-contrast imaging). Astrometry leverages the gravitational effect of a planet orbiting a star, measuring the tiny movements of stars caused by this perturbation. It is most sensitive to massive planets (the method itself is commonly used for binary star systems). Direct imaging uses large-aperture telescopes fitted with coronagraphs to image the planets directly. Currently this method is only sensitive the most massive planets at large separations from their host stars, it is also preferentially suitable for

younger systems where the planets are still self-luminous from formation.

2.1.1 Transits

The most common method of finding the radii of exoplanets is by using the transit method. This is where the periodic dimming in brightness of a star as a planet crosses in front of it, from our line of sight, is used to infer the presence of a companion (Perryman, 2011). The dip in the light is proportional to the relative areas of the planet and star (Borucki and Summers, 1984; Hale and Doyle, 1994). This means that by fitting the light curve it is possible to estimate the radius of the planet, given that the stellar radius is known. This method is enhanced with the use of space-based instruments, which are not subject to the distortion caused by observing through the Earth's atmosphere (Bordé et al., 2003). These space-based instruments enable greater precision for smaller transit measurements, consequently allowing us to detect increasingly smaller planets (Borucki et al., 2010). However, whilst the transit method is useful for detecting planets and finding their sizes, it is not possible to use this method to find the mass of a planet. This sometimes results in the use of mass-radius relations to assume a planet mass from its measured radius. Given the difficulties discussed in 1.1.1, this is not an ideal way to characterise the mass, and therefore density and composition, of planets.

2.1.2 Radial velocity

Of the observation methods which allow for mass characterisation, by far the most successful is the RV technique. The RV method exploits the gravitational effect of a companion planet on its host star (Lee, 2018). As the planet completes its orbits, the star-planet system actually orbits a common centre of mass. In many cases this centre-of-mass is within the star itself, causing a motion often referred to as a 'wobble' of the star. Given that the star is continually radiating in all directions, we can also make use of the Doppler effect to measure the 'wobble'. If the star happens to 'wobble' towards an observer on Earth then any light radiated from the star will be blue-shifted as viewed from Earth, and conversely as the star 'wobbles' away from us the light is red-shifted (Lovis and Fischer, 2010) – see Figure 2.1. By taking a

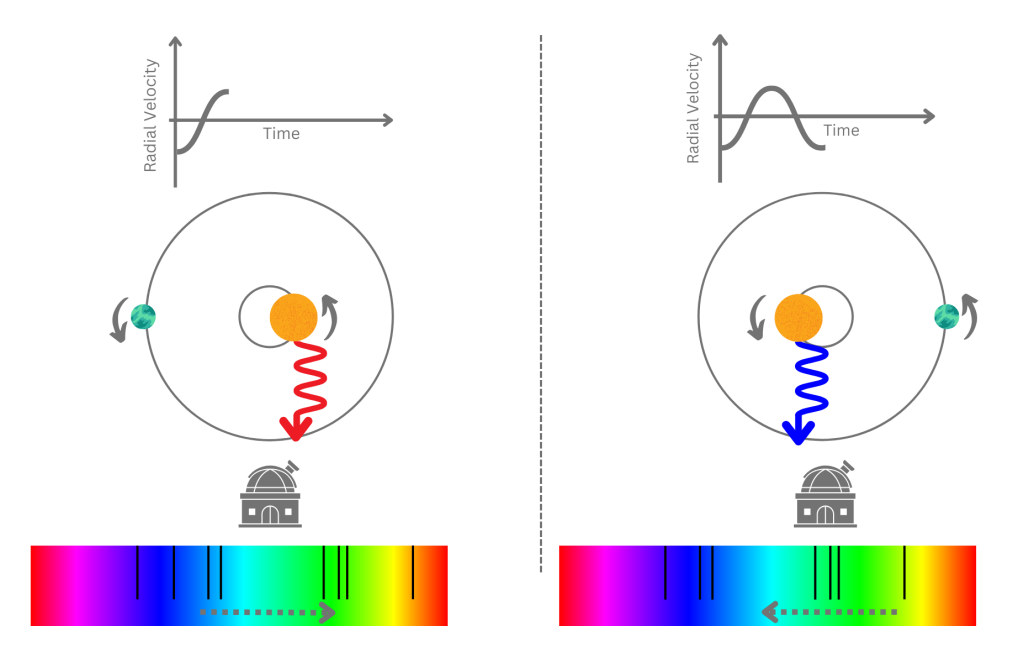


Figure 2.1: Left: in the centre is a graphic of a star and planet system, where both objects orbit a common centre of mass. As the star is moving away from the observer on Earth, the light moving towards the observer is red shifted - the lines on the spectrum in the lower part of the image are shifted towards the red end. The graph at the top shows a simplified view of the radial (i.e. the line-of-sight) velocity of the star. Right: the same set up but for the opposite time in the orbit, when the star is moving towards us and the light is blue shifted. By measuring this periodic shift from red to blue, observers can infer the presence of a planet causing this 'wobble' of the star.

spectrum of the star at different times during its periodic motion, we can detect the radial (i.e. along the line-of-sight) velocity of the star. Provided there is no impact from stellar activity, (see 2.4.2 for how this presents itself in RV observations) and for a given orbital inclination, the greater the amplitude in RV, the larger the planet mass compared to the stellar mass (Lovis and Fischer, 2010). Therefore, if we know the stellar mass and can model the radial motion of the star, we can then estimate the mass of the planet. Note that apparent mass, taken from RV measurements, is related to the actual mass by $m \sin i$, where i is the inclination angle of the system.

2.2 RV instruments

RV instruments consist of a highly-stabilised spectrograph with high spectral resolution. Spectrographs used successfully for exoplanet detection date back several decades (Baranne et al., 1996) when the very first-known exoplanets were being

detected (Mayor and Queloz, 1995). The earliest generation of planet-finding spectrographs, such as ELODIE (Baranne et al., 1996), SOPHIE (Perruchot et al., 2008), and CORALIE (Queloz et al., 2000), had precisions around the $\sim 10~\mathrm{ms}^{-1}$ range. As instrumentation improved and telescope apertures grew, a newer generation of instruments emerged, able to reach increasingly lower RV amplitudes (i.e. lower planet masses). These next-generation instruments include HARPS (Mayor et al., 2003), and northern-hemisphere counterpart HARPS-North (Cosentino et al., 2012), this is the High Accuracy Radial velocity Planet Searcher. HARPS is attached to ESO's 3.6m telescope in La Silla, Chile, and has been operating since 2003, making it one of the most successful ground-based exoplanet detecting instruments. HARPS is currently able to find radial velocity signals of the order or $\sim 1~{\rm ms}^{-1}$ (Lovis et al., 2006). Since reaching this ~1 ms⁻¹ amplitude limit, the improvements in RV sensitivity have somewhat plateaued, this is mainly attributed to the impact of stellar activity, see 2.4.2. However, significant instrumentation efforts are being made to push to lower amplitudes. The current state-of-the-art instrument (in the visible range) is ESPRESSO, the Echelle SPectrograph for Rocky Exoplanets and Stable Spectroscopic Observations, installed at the Very Large Telescope (VLT) and operated by the European Southern Observatory (ESO) (Pepe et al., 2010). ESPRESSO is highly stabilised and has been built with the goal of reaching an RV-precision of 10 cms⁻¹ (the equivalent RV signal the Earth would cause on the Sun) within the next decade (Pepe et al., 2010).

In general, RV observations are restricted by observational constraints (telescope time allocation, observability of the star, local observing conditions etc) and so data is not necessarily well-sampled in time, commonly with large time gaps between groups of data points, meaning the phase coverage is not always ideal (Meunier, 2021). The way that spectra are taken and then used to find radial velocities also varies somewhat from instrument to instrument. As an example, the HARPS instrument first takes spectra of a target star as well as a reference calibration spectrum (in this case thorium-argon). Then to obtain the radial velocities themselves, the HARPS processing pipeline performs a cross-correlation analysis between the

spectra and a binary mask. The binary mask shows the expected line positions for the particular spectral type. A symmetric Gaussian function is then moved until we find the position of the maximum cross-correlation function (CCF) and this provides the stellar RV (Meunier, 2021).

2.3 Masses from RVs

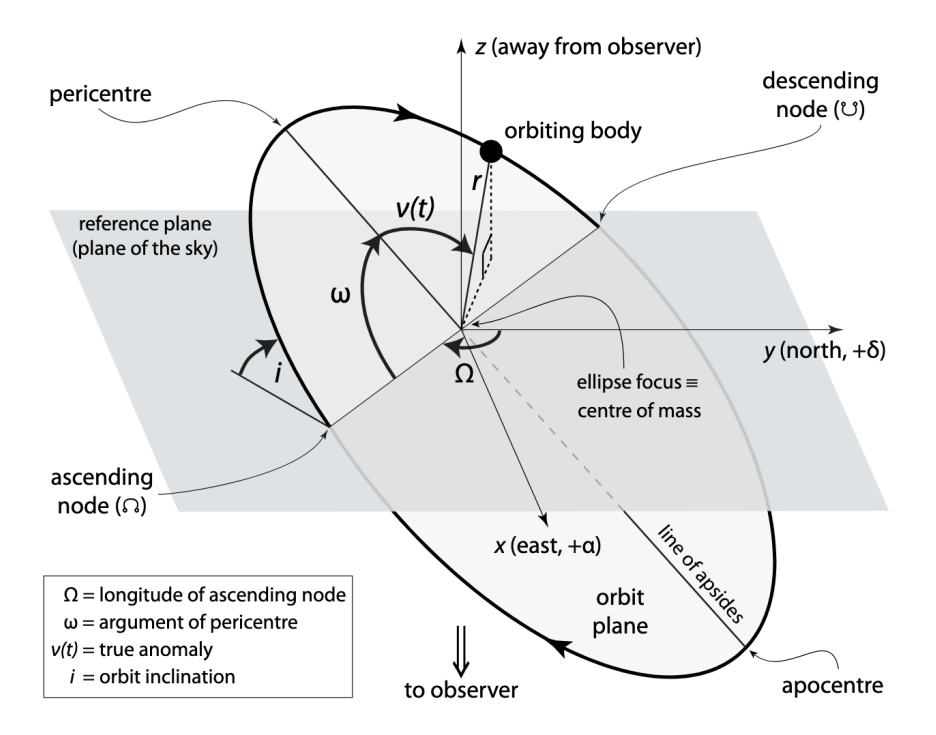


Figure 2.2: Reprinted from Perryman (2018). An elliptical orbit in three dimensions. The reference plane is tangent to the celestial sphere, i is the inclination of the orbit plane, and the nodes define the intersection of the orbit and reference planes. Ω is the longitude of the ascending (receding) node, measured in the reference plane. ω is the fixed angle defining the object's argument of pericentre relative to the ascending node. The true anomaly, v(t), is the time-dependent angle characterising the object's position along the orbit. The right-handed x y z coordinate system has x towards east (increasing α), y towards north (increasing δ), and z away from the observer. The reference axis, y, contrasts with the use of x, the vernal equinox, as adopted for the solar system.

The mass of the planet can be inferred from RV observations. Here, I present a summary of the main points, following Perryman (2011, 2018). First, a Keplerian orbit can be represented in 3 dimensions by seven parameters, a, e, P, t_p , i, Ω , ω , as shown in Figure. 2.2. The size and shape of the elliptical orbit are described by

a and e, the semi-amplitude and eccentricity, respectively. The orbital period, P, is related through Kepler's third law to both a and the masses of the objects. The position of the object along its orbit at a specific time is described by t_p . Lastly, the three angles i, Ω , ω represent how the true orbit is projected onto the observed orbit. The orbital inclination with respect to the reference plane is given by, i, and varies from 0 to 180 °. Ω is the longitude of the ascending node measured in the reference frame, in Figure. 2.2 this is where z goes from negative to positive. Finally, ω is the argument of periastron, the angle of the object's pericentre relative to its ascending node, measured in the orbital plane and in the direction of motion.

Using Figure. 2.2 to represent the orbit of the star around the barycentre, we can use trigonometry to find the z-coordinate of the star along the line-of-sight

$$z = r(t)\sin i \sin(\omega + \nu), \tag{2.1}$$

where r(t) is the distance from the barycentre. Then

$$v_r \equiv \dot{z} = \sin i \left[\dot{r} \sin (\omega + v) + r \dot{v} \cos (\omega + v) \right] \tag{2.2}$$

which can then lead to

$$v_r = K[\cos(\omega + v) + e\cos\omega] \tag{2.3}$$

where the semi-amplitude of the radial velcoity is then given by

$$K \equiv \frac{2\pi}{P} \frac{a_* \sin i}{(1 - e^2)^{1/2}}.$$
 (2.4)

If we then take the general form of Kepler's third law

$$P^2 = \frac{4\pi^2}{GM}a^3, (2.5)$$

where P is the orbital period, G is the gravitational constant, M is the total mass and a is the semi-major axis, and

$$M' \equiv \frac{M_p^3}{(M_{\star} + M_p)^2},\tag{2.6}$$

we can substitute these in to Eq. 2.4 to find

$$k = \left(\frac{2\pi G}{P}\right) \frac{M_p sini}{(M_{\star} + M_p)^{2/3}} \frac{1}{(1 - e^2)^{1/2}}.$$
 (2.7)

So from the radial velocity semi-amplitude, the orbital period, and eccentricity, it is possible to find the mass of the planet, given that the stellar mass is also known. In practice it is common to use an MCMC fitting of the radial velocity as a function of time using the form

$$v_r = k[\cos(\omega + v(t)) + e\cos\omega] + \gamma + d(t - t_0), \tag{2.8}$$

where γ accounts for the systematic velocity of the system relative to the solar system barycentre and d is used to account for long-term linear trends, potentially arising from instrument drifts. By finding best-fit values for these parameters it is then possible to calculate an $M_p \sin i$ for a planet using equation (2.7) and if the inclination is known then this can be converted to an actual mass estimate.

2.4 Sources of uncertainty

There are two main difficulties in obtaining precise RV measurements of small planets: the stability of the spectrograph over large time baselines, and astrophysical sources of jitter. Improvements in instrumentation have allowed for greater spectrograph stability in recent years but the jitter is still a problem for ultra-precise RVs (on the order of ms⁻¹). In this case most of the jitter comes from the host star itself. The stellar variability causes problems for RV measurements in that it can potentially look like a planet (and result in false positives), it can hide planets which are there (false negative), or it can affect the characterisation of a planet – particularly in terms of planetary mass.

2.4.1 Stellar activity

The difficulty in accounting for stellar activity in RV observations is that there are a number of different activity mechanisms that vary over a range of timescales and between different types and ages of stars (see e.g. Meunier, 2021, 2024, for reviews).

On the shortest timescales is the impact of stellar oscillations. The internal pressure of stars fluctuates and produces acoustic waves, known as p-modes, which cause ripples on the stellar surface (Bedding et al., 2001, 2010). These oscillations typically last in the region of 5 - 15 minutes, meaning they can be averaged out with sufficiently long observations – i.e. by ensuring RV observations are longer than 10 minutes (Dumusque et al., 2011).

On the slightly longer timescale of minute to hours is the impact of granulation. Within stars, hot fluid cells rise up to the surface due to convection, before cooling and sinking back to the stellar subsurface. These hot cells appear on the surface as large bright regions, of size around a few hundred kilometres and lifetimes of around 10 minutes (Bahng and Schwarzschild, 1961) – though supergranules have been observed to be as large as 50 Mm and have lifetimes of a day (Del Moro et al., 2004). Because the bright granules are very large compared to the inter-granular lanes where the material cools and sinks down, the overall impact across the entire star is of a net blueshift (Meunier and Lagrange, 2020). The impacts of granulation on RVs and attempts to combat this effect have been investigated in many works (e.g. Cegla et al., 2019; Meunier and Lagrange, 2020; Palumbo et al., 2022; Dalal et al., 2023). It has been found that the signal can be averaged to decrease its impact on exoplanet detectability by taking multiple (typically 2 to 3) RV observations per night, but it is challenging to average out the effect completely due to the differing timescales for different sizes of granules (Dumusque et al., 2011).

On longer timescales (on order of the stellar rotation period of the star), and much more problematic for RV surveys is the impact of spots, plage and faculae. Starspots are region on the stellar surface which are cooler, typically 1000 K cooler (Schrijver, 2002), and therefore appear darker. These temporary regions are caused due to temporal changes in the magnetic field lines of the star. The motion of charged

particles within the stellar plasma creates a magnetic field and the differential rotation between the core and envelope can cause the magnetic field lines to twist and break. Starspots occur when the magnetic activity prevents the warm inner regions from rising up to the surface. In photometry the presence of a spot on the stellar surface can cause a periodic dimming in the total light from the star – reminiscent of an exoplanet transit. This can cause confusion especially in case where spots are long lived over several stellar rotation periods. But even more complex is the effect on RV observations. As a star rotates, one half of the visible disk will be moving towards the observer (therefore blueshifted) while the other half is moving away and so redshifted. Typically, this red and blue shift would average out because the two halves are always equal. However, a spot present on the surface of the star will block some of the light from that region and therefore lead to asymmetries which distort RV spectral lines, this distortion will also be present in the CCF and causes increased uncertainties in the RV measurement.

Plage and faculae are bright regions present on the stellar chromosphere and photosphere, respectively. The temperature difference is less than for spots (around 100 K) and so the photometric effect of these bright regions is not so significant. However, they do have a noticeable impact on the spectroscopic observations. The strong magnetic fields present in these regions inhibit the convection process which causes granulation. This means that the net blueshift due to convection is suppressed in these regions, causing RV variations of up to 10 ms⁻¹ (Meunier and Lagrange, 2020; Haywood et al., 2014). The impact of spots, faculae and plage on RV observations has been studied extensively in the past decade (Lisogorskyi et al., 2020; Zhao et al., 2024a; Yu et al., 2024; Siegel et al., 2024). In some cases this analysis has even led to previous planet detections being reclassified as stellar activity (e.g. Burrows et al., 2024; González et al., 2024).

2.4.2 Mitigating stellar activity

Many attempts have been made to mitigate the impacts of stellar activity in RV observations but so far no perfect solution exists.

Some methods seek to adapt the way that the RVs themselves are extracted

from the raw spectra, either through new data reduction pipelines (Zechmeister et al., 2018), or by taking a line-by-line approach (Cretignier et al., 2023; Dumusque, 2018; Meunier et al., 2017), where individual spectroscopic lines and groups of lines are analysed, rather than the entire spectrum at once.

Historically, attempts to subtract the impact of stellar activity involved modelling the activity as a sinusoid and removing this (and subsequent harmonics of this) from the RV data (Queloz et al., 2009; Hatzes et al., 2010), often in combination with activity indicators from the spectra (Queloz et al., 2001; Desort et al., 2007). These activity indicators can be measured directly from the star – such as the S-index which is a measure of the emission in the core of the Calcium II H and K lines (Meunier and Lagrange, 2013). Alternatively, activity indicators can be calculated from the CCF in the process of finding RVs, such as the bisector span (BIS, Queloz et al., 2001) which measures the difference in centre position of the CCF between the top and bottom, or the full width at half maximum (FWHM) which measures the width of the spectral line profiles (Queloz et al., 2009).

Zhao et al. (2022) led a community-driven investigation into the effectiveness of different stellar activity mitigation techniques for radial velocities. They analysed 22 separate methods which had been applied to the same 4 datasets from different stars. They found that no one method provided better reduction in noise (quantified in this study as the root mean squared error, RMS) for all the stars tested. It was however noted that the more recent methods provided lower RMS values then the traditional linear decorrelation methods in nearly all cases (Zhao et al., 2022).

The subfield of extreme precision radial velocities (EPRV) has grown in the past few years and now is the focus of multiple conferences and a community research coordination network¹. The researchers who contribute to this network focus on many areas of improving the mitigation of stellar activity in RVs, including: understanding the Sun as a star (e.g. Ford et al., 2024; Klein et al., 2024; Zhao et al., 2023; Cegla et al., 2019) and using this to test mitigation techniques; finding new activity indicators (e.g. Al Moulla et al., 2024; Siegel et al., 2022); using machine

¹https://exoplanets.nasa.gov/exep/NNExplore/EPRV-RCN/ EPRV-RCN-welcome/

learning methods (e.g. de Beurs et al., 2022; Perger et al., 2023; Liang et al., 2024; Zhao et al., 2024b; Colwell et al., 2025); understanding the impact of joint modelling with photometric data (e.g. Kosiarek and Crossfield, 2020; Tran et al., 2023; Beard et al., 2025); finding the best way to plan RV observations (e.g. Newman et al., 2023; Gupta and Bedell, 2024; Lam et al., 2024); and developing tools for Gaussian process regression to be used (e.g. Gilbertson et al., 2020; Yu et al., 2024).

The main method for stellar activity mitigation that I use in this thesis is Gaussian processes (described in Section 2.4.3). This is a relatively-new technique with promising results and is becoming widely accepted within the EPRV community as the solution of choice for most RV-observers (Aigrain and Foreman-Mackey, 2023).

2.4.3 Gaussian Processes

Some recent successes in mitigating stellar activity in RV observations have been found using Gaussian processes (GPs) based on activity indicators measured from the star at the time of observations. GPs are suitable for modelling functions where the underlying physics is not well-understood and so can be very useful in this case, see Rajpaul et al. (2015); Aigrain and Foreman-Mackey (2023) for full description of using GPs for modelling stellar activity in RV signals.

In basic terms, we assume that there is a quasi-periodic nature to stellar variations – i.e. the presence of star spots (or faculae etc) vary as some function of the rotation period of the star. We can use a GP to fit this function by specifying a covariance kernel which defines an arbitrary element, C_{ij} of that covariance matrix (this describes how much different parameters are inter-related). There are a range of different covariance kernels that can be used but a common choice is the Celerite kernel (Foreman-Mackey et al., 2017) which has associated hyperparameters: L (which is related to the characteristic length i.e. how much one data points can affect a data point further away), P_{rot} (the rotation period of the star), B and C (which together describe the amplitude of the GP). C_{ij} is then defined using the following,

$$C_{ij} = B/(2+C) * \exp\left(\frac{-|t_i - t_j|}{L}\right) * \cos\left(\frac{2\pi|t_i - t_j|}{P_{rot}}\right) + (1+C)$$
 (2.9)

Typically, priors for these hyperparameters are given to ensure B and C are both positive, L is usually given a uniform prior with an upper boundary of a few days (e.g. [0,10]), if the rotation period of the star is known then a Gaussian prior centred on this value can be used, if not then a wide, uniform prior is used instead to restrict this to reasonable values (e.g. [1,200]). We then simultaneously run a joint fit of the orbital model for the planet alongside this GP i.e. we say that the RV as a function of time is a function of the periodic motion of the planet + instrument noise + stellar variations. The aim is to find optimal values for the hyperparameters of the covariance kernel using the given data set. By fitting for the quasi-periodic variability with a GP we can then subtract this from the data to leave a fit for just the periodic motion of the planet, see Figure 2.3 for a visual example of this. The reason for using a GP fit rather than just a series of sine functions is that it allows us to quantify our error bars which would not be possible with a Fourier transform. It also keep the number of parameters, and hyperparameters, to be modelled at a reasonable level. Equally, a GP is not used to model the orbital motion of the planet as we know mathematically that the motion should be described by a sinusoid.

2.5 Structure of this thesis

My scientific goals for my PhD have been focused on using the RV method to better understand exoplanets, specifically in terms of their composition. Early on in my PhD I became a contributing member of the KESPRINT consortium, an international collaboration focused on the RV follow-up of exoplanet candidates detected by space telescopes. As part of this collaboration I led the analysis team of one of the targets we confirmed: TOI-544 b. This paper, already published, is presented in Chapter 3. In the modelling of this system I made a variety of different (but equally valid) choices: I tried fixing the orbits as circular or allowing them to be eccentric and tried using different combinations of additional data to mitigate stellar activity. Whilst each model resulted in a planet mass which was within $1-\sigma$ of each other, it did open an interesting question: how much does model choice impact the planet mass found? And in turn: how does this impact our understanding of the

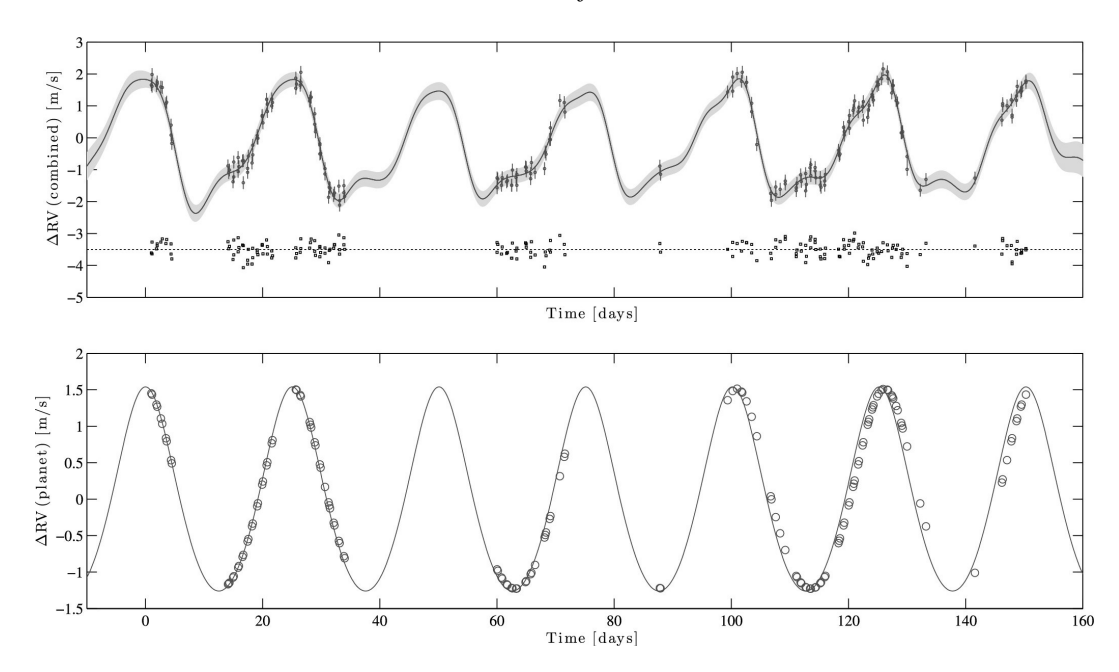


Figure 2.3: Reprinted from Rajpaul et al. (2015). GP model fit to SOAP 2.0 data, based on a simulation of four rotating spots (each with radius 5% of the stellar radius) at latitudes $\phi = 0^{\circ}$, 30° , 45° , 60° , equally spaced in longitude, with time sampling and noise levels taken from one season of a real HARPS dataset, plus an injected Keplerian signal. Here the injected signal has an amplitude comparable to, but period different from, the rotationally-modulated activity signals. The top panel shows the model fit to the Δ RV time series, including residuals – the total combined GP and Keplerian fit (black line) with 1- σ uncertainty shown in grey; the bottom panel shows the Keplerian component of the fit.

mass-radius distribution of planets?

To begin addressing these questions I then focused on completing a homogeneous analysis of RV observations of exoplanet host stars. I reanalysed publicly available RV observations in a consistent way for a sample of 85 small planets. I modelled every planet with 12 different models to investigate how model choice impacts the planet mass determined. The results of this RV re-analysis have been published and are presented in Chapter 4. A follow-up paper will then present the new planet masses and investigate how planet compositions link to the radius valley – and whether there is a difference for planets orbiting FGK stars and M dwarf stars. This paper in progress is presented in Chapter 5.

For the last project of my PhD, I have two of my own PI observing programmes equalling more than 70 hours of telescope time. This project is observing a sample of currently-known warm Jupiter planets to search for additional companions in the

same system. Warm Jupiters are giant planets at intermediate distances from their host stars, often with high eccentricities. One possible formation pathway is through perturber-coupled high-eccentricity migration, where a second planet in the system perturbs a warm Jupiter progenitor planet (at a larger distance from its host star) onto a highly eccentric orbit which eventually circularises, causing the inward migration. To test whether this theory is likely, my project is searching for companions which could be capable of causing this migration. In Chapter 6 I present the analysis and RV modelling of the first 5 targets from this study.

Chapter 3

TOI-544 b: a potential water-world inside the radius valley in a two-planet system

3.1 Abstract

We report on the precise radial velocity follow-up of TOI-544 (HD 290498), a bright K star (V=10.8), which hosts a small transiting planet recently discovered by the Transiting Exoplanet Survey Satellite (TESS). We collected 122 high-resolution HARPS and HARPS-N spectra to spectroscopically confirm the transiting planet and measure its mass. The nearly 3-year baseline of our follow-up allowed us to unveil the presence of an additional, non-transiting, longer-period companion planet. We derived a radius and mass for the inner planet, TOI-544 b, of $2.018 \pm 0.076 \, R_{\oplus}$ and $2.89 \pm 0.48 \, M_{\oplus}$ respectively, which gives a bulk density of $1.93^{+0.30}_{-0.25} \, g \, cm^{-3}$. TOI-544 c has a minimum mass of $21.5 \pm 2.0 \, M_{\oplus}$ and orbital period of $50.1 \pm 0.2 \, days$. The low density of planet-b implies that it has either an Earth-like rocky core with a hydrogen atmosphere, or a composition which harbours a significant fraction of water. The composition interpretation is degenerate depending on the specific choice of planet interior models used. Additionally, TOI-544 b has an orbital period of $1.55 \, days$ and equilibrium temperature of $999 \pm 14 \, K$, placing it within the predicted location of the radius valley, where few planets are expected. TOI-544b

is a top target for future atmospheric observations, for example with JWST, which would enable better constraints of the planet composition.

3.2 Introduction

The radius valley describes the region in the size distribution of exoplanets where few planets exist, specifically between 1.5 and 2.0 R_{\oplus} . This feature was first observationally identified in Fulton et al. (2017) and Van Eylen et al. (2018) and a variety of theories have been proposed to explain this gap in planetary radii, including photo-evaporation (Owen and Wu, 2017; Fulton et al., 2017; Van Eylen et al., 2018) and core-powered mass loss (Collier Cameron and Jardine, 2018; Gupta and Schlichting, 2019, 2021).

Photo-evaporation models argue that planets generally form with rocky cores and atmospheric layers composed of hydrogen and helium (H-He) of around 1% by mass. Such planets, with a rocky core and H-He atmosphere, are termed sub-Neptunes and located above the radius valley in radius-period space. In some cases, the intense X-ray flux from the nearby host star strips away these volatile gases, leaving behind a bare rocky core, a so-called super-Earth planet, with a radius placing it below the radius valley (Owen and Wu, 2017).

Core-powered mass loss models are similar in that they predict planets to form with atmospheric layers and be located above the valley and subsequent atmospheric loss reduces the radius and locates the planet below the valley. In the latter model, the energy enabling the mass loss has come from within the planet itself; stored heat from the formation of the planet escapes from the core and heats the atmospheric layer from the inside, leading to gaseous escape (Gupta and Schlichting, 2019).

More specifically, Ginzburg et al. (2016, 2018) demonstrate that once the protoplanetary disk has dispersed following formation, the loss of pressure support triggers atmospheric mass loss. This causes planets to shed their outer atmospheric layers until roughly comparable to the radius of the inner rocky core. After this stage, planets with heavier atmospheres will not have sufficient energy available to lose their entire atmospheres and so will cool and contract over time. However, planets

with light atmospheres will continue to lose mass over time, provided that the escape rate of molecules at the Bondi radius is high enough (Ginzburg et al., 2016). In other words, there needs to be sufficient heat available for the gas in the planet's atmosphere to expand out to the Bondi radius. In the case of photo-evaporation this heat comes from the high-energy stellar flux which accelerates atoms in the atmosphere. In the case of core-powered mass-loss the heat is provided mainly though the thermal energy of the planet, plus the bolometric luminosity of the host star (Nielsen et al., 2025).

Despite several attempts (e.g. Lopez and Rice, 2018; Owen and Wu, 2017; Gupta and Schlichting, 2019; Estrela et al., 2020; Gupta et al., 2022; Ho and Van Eylen, 2023) no significant observational evidence has been found that can differentiate between models. There is also an additional complication in the fact that the location of the radius valley seems to change based on other parameters, in particular on stellar mass (see e.g. Petigura et al. (2022). Cloutier and Menou (2020) calculated the occurrence rates of small planets orbiting low mass stars to show that the location of the radius valley shifts to smaller sizes for decreasing stellar mass. They also argue that for planets around lower mass stars the radius valley may have a different formation mechanism or mechanisms, and highlight the need for high-precision RV follow-up of a number of key targets including TOI-544 b.

Additionally, recent works have suggested that the observed distribution of small planets (particularly those orbiting M-dwarf stars) is the result of a distribution in core composition at formation. Specifically, Luque and Pallé (2022) argue that the small planets around M dwarfs can be separated into super-Earths (with rocky cores) and water worlds (with large fractions of ice or water layers). Other recent detections have also seemed to provide evidence towards this divergence in core compositions. Piaulet et al. (2022) presents a detailed study of Kepler-138 d, a small planet with a bulk density which they argue can only be explained with a water world composition (see also e.g. Diamond-Lowe et al. (2022); Cadieux et al. (2022)). However, Rogers et al. (2023) use models which include atmospheric boil-off shortly after planet formation to show that the group of water-world planets presented in Luque and

Pallé (2022) are consistent with atmospheric loss models where a rocky planet with a H-He atmosphere loses its atmospheric layers to become a stripped core.

In this context, we have performed follow-up high-resolution radial velocity observations within the KESPRINT consortium ¹ of the small planet TOI-544 b discovered by the Transiting Exoplanet Survey Satellite (TESS, Ricker et al., 2014). The planet is particularly interesting since it is located in the middle of the radius valley and has a short period of 1.5 days. It was recently validated by Giacalone et al. (2022), where they present observations from the TESS follow-up programme, who argued that TOI-544 b is a potentially interesting target for JWST.

In Section 3.3 we present the space-based and ground-based observations of TOI-544, including the extensive RV measurements. In Section 3.4 we describe our stellar parameter fitting method and results. In Section 4.7 we describe both the transit fitting and the RV fitting and in Sections 3.6.1 to 3.6.4 we explore the composition of the inner planet, its location in relation to the radius valley and potential atmospheric observations of this planet. Finally, we present conclusions in Section 3.7.

3.3 Observations

3.3.1 Space-based Photometry

As part of its all-sky survey, TESS observed the star TIC 50618703 in Sectors 6 and 32. The cadence of observations is 120 s, the time span of Sector 6 (32) is 2018 Dec 12 to 2019 Jan 06 (2020 Nov 19 to 2020 Dec 16), and 44/14691 (817/17977) cadences were omitted due to bad quality flags in Sector 6 (32). After data reduction though the standard Science Processing Operations Centre (SPOC, Jenkins et al., 2016; Twicken et al., 2019) pipeline, likely transits were detected and the planetary candidate was promoted to a TESS object of interest (TOI), named TOI-544, by the TESS team. TESS observations of TOI-544 are shown in Figure 3.1.

¹https://kesprint.science

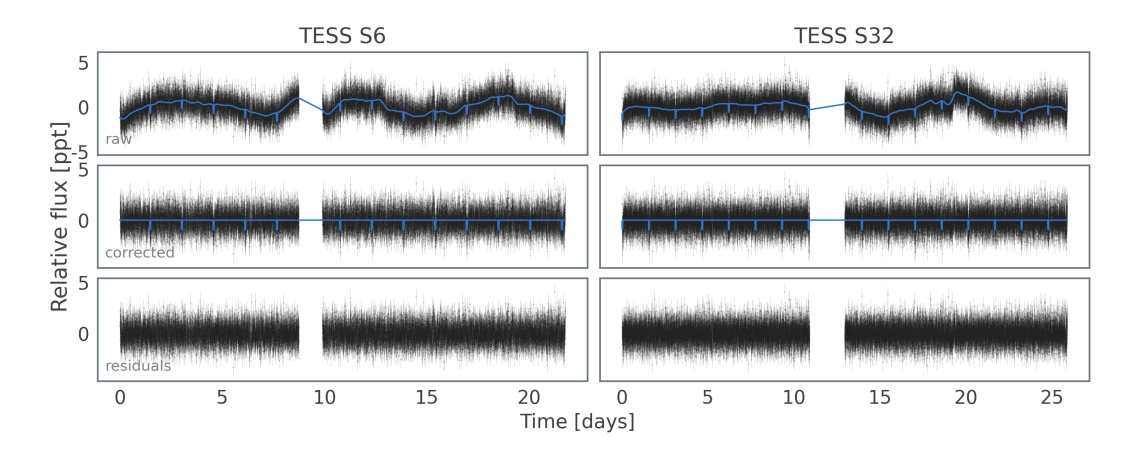


Figure 3.1: TESS light curves from Sector 6 (left) and 32 (right). SPOC light curves are shown in the upper panel, with a full transit and noise model (see Section 3.5.1) shown in blue. In the middle panel, TESS light curves are shown after subtracting the best-fit GP model, and residuals are shown in the bottom row.

3.3.2 Ground-based photometry

Prior to the initial planet detection by TESS, the Wide Angle Search for Planets (WASP) survey (Pollacco et al., 2006) observed the field of TOI-544 between 2008 and 2011, obtaining 18 000 photometric datapoints using Canon 200-mm, f/1.8 lenses with a 400–700 nm filter and CCDs with a plate scale of 13.7"/pixel. The data have a typical 15-min cadence and covered an observing season of \sim 100 nights in each year. TOI-544 is by far the brightest star in the 48-arcsec extraction aperture, with a V magnitude of 10.777 \pm 0.017. We make use of this archival data by searching the resulting WASP lightcurves for a stellar rotational modulation, adopting the methods described in Maxted et al. (2011). We find a significant modulation at a period of 20 \pm 1 days and an amplitude of up to 3 mmag. In the combined dataset the modulation is significant to a level of >99% confidence. Figure 3.2 shows Generalised Lomb-Scargle periodograms, adapted as described in Maxted et al. (2011), of the WASP data for TOI-544. The 1% false-alarm probability is shown by the horizontal line and the panels to the right show the data folded on the 20 day rotation period.

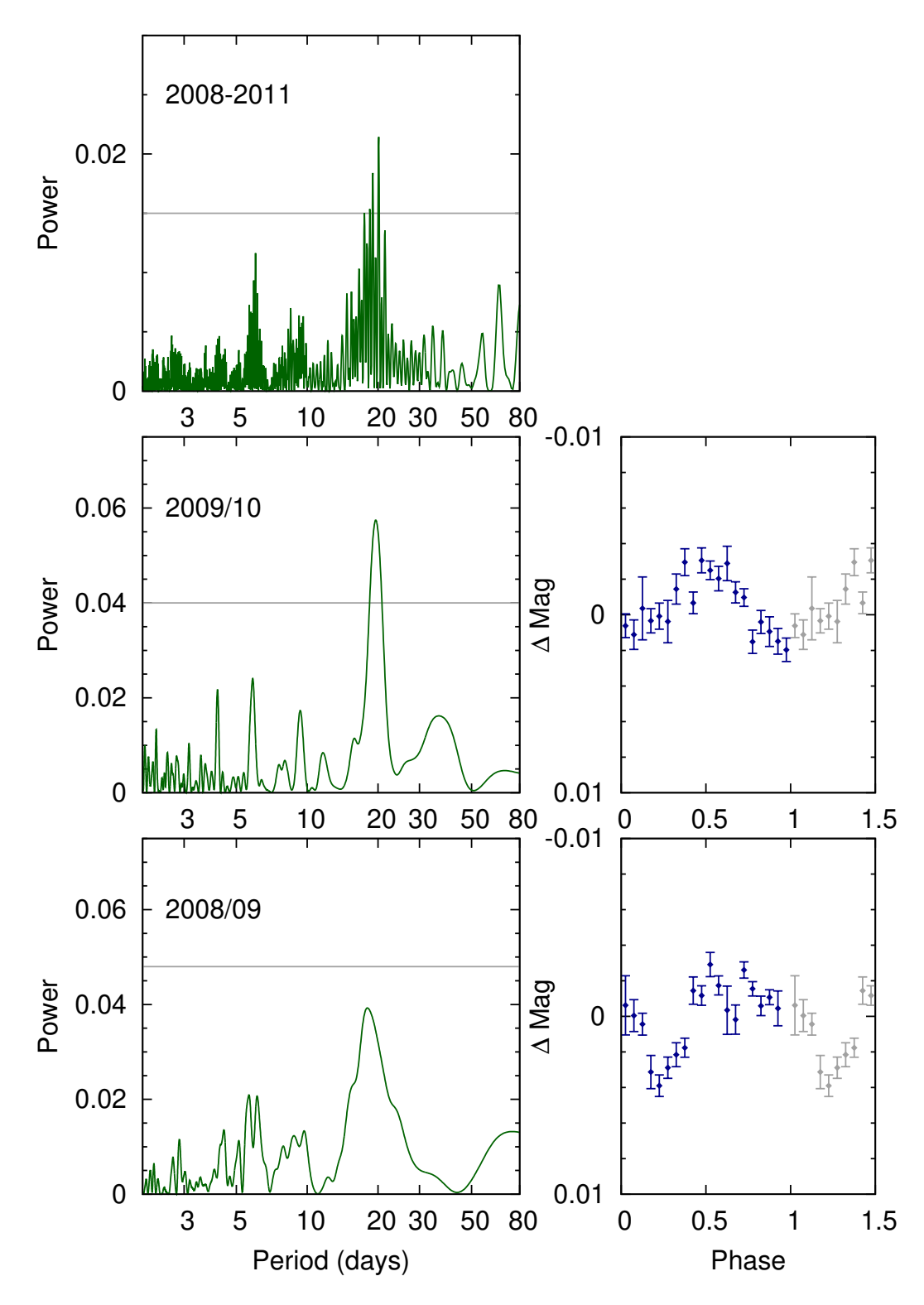


Figure 3.2: Generalised Lomb-Scargle Periodograms of the WASP-South data for TOI-544. The horizontal line is the estimated 1% false-alarm probability, data after phase 0.5 are in grey. The right-hand panels show the data folded on the 20-d rotational period.

3.3.3 High-resolution HARPS and HARPS-N spectroscopy

We obtained a total of 108 high-resolution ($R = \lambda/\Delta\lambda \approx 115\,000$) spectroscopic observations of TOI-544 using the High Accuracy Radial velocity Planet Searcher (HARPS) mounted on the European Southern Observatory (ESO) 3.6-m telescope at La Silla Observatory. One hundred and six spectra were acquired between December 2020 and March 2022 as part of our large observing programme 106.21TJ.001 (PI: Gandolfi). There are an additional 2 observations taken during April 2019 as part of observing programme 0103.C-0442(A) (PI: Diaz). Each observation has an exposure time between 1500 s and 2700 s, leading to a median signal-to-noise (S/N) ratio of 53.7 per pixel at 550 nm (Table A.1), and a median RV uncertainty of $\sim 1.6 \,\mathrm{m\,s^{-1}}$, as extracted using the SpEctrum Radial Velocity Analyser SERVAL (see below; Table A.2).

TOI-544 was also observed using the High Accuracy Radial velocity Planet Searcher for the Northern hemisphere (HARPS-N; Cosentino et al., 2012) mounted at the 3.58-m Telescopio Nazionale Galileo (TNG) of Roque de los Muchachos Observatory in La Palma, Spain, between April 2019 and December 2020, resulting in a total of 14 high-resolution ($R \approx 115\,000$) spectra from programmes CAT19A_162 and CAT19A_97 (PIs: Nowak and Casasayas-Barris). Each observation has an exposure time between 1230 s and 2400 s, a median S/N ratio of 52 per pixel at 550 nm (Table A.3), and a median RV precision of $\sim 1.2\,\mathrm{m~s^{-1}}$, as extracted using SERVAL (see below; Table A.4). We include these 14 observations in our RV analysis. The total number of HARPS and HARPS-N spectra is thus 122.

Versions 3.8 and 3.7 of the Data Reduction Software (DRS; Pepe et al., 2002; Lovis and Pepe, 2007) were used to reduce the HARPS and HARPS-N spectra, respectively, and extract absolute RVs by cross-correlating the spectra with a K5 numerical mask (Baranne et al., 1996), along with three diagnostics of the cross-correlation function (CCF), namely, the full width at half maximum (FWHM), the bisector inverse slope (BIS), and the contrast. We also used the SERVAL code (Zechmeister et al., 2018) to measure relative RVs and extract two additional activity diagnostics, namely, the differential line width (dLW) and the chromatic

index (CRX). SERVAL implements a template-matching algorithm that is suitable to derive precise Doppler measurements for M- and late K-type stars when compared to the CCF technique employed by the DRS (see, e.g., Luque et al., 2021; Serrano et al., 2022; Goffo et al., 2023).

We finally extracted the $H\alpha$, Na D1 & D2, and Ca II S-index activity indicators using the Template Enhanced Radial velocity Re-analysis Application (TERRA; Anglada-Escudé and Butler, 2012). The standard deviation of the RV data is $\sim 7.5 \, \mathrm{m \, s^{-1}}$ for HARPS and HARPS-N and in both cases of using the SERVAL and DRS codes. The absolute (DRS) and relative (SERVAL) RV measurements are given in Appendix A, along with the stellar activity indicators and line profile diagnostics. For the analysis presented in Sects. 3.5.2 and 3.5.3 we used the SERVAL RV measurements due to the lower jitter terms and root-mean-square of the fit residuals with respect to the DRS RVs.

3.4 Stellar Parameters

Table 3.1: Stellar parameters for TOI-544, modelled with SpecMatch-Emp and SME, and BASTA and astroaRIADNE.

																				a Adopted as priors for the stellar mass and radius modelling. b Adopted as our final stellar parameter values to be used in analysis of the planetary system. I Taken from TESS Input Catalogue (TIC) version 8 (Stassun et al., 2019). 2 Taken from Gaia DR3 (Gaia Collaboration et al., 2021).
								Luminosity	(L_{\odot})	:	0.13 ± 0.02									er values to be us llaboration et al.,
								$V \sin i$	$({\rm km}\ {\rm s}^{-1})$:	2.3 ± 0.8	Ü	10.41430 ± 0.00059		Age	(Gyear)	0 ±7	$5^{+5.3}_{-3.1}$:	our final stellar paramet om Gaia DR3 (Gaia Col
								[Fe/H]	(dex)	-0.17 ± 0.09	-0.15 ± 0.08 2.3 ± 0.8	Parallax	24.44 ± 0.02		Distance	(Pc)	40 ± 1	40.9 ± 0.03	:	b Adopted as call 19). 2 Taken from
				.43		91		log 8*	(cgs)	4.68 ± 0.12	4.60 ± 0.12	DEC	-0.3428983		R_{\star}	(R_{\odot})	0.624 ± 0.013	0.617 ± 0.015	$0.630^{+0.044}_{-0.017}$	adius modelling. (Stassun et al., 20
	TOI-544	TIC 50618703	HD 290498	05:29:09.62 -00:20:34.43	$V = 10.777 \pm 0.017$	TESS = 9.6504 ± 0.006		$T_{ m eff}$	(K)	4169 ± 70	4248 ± 130	RA	82.2900716		M_{\star}	(M_{\odot})	0.630 ± 0.018	0.645 ± 0.021	$0.651^{+0.015}_{-0.026}$	stellar mass and re (TIC) version 8
Stellar Parameters	Identifiers TOI	TIC	H	Coordinates ¹ 05:2	$Magnitudes^1$ $V =$	TES	Spectroscopic Parameters	Method		SpecMatch-Emp ^a	SME		GAIA ²	Derived Parameters	Method		\mathtt{BASTA}^b	MIST	astroariadne	a Adopted as priors for the stellar mass and radius modelling. b Adopted as our final stellar parameter values to be used in from TESS Input Catalogue (TIC) version 8 (Stassun et al., 2019). 2 Taken from Gaia DR3 (Gaia Collaboration et al., 2021).

Stellar parameters for TOI-544 were calculated using BASTA (Aguirre Børsen-Koch et al., 2022) run on the co-added HARPS spectra, as follows. First, Gaia magnitude G, RA, DEC, and Parallax ϖ were taken from Gaia DR3 (Gaia Collaboration et al., 2021). T_{eff} and [Fe/H] were determined using the empirical software SpecMatch-Emp (Yee et al., 2017) which compares the observed data to a library of FGKM stars. We also compared the Spec-Match-Emp results with SME² (Spectroscopy Made Easy; Valenti and Piskunov, 1996; Piskunov and Valenti, 2017). SME computes synthetic spectra with line data from VALD³ (Ryabchikova et al., 2015) and a chosen stellar atmosphere grid, in our case Atlas12 (Kurucz, 2013), which is fitted to the observed spectra. The macro- and micro-turbulent velocities, $V_{\rm mac}$ and $V_{\rm mic}$, were held fixed to 1.5 km s⁻¹ and 0.5 km s⁻¹, respectively (Gray, 2008). A more detailed description of the modeling procedure can be found in Fridlund et al. (2017) and Persson et al. (2018). The results were in very good agreement with SpecMatch-Emp within 1 σ . Table 3.1 gives the spectroscopic parameters for TOI-544 modelled with SME and SpecMatch-Emp, we select the parameters using SpecMatch-Emp for our modelling of stellar mass and radius.

An age and metallicity independent prior was placed on stellar mass following the standard Salpeter Initial Mass Function, and reddening and dust were accounted for using the 'Bayestar' dustmap (Green et al., 2019). A prior was also set for [Fe/H] allowing for the parameter space to be searched only within an absolute tolerance range of 0.5 dex of the input value. For the isochrones, we used the latest version of BASTI (BAg of STellar Isochrones) (Hidalgo et al., 2018), set to the 'Diffusion' science case, described in Pietrinferni et al. (2021), to account for diffusion processes in low-mass stars.

BASTA determines model dependent parameters using a Bayesian approach, detailed in Silva Aguirre et al. (2015) and following the formalism of Serenelli et al. (2013).

We also used the Python isochrones (Morton, 2015) interface to the MIST stellar evolution models (Choi et al., 2016) using the same inputs as for BASTA,

²http://www.stsci.edu/~valenti/sme.html

³http://vald.astro.uu.se

which resulted in very good agreement for the stellar mass and radius (within $\sim 0.5\sigma$).

We compared our results from BASTA with the software astroARIADNE⁴ (Vines and Jenkins, 2022). This python code fits the observed spectral energy distribution via broad band photometry to atmospheric model grids to obtain the stellar radius. We fitted the bandpasses $GG_{BP}G_{RP}$ (Gaia eDR3), WISE W1-W2, JHK_S magnitudes (2MASS), the Johnson B and V magnitudes (APASS), and the Gaia eDR3 parallax. We used the Phoenix v2 (Husser et al., 2013) and the BtSettl (Allard et al., 2012) atmospheric models. The final radius was computed with Bayesian Model Averaging and the errors with a sampling method for conservative uncertainties as described in Vines and Jenkins (2022). In this way we obtained a stellar radius of $0.630^{+0.044}_{-0.017} R_{\odot}$. The stellar mass was computed with ARIADNE and the MIST (Choi et al., 2016) isochrones and was found to be $0.651^{+0.015}_{-0.026} M_{\odot}$. Table 3.1 gives the stellar parameters derived from our analysis, as well as the comparisons with ARIADNE, which are within 1 σ of our results from BASTA.

3.5 Analysis and Results

3.5.1 Transit model

We jointly fit the SPOC Pre-Search Data Conditioning Simple Aperture Photometry (PDCSAP) light curves from TESS Sectors 6 and 32 using the PyMC3 (Salvatier et al., 2016), exoplanet⁵ (Foreman-Mackey et al., 2019), starry (Luger et al., 2019), celerite2 (Foreman-Mackey et al., 2017; Foreman-Mackey, 2018) software packages.

To account for stellar activity signals and instrumental Systemics we included a Gaussian Process (GP, Rasmussen and Williams, 2005) model, using a Matérn-3/2 covariance function. We placed Gaussian priors on the stellar mass and radius based on the results in Table 3.1. We also placed Gaussian priors on the limb darkening coefficients based on interpolation of the parameters tabulated by Claret et al. (2012) and Claret (2017), propagating the uncertainties in the stellar parameters in Table 3.1 via Monte Carlo simulation.

⁴https://github.com/jvines/astroARIADNE

⁵https://docs.exoplanet.codes/en/stable/

Visual inspection of the TESS lightcurves reveals quasiperiodic variability with a \sim 1 ppt amplitude, and their Lomb-Scargle periodograms reveal peaks at \sim 8 and \sim 10 days, which are likely the first harmonic of the stellar rotation signal modulo instrumental noise. We thus placed loose Gaussian priors on the GP amplitude and timescale hyperparameters of 1.0 ± 0.5 ppt and 10 ± 5 days, respectively.

We used separate white noise parameters for each TESS sector to account for the possibility of differences in photometric precision, which could potentially arise from different background light conditions or different phases of the spacecraft's operational lifetime. We used the gradient-based BFGS algorithm (Nocedal and Wright, 2006) implemented in scipy.optimize to find initial maximum a posteriori (MAP) parameter estimates. We used these estimates to initialize an exploration of parameter space via "no U-turn sampling" (NUTS, Hoffman and Gelman, 2014), an efficient gradient-based Hamiltonian Monte Carlo (HMC) sampler implemented in PyMC3.

We sampled four chains with 4500 tuning iterations and 3000 additional draws, for a total of 12,000 samples after burn-in; the resulting chains were well-mixed according to a Gelman-Rubin statistic (Gelman and Rubin, 1992) value of <1.01, and the sampling error was $\lesssim 1\%$, suggesting a sufficient number of independent samples had been collected.

The phase-folded TESS photometry from Sector 6 and 32, along with the best-fit transit model, is shown in Figure 3.3 and the results of the transit fit are given in Table 3.2.

3.5.2 Frequency analysis of HARPS data

We performed a frequency analysis of our RV time-series to search for the Doppler reflex motion induced by the transiting planet discovered by TESS, spectroscopically confirm its planetary nature, and possibly unveil the presence of additional signals induced by stellar activity and/or additional orbiting companions. In order to avoid having to account for the RV offset between the two spectrographs, we did not include the 14 HARPS-N data points, and used only the 108 HARPS measurements, which cover a baseline of ~1051 d (nearly 3 years), implying a frequency resolution

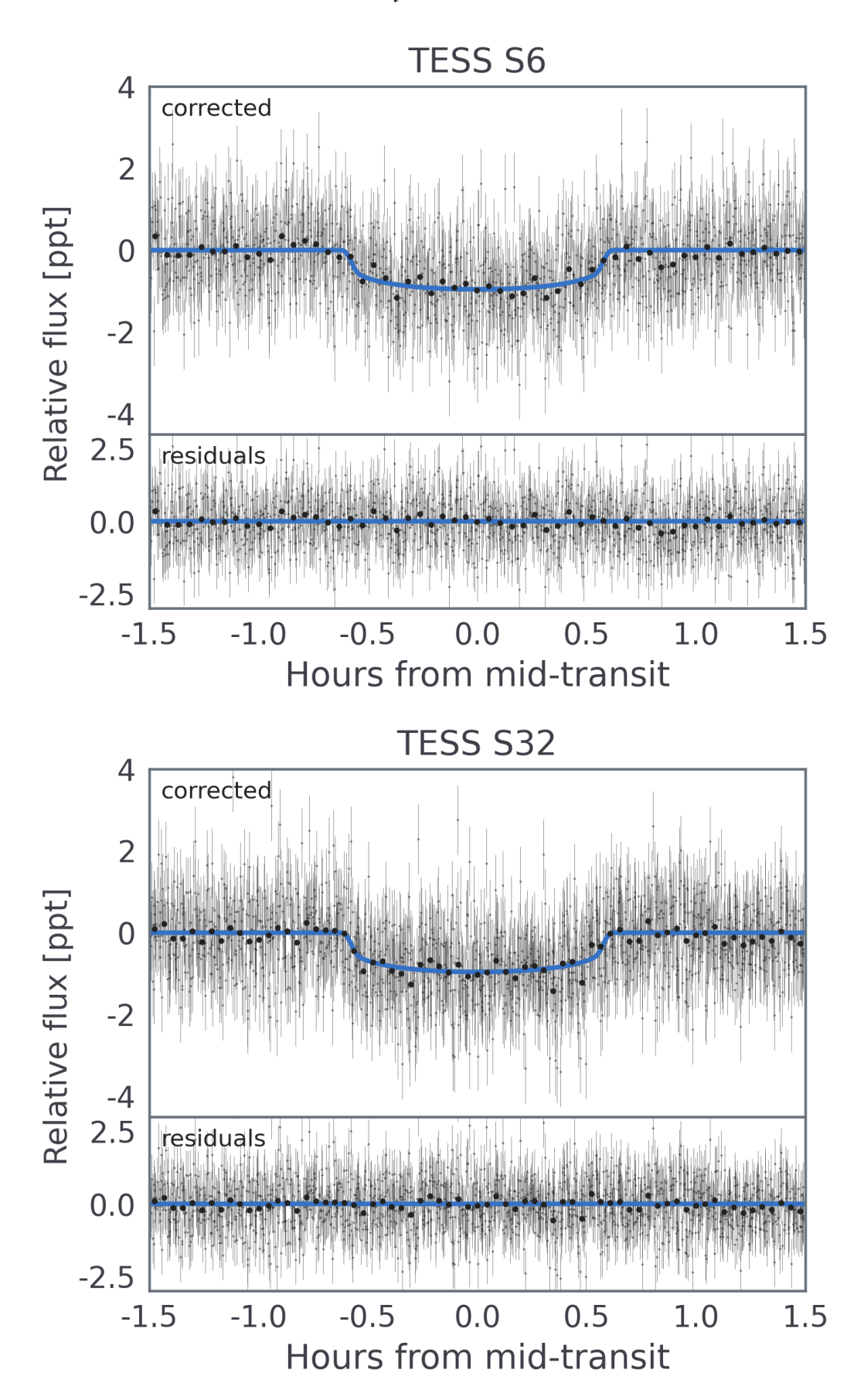


Figure 3.3: Phase-folded TESS photometry from Sector 6 (top) and Sector 32 (bottom), with the best-fit transit model in blue, the lower panel of each shows the residuals to the best fit model. The larger black points show the data binned by a factor of 30.

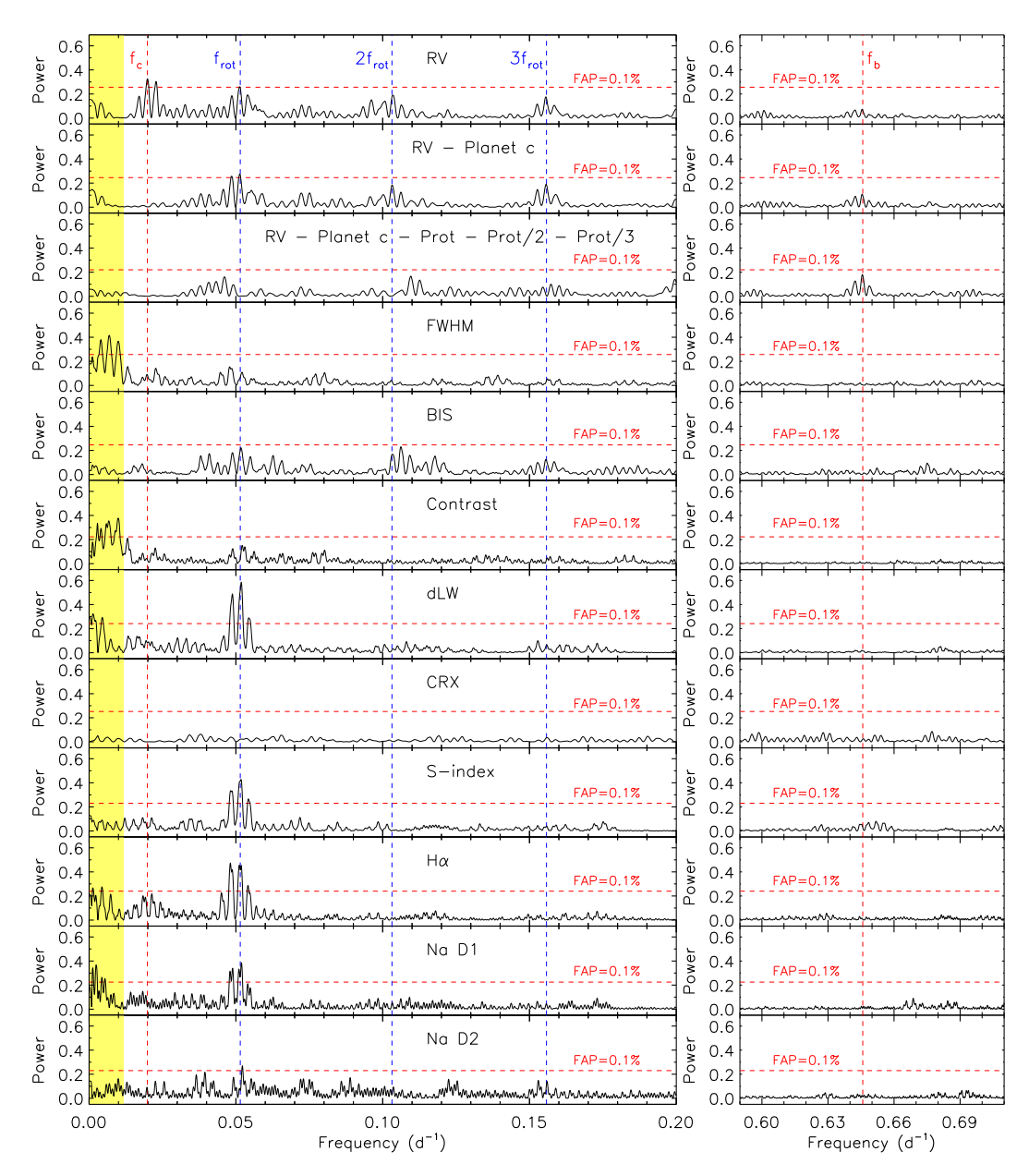


Figure 3.4: Generalised Lomb-Scargle periodograms of the SERVAL RV measurements and activity indicators of TOI-544. The right and left columns cover two frequency ranges encompassing the orbital frequency of TOI-544c, the stellar rotation frequency and its first two harmonics (left panels), and the orbital frequency of TOI-544 b (right panels). The Doppler signals from the two planets are marked as vertical red dashed lines at $f_c \approx 0.02 \, d^{-1}$ (TOI-544 c) and $f_b \approx 0.646 \, d^{-1}$ (TOI-544 b). Vertical, blue dashed lines indicate the stellar rotation frequency ($f_{rot} \approx 0.051 \,d^{-1}$) and its first two harmonics ($2 \,f_{rot} \approx 0.102 \,d^{-1}$ and $3 f_{rot} \approx 0.153 d^{-1}$). The horizontal red dashed line mark the 0.1% false alarm probability. The shaded yellow band highlights the frequency range encompassing the long-period activity signals that we significantly detected in the the FWHM, contrast, dLW, $H\alpha$, and Na D1, and that are likely related to spot evolution, along with their 1-year aliases (Sect. 3.5.2), last paragraph. From top to bottom: the SERVAL RV measurements; RV residuals following the subtraction of the Doppler reflex motion induced by TOI-544 c; RV residuals after subtracting the signals of the star rotation, its first two harmonics, and TOI-544 c; FWHM; BIS; contrast; dLW; CRX; S-index; H α ; Na D1; Na D2.

of $\sim 0.00095 \,\mathrm{d}^{-1}$.

Figure 3.4 displays the generalised Lomb-Scargle (GLS; Zechmeister and Kürster, 2009) periodograms of the HARPS SERVAL RV measurements and of the activity indicators in two frequency ranges. The panels to the left show the periodograms between 0.0 and $0.2\,\mathrm{d^{-1}}$, a range that includes the frequencies at which we expect to detect the Doppler signals induced by active regions corotating with the star. The panels to the right display the periodograms in the range $0.59\text{-}0.71\,\mathrm{d^{-1}}$, which encompasses the transit frequency of TOI-544b. We note that the gap between these frequencies shows nothing of note and is excluded. For each panel, the horizontal dashed line mark the false-alarm probability (FAP) of 0.1,%, as derived using the bootstrap method (Murdoch et al., 1993; Kuerster et al., 1997). We considered a peak to be significant if its FAP < 0.1%.

The GLS periodogram of the HARPS RVs (Figure 3.4, upper left panel) displays its most significant peak at $\sim 0.02 \, d^{-1} \, (\sim 50 \, d)$. This peak does not appear in any other periodograms of the activity indicators⁶, providing evidence that the 50-d signal is very likely caused by an additional companion, which we refer to as TOI-544 c throughout the chapter.

We removed the Doppler reflex motion induced by TOI-544 c fixing period and phase to the values derived from the periodogram analysis, while fitting for the RV semi-amplitude and systemic velocity. The periodogram of the RV residuals following the subtraction of the Doppler reflex motion induced by TOI-544 c (Figure 3.4, second left panel) shows 3 equally spaced peaks at $\sim 0.051 \, d^{-1} \, (\sim 19.4 \, d)$, $\sim 0.102 \, d^{-1} \, (\sim 9.8 \, d)$, and $\sim 0.153 \, d^{-1} \, (\sim 6.5 \, d)$. The former is significantly detected also in the periodograms of the dLW, CCF-BIS, S-index, H α , Na D1, and Na D2 lines (Figure 3.4, lower left panels), implying that this is very likely due to stellar activity. We interpreted the peak at $\sim 19.4 \, d$ as the stellar rotation period, in excellent agreement with the WASP results (Sect. 3.3.2). The two peaks at $\sim 9.8 \, d$ and $\sim 6.5 \, d$ are the first and second harmonics of the stellar rotation period, which are likely caused by the

⁶We note that there are two peaks in the periodogram for Hα which are symmetrically located around the peak at $\sim 0.02 \, d^{-1}$. However, neither these are at the same frequency as the signal, nor they are significant (FAP > 0.1 %)

presence of spots equally spaced in longitude and/or by the non-coherent nature of the activity-induced signal.

We removed the stellar signal by fitting 3 Fourier components at the stellar rotation period and its first two harmonics. The GLS periodogram of the RV residuals (Figure 3.4, third right panel) shows its strongest power at ~0.646 d⁻¹ (~1.55 d), the orbital frequency f_b of the transiting planet TOI-544 b. Although the FAP of this feature anywhere in the frequency range of the periodogram is higher than 0.1 %, the presence of a peak at a known frequency, i.e., the transit frequency, provides strong evidence that this signal is due to planet b. We estimated the FAP at the orbital frequency of TOI-544 b using the windowing bootstrap method described in Hatzes (2019). Briefly, we estimated the bootstrap FAP over a $\Delta v = 0.1$ d⁻¹ wide frequency window centered on f_b . We successively narrowed the spectral window at steps of 0.01 d⁻¹ for 10 additional bootstrap randomizations, down to $\Delta v = 0.01$ d⁻¹. The fit of the FAP versus window size, extrapolated to the intercept (i.e., the zero window length), yields a FAP=0.004 % at f_b , spectroscopically confirming the planetary nature of the transit signal discovered by TESS.

The periodograms of the FWHM, contrast, dLW, H α , and Na D1 (Figure 3.4, yellow strip) display significant peaks at frequencies $\lesssim 0.01 \, d^{-1}$ ($\gtrsim 100 \, d$), which are equally spaced by about $1/365 \approx 0.0027 \, d^{-1}$, i.e., the seasonal sampling of our time series. Hence, most of these peaks are 1-year aliases of true signals with periods of about $100\text{-}250 \, d$. This range includes the evolution timescale of active regions $\lambda_e = 112^{+28}_{-29} \, d$, as inferred by our multi-dimensional Gaussian process analysis (see Sect. 3.5.3), suggesting that these signals are associated to long-term stellar variability and spot evolution.

3.5.3 Radial velocity analysis

We modelled the RV data using the code pyaneti (Barragán et al., 2019, 2022), which implements a multi-dimensional GP to help account for the impact of stellar activity. The implementation of GPs for this purpose is described in detail in Rajpaul et al. (2015). Essentially, this method models the RVs and an activity indicator of choice, assuming that the same GP, $G(t_i, t_i)$, can describe both of them. We used the

S-index as the activity indicator to model alongside the RVs. As the RVs and the S-index of TOI-544 show a significant stellar rotation signal (Figure 3.4), we chose the quasi-periodic (QP) kernel for the GP

$$G\left(t_{i},t_{j}\right) = A^{2}exp\left[\frac{\sin^{2}\left[\pi\left(t_{i}-t_{j}\right)/P_{GP}\right]}{2\lambda_{p}^{2}} - \frac{\left(t_{i}-t_{j}\right)^{2}}{2\lambda_{e}^{2}}\right],\tag{3.1}$$

where P_{GP} is the GP characteristic period (which here represents the stellar rotation period), λ_p is the inverse of the harmonic complexity (related to distribution of active regions on the stellar surface), and λ_e is the long-term evolution timescale (the lifetime of active regions on the stellar disk). The two-dimensional GP used to model the system is then given by

$$RV = A_0G + A_1dG \tag{3.2}$$

and

$$S-index = A_2G + A_3dG (3.3)$$

where A_0 , A_1 , and A_2 are GP hyperparameters in the form of amplitudes that work as a scale factor that determines the typical deviation from the mean function, and dG is the time derivative of our GP function, $G(t_i,t_j)$. From first principles, $A_3 \equiv 0$, see Rajpaul et al. (2015) for more details. We used the stellar parameters listed in Table 3.1, and informative Gaussian priors on the orbital period and time of mid-transit for planet b based on those found in the transit fit (Sect. 3.5.1). We used the orbital period and time of inferior conjunction we derived from our GLS periodogram to place uniform priors for planet c (see Figure 3.4 and Sect. 3.5.2 for description of this search). We adopted a uniform prior on P_{GP} centered on the stellar rotation period found by the WASP photometry, and wide uniform priors on the remaining model parameters. Pyaneti infers the systemic velocity (aka offset) for each instrument, the exact values found by Pyaneti are given in Table 3.2. We then performed a Markov chain Monte Carlo (MCMC) analysis, fitting for an eccentric orbit for both planets. We sampled the parameter space with 500 Markov chains and used the final set of 5000 steps with a thin factor of 10 to produce our

posterior distributions, the total iterations during the burn-in phase was 5000, which led to a total of 250000 independent points for each sampled parameter.

We find that TOI-544 b has an orbital period of ~ 1.55 days and a $K_{\rm b}$ amplitude (the radial velocity semi-amplitude) of 2.66 ± 0.44 m s⁻¹, equating to a planet mass of 2.89 ± 0.48 M_{\oplus}. The eccentricity of TOI-544 b is found to be $0.35^{+0.14}_{-0.12}$ and its argument of periastron is 41.2^{+17}_{-26} degrees. TOI-544 c has a period of 50.1 ± 0.2 days, K_c amplitude of 5.21 ± 0.57 m s⁻¹, implying a minimum mass of 21.5 ± 2.0 M_{\oplus}. The eccentricity of TOI-544 c is found to be 0.30 ± 0.09 and argument of periastron is 17^{+21}_{-18} degrees.

We assessed the significance of the eccentric solutions for the two planets by creating 5000 sets of synthetic RV time-series that sample the best-fitting circular solutions at the epochs of our real observations. We added Gaussian noise at the same level of our RV measurement uncertainties and fitted the simulated time series allowing for non-zero eccentricities. For TOI-544 b there is a ~3.5% chance that a best-fitting eccentric solution with $e \ge 0.35$ could arise by chance if the orbit is actually circular. As for TOI-544 c, the probability that noise can account for $e \ge 0.30$ is only 0.2 %. Assuming a significance level of 1%, the eccentric solution for TOI-544 b is likely not real, while the eccentricity of TOI-544 c is real. Therefore, our adopted results are for the case where the inner planet is on a circular orbit and outer planet is on an eccentric orbit, i.e., TOI-544 b has an orbital period of ~ 1.55 days and a K_b amplitude of 2.17 ± 0.36 m s⁻¹, equating to a planet mass of $M_{\rm b} = 2.89 \pm 0.48 \, \mathrm{M}_{\oplus}$, TOI-544 c has a period of 50.1 ± 0.2 days, $K_{\rm c}$ amplitude of $5.36 \pm 0.55 \text{ m s}^{-1}$, implying a minimum mass of $M_c \sin i_c = 21.5 \pm 2.0 \text{ M}_{\oplus}$. The eccentricity of TOI-544 c is found to be $e_c = 0.32 \pm 0.09$ and argument of periastron is $\omega_{\rm c} = 12^{+19}_{-17}$ degrees.

The priors used for all parameters are shown in Table A.6, and the results, showing the median value and 68 % credible interval for each parameter, are given in Table 3.2. The best fit model alongside the data are shown, as a function of time, in Figure 3.5 and phase-folded for each planet in Figures 3.6 and 3.7.

We additionally chose to model the RV data using several other methods to

ensure the robustness of our results. Using pyaneti, we ran similar fits to the one described above, but with: a) both planets on circular orbits; b) the inner planet on a circular orbit and the outer planet on an eccentric orbit; c) a fit with pyaneti but not multi-dimensional (i.e., fitting on only the RV data points); d) a joint model including both transit and RV data. Our joint fit of transit and RV data provides consistent results with the planet mass within 1 σ of our other models (see Table A.5).

We also make use of the radial velocity fitting toolkit RadVel (Fulton et al., 2018). Using RadVel we ran fits for: a) a two planet system with no GP to account for stellar activity; b) a 1 planet system (only the transiting inner planet) including a GP using the Celerite quasi-periodic kernel (Foreman-Mackey et al., 2017); c) a 2 planet system using the Celerite quasi-periodic kernel where both planets are on circular orbits; d) the same kernel again but where both planets are on eccentric orbits; e) a 2 planet system where we use the square-exponential GP kernel (described in Fulton et al. (2018)). As well as this, we checked for possible additional signals by fitting for a 3-planet system. We found that the third signal is unconstrained and the BIC and AIC increase slightly over the 2-planet case – therefore we do not believe there are signs of additional planets in the system. We also changed the choice of priors in our models, in particular for the period of planet c to ensure we are not biasing our results. For example, the RadVel fit for a 2-planet system with the square exponential kernel has a uniform prior on P_c of 0 to 100 days, and the RadVel fit for a 2-planet system with the Celerite quasi-periodic kernel has a Gaussian prior of 50.6 ± 1.0 days. In all cases the results are consistent. The resulting K semi-amplitude of TOI-544 b found from all models are shown in Table A.5.

RadVel also allows for model comparison. We found that in models which include more than one planet, a single-planet model is ruled out in every case - providing greater assurance of the existence of the second planet. Specifically, for a 1-planet system, the BIC is 1993.90 and AIC is 1965.46, and for 2-planet system 801.24 and 765.90 respectively. We also ran additional models using only the

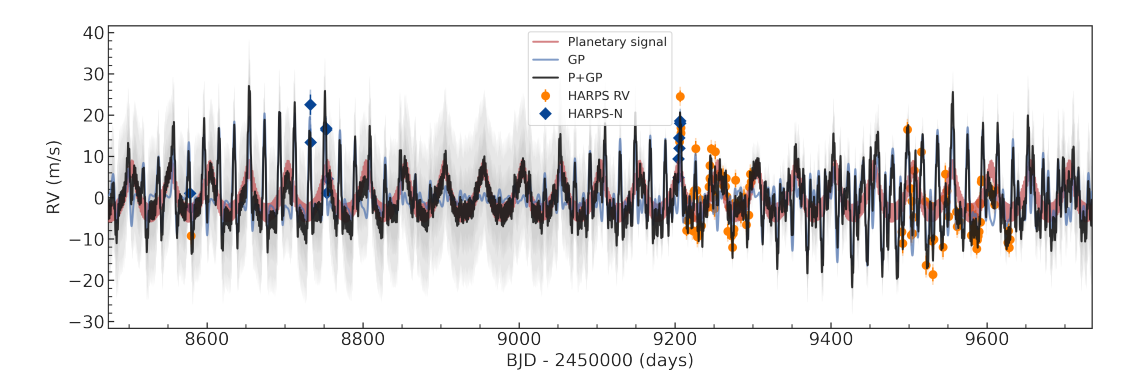


Figure 3.5: Best-fit 2-planet Keplerian orbital model for TOI-544. HARPS data shown by orange circles, and HARPS-N data shown by blue diamonds, both shown as a function of time. The best-fit model for the planet signals is shown in red, the GP model in blue, and the combined planets and GP shown in black. The dark and light shaded areas showing the 1σ and 2σ credible intervals of the corresponding GP model, respectively.

HARPS data points to ensure the HARPS-N points (which have a slightly higher level of scatter) are not influencing our fit, and with RVs extracted with TERRA rather than SERVAL, in all cases the results are consistent within 1- σ . As well as this, we ran pyaneti fits with different activity indicators: FWHM, and contrast, and combinations of indicators: S-index and FWHM, S-index and contrast, and FWHM and contrast. In all cases the derived planet parameters are consistent with our other models within 1- σ , however the GP hyperparameters are not all so well constrained so we still use the model with the S-index as our adopted results.

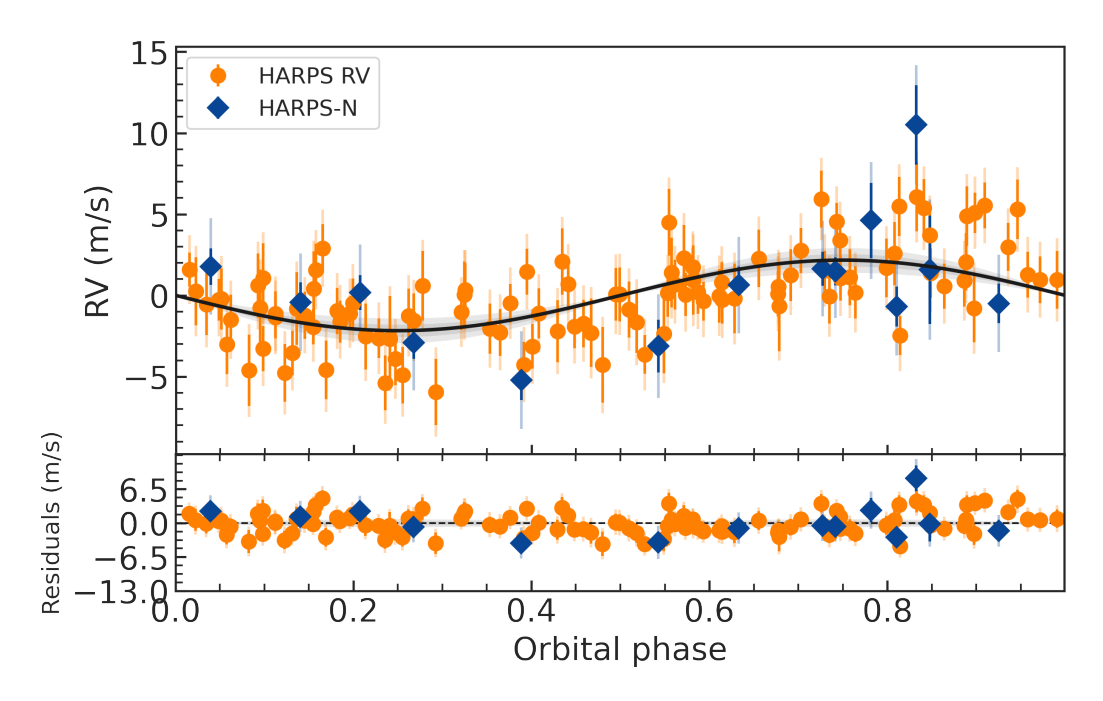


Figure 3.6: The phase-folded RV data from HARPS (orange circles) and HARPS-N (blue diamonds) alongside the best-fit planet model for TOI-544 b. The effect of TOI-544 c and the GP model have been subtracted. The lower part shows the residuals from the fit. There appears to be no trends visible in the residuals.

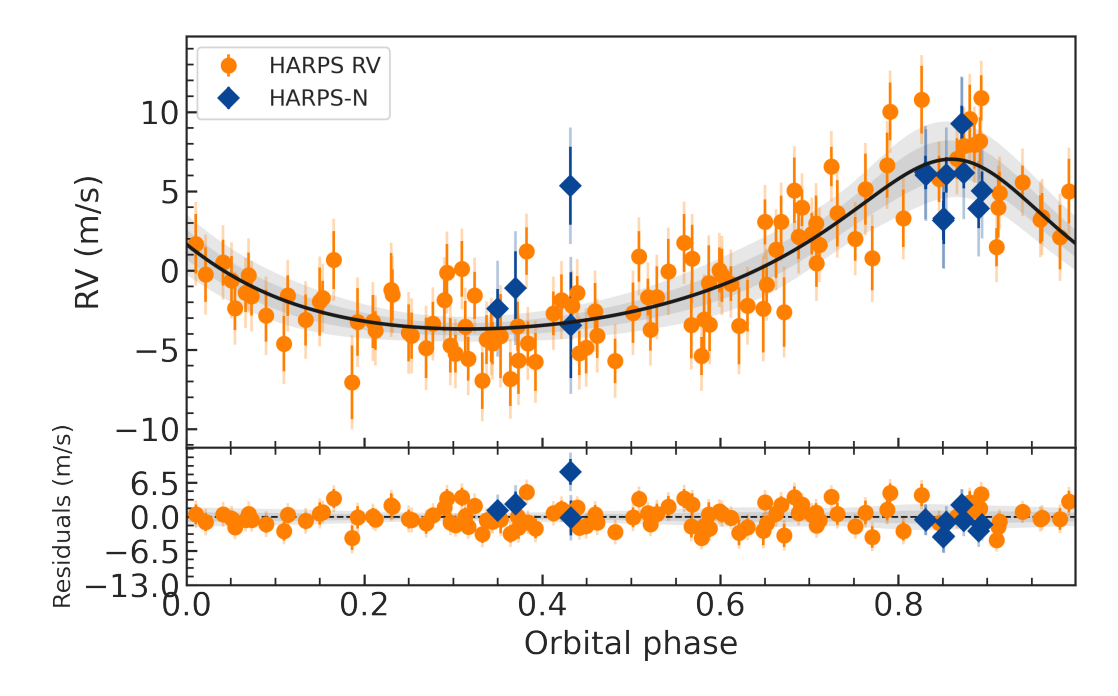


Figure 3.7: The phase-folded RV data from HARPS (orange circles) and HARPS-N (blue diamonds) alongside the best-fit planet model for TOI-544 c. The effect of TOI-544 b and the GP model have been subtracted. The lower part shows the residuals from the fit. There appears to be no trends visible in the residuals, and the augmented sinusoid representative of an eccentric orbit is present in the phase-folded plot.

Table 3.2: Results of the transit and RV fit for TOI-544, showing the median value and 68 % credible interval for each parameter.

Fitted Parameter	Median value					
Planet Transit Parameters						
Stellar Mass M_{\star} [M_{\odot}]	0.631 ± 0.018					
Stellar Radius R_{\star} $[R_{\odot}]$	0.623 ± 0.012					
Time of Mid-Transit T_0 [BJD _{TDB} – 2450000]	$9199.031363^{+0.000614}_{-0.000703}$					
Orbital Period P _b [days]	1.548352 ± 0.000002					
$R_{ m b}/R_{\star}$	0.0297 ± 0.0007					
Impact Parameter b	$0.66^{+0.03}_{-0.04}$					
$\sigma_{ ext{GP}}$ [ppm]	707^{+113}_{-86}					
$ ho_{ ext{GP}}$ [hours]	$22.0_{-2.8}^{+3.5}$					
u_1	0.43 ± 0.16					
u_2	0.24 ± 0.15					
$\log \sigma_{\rm S6}$ [ppt]	$-0.159094^{+0.005981}_{-0.005915}$					
$\log \sigma_{ m S32}$ [ppt]	$-0.157482^{+0.005387}_{-0.005275}$					
Planet Radius R_b [R_{\oplus}]	2.018 ± 0.076					
Semi-major Axis a_b [AU]	0.0225 ± 0.0002					
Equilibrium Temperature $T_{\rm eq}$ [K]	999 ± 14					
Transit Duration T_{14} [hours]	1.21 ± 0.03					
Planet RV Parameters						
Planet b						
Orbital Period, P_b [days]	1.548352 ± 0.000002					
Time of Inf. Conjunction, $T_{\text{conj,b}}$ [BJD _{TDB} – 2450000]	9199.0314 ± 0.0007					
Time of Periastron, $T_{\text{peri,b}}$ [BJD _{TDB} – 2450000]	9198.6443 ± 0.0007					
Eccentricity, e_{b}	≡ 0					
Argument of Periastron, $\omega_{\rm b}$ [°]	≡ 0					
$ew1_{\rm b}$, $\sqrt{e_{\rm b}}\sin\omega_{\rm b}$	≡ 0					
$ew2_{\rm b}$, $\sqrt{e_{\rm b}}\cos\omega_{\rm b}$	≡ 0					
RV Semi-Amplitude, K_b [m s ⁻¹]	2.17 ± 0.36					
Planet Mass, M_b [M_{\oplus}]	2.89 ± 0.48					
Planet c						
Orbital Period, P _c [days]	50.089 ± 0.24					
Time of Inf. Conjunction, $T_{\text{conj,c}}$ [BJD _{TDB} – 2450000]	$9212.0^{+1.8}_{-1.9}$					
Continued on next page						

Table 3.2 – continued from previous page.

Table 3.2 – Continued from previous page.					
Fitted Parameter	Median value				
Time of Periastron $T_{\text{peri,c}}$ [BJD _{TDB} – 2450000]	$9205.4^{+2.2}_{-2.8}$				
Eccentricity, $e_{\rm c}$	$0.32^{+0.08}_{-0.09}$				
Argument of Periastron, $\omega_{\rm c}$ [°]	11^{+19}_{-17}				
$ew1_{\rm c}, \sqrt{e_{\rm c}}\sin\omega_{\rm c}$	0.11 ± 0.17				
$ew2_{\rm c}$, $\sqrt{e_{\rm c}}\cos\omega_{\rm c}$	$0.52^{+0.08}_{-0.11}$				
RV Amplitude, K_c [m s ⁻¹]	5.36 ± 0.56				
Planet Minimum Mass, $M_c \sin i_c [M_{\oplus}]$	21.5 ± 2.0				
Other Parameters					
Offset RV _{HARPS-N} [km s ⁻¹]	-0.016 ± 0.002				
Offset RV _{HARPS} [km s $^{-1}$]	0.006 ± 0.001				
Offset S-index _{HARPS-N}	1.13 ± 0.03				
Offset S-index _{HARPS}	$1.25^{+0.03}_{-0.04}$				
Jitter Term RV _{HARPS-N} , $\sigma_{\text{HARPS-N}}$ [m s ⁻¹]	$2.75^{+1.44}_{-1.13}$				
Jitter Term RV _{HARPS} , σ_{HARPS} [m s ⁻¹]	$1.85^{+0.36}_{-0.33}$				
Jitter Term S-index _{HARPS-N}	$45.5^{+17.7}_{-12.8}$				
Jitter Term S-index _{HARPS}	$42.6^{+3.5}_{-3.2}$				
GP Hyperparameters					
A_0	$0.002^{+0.001}_{-0.001}$				
A_1	$0.025^{+0.008}_{-0.005}$				
A_2	$0.076^{+0.025}_{-0.016}$				
A_3	≡ 0				
$\lambda_{\rm e}$ [days]	112^{+28}_{-29}				
$\lambda_{ m p}$	$0.519^{+0.091}_{-0.074}$				
Rotation Period, P _{GP} [days]	$19.343^{+0.073}_{-0.076}$				

3.6 Discussion

3.6.1 Composition of TOI-544 b

The calculated density of TOI-544 b is $\rho_b = 1.93^{+0.30}_{-0.25}$ g cm⁻³, which is not dense enough to be composed of entirely rock and iron, where densities are typically between 3 g cm⁻³ and 10 g cm⁻³ (Zeng et al., 2019). This implies that a composition of a bare rocky-iron core can likely be excluded. TOI-544 b must have some

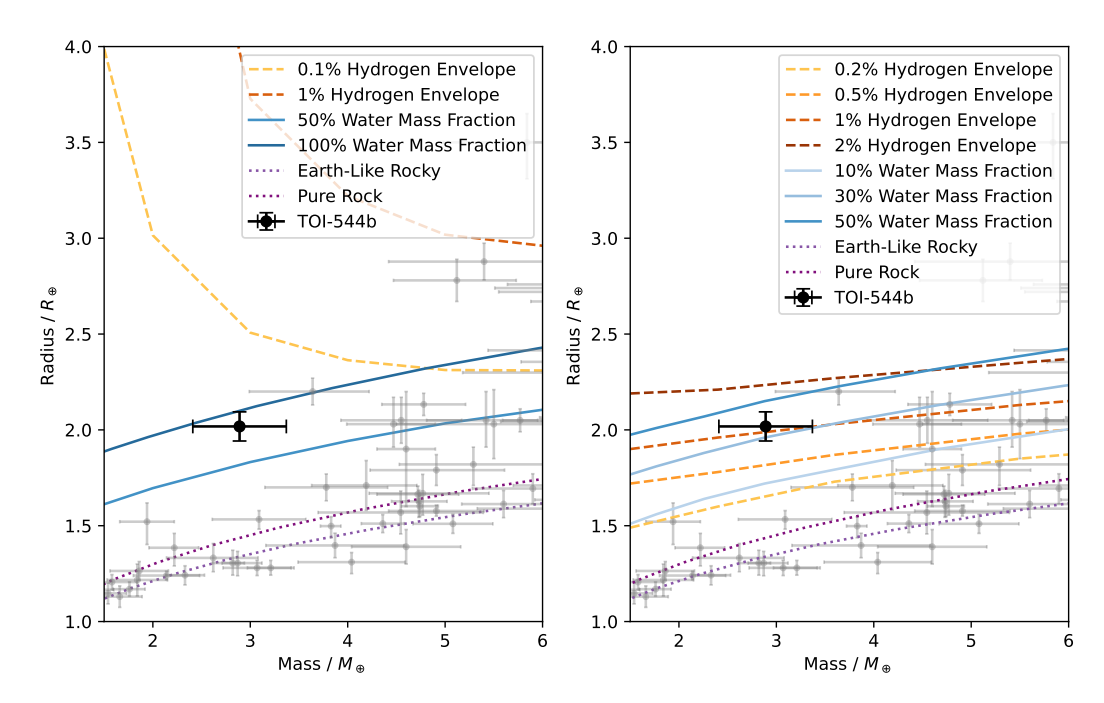


Figure 3.8: Mass-radius diagram showing confirmed planets with mass uncertainties < 20% in grey circles, with TOI-544 b shown as the black circle. Left: the coloured tracks show different potential planet compositions from Zeng et al. (2019), assuming a planetary equilibrium temperature of 1000 K. The dashed lines show compositions of an Earth-like rocky core surrounded by a layer of H-He in varying percentages by mass, the solid lines show water world compositions with varying water mass fractions, the dotted lines show rocky and Earth-like rocky compositions. TOI-544 b is closest to the tracks with 100% H₂O and 50% H₂O with 50% rock. Right: the same as the left panel but the the dashed lines show compositions of an Earth-like rocky core surrounded by a layer of H-He in varying percentages by mass from Lopez and Fortney (2014) using the models for a 10Gyr planet, with solar metalicity and flux of 10F_{\text{\omega}}, the solid lines show compositions from Aguichine et al. (2021) of irradiated ocean worlds with varying water mass fractions, and the dotted lines show the same rocky and Earth-like rocky compositions from Zeng et al. (2019). TOI-544 b is closest to models with either 30% water mass fraction, or a rocky core with a Hydrogen envelope of between 0.5 - 1%. The data is downloaded from the NASA Exoplanet Archive.

additional component to its composition, but whether it is in the form of water/ice layers or a H-He atmosphere depends on which particular composition models are used. Figure 3.8, left panel, shows the mass radius diagram for small planets (< 4 R_{\oplus} , with mass uncertainties < 20 %) with TOI-544 b highlighted and composition tracks from Zeng et al. (2019) shown in different colours. As noted in Rogers et al. (2023), these models are often misinterpreted when used in mass-radius diagrams. Specifically, there are a range of models available depending on the chosen temperature, this temperature is often assumed to be the equilibrium temperature of the planets but is actually the temperature at a pressure of 100 bars. In this case we have used the *incorrect* temperature (equal to the planet equilibrium temperature of ≈ 1000 K) in order to show a direct comparison to many other mass-radius diagrams available in the literature. Using these models alone, it appears that TOI-544 b does not fit the super-Earth (rocky/iron core) scenario, and that it also does not fit the typical sub-Neptune composition of a rocky core surrounded by atmospheric H-He. From these models it seems likely that TOI-544 b is a water-world planet with a sizeable fraction of H₂O present. From the Zeng et al. (2019) models it seems that a water fraction by mass of over 50% is possible for this planet. There are few other planets detected in a similar area of parameter space, however we note that many of the planets in this regime have multiple mass values listed on the NASA Exoplanet Archive so their exact location on the mass-radius diagram depends on the specific choice of literature parameters, and many have longer orbital periods, meaning it is difficult to do a real comparison.

To further investigate the compositional nature of the planet, we use the dimensionless parameter ζ from Zeng et al. (2021)

$$\zeta \equiv \frac{(R_c/R_{\oplus})}{(M_c/M_{\oplus})^{0.25}},$$
(3.4)

where R_C and M_C are the core radius and mass respectively, similar to the approach taken in Nava et al. (2019). This parameter can be used to distinguish between the 3 possible compositions of small exoplanets – either rocky and earth-like ($\zeta = 1$), having significant amounts of ices ($\zeta = 1.4$), or icey cores with hydrogen/helium

envelopes ($\zeta = 2.2$). For small planets the core radius and mass can be approximated the planet radius and mass (in units of Earth radii and mass). The value of ζ for TOI-544 b is 1.5, which suggests an ice dominated composition.

Another approach is noting that TOI-544 b is a highly irradiated planet due to its short semi-major axis. We make use of the Structure Model Interpolator (SMINT) 7 which obtains posterior distributions of H_2O mass fraction based on interpolation onto the Aguichine et al. (2021) model grids. Using the stellar and planetary parameters listed previously, with conservative uncertainties, we obtain an H_2O fraction of 0.25 ± 0.12 . This is lower than the expected H_2O fraction seen in the mass-radius diagram. We note, however, that the models from Zeng et al. (2019) do not account for the high level of radiation such a close-in planet would receive.

However, whilst Zeng et al. (2019) models are commonly used in mass-radius diagrams for small planets, Rogers et al. (2023) recommend using the mass-radius relations for sub-Neptune compositions given in Lopez and Fortney (2014), which assume a constant planet age, rather than the Zeng et al. (2019) models which assume a constant specific entropy. In the right panel of Figure 3.8, we plot a mass-radius diagram with composition tracks from Lopez and Fortney (2014) and Aguichine et al. (2021). The dashed lines show compositions of an Earth-like rocky core surrounded by a layer of H-He in varying percentages by mass from Lopez and Fortney (2014). The solid lines show compositions from Aguichine et al. (2021) of irradiated ocean worlds with varying water mass fractions. The dotted lines show the same rocky and Earth-like rocky compositions from Zeng et al. (2019) which are shown in the left panel. Setting TOI-544 b on this graph, we see that according to the Lopez and Fortney (2014) models, a composition of an Earth-like core surrounded by a layer of H-He of between 0.5 and 1% by mass can also explain the observed mass and radius. The composition tracks from Aguichine et al. (2021) for irradiated water-worlds suggest an alternative composition of TOI-544 b of a rocky core with a layer of water/ice of around 30% by mass.

⁷https://github.com/cpiaulet/smint

As discussed in Rogers et al. (2023), for individual planets such as TOI-544 b, mass and radius alone are insufficient to uniquely constrain planet composition. In order to break the degeneracy between the water-worlds and sub-Neptune models, atmospheric observations of the planet are needed to rule out (or in) the potential for H-He or H₂O atmospheres. Fortunately, as described in Section 3.6.4, TOI-544 b is an ideal candidate for atmospheric studies. Future observations, with for instance JWST, should be able to help determine more definitively whether this is a water-world or not.

From Figure 3.8 it can also be seen that TOI-544 b sits within an area of the mass-radius diagram where few planets have been observed. Of the more than 5000 exoplanets confirmed to date, there are less than 200 small (< 4 R_{\oplus}) planets which have precisely characterised masses (uncertainties < 20%), and of those, less than 30 are low mass (< 4 M_{\oplus}). The majority of these small, low mass planets with precise characterisation cluster around the composition tracks for rocky silicates or iron composition – similar to an Earth-like composition. The most similar planet is Kepler-307c, which is one of the only low mass planets that has a similarly low density (seen to the top right of TOI-544 b in Figure 3.8). The mass of Kepler-307c was determined through transit timing variations rather than through RV observations. As there have been suggestions of a potential offset between the two methods (Steffen, 2016; Mills and Mazeh, 2017), it is possible that these two planets are not fully comparable. In general, there are few precisely-characterised masses for small planets, and even fewer for potential water-worlds, meaning TOI-544 b is an important addition to this region of parameter space.

3.6.2 Location in relation to the radius valley

In the most recent comprehensive study of the radius valley, Ho and Van Eylen (2023) refitted Kepler data to find an empirical radius valley location, as a function of various other parameters. In particular, they find a dependence on the location of the valley as a function of stellar mass. Figure 3.9 shows the period-radius diagram for confirmed Kepler planets orbiting stars with stellar mass < 0.8 M_{\odot} fitted in a homogeneous way in Ho and Van Eylen (2023). Additionally, planets with precise

mass measurements from the NASA Exoplanet Archive which orbit stars with masses $< 0.8~M_{\odot}$ are highlighted, and TOI-544 b shown. TOI-544 b sits within the radius valley region calculated for this specific stellar mass - using Equation 11 from (Ho and Van Eylen, 2023):

$$\log_{10}(R_p/R_{\oplus}) = A \log_{10}(P/days) + B \log_{10}(M_*/M_{\odot}) + C$$
 (3.5)

with A = $-0.09^{+0.02}_{-0.03}$, B = $0.21^{+0.06}_{-0.07}$, C = $0.35^{+0.02}_{-0.02}$ and using TOI-544's stellar mass (see Table 3.1). TOI-544 b is more than 3σ away from the upper and lower bounds of the radius valley (shown by the dashed lines). We also ran a number of fits for stellar radius; we use the calculated stellar radii from 3.1, taking the most extreme cases of the BASTA fit -1σ , and the astroARIADNE fit $+1\sigma$ (i.e.the smallest and largest possible from our results), we find planet radii of 2.16 and 1.98 R_{\oplus} respectively. These values still put TOI-544 within the limits of the valley given in Ho and Van Eylen (2023).

We also compare the location of the radius valley presented in Ho and Van Eylen (2023) with other works. In particular, Petigura et al. (2022) also find that the location of the valley varies based on stellar mass, finding a similar relation to Equation 3.5. For a star of mass 0.5 - 0.7 M_{\odot} , Figure 8 in Petigura et al. (2022) shows that TOI-544 b would be inside the valley. Cloutier and Menou (2020) also investigated the location of the radius valley for low mass (mid-K to mid-M dwarf) stars and similarly find that a planet such as TOI-544 b, with radius of 2.018 \pm 0.076 R_{\oplus} and orbital period of 1.55 days would be located inside the valley in the region they dub "keystone planets", see Figure 15 of Cloutier and Menou (2020).

The observational results for the location of the radius valley can be compared with theoretical models such as in Owen and Wu (2017), which predicts that the location of the valley also depends on the planetary core composition. If we assume that planets form uniformly with an icey core – rather than a rocky one – then the theoretical models predict that the radius valley will be shifted to a higher radius for a given orbital period. This means that, for planets with icey cores - sometimes referred to as water world planets - the location of TOI-544 b in the

radius-period space would not put it inside the radius valley. Instead it would sit below the valley, in a region which predicts planets with a sizeable water/ice faction but without significant hydrogen/helium atmospheres, potentially having undergone atmospheric loss.

Luque and Pallé (2022) argue that the radius valley distribution may in fact be the result of two different core compositions of planets rather than purely from atmospheric loss mechanisms, in the case of planets orbiting M dwarfs. They state that small planets come in two distinct types: super-Earths with rocky/iron composition, and water worlds with a combination of both rock and water/ices. This interpretation is disputed by Rogers et al. (2023), who argue that the properties of the sample of planets around M dwarfs studied by Luque and Pallé (2022) can also be explained by the more traditional super-Earth sub-Neptune classifications which arise from atmospheric loss models.

We note that at this stage there is no conclusive evidence either way to support the water worlds versus atmospheric loss explanation of the radius valley, and further investigation is needed to fully distinguish between the two theories. In particular, confirmation of TOI-544 b as a water world or not (as well as other small planets) would help to provide evidence for the formation mechanisms which carve the radius valley.

3.6.3 Planet c

We searched the TESS lightcurves for signs of a transit of TOI-544 c but none were found. If we assume that both planets are at the same orbital inclination (which may not be the case) then planet c would not be expected to transit given its impact parameter of 5. As a result, we can only constrain a minimum mass for TOI-544 c of $21.5 \pm 2.0 \, M_{\oplus}$, for reference this is slightly higher than the mass of Neptune. Planet c is found to have a non-zero eccentricity, and, if it is confirmed that TOI-544 b has a large fraction of water within its composition, then it is likely that it must have formed exterior to the snow-line, and then migrated inwards - this migration could have been facilitated by TOI-544 c. A full dynamical investigation of the system architecture is beyond the scope of this chapter, but could be interesting in

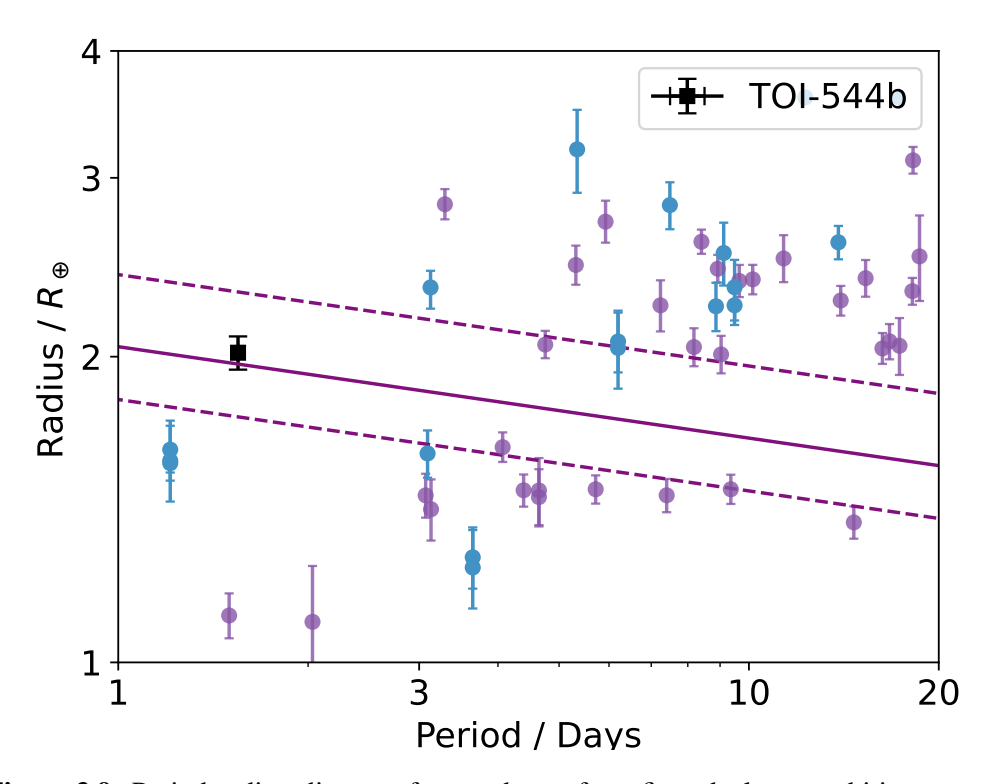


Figure 3.9: Period-radius diagram for a subset of confirmed planets orbiting stars with masses $< 0.8 \ M_{\odot}$. Purple circles are confirmed Kepler planets fitted in a homogeneous way in Ho and Van Eylen (2023). Blue circles show planets with precise mass measurements from the NASA Exoplanet Archive. TOI-544b is shown by the black square. TOI-544b sits within the expected location of the radius valley (between the dashed lines) for this specific stellar mass - calculated from Equation 11 in Ho and Van Eylen (2023).

the future, particularly if the composition of the inner planet is better constrained, and it is possible that if the planets do not orbit in the same plane then planet c could in fact transit.

3.6.4 Potential atmospheric studies of TOI-544 b

We calculated the transmission spectroscopy metric (TSM, Kempton et al., 2018) for TOI-544 b, finding a value of 163, much higher than the recommended threshold value (90) from (Kempton et al., 2018) for planets with radii above 1.5 R_{\oplus} , placing TOI-544 b among the most appealing targets for transmission spectroscopy characterisation with JWST (within the top 15 targets for similar planets, see Figure 3.10). Moreover, the emission spectroscopic metric (ESM, Kempton et al., 2018) is found

to be 16. Considering the Kempton et al. (2018) cutoff of 7.5, TOI-544 b lies among the top 10 most favourable targets (see Figure 3.10). TOI-544 b is within the top 5 targets for both TSM and ESM for planets with radii between 1.5 and 2.75 R_{\oplus} and temperature between 800 and 1250K, as identified by the TESS follow-up atmospheric working group. We also calculate the predicted S/N ratio for atmospheric observations of TOI-544 b with JWST (using the method in Niraula et al. (2017), finding a value of 1.000. This puts TOI-544 b within the top dozen small planets with temperature less than 1250K in terms of potential JWST observations. Atmospheric observations should help to reduce the degeneracy between composition models for this planet and determine whether a water world or a rocky and hydrogen composition is more likely, similar to a recent study of TOI-270 d (Van Eylen et al., 2021) for which transmission spectroscopy revealed a possible hydrogen-rich atmosphere (Mikal-Evans et al., 2022).

3.7 Conclusions

We present the results of an extensive high-precision RV campaign of TOI-544. We confirm the planet TOI-544 b and derive a mass of M_b = 2.89 \pm 0.48 M_{\oplus} which, combined with the planetary radius of R_b = 2.018 \pm 0.076 R_{\oplus} gives a bulk density of ρ_b = 1.93 $^{+0.30}_{-0.25}$ g cm⁻³. The density of the planet means it most likely has either a significant fraction of ice within its composition (around 30% by mass) or is composed of an Earth-like rocky core surrounded by a layer of atmospheric H-He (around 0.5 - 1% by mass). TOI-544 b also sits within the expected location of the small planet radius valley for FGK stars, although improvements in the radius measurement with additional transit observations would help confirm this further. The calculated TSM and ESM of TOI-544 b put it within the top few planets for atmospheric observations with similar size and temperature, meaning it is an excellent candidate for future observations with JWST. We additionally confirm the existence of a second, non-transiting planet within the system, TOI-544 c, with a minimum mass of $M_c \sin i_c = 21.5 \pm 2.0 \, M_{\oplus}$. Both planets have well-characterised masses (uncertainties of < 20%) and contribute to the small but growing number of

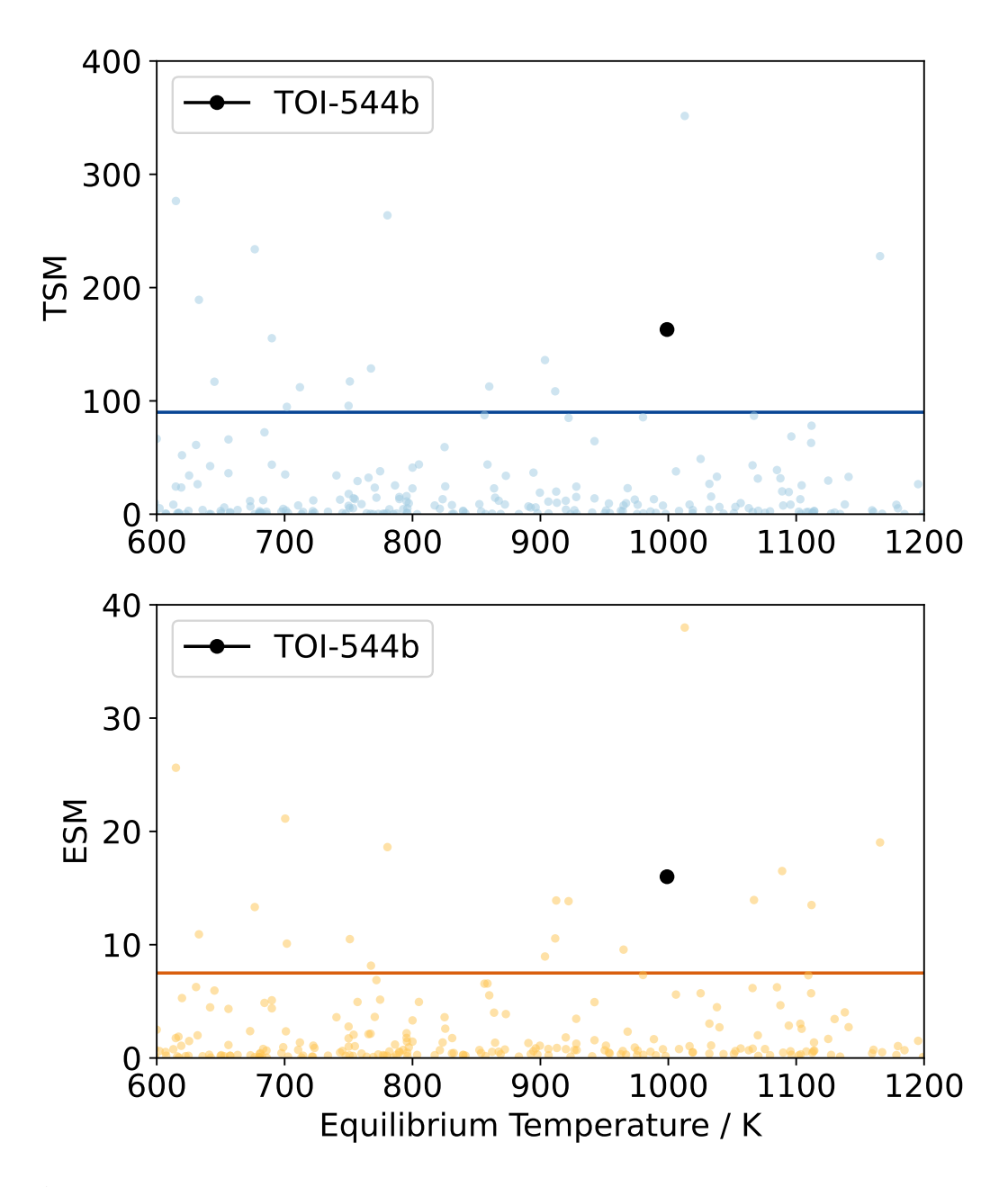


Figure 3.10: Top panel: The transmission spectroscopy metric (TSM) against equilibrium temperature of all small ($R < 4R_{\oplus}$) confirmed planets with a mass measurement, blue dots. The threshold given in Kempton et al. (2018) is shown by the solid line. TOI-544b is shown in the black circle, it is within the top 15 planets for TSM value. Bottom Panel: Same as above but for the emission spectroscopy metric (ESM). TOI-544b is within the top 10 planets for ESM value. The data is downloaded from the NASA Exoplanet Archive.

small planets with precisely characterised masses.

Chapter 4

Homogeneous planet masses I: Reanalysis of archival HARPS radial velocities

4.1 Abstract

Empirical exoplanet mass—radius relations have been used to study the demographics and compositions of small exoplanets for many years. However, the heterogeneous nature of these measurements hinders robust statistical analysis of this population, particularly with regard to the masses of planets. For this reason, we perform a homogeneous and consistent re-analysis of the radial velocity (RV) observations of 87 small exoplanets using publicly available HARPS RV data and the fitting toolkit Pyaneti. For the entire sample, we ran 12 different models to investigate the impact of modelling choices, including the use of multidimensional Gaussian processes (GPs) to mitigate stellar activity. We find that the way orbital eccentricity is modelled can significantly impact the RV amplitude found in some cases. We also find that the addition of a GP to mitigate stellar activity impacts the RV amplitude found; though the results are more robust if the GP is modelled on activity indicators in addition to the RVs. The RV amplitude found for every planet in our sample using all the models is made available for other groups to perform demographics studies. Finally, we provide a list of recommendations for the RV community moving forward.

4.2 Introduction

While many exoplanets have now been confirmed, significantly fewer have a mass measurement. This means that efforts to characterise the planets and their planetary systems in more detail is hindered. Planet mass measurements are important for several reasons: combined with measurements of radius they provide a bulk density estimate that can be used to constrain compositions (Rice, 2014; Goffo et al., 2023); the predominant method for finding masses also provides information on system architectures and multiplicity; and a precise mass measurement is essential for atmospheric characterisation (Batalha et al., 2019; Di Maio et al., 2023). Despite this importance, only $18\%^1$ of known small (R < 4 R_\oplus) exoplanets have a mass measurement, and even fewer have precise (uncertainty < 20%) mass measurements. To fully understand the exoplanet systems we have detected so far, it is essential that we have precise mass measurements.

Many current and future exoplanet-focused missions aim to characterise the atmospheres of small planets. Around 30% of the observing time requested for JWST in Cycle 3 was for the topic of exoplanets and discs, and a new Directors Discretionary Time proposal is focused specifically on finding the atmospheric components of small planets orbiting M type stars. Further ahead, the PLAnetary Transits and Oscillations of stars mission (PLATO, Rauer et al., 2014) is due to launch in 2026 with the aim of characterising the bulk properties (mass, radius, and composition) of small planets orbiting bright stars. The Ariel mission will also launch towards the end of the decade, and will focus on characterising the atmospheres of around 1000 exoplanets (Tinetti et al., 2018). For all these missions, it is essential to not only have precise mass measurements, but also to understand the impact of homogeneous (or inhomogeneous) modelling on the planet masses found.

The vast majority of the existing mass measurements come from radial velocity (RV) measurements.

Whilst these continuing efforts of the EPRV community have enabled many more small exoplanets to gain precise mass measurements, there is a cost: each

¹According to the NASA Exoplanet Archive Composite Planet Parameters Table Accessed 31-07-2024

exoplanet mass is typically found using one of a variety of methods. Specifically, choices of whether or not a planetary orbit is fixed as circular or is allowed to vary in eccentricity; whether or not a long-term trend parameter is included; and how stellar activity in mitigated, namely through the used of GPs or other methods. There are also potential impacts from differing data sets with different observational sampling and cadence, and possible instrumental systematic uncertainties; see Montet (2018) for discussions on RV survey biases. This inconsistency means that it is challenging to perform robust statistical analysis using exoplanet masses. By changing a few choices in the modelling of data for a single system, the extracted mass can vary significantly.

To be able to complete statistical studies and truly understand the demographics of these systems, we need a homogeneous analysis of exoplanet masses. Some recent surveys have chosen to tackle this issue as new data comes in by performing a homogeneous RV analysis (see e.g. Polanski et al. 2024) or by designing their survey in a more unbiased way, as presented by Teske et al. (2021). Dai et al. (2019) performed a homogeneous analysis of the masses (and compositions) of 11 hot-Earth planets using archival data, but since then many more small planets have been observed with RVs meaning this very small sample could be expanded.

In this chapter we present a homogeneous analysis of the RV observations of a sample of small exoplanets. This is the first time such a large-scale homogeneous analysis of RV observations has been completed. We choose to focus on small planets for multiple reasons: they are most likely to be impacted by model choices and activity mitigation techniques; and they are a primary focus for upcoming missions such as Ariel, the Extremely Large Telescope (ELT), and the future Habitable Worlds Observatory (HWO). Additionally, the internal composition of small planets is not well understood.

We focus specifically on HARPS data for several reasons: we want to have a consistent choice of instrument rather than using data from multiple sources; HARPS is one of the top performing high-resolution spectrographs, and was designed for precision RV observations; also, it has been collecting RVs for over 20 years, yielding

a considerable archive of publicly available data ². In an ideal world, there would be one set 'best method' for modelling exoplanet RVs; however, much work is still ongoing on this topic and the community as a whole has yet to reach a consensus. Instead, we present here a variety of modelling choices commonly used by the community as a comparison. We also provide recommendations for best practices for teams modelling their own RV data. Finally, we make available our entire workflow for this project, meaning that other teams can apply the procedures to their own data sets, or complete their own homogeneous analysis of the same data but using their method of choice. The final set of planet masses and a new, homogeneously derived mass—radius diagram for small planets is presented in Chapter 5.

4.3 Sample selection

To reach our aim of producing a homogeneously derived sample of small planet masses, we start by using the NASA Exoplanet Archive³. We query the archive for all confirmed planets with a radius of less than $4R_{\oplus}$ and a declination (Dec.) of below +20 degrees, taking the default parameters. We note that individual systems within the Archive often have multiple published solutions; we choose to take the default values at this stage for simplicity. We cut on Dec., even though this will be done implicitly when we cross-reference with the HARPS archive; however, this approach significantly reduces the number of systems we have to cross-check. This leaves us with 1770 planets.

The next stage is to check which of these possible targets has RV data available in the HARPS public archive. There are some challenges related to the fact that this large archive spans several principle investigators and many observing seasons, including instrument upgrades. In particular, inconsistent naming of targets makes it difficult to accurately assess how many observations each star has. To overcome this, we used the catalogue of HARPS observations in Barbieri (2023) who were able to construct a table of HARPS RVs for the entire 20 years; these authors checked the coordinates of individual systems in order to properly match up any variation in

²https://archive.eso.org/scienceportal/home

³https://exoplanetarchive.ipac.caltech.edu/ Accessed 24-01-2024

naming.

The final sample was made by cross-referencing our targets from the NASA Archive with those of the HARPS archive. We removed any individual observations that had a signal-to-noise ratio (S/N) of less than 25, and also set a minimum threshold of at least 50 HARPS observations to ensure we have sufficient data epochs to perform GP regression. For some targets, there is a large amount of data available, but these are from observations of transits, which were typically obtained for studies of planet obliquity (e.g. Knudstrup et al., 2024). In these cases, many observations are taken over the course of one night and so the total number of observations appears much higher; however, the phase coverage of these observations is not as good. Additionally, the Rossiter-McLaughlin effect would have to be modelled for these data (Rossiter, 1924; McLaughlin, 1924), which would unnecessarily increase the complexity of our models. Therefore, we removed such data before modelling (see B.1.1 for details). In the case of TIC 301289516, the removal of the in-transit data means we are left with only 35 RV observations, which is below our minimum threshold for modelling. Therefore, we removed this target from the sample. From this, we have our final list of 87 small planets orbiting 44 stars. The total number of planets orbiting the 44 target stars is 113; however, the extra 26 are not in the small planet range (or do not have a published radius). We account for these planets in our modelling but not in our model comparison analysis.

Figure 4.1 shows histograms of the targets in our sample. Panel (a) shows the distribution in effective temperature of the 44 stars, and panel (b) the stellar mass. These plots show that the sample covers a fairly wide range of stellar types, with peaks around M-dwarfs and K-dwarfs. These are often specifically targeted in RV surveys as the amplitude of the Doppler reflex motion of planets around less massive stars is larger than for the same planet around a more massive star. The stars in the sample are all brighter than V magnitude 15, and have a median brightness of V magnitude 11. The stars are uniformly distributed across the southern sky with Dec. ranging from +10 to -80 degrees. Panel (c) shows the distribution of the orbital periods of the planets in our sample, and panel (d) shows the planet radii. The

majority of planets have short (< 20 days) orbits, which is expected as these planets are by far the easiest to detect in transits. The distribution of planet radii peaks at around 2.0 - 2.5 R_{\oplus} and drops off towards larger radii, as seen in demographic studies of small planets. The lack of planets at very short radii (< 1 R_{\oplus}) is likely due to observation biases. Interestingly, the radius valley is seen in our sample between 1.5 and 2.0 R_{\oplus} , even with a relatively small sample. Our sample of planets is therefore a reasonable representation of the wider distribution of small exoplanets found in demographics studies; see Zhu and Dong (2021) for a review of exoplanet statistics. We also show the number of planets per target star in our sample, in panel (e). The majority of planets in our sample are in multi-planet systems, most commonly in a two-planet system.

Finally, in panel (f), we show the number of observations per star available within the HARPS data. The majority of our targets have below 200 observations; however, 9 targets have more than this, with one target having over 650 epochs of RV observations.

4.4 HARPS observations

For our analysis, we used RV measurements and activity indicators from the HARPS spectrograph, which are based on publicly available reduced data from the ESO archive, as described in Barbieri (2023). HARPS is a stabilised high-resolution spectrograph with a resolving power of 110000, and is capable of sub-m s⁻¹ RV precision for bright, slowly rotating stars. The instrument is mounted on the ESO 3.6 m telescope at the La Silla Observatory in Chile. The observations used in this study all use the high-accuracy mode with a 1 arcsec science fibre on the science target. The second fibre can be used for simultaneous wavelength calibrations. The stars in this sample span a wide range of magnitudes and thus exposure times from a few minutes up to an hour.

The data available through the ESO archive have been processed using the online HARPS pipeline (Pepe et al., 2002), which includes the extraction of 2D spectra that are flux corrected to match the slope of the spectra across echelle orders.

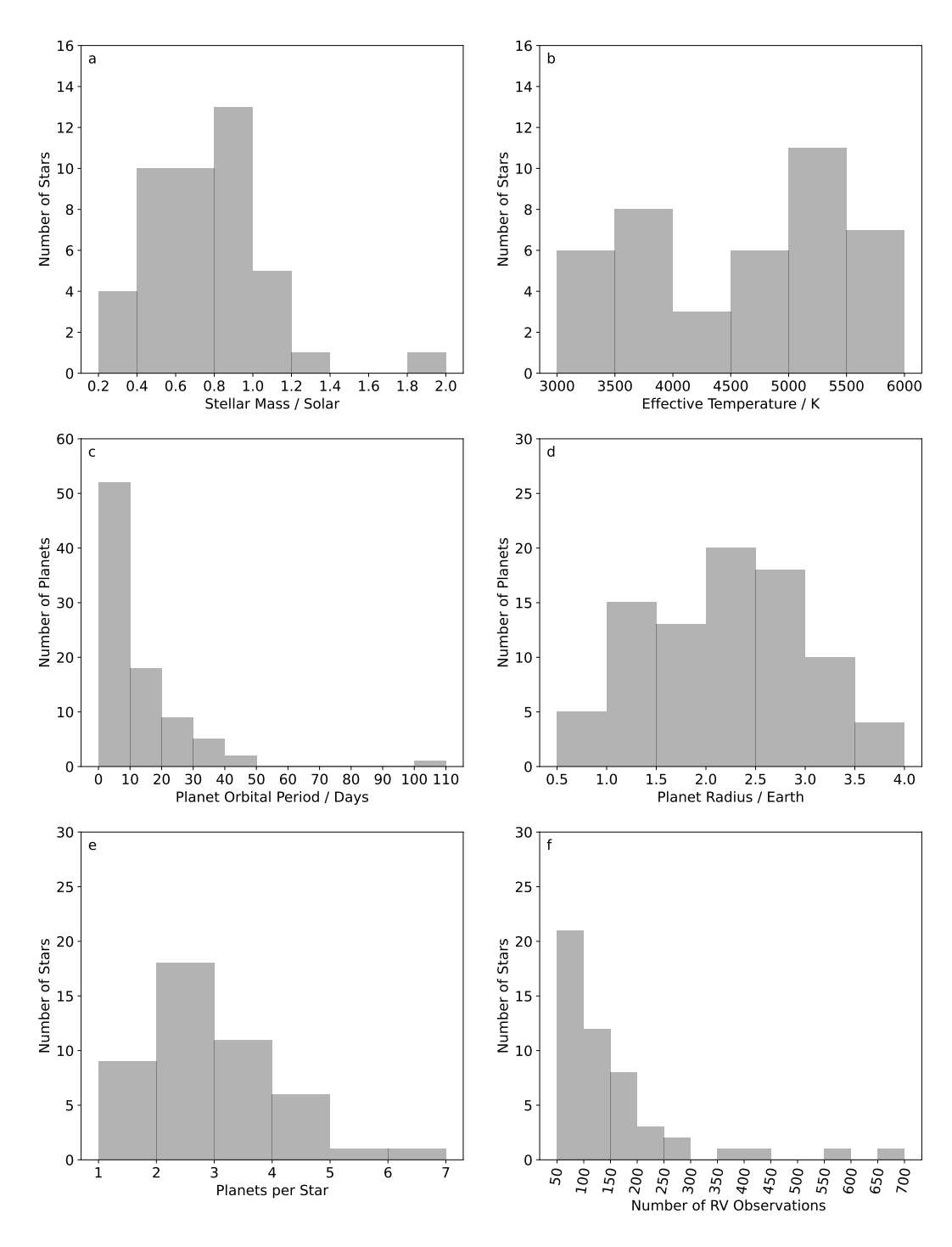


Figure 4.1: Histograms showing the properties of the stars and planets in our sample: (a) Stellar mass. (b) Stellar effective temperature. (c) Planet orbital period. (d) Planet radius. (e) Multiplicity (number of planets per star). (f) Number of RV observations per system.

RV information is extracted from the spectra by cross correlating with a binary mask that matches the stellar type of the star (Baranne et al., 1996). The S/N cut at 25 enforced when cross referencing with the list of small, known planets from the NASA Exoplanet Archive means that most RVs have precisions of $1-5 \,\mathrm{m\,s^{-1}}$. The median RV uncertainty of this entire dataset is $1.7 \,\mathrm{m\,s^{-1}}$, but this increases up to $12.2 \,\mathrm{m\,s^{-1}}$ for some systems. We note that a few individual data points appear to have very large uncertainties; it is possible that their S/N is incorrectly labelled in the database and so they are not removed by the cut on S/N as they should be; however these do not significantly affect our results. In the later analysis, we use activity indicators based on the cross-correlation function (CCF). These are the bisector inverse slope (BIS) and full width at half-maximum (FWHM). We use these activity indicators as we find these are more robust for the largest sample of spectra than chromospheric activity indicators, such as Ca II H&K, and H α , which may be more sensitive to low data fidelity.

The only additional step to the data collection was to also do a sigma-clip on the RV data. We used the astropy sigma-clip tool to cut out any RVs more than 3 sigma away from the median, with a maximum of two iterations of this. This finds the median and standard deviation of the data and then removes points that are more than three standard deviations above or below that median value. This is done for two iterations. We visually inspected each system to see how many data points have been removed. For most targets, the sigma-clipping does not remove any data because the standard deviation is large anyway. For a few targets with many (> 500) observations, it does remove more observations, but still leaves most for the modelling. For one single target, we have only 49 RV observations left after sigma-clipping, this is below our original threshold of 50 epochs, but we chose to include it in the sample anyway.

For a few targets, we also needed to remove specific data points that were clear outliers; see B.1.1 for details of this. After the sigma-clipping and removal of data for specific targets, we are left with 6428 individual RV observations. The baseline of observations ranges from approximately 60 to 6700 days, with a median baseline

of around 600 days.

It is becoming increasingly common in RV analyses to use multidimensional GPs to help mitigate the effects of stellar activity, see 2.4.3. There are a range of different activity indicators that can be used. In our analysis, we chose to include some of the most commonly used ones: the FWHM and the BIS.

While we have chosen to use HARPS data to ensure the consistency in the RV instrument used, given the long time HARPS has been observing, there are some offsets in the data. In particular, the HARPS fibre was upgraded in 2015, causing a possible RV offset. It is recommended to account for this shift by modelling the HARPS pre-upgrade data as if they were from a different instrument from that providing the HARPS post-upgrade data. For this reason, we label all RV data as either 'HARPS_pre' or 'HARPS_post'. Within the modelling, we set these as two separate instruments – meaning we account for an offset between them. In most cases, the data are all after the upgrade, but in a few cases, the data are from before the upgrade or are a mixture of pre- and post-fibre-upgrade data.

4.5 Automating the process

One of the biggest challenges of this project was in the initial setup of the RV modelling. We wanted to move away from an 'artisanal' approach of looking at one system at a time, to automating a process to model many systems at once. This is for two reasons: we want our method to be generally applicable to any system; and we did not want to introduce any biases by manually setting the priors and input parameters.

To overcome this, we first query the NASA archive to find the required parameters for each individual target: the stellar mass, radius, and temperature, and the planet period, transit midpoint, radius, and mass. We use the composite parameters table from the archive for these values. The planet orbital period and transit midpoint (for non-transiting planets, this parameter has the same name but refers to the time of conjunction) are used as priors in our RV modelling. The other parameters are used for comparison in our results and discussion, but are not used directly in the

modelling. We separate the HARPS archive data into individual files for each star, applying our sigma-clipping and removal of specific data where necessary. For each model, we create an input file for the fitting toolkit that can be used for all targets; that is, we have one input file per model, as opposed to having one per target. This significantly reduces the time needed to set up each model run.

4.6 Radial velocity modelling choices

Distinguishing between planetary and stellar signals in RV data remains a challenge in exoplanet detection. The task is particularly difficult when dealing with active stars, where stellar activity can produce RV signals that mimic or obscure those of orbiting planets. Gaussian processes have emerged as one of the most powerful tools for addressing this issue. GPs offer a highly flexible and semi-parametric approach to modelling complex stochastic variations, such as those induced by quasi-periodic stellar activity using tailored quasi-periodic kernels (see Barragán et al., 2022).

The benefits of using GPs extend beyond their flexibility. They can incorporate prior knowledge about the system, such as the expected periodicity of stellar activity, and can be combined with other models to account for additional physical processes. This adaptability makes GPs particularly well-suited for analysing spectroscopic time series of active stars, where traditional methods often struggle. Indeed, numerous studies have demonstrated the effectiveness of GPs and their variants —such as multidimensional GPs— in identifying RV signals of planets in the presence of significant stellar activity (see Rajpaul et al., 2015; Barragán et al., 2022). The multidimensional variant of GPs has demonstrated its effectiveness in enhancing the precision of planetary detection, particularly in scenarios where activity indicators provide significant information about the underlying stellar signals (see Barragán et al., 2019). This approach leverages the underlying relation between RV data and activity indicators, allowing for a more accurate separation of planetary and stellar signals. However, the advantages of this multidimensional GP framework diminish under certain conditions. Specifically, when the data suffer from suboptimal sampling or are dominated by large amounts of white noise, the activity indicators

may fail to capture information about the stellar signals. In such cases, the use of a multidimensional GP does not offer any significant improvement over traditional methods, as the lack of reliable activity information limits the framework's ability to accurately model the stellar signal (see Barragán et al., 2022).

A commonly employed kernel that allows stochastic periodic behaviour to be modelled is the quasi-periodic (QP) kernel (as introduced by Roberts et al., 2013), defined as

$$\gamma_{\text{QP}}(t_i, t_j) = A^2 \exp\left\{-\frac{\sin^2\left[\pi \left(t_i - t_j\right) / P_{\text{GP}}\right]}{2\lambda_{\text{p}}^2} - \frac{\left(t_i - t_j\right)^2}{2\lambda_{\text{e}}^2}\right\},\tag{4.1}$$

where A, the amplitude, is a parameter that works as a scale factor that determines the typical deviation from the mean function, P_{GP} represents the characteristic periodicity of the GP, λ_p denotes the inverse of the harmonic complexity (indicating the complexity within each period), and λ_e represents the timescale of long-term evolution.

Once we have our data files for each system, we then have to choose how we model the RVs to find the planet masses. We chose to use the package Pyaneti (Barragán et al., 2019, 2022) for all of our modelling, as it offers a variety of options for the fitting and is partly written in fortran90, meaning it runs much faster than an entirely Python-based code. Pyaneti is also a fairly common choice of package within the RV modelling community and makes use of multidimensional GPs (Rajpaul et al., 2015; Jones et al., 2017) to mitigate stellar activity. For a full description of how pyaneti implements the QP kernel described in (4.1) within the multi-GP framework, see Barragán et al. (2022). Other RV fitting toolkits that make use of multidimensional GPs include PyORBIT (Malavolta et al., 2016, 2018) and S+LEAF (Delisle et al., 2022). In addition to our goal of providing a homogeneously derived sample of small planet masses, we also wanted to investigate how the choices in modelling affect the derived planet mass. For this reason, we chose to run 12 different models on the data. We wanted to compare the impact of using a GP versus no GP; the dimension of GP used; adding a long-term trend parameter; and modelling orbits as circular or eccentric. See Table 4.1, which outlines all the models we used.

For all runs, we performed Markov chain Monte Carlo (MCMC) samplings using the sampler included in pyaneti, which is based on an ensemble sampler (Foreman-Mackey et al., 2013). We sample the parameter space with 200 Markov chains. Each chain is initiated randomly with values within the prior ranges. We create posterior distributions with the last 1000 iterations of converged chains with a thin factor of 10. This generates distributions with 200000 independent points per each sampled parameter.

 Table 4.1: Overview of the 12 models applied to RVs and activity indicators in this study.

Model	GP dimension	Orbital eccentricity	Long-term trend	Activity indicator	GP kernel
а	0	circular	no trend	none	none
þ	0	circular	linear trend	none	none
၁	0	circular	quadratic trend	none	none
p	0	eccentric	no trend	none	none
e	0	beta distribution	no trend	none	none
J	1	circular	no trend	none	f 1 circular no trend none Quasi-Periodic
ad	1	eccentric	no trend	none	Quasi-Periodic
h	2	circular	no trend	FWHM	Quasi-Periodic
.—	2	eccentric	no trend	FWHM	Quasi-Periodic
¥	3	circular	no trend	FWHM+BIS	Quasi-Periodic
ш	3	eccentric	no trend	FWHM+BIS	Quasi-Periodic
u	3	beta distribution	no trend	FWHM+BIS	Ouasi-Periodic

Each row represents a single model, with the columns indicating the choices made for that model. Note: we do not label models as i or I to avoid confusion with the

number 1.

As well as the specific model choices, we also wanted to be consistent in our application of priors for the modelling parameters. We chose to set a Gaussian prior on both the orbital period, P, and time of conjunction, T_c , listed in the NASA archive using the 1σ errors. Typically, these values have been found through transit fitting of the planets. For several systems, there are no listed values of this in the archive, and for these we manually checked the original publications and added in the values ourselves; details of this procedure are provided in Appendix B.1.2. For all other planetary orbit parameters, we chose to use wide uniform (uninformative) priors. For the eccentricity of the planetary orbit, we set either an eccentricity fixed at zero (for our circular model cases) or parameterised the eccentricity and argument of periastron to

$$e\omega_1 = \sqrt{e\sin\omega_*}$$
 and $e\omega_2 = \sqrt{e\cos\omega_*}$. (4.2)

This has the benefit of not truncating at zero, which is often a problem in modelling eccentricities (Lucy and Sweeney, 1971). However, after running models including eccentricity, we noticed that, in some cases, a very high eccentricity is found, which seems unlikely for so many systems. This is likely due to the model fitting high-eccentricity orbits to spurious outliers in the data (Hara et al., 2019). For this reason, we also chose to run two additional models (models e and n, as described in Table 4.1), which put a prior on the eccentricity as a beta distribution. We used the form of Van Eylen et al. (2019) for single-planet systems, as this is the more general case.

For the GP hyperparameters, we again used wide uniform priors. Except in the case of the GP period, P_{GP} , where we set this based on the stellar type. It has been shown that the GP period links strongly to the stellar rotation period (Nicholson and Aigrain, 2022). For each star in our sample, we used the published stellar effective temperature and converted this to a B-V magnitude; using the relation from Mamajek and Hillenbrand (2008), we then estimated the maximum stellar rotation period for a given stellar age. Taking the upper limit of 9 Gyr, we assigned maximum rotation periods of 60, 50, 40, and 20 days for stars with temperatures of < 4000K, 4000 - 5000K, 5000 - 6000K, and > 6000K, respectively. We also then set the maximum timescale of evolution of active regions, λ_e , to be twice this rotation

Table 4.2: Priors used for all parameters in all models.

Parameter	Prior	Notes
Orbital Parameters		
Mid-transit time, T_0 ,	$\mathcal{N}[a,b]$	Where a is the mid-transit time
days		from the archive, and <i>b</i> is the uncertainty on that time.
Period, P, days	$\mathcal{N}[c,d]$	Where c is the period from the archive, and d is the uncertainty on that period.
eccentricity, e	$\mathcal{F}[0]$	For the circular model.
argument of periastron,	$\mathcal{F}[0]$	For the circular model.
omega		
ew1	$\mathcal{U}[-1,1]$	For the eccentric model.
ew2	$\mathcal{U}[-1,1]$	For the eccentric model.
RV amplitude, k, km/s	$\mathcal{U}[0,0.5]$	
GP Hyperparameters		
A0, km s ⁻¹	U[0,0.5]	
B0, $km s^{-1} d^{-1}$	U[0, 0.5]	
$A1, km s^{-1}$	$\mathcal{U}[-0.5, 0.5]$	
B1, $km s^{-1} d^{-1}$	$\mathcal{U}[-0.5, 0.5]$	
A2, km s ⁻¹	$\mathcal{U}[-0.5, 0.5]$	
B2, $km s^{-1} d^{-1}$	$\mathcal{U}[-0.5, 0.5]$	
Timescale of active re-	U[1,160]	The upper limit is set to twice the
gions, $\lambda_{\rm e}$, days		period of the GP
Inverse of Harmonic	$\mathcal{U}[0.01,2]$	
Complexity, λ_p		
Period of GP, P_{GP} , days	$\mathcal{U}[0,80]$	This is set based on the stellar effective temperature

period. We note that future work may benefit from using more physically motivated GP hyperparameter priors based on stellar type and age.

The choice of priors for the multi-GP amplitudes was informed by the results of previous analyses that reflect the underlying correlations between the RVs and the CCF-derived activity indicators. (e.g. Barragán et al., 2019, 2022, 2023). Specifically, previous studies observed that when the RV amplitudes (A_0 and B_0) are positive, the corresponding amplitudes for the FWHM are also positive, while those for the BIS are negative. For this reason, we set A_0 and B_0 to be positive, and left the amplitudes for the other hyper-parameters to vary more freely.

4.7 Results and discussion

We remodelled 6428 HARPS RV measurements for 44 stars harbouring 87 small, transiting planets. In this section, we summarise our findings and analyse the impact of model choice when fitting RV signals. For three of our targets, TOI-269, TOI-4399, and HD 3167, our models cannot provide a good fit to the available data. TOI-269 is an active M dwarf star where a custom RV extraction was used in the discovery paper alongside additional photometric data to provide a good fit (Cointepas et al., 2021). TOI-4399 is a very young star with strong activity signals and no published mass measurement (only an upper limit, Zhou et al., 2022). Our modelling suggests that additional data are required for this system in order to fully characterise the planetary mass. HD 3167 has only 50 RV observations but is a four-planet system, which leaves only a low degree of freedom when fitting more than 20 parameters, depending on the model choice. When modelling this system with a GP, this issue is amplified and the degrees of freedom are too few to fit the data well. For the following sections, we remove these three target stars from our analysis, resulting in a total of 83 small planets orbiting 41 stars. For completeness, the final results tables include the fits for these three planets.

The extracted RV amplitude, eccentricity, Bayesian information criterion (BIC), and the Akaike Information Criterion (AIC) for all models for each planet are shown online in Table B.1. Chapter 5 provides a homogeneous set of planet masses using a consistent stellar characterisation method. Here we summarise the main findings by comparing the impact of different modelling choices.

4.7.1 Impact of long-term trends

We compare the extracted K amplitude (RV amplitude) for each target with the different models. Panel (a) of Figure 4.2 shows the extracted K amplitude for the three models (a, b, and c), which have no GP added to mitigate stellar activity. The difference between the models is that model (b) has a long-term linear trend added, model (c) has a long-term quadratic trend added, and model (a) has no long-term trend. The purpose of adding a long-term trend in RV modelling is typically to account for potential changes in the instrument or telescope over long baselines,

or to account for the impact of a longer-period unknown planet (or star) in the system (e.g. Espinoza et al., 2019; Korth et al., 2023). In some cases, a significant measurement of a long-term trend in RV data has been used to claim the discovery of a planet candidate (Lubin et al., 2022). We wanted to test whether adding a model of a long-term trend to all systems —regardless of whether we think there is a potential for an additional planet— makes a difference to the extracted RV amplitude. Panel (a) of Figure 4.2 shows that the addition of any long-term trend makes only a very small difference to the K amplitude found for most targets. This is likely because no trends are evident in the data for these targets. However, in a few cases, a more noticeable difference is seen, and although the error bars typically overlap, the median amplitude found can vary by 1 m s⁻¹ or more. The difference between a linear and quadratic long-term trend is very minor, and the 1σ error bars overlap almost completely for all planets.

In panel (b) of Figure 4.2, we show a histogram of the root mean squared (RMS) of the residuals for the three models (a, b, and c). The highest RMS of residuals is for model (a), with no long-term trend added. The overall distribution is very similar for all three models.

Panel (c) of Figure 4.2 shows a histogram of the difference in RV amplitude of our models compared to the most simple model; that is, the RV amplitude for model (c) minus the RV amplitude for the same planet for model (a). In both the linear and quadratic trend cases, the distribution centres around 0 m s^{-1} , and almost all targets have a difference within $\pm 1 \text{ m s}^{-1}$.

The amplitude of the trend itself for both the linear and quadratic cases is shown in panel (d) of Figure 4.2. We note that the quadratic trend case has been multiplied by 1000 to allow it to be visible on the same axes. For the linear case first (model b), the amplitude of the trend is below $0.20~{\rm m\,s^{-1}\,days^{-1}}$ in all cases, with most targets exhibiting a value of lower than $0.05~{\rm m\,s^{-1}\,days^{-1}}$. For the quadratic trend case, all targets have trend amplitudes of below $0.35\times10^{-3}~{\rm m\,s^{-1}\,days^{-2}}$, with almost all targets showing values of less than half this amount. Based on these results, the indiscriminate addition of a long-term trend to the model does not make a significant

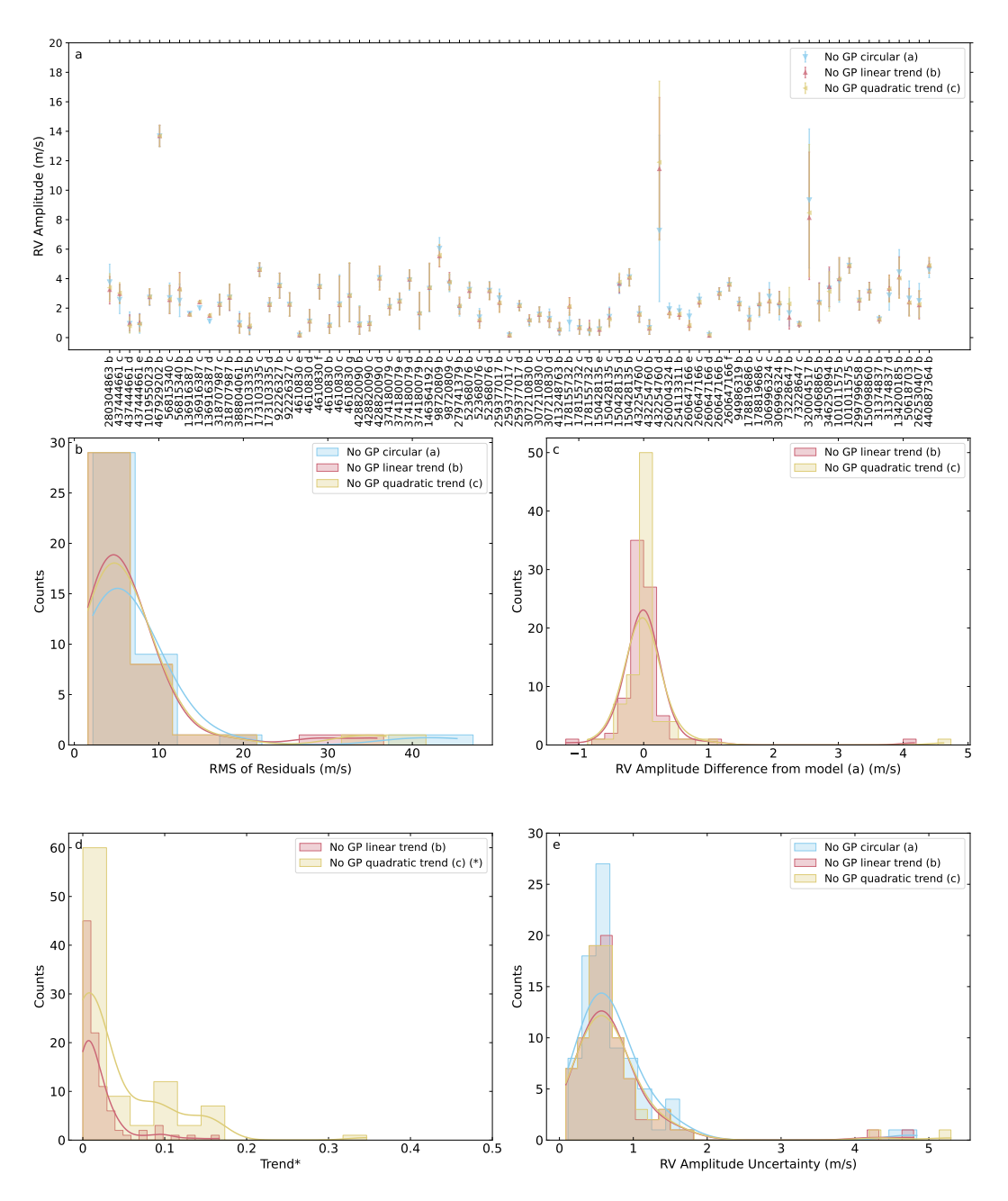


Figure 4.2: Impact of long-term trends. Panel (a): Comparison of the RV amplitude found for each target for three different models, (a), (b), and (c). Error bars show the 1σ uncertainty from the MCMC posteriors. Target names are given as TIC IDs with the letter of the planet. Panel (b): Histogram showing the root-mean-squared error of the residuals to the fit. Panel (c): Histogram showing the RV amplitude found compared to model (a). Panel (d): Histogram showing the amplitude of the trend found (for the linear trend in m s⁻¹ days⁻¹, for the quadratic trend in m s⁻¹ days⁻²). The asterisk marks cases where the value for the quadratic trend amplitude has been multiplied by 1000 to plot on the same axes. Panel (e): Histogram showing the 1σ uncertainty in the RV amplitude found for the different models.

difference on the planet mass found because the amplitude of the trend is very small.

Finally, in panel (e) of Figure 4.2, we show the distribution of RV amplitude uncertainties for the three models (a, b, and c). The peak of the distribution in all cases is around $0.6 \,\mathrm{m\,s^{-1}}$, with the highest uncertainties being of around $5 \,\mathrm{m\,s^{-1}}$. The difference between the three models is not significant, and it is likely that the systems in our sample do not have an external high-mass companion, or that the RV observations we have are not sensitive to the long-term trend.

4.7.2 Impact of eccentricity

When investigating how modelling orbits as circular or eccentric impacts the planet masses found, we take the no-GP model and either set a uniform eccentricity prior, model d, or we set the prior on eccentricity in the form of a beta distribution, model e. Both of these cases are described in Sect. 4.6. Figure 4.3 shows the results of these models compared to the circular case (model a).

In panel (a) of Figure 4.3, we show how the RV amplitude changes for the three models for each planet in our sample. For some very small planets, the eccentric case gives an RV amplitude that is significantly different from the circular or beta distribution case; for example for TIC 437444661 d, and TIC 4610830 f. Even for planets where the 1σ error bars overlap, the difference in the median value of RV amplitude varies by as much as a factor of 3; for example, for TIC 428829990 d, it ranges from approximately $2 \,\mathrm{m\,s^{-1}}$ to $7 \,\mathrm{m\,s^{-1}}$. For all planets, the circular and beta-distribution models, that is, (a) and (e), give the most similar results, with (d), the eccentric case, giving the most different ones. Panel (b) in Figure 4.3 shows the RMS of the residuals for the three models. The distributions for all three models are very similar, with no significant differences between them.

When comparing the RV amplitude found for models (d) and (e) to that found for model (a), as shown in panel (c) of Figure 4.3, we find that a uniform prior on the eccentricity (model d) gives, on average, higher values of RV amplitude, and therefore higher planet masses. For this eccentric case, the RV amplitude difference is found to be slightly offset from 0 m s^{-1} and has a much wider range, up to around $\pm 6 \text{ m s}^{-1}$. For the beta distribution case, model (e), the amplitude difference centres

around $0 \,\mathrm{m\,s^{-1}}$ and has a much smaller range of values, with almost all planets showing a less than $1 \,\mathrm{m\,s^{-1}}$ difference in RV amplitude compared to the circular case. The model with a beta distribution on eccentricity gives much more similar RV amplitudes to the circular case, whereas the uniform prior on eccentricity gives higher RV amplitudes on average. This highlights the importance of choosing the prior on eccentricity with care.

We also performed this analysis for the 3D GP models, which have different eccentricities: the circular case (model k), the case with a uniform prior on eccentricity (model m), and the case with a beta distribution on eccentricity (model n). We find very similar results: the beta distribution gives the most similar results to the circular case. The model with a uniform prior on eccentricity tends to find higher RV amplitudes on average.

The distributions of eccentricity values found for the models with a uniform prior on e (model d) and a beta distribution (model e) are shown in panel (d) of Figure 4.3. For model (d), the distribution is almost flat, with eccentricity values ranging all the way up to 0.9. For the beta distribution case, model (e), the eccentricities found centre close to zero, with the highest value being 0.2, fairly closely following the prior distribution set. Given the very high values of eccentricity found in the case for model (d), we wanted to check that the wide priors set on the RV amplitude were not contributing to this. We ran model (d) again for all targets but restricted the RV amplitude to be less than $50 \,\mathrm{m \, s^{-1}}$. We found that the eccentricity and RV amplitude did not change by more than 1% in any case, and so the wide priors on RV amplitude are not the reason for the high eccentricities. In some ways, it is surprising to find such high values of eccentricity, especially as we chose to parametrise the eccentricity and argument of periastron as in Equation 4.2, which should help with this issue. It is possible that the model is finding such high eccentricities due to spurious data points (Hara et al., 2019).

Finally, panel (e) of Figure 4.3, shows the RV amplitude uncertainty for each planet found with models (a), (d), and (e). The circular and beta distribution models, (a) and (e), have the most similar RV uncertainties, both with distributions peaking

below $1 \,\mathrm{m\,s^{-1}}$ and only a few higher outliers. For the eccentric case, model (d), the distribution in RV amplitude uncertainty peaks at a higher value and has higher outliers of up to $7 \,\mathrm{m\,s^{-1}}$.

Based on our results, it is clear that using a uniform prior on eccentricity is not a suitable approach for modelling large sets of RV data. Instead, we suggest using an informative prior distribution on the eccentricity, such as a beta distribution. We note that the RV amplitude (and therefore planet mass) found for the whole sample does not change much between simply fixing the orbits as circular and using a beta distribution in eccentricity. However, we believe that the use of a beta distribution is more physically motivated, as we would not expect every planet in our sample to be on a perfectly circular orbit. Alternatively, the simultaneous modelling of photometric data may help accurately constrain the eccentricity, though testing this in more detail is beyond the scope of this chapter.

4.7.3 Impact of GP dimension

We compare the *K* amplitude found with different dimensionalities of GP: no GP, model (a); a 1D GP (fitting just to the RVs), model (f); a 2D GP (fitting to the RVs and an activity indicator, in this case the FWHM), model (h); and a 3D GP (fitting to the RVs and two activity indicators, in this case FWHM and BIS), model (k). In all cases, the models are for a circular orbit.

Figure 4.4 shows the results of these four models with different dimensions of GP. In panel (a) we compare the extracted RV amplitude for all planets in our sample with the different models. There are two things of note: the biggest error bars tend to be from the no GP case, and the biggest differences also tend to be for the no GP case. However, for nearly all the planets in the sample, the dimension of the GP does not significantly change the extracted RV amplitude. Although we note that the median value of RV amplitude for a given planet indeed does vary a little between the models, which would have an impact on statistical studies of the population.

Panel (b) of Figure 4.4 shows the RMS of the residuals for the four models. All the GP models have very similar distributions, with the no GP case having the largest RMS values. Therefore, the inclusion of a GP indeed reduces the RMS of

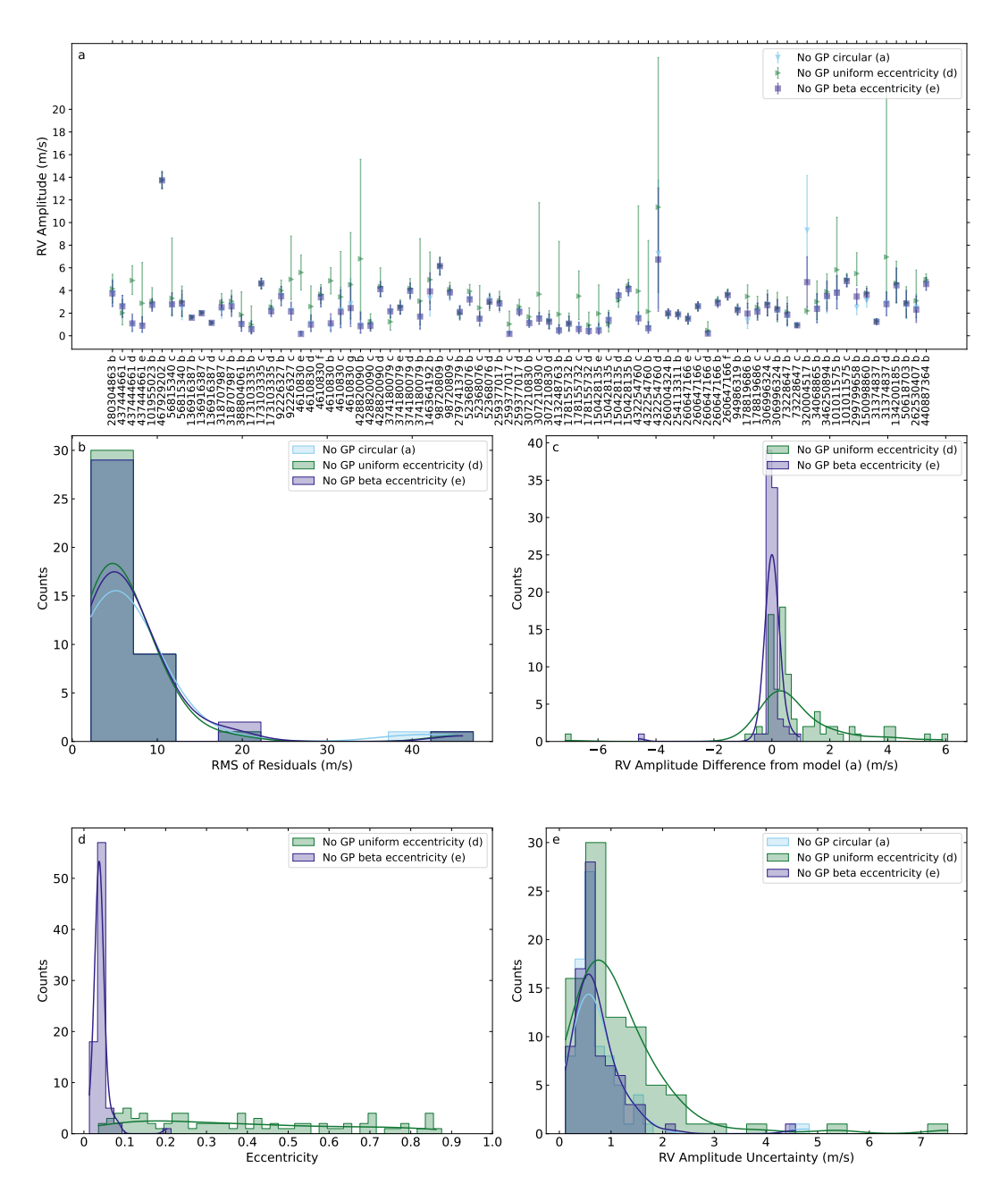


Figure 4.3: Impact of orbital eccentricity. Panel (a): Comparison of the RV amplitude found for each target for three different models, (a), (d), and (e). Error bars show the 1σ uncertainty from the MCMC posteriors. Target names are given as TIC IDs with the letter of the planet. Panel (b): Histogram showing the RMS error of the residuals to the fit. Panel (c): Histogram showing the RV amplitude found compared to model (a). Panel (d): Histogram showing the value of eccentricity found. Panel (e): Histogram showing the 1σ uncertainty in the RV amplitude found for the different models.

the residuals on average.

Panel (c) of Figure 4.4 shows the difference in RV amplitude found for each model compared to the no GP case. Here, there is a slight shift seen for the 1D GP case compared to the 2D and 3D cases. The 1D GP case finds slightly higher RV amplitudes on average, and is most different from the other GP models.

Panel (d) of Figure 4.4 shows the difference in RV amplitude found for the 2D and 3D GP models compared to the 1D GP case. The 2D and 3D GP models overlap very well in terms of RV amplitude. They both show some differences from the 1D GP model (which would be at zero in this plot). The 1D GP model is the most inconsistent of the three models.

Finally, in panel (e) of Figure 4.4, we show the uncertainty in the RV amplitude found for every planet with each model. All models have a peak in uncertainty at below 1 m s^{-1} . The no GP case has a slightly shifted peak uncertainty and also has the highest outliers. The models including a GP show a very similar distribution in RV amplitude uncertainty.

Based on these results, if using a GP, we would recommend using a multidimensional GP that fits to an activity indicator. This is because the 2D and 3D GP results seem the most robust compared to the 1D case; the 1D GP model finds the biggest difference in RV amplitude.

4.7.4 Model comparison

We compared each of our models by computing the BIC and the AIC. Table B.1 gives the value of each of these for each model of every system. However, we note that none of these metrics are perfect indicators of goodness of fit, and additionally, the use of different data sets (in the case of the 2D and 3D GP models) means that you cannot directly compare these metrics. Regardless, we provide this information as an overview. For the models that use only the RV data, the lowest AIC model for 78 planets is the 1D GP circular model (f), followed by the 1D GP model with a uniform prior on eccentricity (g) for 11 planets. The remaining planets all prefer a no GP model. For the 2D GP models, 85 planets prefer the circular model (h) over the uniform prior eccentric model (j). For the 3D GP case, 80 planets prefer

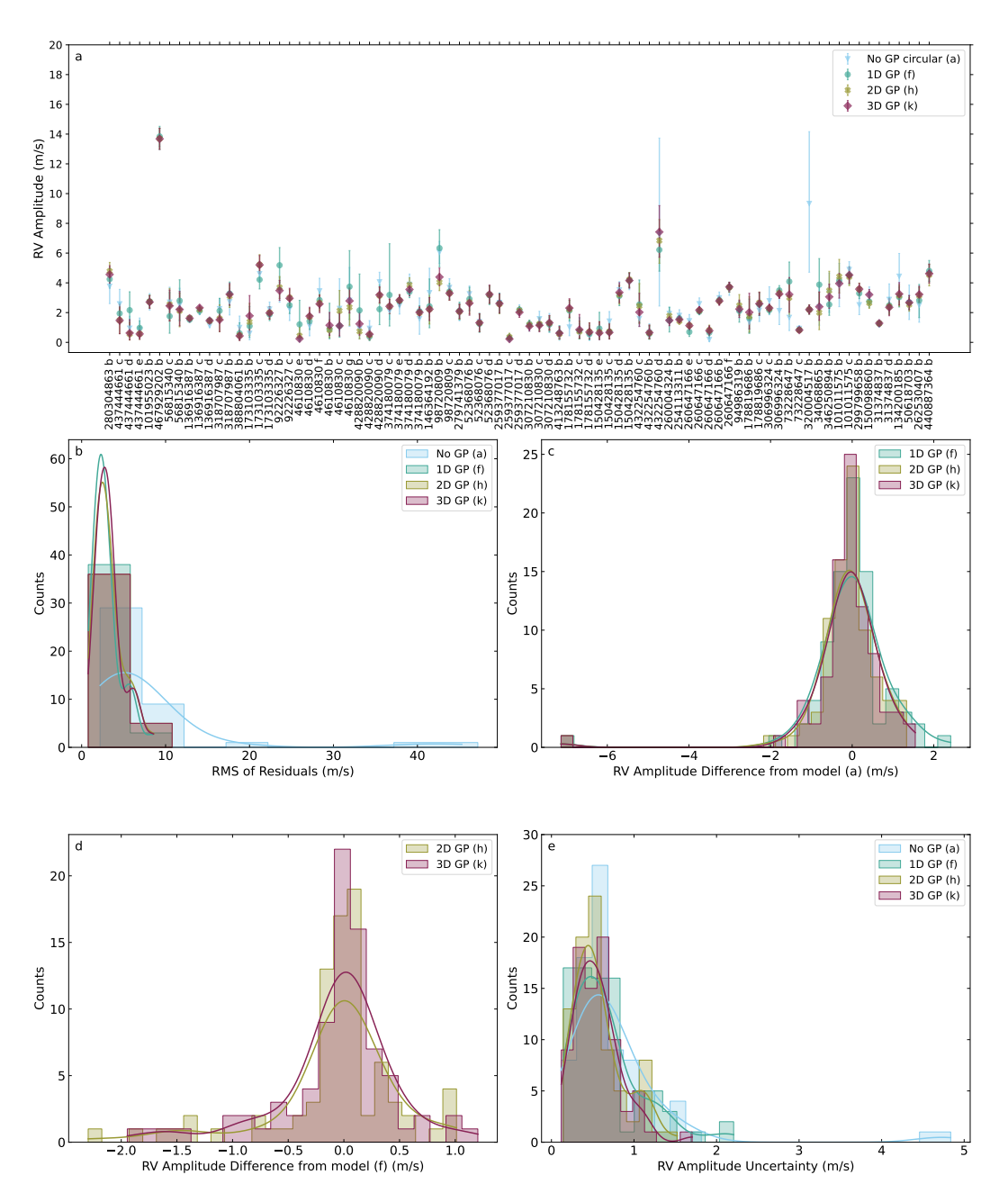


Figure 4.4: Impact of GP dimension. Panel (a): Comparison of the RV amplitude found for each target for four different models, (a), (f), (h), and (k). Error bars show the 1σ uncertainty from the MCMC posteriors. Target names are given as TIC IDs with the letter of the planet. Panel (b): Histogram showing the RMS error of the residuals to the fit. Panel (c): Histogram showing the RV amplitude found compared to model (a). Panel (d): Histogram showing the RV amplitude found for models (h) and (k) compared to model (f). Panel (e): Histogram showing the 1σ uncertainty in the RV amplitude found for the different models.

the circular case (k), 18 the eccentric model with beta distribution (n), and 15 the uniform eccentric model (n). In general, the circular models seem to be preferred by the AIC, possibly because these have fewer parameters and so are not penalised by the goodness-of-fit metrics; though in some cases the non-circular models are still preferred.

To define our 'best' model for the adopted set of planet parameters for each target, we first find the lowest AIC model from the models that use only the RV data (models a to f). If the best model for a given target corresponds to the 1D GP model, we take this as an indication that a GP is required for that specific target. For the targets that require a GP, we assign the 3D GP with beta distribution as the best model. Looking at panel (e) of Figure 4.4, the histogram shows the peak for the 2D model to be at slightly lower RMS then the 3D model. However, we still assign the 3D GP model as the best model as it makes use of the most information, and this difference in peak is very small. Future investigations may wish to compare whether adding more data is always better. For the targets that prefer a no GP model, we assign the no GP beta distribution model as the best model.

We note that the beta distribution models do not always give the 'best' fit in terms of AIC and BIC. However, we choose these as our final models as the treatment of eccentricity is the most realistic: not all planets in our sample will be on circular orbits, and using a uniform prior for eccentricity gives spuriously large eccentricity values. Additionally, the beta distribution is an empiric result based on transit observations of small planets and so has good physical motivation (Van Eylen et al., 2019). We chose the 3D GP case rather than the 1D or 2D case because the 1D GP case appears to be the least consistent with the others (in terms of extracted RV amplitude), and because the 3D GP case makes use of the most information —in the form of the FWHM and BIS indicators. We note that the 3D GP model will always have a lower value of AIC compared to the 2D GP case because it has more data points, but this is not why we chose this model. The fitted planet parameters for the best model chosen for each target are shown in Table B.2.

Panel (a) of Figure 4.5 shows the RV amplitude of the best model for each planet

in our sample compared to the default published value from the NASA Exoplanet Archive (though we note that some planets do not have a published RV amplitude, and that for many of those that do have one, the data are different from those used here). For some planets, there is a significant difference between the two. Even where the 1σ error bars overlap, the difference in the median RV amplitude for a given planet can vary by up to a factor of 2. This would have a big impact on the calculated bulk density of the planet and therefore change the estimated composition.

Finally, in panel (b) we present a histogram of the RV amplitude uncertainties for our best model compared to those of the default published amplitudes. It is clear that these latter amplitudes have a lower uncertainty on average compared to our best model. We discuss why this may be the case in Sect. 4.8 (most likely due to additional data being used in the published works) and note that the aim of this work is not to find the most precise planet masses, but rather to provide a sample where the masses have been found homogeneously. Overall, this comparison shows that a homogeneous approach finds a different distribution in RV amplitudes for some targets (and therefore planet mass) compared to a heterogeneous sample.

Finally, in panel (c) we show a histogram of the RV amplitude differences from our best model compared to the default published values (for targets that have this published value). The distribution here does peak around $0\,\mathrm{m\,s^{-1}}$; however, some targets have difference in amplitude of up to $5\,\mathrm{m\,s^{-1}}$. On the one hand, this is reassuring as it seems that our results are broadly consistent with the literature. On the other hand, there are still differences seen for some targets, which would have an impact on the overall demographics of this sample. This highlights the need for a homogeneous analysis approach if we want to study populations of planets rather than individual systems.

4.7.5 TIC 98720809: A representative example

In this section, we show the full results for one example, TIC 9870809, a two-planet system that has a very consistent RV amplitude found across all models with a GP. For this target, we take the 120 HARPS RV observations (all post-fibre-upgrade) and the priors found from the NASA Exoplanet Archive composite parameters table.

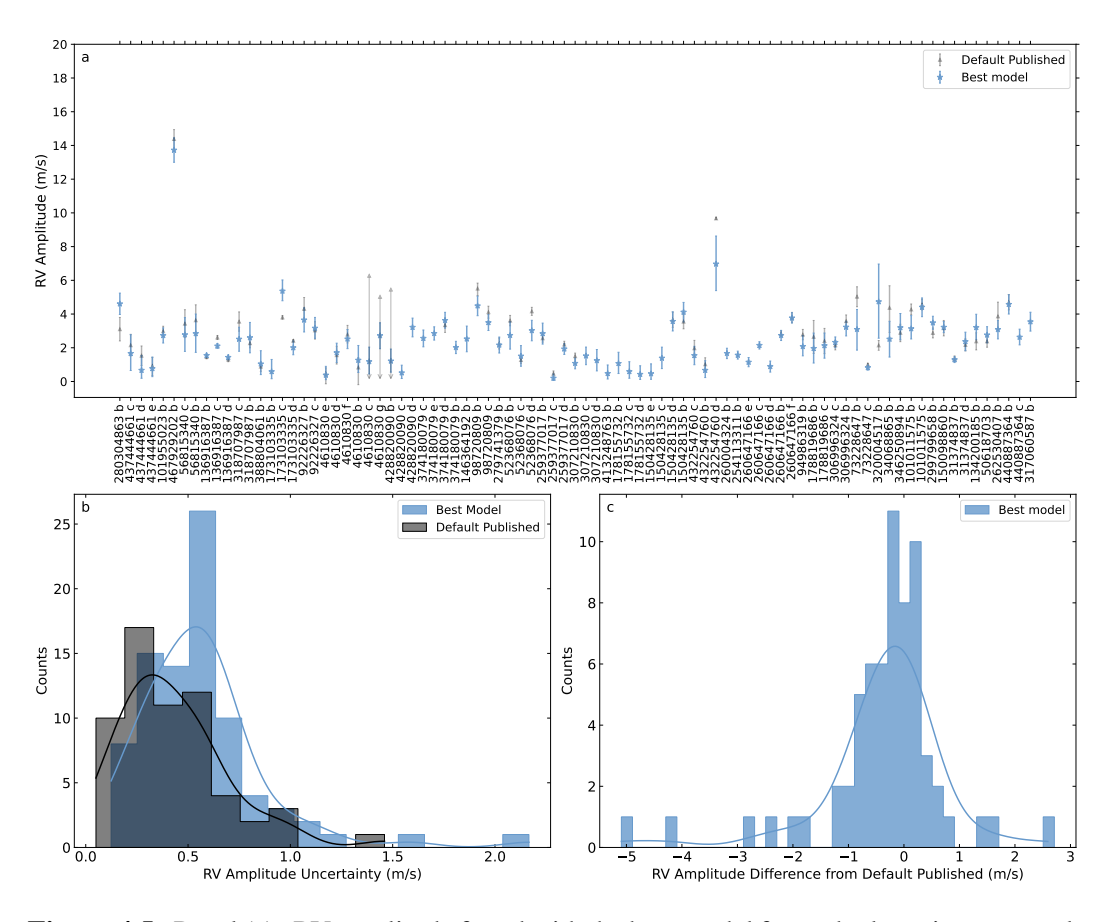


Figure 4.5: Panel (a): RV amplitude found with the best model for each planet in our sample (blue stars) compared to the default published value from the NASA Exoplanet Archive (grey squares). Some planets do not have a published RV amplitude on the archive. Panel (b): Histogram showing the RV amplitude uncertainty for our best model compared to the uncertainties of the default published amplitudes. Panel c: Histogram showing the RV amplitude of our best model for each planet subtracted by the default published value.

This gives the priors listed in Table B.2.

Our best model for this target is the 3D GP model with beta distribution on the eccentricity, and we focus on that specific case here. After the MCMC fitting, we find the parameters given in Table B.3. Figure 4.6 shows the full time series data for this target, with the best-fit model shown for the 3D GP with beta distribution on eccentricity case. The impact of the GP is clear in this plot: the planet signal alone would not reproduce the observations well without an activity model. In Figs. 4.7 and 4.8 we show the phase-folded RV data with best-fit model (including the GP) for planets b and c, respectively. Finally, the full posterior distribution found for all fitted parameters is shown in Figure B.1.

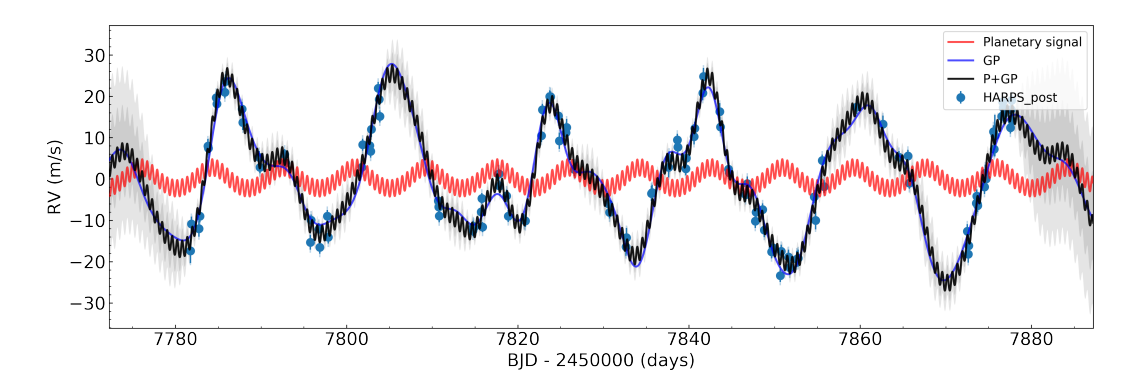


Figure 4.6: Best-fitting two-planet orbital model for TIC 9870809. HARPS data shown by blue circles as a function of time. The best-fitting model for the planet signals is shown in red, the 3D GP model in blue, and the combined planets and GP shown in black. The dark and light shaded areas show the 1σ and 2σ credible intervals of the corresponding GP model, respectively.

As a comparison, we now show the result plots for this same target but without a GP added to mitigate stellar activity. Specifically, we show the no GP model with a beta distribution on eccentricity, so that we can directly compare. In Figure 4.9 we show the time-series data with this no GP model; the data are very clearly not well fitted by this model, demonstrating the positive effect of the addition of a GP in this case. In Figs. 4.10 and 4.11, we show the phase-folded RV data with best-fit model (with no GP) for planets b and c, respectively. Again, it is clear that this model does not fit the data well, and in this case the planet signals would not be recovered. Finally, Figure B.2 shows the full posterior distribution of fitted parameters for this no GP model. In this case, the RV amplitude found for both planets is not significant; that is, it is within 1σ of 0 m s^{-1} and so using only this model with these data would result in non-detections for both planets.

4.8 Caveats and recommendations

This work presented a number of challenges, which are mostly related to the use of archival data. Barbieri (2023) discusses the possibility that some data and/or targets are potentially missing from our sample, which could impact the RV amplitudes found. We also note that we did not reprocess the raw observations to find the RVs ourselves; this would likely reduce some of the challenges we faced and could be a useful additional step in future work.

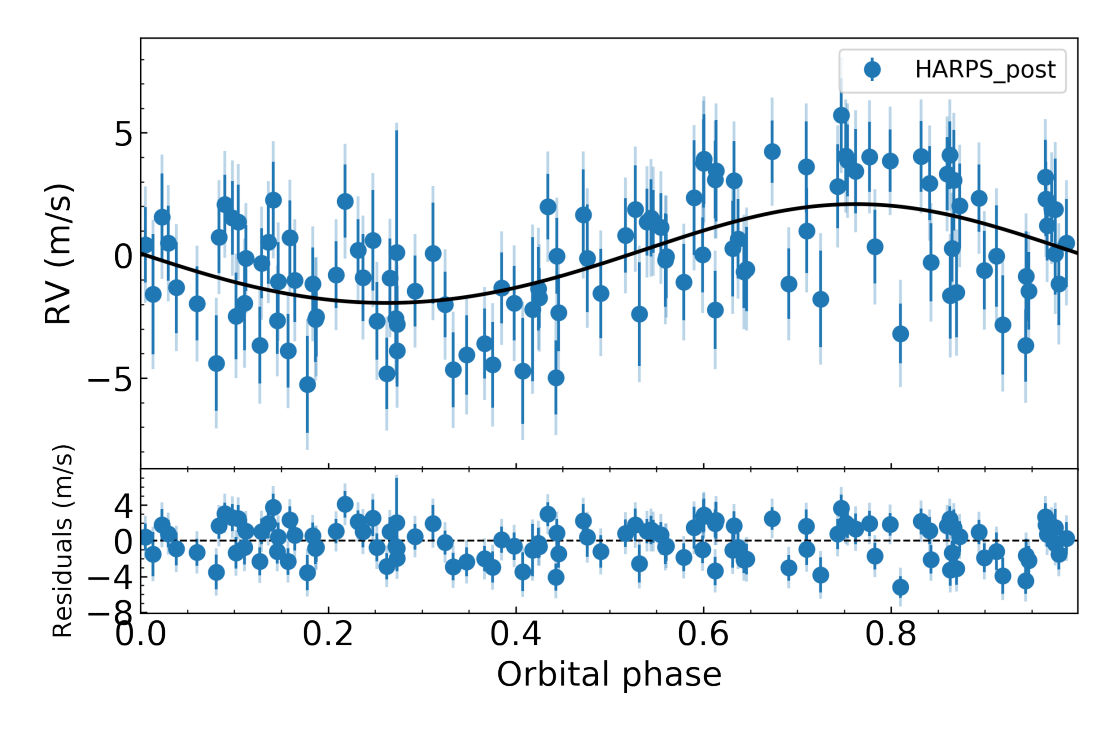


Figure 4.7: Phase-folded RV data from HARPS (blue circles) alongside the best-fitting planet model for TIC 9870809 b (with the effect of the other planet and the GP model subtracted). The lower part shows the residuals from the fit. There appears to be no trends visible in the residuals.

Another difficulty with using archival data is that we have no control of the observing strategy. In some cases, the cadence and baselines of observations for a target are not ideal for fitting GPs. Having long gaps between seasons of data makes it harder for the GP to capture the stellar activity signal. In future we recommend teams to think about trying to reduce the length of the gaps between their observing seasons where possible. We also recommend that large RV surveys be designed to mitigate the biases inherent to the observing strategy where possible, following the work of Teske et al. (2021) for example.

Another caveat of our results is that we used only the RVs available from HARPS. For some of our targets, there are additional data available from other RV instruments. In some cases, this means that the published *K* amplitudes are more precise than the ones we have found in our work. We would recommend that future studies investigate the impact of adding additional data.

Finally, we note that some activity indicators or combinations of indicators may be more capable of mitigating different manifestations of stellar activity than others.

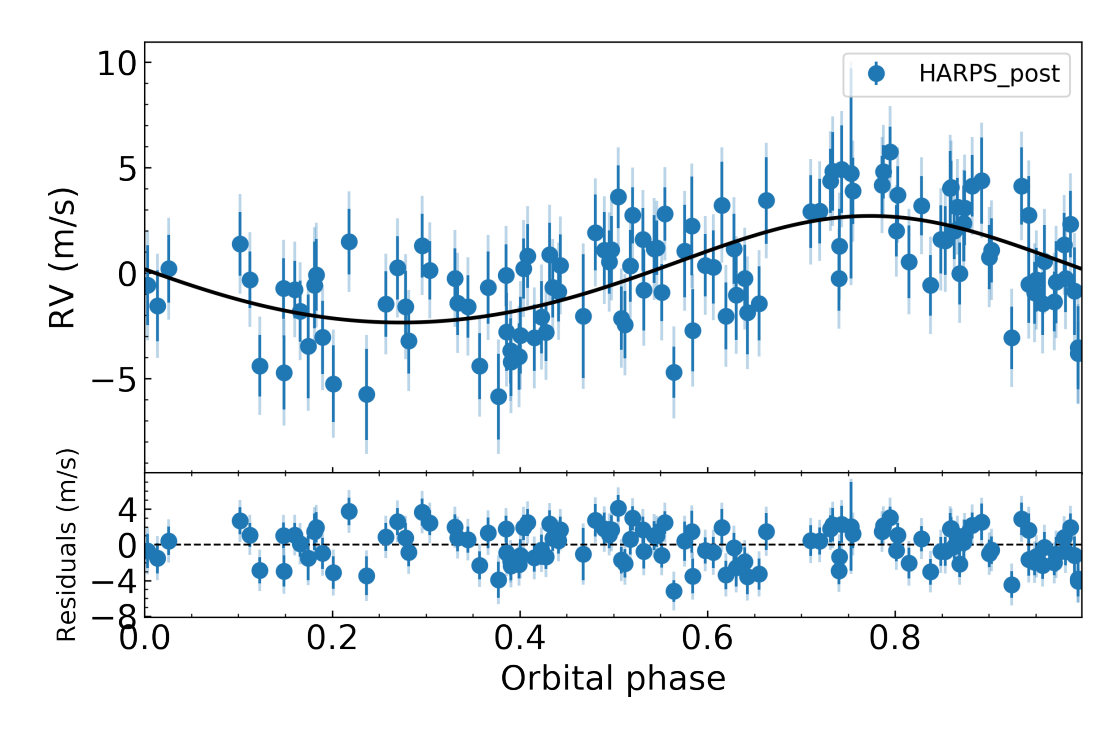


Figure 4.8: Phase-folded RV data from HARPS (blue circles) alongside the best-fitting planet model for TIC 9870809 c (with the effect of the other planet and the GP model subtracted). The lower part shows the residuals from the fit. There appears to be no trends visible in the residuals.

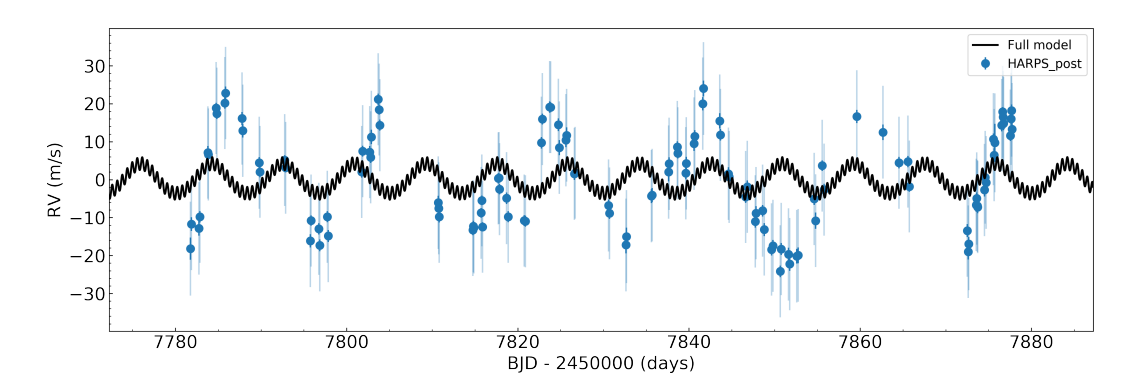


Figure 4.9: Planet model with no GP beta distribution on eccentricity for TIC 9870809. HARPS data shown by blue circles as a function of time. The best-fitting model for the planet signals is shown in black. The model does not fit the data well.

The typical activity seen in an M dwarf star is not the same as a G type star, and so having a one-size-fits-all approach may not be the most effective. However, the aim of this work is not to provide the 'best' RV amplitude for each small planet, but is instead to create a database of homogeneously derived planet parameters that can be used for demographics studies.

Based on the experience of this experiment, we propose a general set of rec-

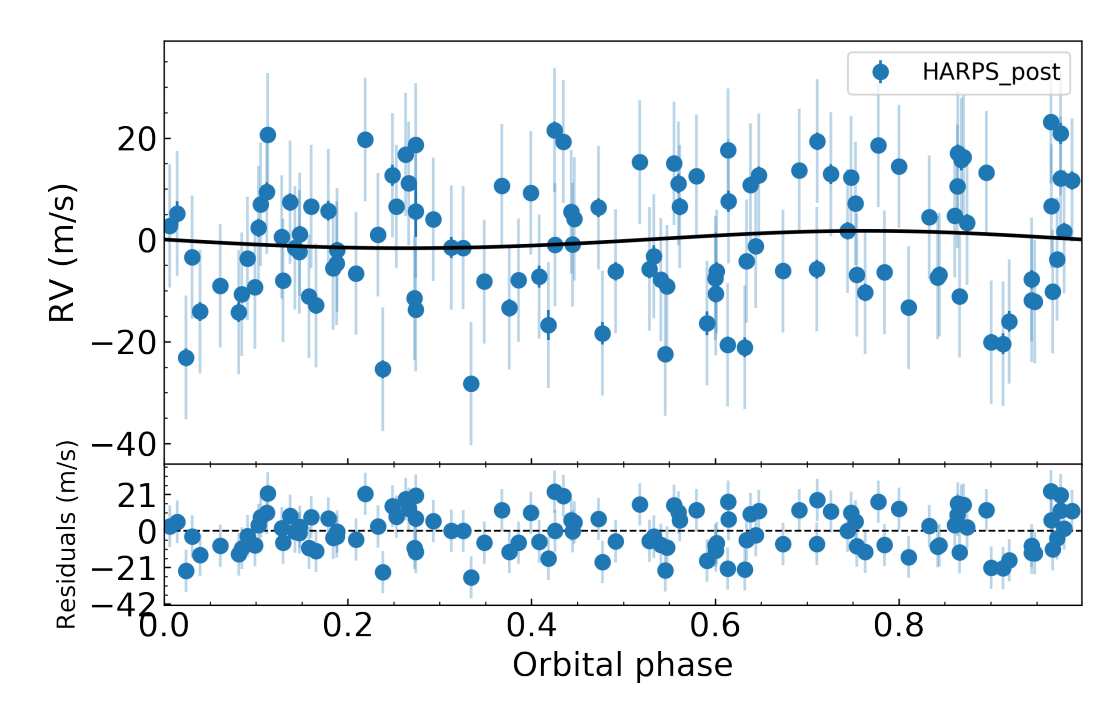


Figure 4.10: Phase-folded RV data from HARPS (blue circles) alongside the planet model with no GP beta distribution on eccentricity for TIC 9870809 b (with the effect of the other planet subtracted). The planet signal is hardly visible.

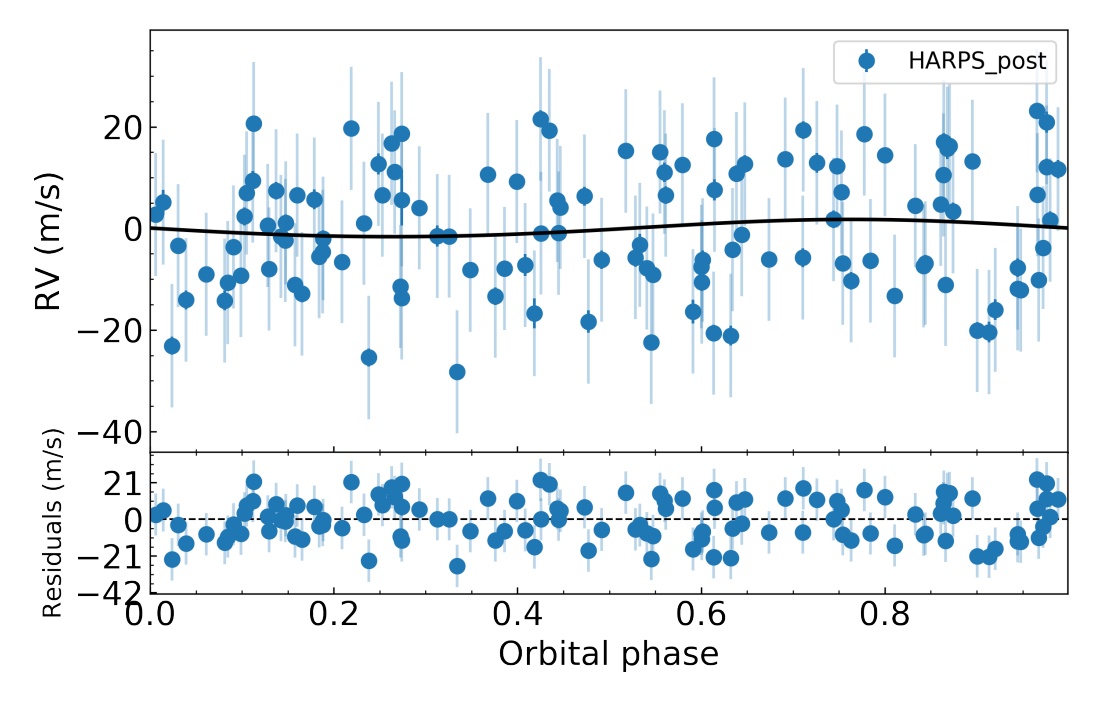


Figure 4.11: Phase-folded RV data from HARPS (blue circles) alongside the planet model with no GP beta distribution on eccentricity for TIC 9870809 c (with the effect of the other planet subtracted). The lower part shows the residuals from the fit. The planet signal is hardly visible.

ommendations for observing and modelling RVs of planet hosting stars in large batches:

- 1. Avoid having multiple seasons of observations with large (> 1 year) gaps in between if a GP is required to mitigate stellar activity signals.
- 2. Avoid modelling orbits as eccentric without a prior on the eccentricity (e.g. in the form of a beta distribution).
- 3. If using a GP, it should be used in combination with at least one activity indicator.
- 4. Using a heterogeneously derived sample of planet masses will likely induce some biases when looking at a large sample: to complete demographics studies, we recommend modelling planet masses in a homogeneous way.
- 5. As a community, we should collate a database of homogeneously derived masses wherever possible.

Plenty of work still needs to be done to understand the importance of homogeneous mass analysis in exoplanets. In future work, it will be beneficial to look at: the impact of how the RVs are extracted from the spectra; the potential systematic difference between the RV fitting toolkits; and the degree to which a joint fit with photometry changes planet masses. We also note that it would be important to test the robustness of the RV amplitude found when changing the priors on the GP and also the choice of GP kernel, particularly for different stellar types.

4.9 Conclusions

In this work, we re-fitted all publicly available HARPS RV observations for 44 stars hosting small planets with a planet radius of smaller than $4\,R_\oplus$. For each target system, we used 12 different models to investigate how model choice impacts the planet mass found.

We find that the addition of long-term trends to the model (either linear or quadratic in nature) makes a difference in some specific cases but that overall this model choice has only a very small impact. Almost all targets have an RV amplitude within 1 m s^{-1} of that found with a model with no trend.

The impact of eccentricity is much more significant. We find that the RV amplitudes found for fixed circular orbits differ (in some cases significantly) from those found for orbits that are modelled as eccentric with wide uniform priors. We recommend using a prior on the eccentricity, such as the beta distribution presented in Van Eylen et al. (2019) to ensure that the model does not find very high values of eccentricity.

Finally, we find that the addition of a GP, and in particular a multidimensional GP that fits on RVs and activity indicators, indeed impacts the mass found. On average, the RV amplitude found is within 1 m s⁻¹ of that found for the no GP case; however this can vary by up to more than 6 m s⁻¹. The 1D GP model, fitted just on the RVs, is the most different from the others. Therefore, we recommend using either a 2D or a 3D GP model for active stars. A 3D GP model takes longer computationally and so a 2D GP may be better where time is restricted and/or many targets need to be modelled.

Overall, our results demonstrate the importance of considering homogeneity in the analysis of RV observations to find planet masses. This will be particularly important for future surveys, such as the PLATO mission, which aims to provide a catalogue of accurate and precise planet parameters for many new systems. To ensure this sample is accurate at the population level, it will be necessary for the analysis to be done in a homogeneous way.

In Sect. 4.8 we describe some of the caveats of our work. In particular, we note that the RV amplitudes found in this work may not be the most precise for each individual planet in the sample. Rather, our aim is to provide a sample of masses determined homogeneously. We also note that future work should investigate the impacts of different models for different stellar types, and whether a joint model with photometric data would be of benefit. In Chapter 5 we investigate how the mass—radius distribution changes for our homogeneous sample from that seen for the heterogeneous sample. We will also comment on the future characterisation

possibilities of these small planets.

Chapter 5

Homogeneous planet masses II: Small planet demographics

5.1 Introduction

Precise and accurate planet mass measurements are essential for understanding the composition of exoplanets, placing constraints on their formation pathways (Mordasini and Burn, 2024), and to enable atmospheric observations (Batalha et al., 2019; Di Maio et al., 2023). The most common method for finding exoplanet masses is through precision radial velocity (RV) observations. However, the heterogeneity in the modelling of these RVs leads to a sample of planet mass which is challenging to use for statistical analysis and demographics studies. In 4 we show that making just one different choice in the modelling can lead to differences in extracted RV amplitude, even for identical data sets. In this chapter we take these new, homogeneously fitted planet RV amplitudes and use the derived planet masses they provide to investigate how this new sample changes our view of small planet compositions.

We also aim to investigate how the compositions of small planets change in and around the radius valley.

Others suggest that it could be the result of a variation in core composition at formation (Burn et al., 2024) with some evidence of a new class of small planets which contain significant fractions of water in their composition, e.g. Osborne et al. (2024); Piaulet et al. (2022); Diamond-Lowe et al. (2022); Cadieux et al. (2022).

This class of water-world planets is also supported by planet formation models which predict the formation of many such planets (Chakrabarty and Mulders, 2024).

Recent works have given evidence that the location of the radius valley changes as a function of host star mass (Ho and Van Eylen, 2023; Petigura et al., 2022; Cloutier and Menou, 2020). And more specifically, that the radius valley is less empty for M dwarf stars compared to FGK stars (Ho et al., 2024). Luque and Pallé (2022) suggest that, for M dwarf systems, this is actually a difference in density rather than radius, arguing that a population of water-world planets explain the observed trends. However, Parc et al. (2024) find no evidence of a distinct population of water-worlds. And Bergsten et al. (2023) find no signs of a difference in the occurrence rates of Earth-size planets around FGK and M dwarf stars. The ongoing questions over the nature of small planet compositions and the cause of the radius valley are confused by two things: the degeneracies in theoretical planet compositions; and the heterogeneous sample of planet mass and densities used in analyses.

For this work we wanted to attempt to answer these specific questions: are planets below the radius valley consistent with rocky compositions, and are those above consistent with a rocky plus H-He atmosphere? And, in addition, is there a difference in this for planets orbiting M dwarf stars compared to FGK stars? To help answer these questions we use our new homogeneously-derived set of planet masses and densities and theoretical composition tracks (in mass radius space) to compare these to.

In Section 5.3 we present the homogeneous planet masses derived from the radial velocity amplitudes in Osborne et al. (2025), in Section 5.4 we describe how these planet masses fit into our view of planet compositions in and around the radius valley. Finally in Section 5.5 we provide a prioritised list of important targets for future atmospheric characterisation.

5.2 Stellar Parameters

One important factor to consider in deriving the masses of planets is that the planet mass found is dependant on the stellar mass. If our sample of stellar masses is not

sufficiently precise and accurate then it will introduce additional uncertainties in the planet masses which we derive – as described in Weeks et al. (2025) . For this reason we carefully consider which measured stellar masses to use for our sample.

We chose to use the community database provided by Sousa et al. (2021) which provides stellar parameters for exoplanet host stars. For some of the stars in this catalogue the parameters are found in a homogeneous method, though for a few of our sample this is not the case. Specifically, M dwarf stellar parameters are not found in the same method as FGK stars. However, this is still the most complete and most homogeneous catalogue of exoplanet host stars available to us. Table 5.1 gives the stellar parameters used for all stars in our sample.

Table 5.1: Stellar parameters used for the stars in our sample, from Sousa et al. (2021). The name of the star, mass in solar masses, mass uncertainty, magnitude in V band, and effective temperature in K, are all given.

Name	Mass / M_{\odot}	Mass error / M_{\odot}	V Magnitude	Teff/ K
CoRoT-7	0.846	0.009	11.73	5336
K2-32	0.808	0.007	12.31	5322
GJ 1132	0.417	0.077	13.5	3270
GJ 1214	0.377	0.072	14.47	3109
HD 106315	1.244	0.028	8.95	6591
HD 136352	0.886	0.005	5.65	5659
HD 3167	0.836	0.008	8.94	5286
K2-18	0.443	0.031	13.5	3587
K2-3	0.499	0.021	12.17	3788
LHS 1140	0.346	0.041	14.15	3131
K2-138	0.846	0.008	12.21	5313
K2-233	0.717	0.007	10.7	4802
K2-266	0.624	0.013	11.81	4184
K2-265	0.884	0.006	11.19	5453
K2-229	0.779	0.006	10.98	5125
GJ 143	0.688	0.015	8.14	4497
TOI-125	0.815	0.006	11.02	5259
TOI-270	0.41	0.026	12.62	3539
L 98-59	0.385	0.028	11.7	3420
GJ 357	0.388	0.024	10.91	3458

Table 5.1 continued from previous page

Name	Mass / M_{\odot}	Mass error / M_{\odot}	V Magnitude	Teff / K
HR 858	1.2	0.009	6.38	6360
TOI-700	0.421	0.032	13.08	3480
EPIC 249893012	1.096	0.007	11.4	5567
LHS 1815	0.482	0.023	12.2	3678
TOI-1130	0.685	0.022	11.4	4609
HD 108236	0.883	0.101	9.2	5720
TOI-421	0.833	0.005	9.9	5316
TOI-763	0.882	0.014	10.16	5450
TOI-776	0.486	0.021	11.5	3765
HD 110113	1.889	0.012	10.05	5732
HD 183579	0.964	0.014	8.68	5788
GJ 367	0.465	0.03	10	3651
HD 137496	1.09	0.015		5799
HD 73583	0.684	0.119	9.67	4511
TOI-1062	0.865	0.012	10.25	5328
TOI-220	0.801	0.01	10.4	5298
TOI-431	0.76	0.013	9.12	4850
TOI-500	0.698	0.019		4621
TOI-544	0.647	0.033	11	4369
GJ 3090	0.48	0.022	11	3701
TOI-836	0.648	0.031	9.9	4552
TOI-1052	1.195	0.014	9.5	6146

5.3 A new sample of homogeneous planet masses

We use the RV amplitudes derived in Osborne et al. (2025) and our stellar masses from 5.2 to derive the masses of the 83 small planets in our sample. In Osborne et al. (2025) we did not model planet radii for our sample, and so for each of our planets we use the radius published in the Composite Parameters table on the NASA Exoplanet Archive. We note that it is possible that the planet radii could introduce some heterogeneity in our analysis, however typical transit surveys have standardised pipeline which should reduce this impact, e.g. in the case of TESS Ricker et al. (2014).

Table 5.2 gives the extracted mass of each planet in our sample, plus the planet radius, orbital period, and eccentricity.

5.4 The radius valley

To investigate how these planet masses and radii relate to the radius valley we calculate the location of the upper and lower boundaries of the radius valley. We do this for each individual target as the valley location changes based on stellar mass (Ho et al., 2024). We use Equation 11 from Ho and Van Eylen (2023) to calculate the specific planet radius needed at the observed orbital period to be at the valley boundaries. We then assign each planet to be either 'below', 'above', or 'inside' the valley by comparing this predicted radius with the observed radius. We also split our sample into M dwarf and FGK hosts, with a cut at stellar effective temperature 4000 K. This is because some works have suggested that different stellar types may host different populations of planets (see e.g. Neil and Rogers, 2018). In the left panel of Figure 5.1 we show the radius period distribution of planets orbiting M dwarfs in our sample, colour coded by location relative to the valley. The right hand panels show this same sample and colour coding but now in the mass-radius plane. Figure 5.2 shows these same plots but for our sample of planets orbiting FGK host stars.

lanet

Name	Mass	$-\sigma$ Mass	$+\sigma$ Mass	Radius	$-\sigma$ Radius	$+\sigma$ Radius	Period	$-\sigma$ Period	$+\sigma$ Period	မ	-де	+ <i>σ</i> e
CoRoT-7 b	5.91	1.116	1.215	1.681	0.112	-0.112	0.854	0	0	0.023	0.014	0.029
K2-32 c	6.282	3.821	4.203	3.134	0.123	-0.102	20.661	0.001	0.001	0.05	0.032	0.051
K2-32 d	2.916	2.091	3.828	3.484	0.112	-0.129	31.717	0.001	0.001	0.041	0.026	0.05
K2-32 e	1.726	1.084	1.535	1.212	0.052	-0.046	4.349	0	0	0.047	0.03	0.053
GJ 1132 b	1.59	0.279	0.297	1.13	0.056	-0.056	1.629	0	0	0.029	0.018	0.029
GJ 1214 b	13.009	1.813	1.79	2.733	0.033	-0.031	1.58	0	0	0.023	0.013	0.017
HD 106315 c	13.831	4.93	5.08	4.35	0.23	-0.23	21.057	0	0	0.04	0.025	0.042
HD 106315 b	10.868	4.265	4.426	2.44	0.17	-0.17	9.552	0.001	0.001	0.057	0.036	0.054
HD 136352 b	4.979	0.43	0.439	1.664	0.043	-0.043	11.578	0	0	0.018	0.011	0.019
HD 136352 c	9.063	0.673	0.699	2.916	0.075	-0.073	27.592	0	0	0.017	0.01	0.017
HD 136352 d	9.672	1.047	0.997	2.562	0.088	-0.079	107.253	0.038	0.039	0.028	0.018	0.028
HD 3167 c	11.329	1.997	2.034	3	0.45	-0.21	29.845	0.001	0.001	0.025	0.016	0.026
HD 3167 b	4.847	0.761	0.776	1.67	0.17	-0.1	96.0	0	0	0.025	0.016	0.026
K2-18 b	7.268	2.096	2.088	2.37	0.22	-0.22	32.94	0	0	0.071	0.044	0.065
K2-3 b	5.509	1.914	1.925	2.078	0.076	-0.067	10.055	0	0	0.031	0.02	0.035
K2-3 c	2.977	1.817	2.241	1.582	0.057	-0.051	24.647	0	0	0.041	0.026	0.046
K2-3 d	2.038	1.475	2.514	1.458	0.056	-0.051	44.556	0	0	0.039	0.025	0.042
LHS 1140 b	TTT.T	0.836	0.953	1.73	0.025	-0.025	24.737	0	0	0.055	0.031	0.037
LHS 1140 c	1.552	0.325	0.316	1.272	0.026	-0.026	3.778	0	0	0.041	0.026	0.043

				Table 5.2	continued 1	Table 5.2 continued from previous page	s page					
Name	Mass	-σMass	$+\sigma$ Mass	Radius	$-\sigma$ Radius	$+\sigma$ Radius	Period	$-\sigma$ Period	$+\sigma$ Period	e	-о-	+ <i>σ</i> e
K2-138 e	11.065	2.174	2.198	3.39	0.156	-0.11	8.261	0	0	0.026	0.017	0.028
K2-138 d	8.326	1.594	1.678	2.39	0.104	-0.084	5.405	0	0	0.03	0.019	0.032
K2-138 f	1.342	0.964	1.803	2.904	0.164	-0.111	12.758	0.001	0	0.042	0.027	0.047
K2-138 b	3.406	1.177	1.127	1.51	0.11	-0.084	2.353	0	0	0.034	0.021	0.039
K2-138 c	5.774	1.324	1.289	2.299	0.12	-0.087	3.56	0	0	0.03	0.019	0.033
K2-138 g	6.586	3.811	4.515	3.013	0.303	-0.251	41.968	600.0	0.009	0.05	0.032	0.055
K2-233 b	2.126	1.327	1.547	1.343	0.018	-0.016	2.468	0	0	0.04	0.026	0.048
K2-233 c	6.959	1.987	1.957	1.281	0.022	-0.021	7.06	0	0	0.041	0.026	0.045
K2-233 d	4.715	2.581	2.735	2.358	0.043	-0.036	24.365	0.001	0.001	0.027	0.017	0.034
K2-266 c	1.241	0.818	1.1	0.705	960.0	-0.085	7.814	0.002	0.002	0.049	0.032	0.055
K2-266 e	10.552	1.89	1.826	2.73	0.14	-0.11	19.482	0.001	0.001	0.022	0.014	0.024
K2-266 d	7.64	1.53	1.501	2.93	0.14	-0.12	14.697	0	0	0.049	0.029	0.046
K2-266 b	3.021	0.427	0.433	3.3	1.8	-1.3	0.659	0	0	0.031	0.02	0.032
K2-265 b	7.132	0.913	0.952	1.71	0.11	-0.11	2.369	0	0	0.034	0.021	0.035
K2-229 b	2.397	0.432	0.439	1	0.02	-0.02	0.584	0	0	0.039	0.024	0.036
K2-229 c	7.26	2.198	2.183	2.03	0.12	-0.06	8.327	0	0	0.073	0.046	0.067
GJ 143 b	18.598	2.642	2.738	2.61	0.17	-0.16	35.612	0.001	0.001	0.038	0.023	0.035
TOI-125 b	8.2	1.129	1.159	2.726	0.075	-0.075	4.654	0	0	60.0	0.043	0.043
TOI-125 c	6.397	1.432	1.405	2.759	0.1	-0.1	9.151	0.001	0.001	0.029	0.018	0.034
TOI-125 d	10.447	3.12	3.102	2.93	0.17	-0.17	19.98	0.005	0.005	0.059	0.037	0.059

0.045 0.045 0.037 0.039 0.045 0.045 0.038 0.034 0.034 0.034

				Table 5.2	continued f	Table 5.2 continued from previous page	ıs page					
Name	Mass	-σMass	+σMass	Radius	-\sigma Radius	+\sigma Radius	Period	-\sigma Period	$+\sigma$ Period	e	-∂e	
TOI-270 b	1.943	0.782	0.804	1.206	0.039	-0.039	3.36	0	0	0.047	0.029	_
TOI-270 c	4.633	0.947	0.958	2.355	0.064	-0.064	5.661	0	0	0.034	0.021	_
TOI-270 d	5.498	1.222	1.237	2.133	0.058	-0.058	11.38	0	0	0.043	0.027	_
T 98-59 p	0.172	0.121	0.211	0.85	0.061	-0.047	2.253	0	0	0.036	0.023	_
L 98-59 c	1.938	0.353	0.354	1.385	0.095	-0.075	3.691	0	0	0.026	0.016	_
P 68-86 T	1.367	0.426	0.417	1.521	0.119	-0.098	7.451	0	0	0.033	0.021	_
GJ 357 b	1.99	69.0	69.0	1.2	90.0	-0.06	3.931	0	0	0.039	0.025	_
HR 858 b	3.344	1.656	1.776	2.085	0.068	-0.064	3.586	0	0	0.034	0.022	_
HR 858 c	1.52	1.053	1.619	1.939	0.069	-0.069	5.973	0.001	0.001	0.041	0.027	_
HR 858 d	4.225	2.367	2.616	2.164	0.086	-0.083	11.23	0.001	0.001	0.044	0.028	_
TOI-700 e	1.562	1.058	1.558	0.953	0.089	-0.075	27.81	0	0	0.036	0.023	_
TOI-700 c	0.94	0.672	1.124	2.6	0.14	-0.13	16.051	0	0	0.039	0.025	_
TOI-700 d	1.352	0.975	1.718	1.073	0.059	-0.054	37.424	0	0	0.034	0.022	_
TOI-700 b	2.612	1.18	1.237	0.914	0.053	-0.049	7.26.6	0	0	0.036	0.023	_
EPIC 249893012 c	14.793	2.366	2.357	3.67	0.17	-0.14	15.624	0.001	0.001	0.036	0.022	_
EPIC 249893012 b	10.472	1.505	1.46	1.95	0.09	-0.08	3.595	0	0	0.031	0.019	_
EPIC 249893012 d	8.428	3	2.979	3.94	0.13	-0.12	35.747	0.005	0.005	0.032	0.02	_
LHS 1815 b	0.998	0.651	0.85	1.088	0.064	-0.064	3.814	0	0	0.04	0.025	_
TOI-1130 b	13.838	3.149	3.317	3.56	0.13	-0.13	4.075	0	0	0.026	0.016	_
HD 108236 e	6.373	1.206	1.217	3.083	0.052	-0.052	19.59	0	0	0.048	0.029	_

				Table 5.2	continued f	Table 5.2 continued from previous page	s page					
Name	Mass	$-\sigma$ Mass	+σMass	Radius	-\sigma Radius	$+\sigma$ Radius	Period	$-\sigma$ Period	$+\sigma$ Period	e	-о-	+ <i>σ</i> e
HD 108236 c	4.074	0.631	0.639	2.071	0.052	-0.052	6.203	0	0	9/0.0	0.04	0.047
HD 108236 d	3.945	0.951	0.958	2.539	0.062	-0.065	14.176	0	0	0.054	0.033	0.047
HD 108236 b	4.756	0.518	0.524	1.615	0.051	-0.051	3.796	0	0	0.027	0.017	0.027
HD 108236 f	3.897	1.457	1.457	2.017	0.052	-0.057	29.541	0	0	0.032	0.02	0.036
TOI-421 b	6.633	0.75	0.753	2.64	0.08	-0.08	5.196	0	0	0.016	0.01	0.018
TOI-763 b	9.892	0.824	0.842	2.28	0.11	-0.11	5.606	0.001	0.001	0.046	0.024	0.028
TOI-763 c	7.073	1.908	2.214	2.63	0.12	-0.12	12.273	0.005	0.005	0.039	0.025	0.039
TOI-776 c	4.713	2.078	2.183	2.047	0.081	-0.078	15.665	0	0	0.085	0.054	0.074
TOI-776 b	4.143	1.453	1.473	1.798	0.078	-0.077	8.247	0	0	0.036	0.023	0.04
HD 110113 b	4.936	869.0	0.73	2.05	0.12	-0.12	2.541	0	0	0.041	0.025	0.038
HD 110113 с	9.495	1.613	1.116				6.733	0.004	0.004	0.022	0.014	0.026
HD 183579 b	12.752	5.079	4.897	3.55	0.15	-0.12	17.471	0	0	0.042	0.026	0.046
GJ 367 b	0.524	0.095	0.092	669.0	0.024	-0.024	0.322	0	0	0.033	0.021	0.035
HD 137496 b	9.183	4.207	4.337	1.31	90.0	-0.05	1.621	0	0	0.044	0.028	0.047
HD 73583 b	5.91	2.51	2.484	2.79	0.1	-0.1	6.398	0	0	0.034	0.021	0.031
HD 73583 c	10.747	2.439	2.845	2.39	0.1	-0.09	18.88	0.001	0.001	0.056	0.035	0.049
TOI-1062 b	7.524	1.475	1.865	2.265	960.0	-0.091	4.114	0.001	0.001	0.026	0.017	0.032
TOI-220 b	13.407	1.749	1.709	3.03	0.15	-0.15	10.695	0	0	0.02	0.012	0.022
TOI-431 b	3.624	0.451	0.472	1.28	0.04	-0.04	0.49	0	0	0.018	0.012	0.018
TOI-431 d	9.858	1.131	1.212	3.29	60.0	-0.09	12.461	0	0	0.029	0.018	0.026

0.019

0.047

0.034 0.024 0.021 0.03 0.01 0.016 0.032 $+\sigma$ Period 0 0 0 0 $-\sigma$ Period 0 Period 2.853 3.817 8.595 Table 5.2 continued from previous page 0.548 1.548 $-\sigma$ Radius $+\sigma$ Radius -0.058 -0.076 -0.067 -0.088 -0.11 0.061 0.088 Radius 1.166 2.018 1.704 2.587 2.87 $+\sigma$ Mass 0.188 1.398 0.97 $-\sigma$ Mass 0.919 0.181 1.039 1.409 2.107 5.193 16.83 1.352 4.587 7.608 TOI-1052 b TOI-544 b TOI-836 b TOI-836 c TOI-500 b GJ 3090 b

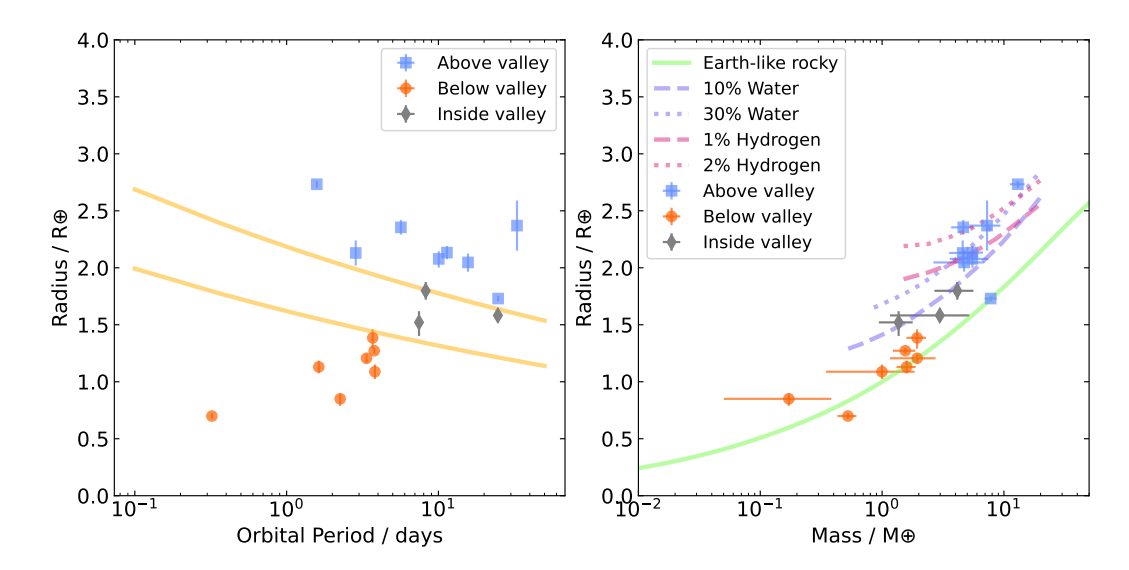


Figure 5.1: Planets in our sample which orbit M dwarf stars. Left: planet radius versus orbital period. The yellow solid lines show the upper and lower boundaries of the radius valley (calculated for the median stellar mass of the sample). The planets are colour coded by their location relative to the radius valley, calculated for their specific stellar mass. Right: the same sample of planets with the same colour coding, this time in mass-radius space. The coloured lines show theoretical composition tracks: pink lines from Lopez and Fortney (2014), purple lines from Aguichine et al. (2021), and green from Zeng et al. (2019).

5.4.1 Below the valley

Now we can focus in on just the planets below the valley, in Figure 5.3, left panel, we show a zoom in of the planets classified as below the valley. We also include three theoretical composition tracks: for an Earth-like rocky composition, a pure iron composition, and a pure rock composition (Zeng et al., 2019). The pure rock and pure iron compositions are provided as a comparison and do not represent a likely actual composition. The first thing to note is that all of these planets below the valley are consistent with 'rocky' compositions i.e. their mass and radius do not require any addition of volatiles to be explained. Secondly, there does seem to be some variation within these rocky planets: some seem closest to an Earth-like composition while others are more likely to be iron-poor (i.e. closer to the pure rock line). Given the size of the error bars and the close proximity of the tracks it is difficult to say conclusively that there are multiple groups within this population. In previous works focused on FGK-type stars it has been suggested that the distribution

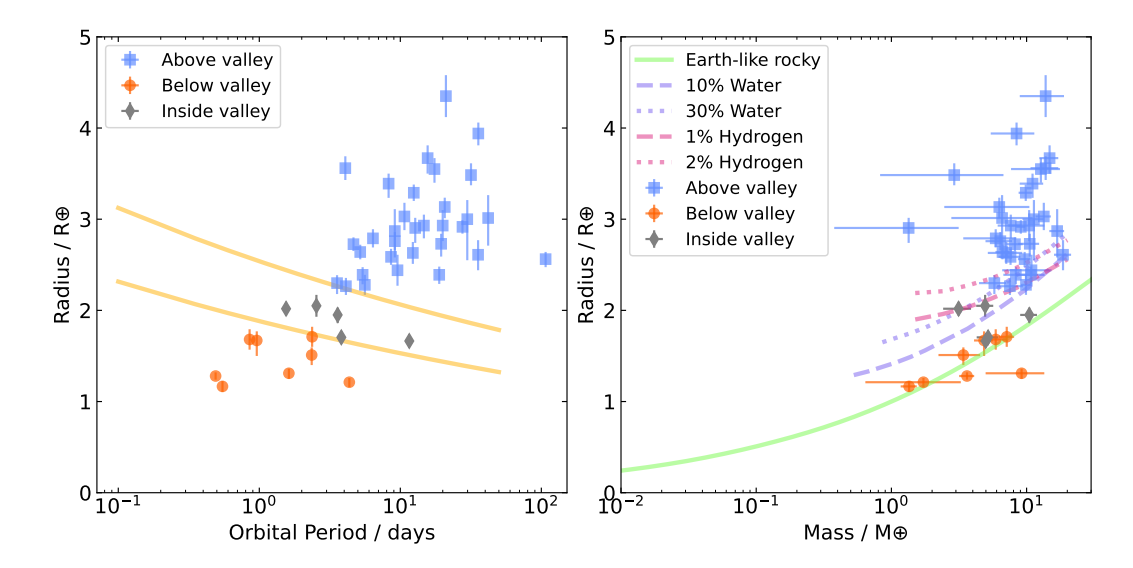


Figure 5.2: Planets in our sample which orbit FGK stars. Left: planet radius versus orbital period. The yellow solid lines show the upper and lower boundaries of the radius valley (calculated for the median stellar mass of the sample). The planets are colour coded by their location relative to the radius valley, calculated for their specific stellar mass. Right: the same sample of planets with the same colour coding, this time in mass-radius space. The coloured lines show theoretical composition tracks: pink lines from Lopez and Fortney (2014), purple lines from Aguichine et al. (2021), and green from Zeng et al. (2019).

in the amount of rock/iron in a planet core could correspond to the stellar metallicity (Adibekyan et al., 2024) and/or stellar age (Weeks et al., 2025), this may also be the case for M dwarfs.

In Figure 5.3, right panel, we show the planets in our sample which orbit FGK type stars and are below the radius valley. Here, again, all planets are consistent with a rocky-like composition, with some variation in the proportion of rock/iron. We note that one planet has a significant difference from the others and appears to be extremely dense, however the uncertainties on this mass are also very large and so the planet is less than 1σ away from a pure iron composition.

One difference between the planets around M dwarf and FGK stars in our sample is that the planets around FGK stars appear to be more massive on average than those around M dwarfs. All of the planets below the radius valley orbiting M dwarfs in our sample are below 3 M_{\oplus} . Conversely, the majority of planets below the radius valley orbiting FGK stars in our sample are above 3 M_{\oplus} . Otherwise, the distributions of planets in these two sample do appear very similar, and in both cases

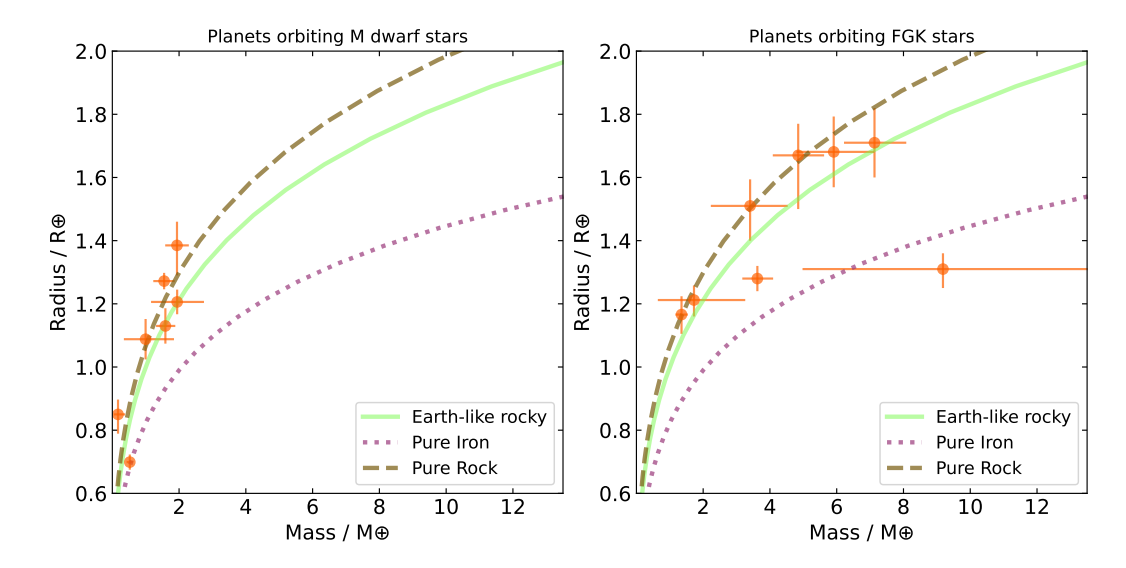


Figure 5.3: Left: Planets in our sample which orbit M dwarf stars and are below the radius valley. Planet mass versus radius for the planets which are below the radius valley shown in Figure 5.1. Right: Planets in our sample which orbit FGK stars. Planet mass versus radius for the planets which are below the radius valley shown in Figure 5.2. Lines show theoretical composition tracks for solid planet scenarios.

the planets do not all fall along a single composition track.

5.4.2 Above the valley

Now we move on to planets located above the radius valley. Here we split each sample (M dwarf and FGK host stars) into two separate mass-radius diagrams. This is so that in one we can plot the composition tracks which are consistent with an Earth-like core surrounded by atmospheric layers of H-He from Lopez and Fortney (2014). And in the other we plot the composition tracks for planets with a combination of Earth-like rock and water from Aguichine et al. (2021). Figure 5.4 shows the two mass-radius diagrams for the planets orbiting M dwarf stars.

The first thing to note is that not all of the planets are consistent with a 'sub-Neptune'-like composition. One planet (lower centre of the plot) is consistent with an Earth-like composition, which is not predicted for a planet above the radius valley. However, this planet, LHS 1140 b, has recently been analysed in Cadieux et al. (2024) where thy use ESPRESSO data rather than the archival HARPS data. Cadieux et al. (2024) find a lower mass for this planet in their new analysis which would put it at a

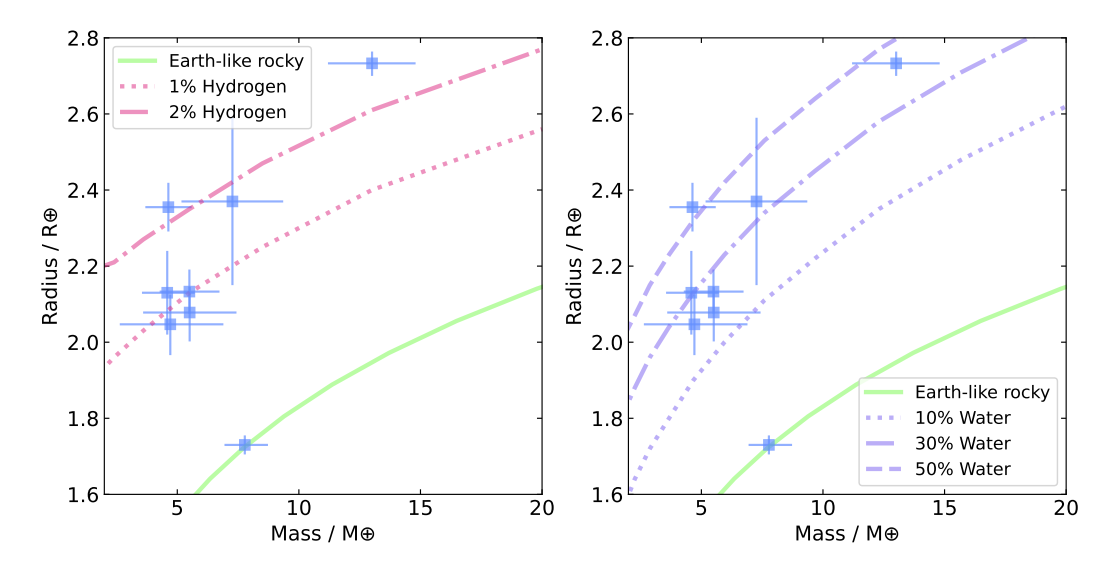


Figure 5.4: Planets in our sample which orbit M dwarf stars and are above the radius valley. Planet mass versus radius for the planets which are above the radius valley shown in Figure 5.1. Left: pink lines show Earth-like rocky core surrounded by a layer of H–He in varying percentages by mass from Lopez and Fortney (2014) using the models for a 10 Gyr planet, with solar metallicity and flux of $10 \ F_{\oplus}$. Right: purple lines show compositions from Aguichine et al. (2021) of irradiated ocean worlds with varying water mass fractions. In both panels: green lines show Earth-like rocky composition from Zeng et al. (2019).

lower density and therefore within the sub-Neptune-like region. This also highlights the importance of investigations into whether different telescopes and instruments find consistent masses for the same planets, though this is beyond the scope of this chapter.

Other than this one example, all of the other planets are consistent with requiring some volatile layers. In the left panel we can see that the planets are spread throughout the composition tracks, i.e. no single track could represent all planet masses and radii. In the right panel the same is true, no single water-world composition track can be used to represent all of these planets. The H-He and water compositions are degenerate with each other and so it is not possible to find a reliable composition for these planets with just mass and radius measurements.

In Figure 5.5 we show the mass-radius diagram for planets above the radius valley orbiting FGK stars in our sample. Again we split this into two panels to show the composition tracks for sub-Neptunes and water-worlds. Firstly, we see that all the planets are consistent with requiring the addition of volatiles, and so are not

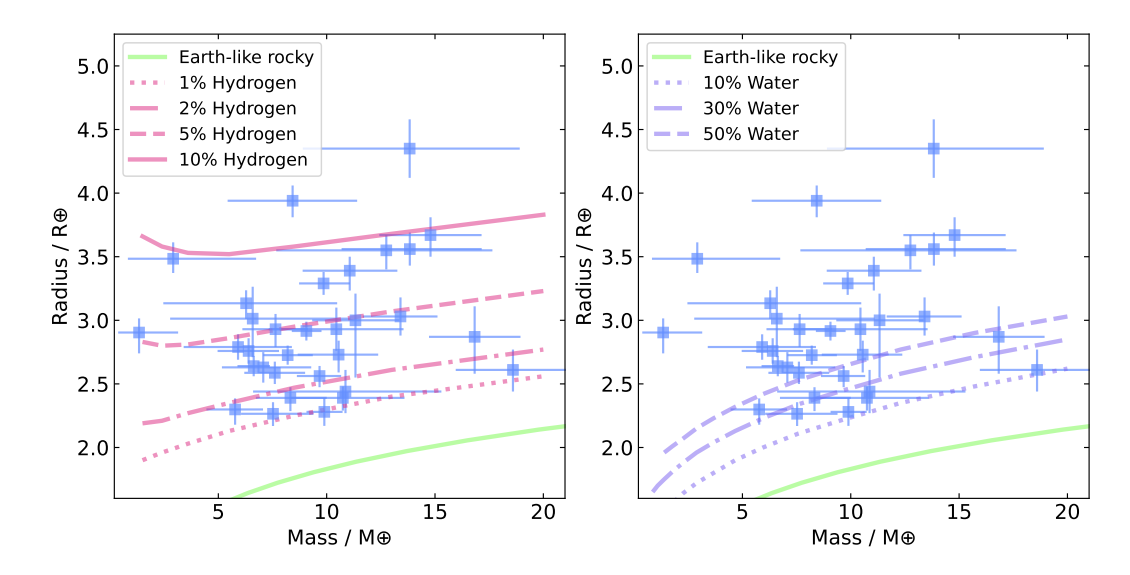


Figure 5.5: Planets in our sample which orbit FGK stars and are above the radius valley. Planet mass versus radius for the planets which are above the radius valley shown in Figure 5.2. Left: pink lines show Earth-like rocky core surrounded by a layer of H–He in varying percentages by mass from Lopez and Fortney (2014) using the models for a 10 Gyr planet, with solar metallicity and flux of $10 \, F_{\oplus}$. Right: purple lines show compositions from Aguichine et al. (2021) of irradiated ocean worlds with varying water mass fractions. In both panels: green lines show Earth-like rocky composition from Zeng et al. (2019).

likely to be only rocky compositions. We also note that in the right hand panel, even the composition track with a 50% fractional mass of water is insufficient to explain the mass and radius of many of the planets. For these planets toward the top of the mass-radius diagram the addition of H-He is required to sufficiently increase the radii for a given mass to match observations. For the planets in the lower part of the mass-radius diagram, the composition tracks between sub-Neptune-like and water-world-like compositions are degenerate and so we would not be able to rule-out the possibility of water worlds in this sample.

When comparing the planets around FGK stars to those around M dwarfs we notice several key differences. Firstly, the planets around M dwarfs are on average much smaller, with all of them below 3 R_{\oplus} . Whereas the planets orbiting FGK stars span a much wider range of radii. Secondly, there are many planets orbiting the FGK stars in our sample which have sufficiently low density they must have much more significant H-He layers – above 10% by mass in some cases.

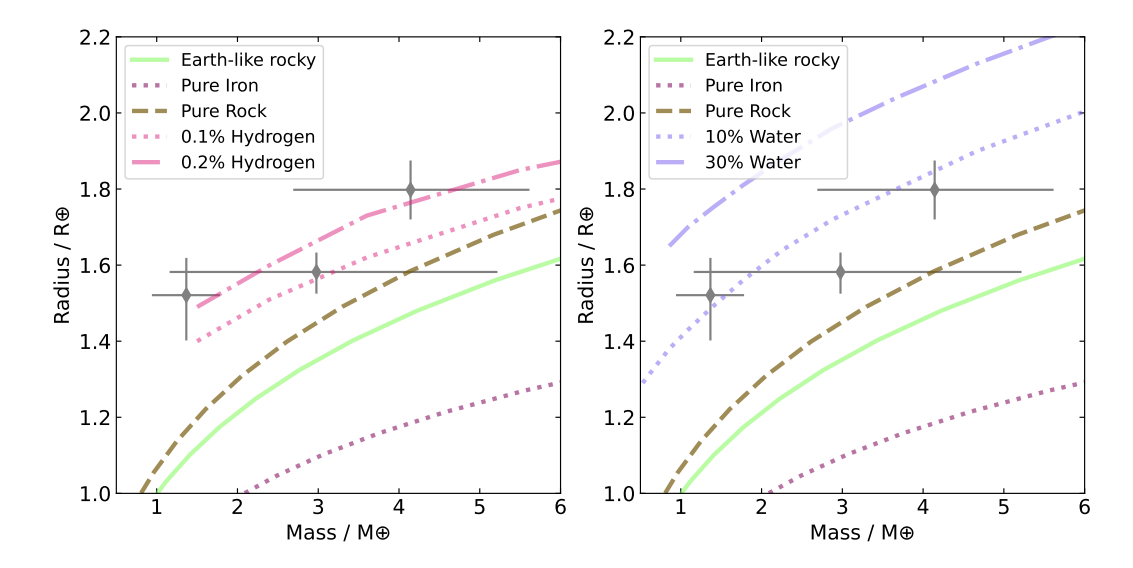


Figure 5.6: Planets in our sample which orbit M dwarf stars and are inside the radius valley. Planet mass versus radius for the planets which are inside the radius valley shown in Figure 5.1. Left: pink lines show Earth-like rocky core surrounded by a layer of H–He in varying percentages by mass from Lopez and Fortney (2014) using the models for a 10 Gyr planet, with solar metallicity and flux of $10 \, F_{\oplus}$. Right: purple lines show compositions from Aguichine et al. (2021) of irradiated ocean worlds with varying water mass fractions. In both panels: green lines show Earth-like rocky composition from Zeng et al. (2019).

5.4.3 Inside the valley

Finally we take a look at the small subset of planets in our sample which sit inside the radius valley in radius-period space. If we assume that the radius valley is formed through atmospheric loss processes then it might be the case that planets found inside the valley are currently undergoing this loss of material. Alternatively, if we believe the water-world scenario we might expect that planets inside the valley could form part of this water-rich population and so could have an unusual density.

Figure 5.6 shows the planets in our sample which orbit M dwarf stars and are inside the radius valley. Again, we show two mass-radius diagrams with the sub-Neptune-like theoretical composition tracks on the left and the water-world-like composition tracks on the right. For all three planets shown, the composition tracks are degenerate. However, in the left panel, with sub-Neptune-like compositions, note that the fractional mass of H-He is required to be very low to explain the measured masses and radii. Whereas a potential water-world with around 10% water by mass is also sufficient to explain to the measured mass and radius of these planets. These

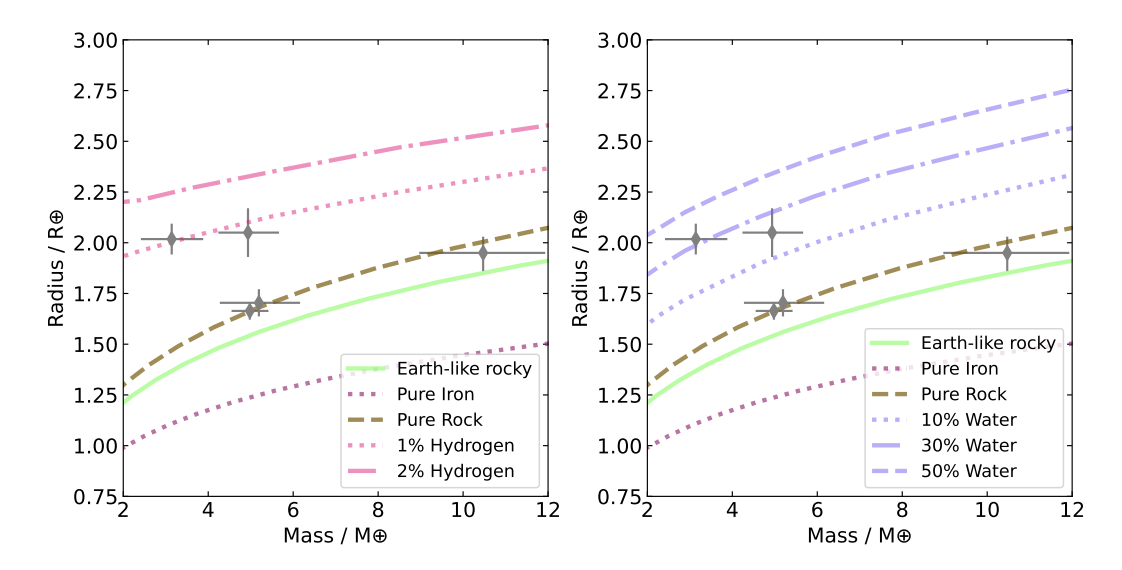


Figure 5.7: Planets in our sample which orbit FGK stars and are inside the radius valley. Planet mass versus radius for the planets which are inside the radius valley shown in Figure 5.2.Left: pink lines show Earth-like rocky core surrounded by a layer of H–He in varying percentages by mass from Lopez and Fortney (2014) using the models for a 10 Gyr planet, with solar metallicity and flux of $10 \, \mathrm{F}_{\oplus}$. Right: purple lines show compositions from Aguichine et al. (2021) of irradiated ocean worlds with varying water mass fractions. In both panels: green lines show Earth-like rocky composition from Zeng et al. (2019).

three planets would require atmospheric characterisation to break the degeneracy in composition.

Finally, we show in Figure 5.7 the planets in our sample which orbit FGK stars and are inside the radius valley. The first thing to note is that 3 of these planets are consistent with rocky compositions. It is possible that these planets are erroneously classified as inside the valley due to incorrect stellar parameters. What is most interesting are the two planets which are not consistent with rocky compositions. Both of these planets are firmly inside the valley and are also consistent with having a sub-Neptune like composition with rocky and 2% H-He or a water-world-like composition of rock and 10-30% water. As with the planets inside the valley orbiting M dwarf stars, detailed atmospheric characterisation of both planets is required to determine whether they really could be water worlds.

5.5 The potential for atmospheric follow-up

As discussed in previous sections, it is clear that the problem of determining the nature of planets between 2 and 4 R_{\oplus} will not be solved with mass and radius measurements alone. Atmospheric characterisation would allow for much greater understanding of the compositions of these planets and may help break the degeneracies in mass-radius relations. In this section we provide a list of priority targets for future atmospheric follow-up efforts.

First, we calculate the transmission spectroscopy metric (TSM, Kempton et al., 2018) for each target using our new planet mass values. We note that this value is not a definitive statistic but rather a way of comparing planets in a simplified way for prioritising telescope time and so should be used in conjunction with other reasoning for observing planets with instruments such as JWST. Nevertheless, the TSM is commonly used as a way of finding potential targets and so we provide the top ranking planets in our sample in terms of TSM for each radius bin as suggested in Kempton et al. (2018) in Table. 5.3.

Table 5.3: The planets in our sample split into three radius bins, then ordered in terms of highest TSM.

Planets $R_{\oplus} < 1.5$		Planets 1.5 < F	$R_{\oplus} < 2.75$	Planets $2.75 < R_{\oplus} < 4$	
Name	TSM	Name	TSM	Name	TSM
L 98-59 b	112	HR 858 c	432	K2-266 b	558
GJ 367 b	38	L 98-59 d	403	HD 136352 c	291
GJ 1132 b	34	GJ 1214 b	269	TOI-431 d	189
L 98-59 c	33	HR 858 b	240	HD 73583 b	167
K2-3 d	30	TOI-270 c	182	HD 106315 c	147
LHS 1140 c	27	TOI-544 b	162	K2-138 f	136
GJ 357 b	26	GJ 3090 b	161	TOI-1130 b	119
TOI-500 b	16	HR 858 d	130	K2-32 d	113
TOI-431 b	13	HD 136352 b	129	HD 183579 b	111
LHS 1815 b	10	TOI-836 c	125	HD 3167 c	69

We also note that several targets lie in particularly interesting parameter space as seen in the mass-radius plots in the previous section. For that reason we also wish to highlight the importance of atmospheric observations of the two planets orbiting FGK stars which are inside the radius valley and do not follow the Earth-like composition track: HD 110113 b and TOI-544 b, and the three planets inside the valley orbiting M dwarf stars: K2-3 c, L 98-59 d, and TOI-776 b. All five of these targets have published precise (better than 25% uncertainty) masses. Two of these (TOI-544 b and L 98-59 d) are also within our top ranked TSM planets and so we would suggest these are top priorities for atmospheric observations.

Some of these highlighted planets have already been the targets of JWST observations to characterise their atmospheres including: L 98-59 d and L 98-59 c (Barclay et al., 2025; Scarsdale et al., 2024; Bello-Arufe et al., 2025); TOI-270 c (Yang and Hu, 2024); and GJ 1214 b (Gao et al., 2023; Nixon et al., 2024; Schlawin et al., 2024; Ohno et al., 2025; Malsky et al., 2025). With the upcoming JWST director's discretionary time programme focussed on the transmission spectroscopy of potentially rocky planets orbiting M dwarf stars, we are likely to see further results of atmospheric characterisation in the coming years.

5.6 Conclusions

In this work we provide a new sample of homogeneously-derived small planet masses. These masses are calculated from the radial velocity analysis in Chapter 4 and, where possible, homogeneously-derived stellar parameters from Sousa et al. (2021). By comparing these new planet masses, and the planet radii from previously published transit measurements, with theoretical composition tracks we have been able to provide potential planet compositions for our sample. In addition, we split the sample based on location relative to the radius valley, investigating the planets above, below, and inside the valley. From this we draw several key conclusions.

First, all planets below the valley (both orbiting FGK and M dwarf stars) are consistent with solid compositions, i.e. without volatiles. There is some variation

seen within these sub samples in terms of the fractions of iron and silicates, which may be linked to stellar properties such as age (Weeks et al., 2025). Hopefully, future work on stellar age characterisation, particularly following the launch of PLATO in 2026 (Rauer et al., 2014), will enable greater analysis of this possible trend. For now, our homogeneous analysis demonstrates that the population of planets below the radius valley is consistent with the atmospheric-loss scenario and there is no discernible difference between the planets orbiting FGK type stars and M dwarf stars.

Secondly, all planets above the valley require the addition of volatile elements to account for their measured mass and radius. In the case of the planets orbiting M dwarf stars and FGK stars, the composition tracks for sub-Neptune-like and waterworld-like compositions are degenerate and so mass and radius measurements alone are insufficient to determine the compositions of these planets. Additionally, no single composition tracks can be used to describe the subsample.

For the planets inside the radius valley there does seem to be a population with unusual densities, possibly hinting to a water-world scenario. Though we cannot rule-out the sub-Neptune-like compositions for these planets they would be ideal targets for future characterisation studies.

Finally, we provide suggested prime targets for future atmospheric characterisation. Accounting for both TSM and location inside the radius valley, we propose that L 98-59 d and TOI-544 b are top targets for observations with e.g. JWST.

Chapter 6

A Search for warm Jupiter companions to test formation pathways

6.1 Introduction

Improvements in instrumentation have allowed for increasingly lower mass planets to be discovered and characterised, yet there is still much to learn from giant planets. Since the very first exoplanet detections of hot Jupiters ($P_{orb} < 10 \text{ days}$) were made (Mayor and Queloz, 1995) it was clear that our previous understanding of planet formation based entirely on our own solar system may not represent the full picture. Most theories suggest that giant planets cannot form interior to the snow line (the minimum distance from the star at which water could condense) and so must have migrated inwards to their observed orbit (Dawson and Johnson, 2018).

While some progress has been made in understanding the formation and migration pathways of hot Jupiter planets, it is the warm Jupiters ($10 < P_{orb} < 200$ days) which pose the biggest challenge to our understanding: their short semi-major axes challenge in situ migration models, while their eccentricity distribution does not match most migration theories (Müller and Helled, 2023).

One potential theory is perturber-coupled high-eccentricity migration (Wu and Murray, 2003), described in 1.2. In this model, planets form at long periods and

their orbital eccentricity and inclination undergoes Kozai-Lidov oscillations due to interactions with a perturber. These perturbing companions need to be massive and nearby to result in perturber-coupled high-eccentricity migration (Dong et al., 2013). Therefore, detecting or ruling out the presence of such companions for warm Jupiter planets is a direct test of this promising formation theory. Detailed simulations show that a dedicated radial velocity (RV) study of warm Jupiters is capable of detecting or ruling out the vast majority of relevant perturbers (Jackson et al., 2021). Specifically, that 20 RV observations with a precision of ~1ms⁻¹ over a 3-month baseline can detect 77% of perturbing companions – only massive companions at relatively short periods outer to the warm Jupiter are capable of exciting eccentricity oscillations (Jackson et al., 2021). With a longer baseline, the detectability further increases, as does limiting the sample to warm Jupiters with periods less than 50 days.

Despite previous RV observations of a number of warm Jupiters, such a detailed RV study has not yet been performed. Most RV studies of warm Jupiters are primarily aimed at measuring the mass of the planet, and are insufficiently precise to detect or rule out these companions. Here we present the initial results of an observing programme aimed at finding signs of potential perturbing companions to known warm Jupiter planets. We combined archival RV data from a range of instruments with new high-precision observations from the High Accuracy Radial velocity Planet Searcher (HARPS, Lovis et al., 2006) to enable us to search for long-term trends which can indicate the presence of a companion. Our full sample contains 11 known warm Jupiter systems, here we present the observations and analysis of the first 5 of these.

6.2 Target Selection

To search for appropriate targets for this observing campaign we use the NASA Exoplanet Archive. We query the archive for confirmed planets which meet our criteria of being a warm Jupiter: planet mass $> 0.1 \, M_{Jupiter}$ and orbital periods between 10 and 200 days, based on the definitions in Jackson et al. (2021). We

remove any multiplanet systems – to remove the ones which have interior planet companions. For our observations we chose to use the HARPS instrument mounted on the European Southern Observatory (ESO) 3.6m telescope at La Silla. Therefore we also make a cut on V-band magnitude of 12 to ensure all are sufficiently bright for RV follow-up and a cut on maximum declination of +20°. We then individually check the visibility of each potential target during the observing periods at La Silla, leaving 11 targets. Table 6.1 lists each target along with information about the star.

Table 6.1: The targets observed in the 109.233Q and 113.26DF observing programmes. Columns show the main ID, additional names, the right ascension and declination, the magnitude in V-band and the exposure time of observations. Stellar data all from the NASA Exoplanet Archive.

Main Identifier	Other Identifiers RA		DEC	V Magnitude	Exposure Time (S)
HD 205158		21h35m40.47s	$-59441m35.93s$ 7.84 ± 0.03	7.84 ± 0.03	009
HD 207229	HIP 107773	21h50m00.12s	-64d42m45.72s	5.62 ± 0.03	300
HD 1397		00h17m47.32s	-66d21m32.14s	7.79 ± 0.03	009
HD 154672	HIP 83983	17h10m04.97s	-56d26m59.29s	8.21 ± 0.03	006
HD 167768		18h16m53.12s	-03d00m30.89s	5.99 ± 0.023	300
HD 114082		13h09m16.11s	-60d18m30.36s	8.20 ± 0.03	006
HD 203949	HIP 105854	21h26m23.09s	-37d49m46.12s	5.64 ± 0.03	300
HD 206255		21h42m22.03s	-50d05m36.92s	7.62 ± 0.03	009
K2-287		15h32m17.84s	-22d21m30.04s	11.41 ± 0.018	2400
HD 221416		23h32m07.96s	-21d48m04.32s	8.15 ± 0.03	009
HD 13445	GJ 86	02h10m29.39s	-50d49m15.58s	6.12 ± 0.03	009

6.3 RV observations

All observations took place in observing periods 109 (April to September 2022) and 113 (April to September 2024); programme IDs 109.233Q (PI Osborne) and 113.26DF (PI Osborne), respectively. For each of the 11 targets we aimed to gain 25 individual observations spaced out over as long a baseline as possible. Due to weather and observing constraints this wasn't always possible, however we do have a minimum of 20 epochs of observations for each target when combined with archival HARPS data. Version 3.8 of the Data Reduction Software (DRS; Pepe et al., 2002) was used to reduce the HARPS spectra and extract absolute RVs by cross-correlating the spectra with a K5 numerical mask (Baranne et al., 1996).

In addition, the majority of targets have publicly available data from other instruments which we can use in combination with ours. Table 6.2 lists each of the 5 targets analysed in this work along with the number of observations from each instrument. Appendix C contains the observation data for each of these 5 targets, with the instrument used for the observations labelled. Note that in some cases instrument interventions have occurred meaning that the same instrument will be modelled separately depending on the time when observations took place. This is the case for HARPS where two major interventions have occurred and so the observations are labelled as 'HARPS1', 'HARPS2', and 'HARPS3' depending on when they took place ¹.

Table 6.2: Number of observations of each of the 5 targets analysed in this work. The first column shows observations as part of our HARPS programme, the following column shows publicly available observations which were included in our analysis. These are from the HIgh Dispersion Echelle Spectrograph, (HIDES, Izumiura, 1999), the Fiber-fed Extended Range Optical Spectrograph, (FEROS, Kaufer and Pasquini, 1998), CHIRON (Schwab et al., 2012), the Planet Finder Spectrograph (PFS, Crane et al., 2010), CORALIE (Queloz et al., 2000), and the University College London Echelle Spectrograph (UCLES Diego et al., 1990).

Target	This programme	Archival	Total
HD 167768	25 HARPS	102 HIDES ^a	127

¹See details here: https://www.eso.org/sci/facilities/lasilla/instruments/harps/news.html

Target This programme Archival Total 13 FEROS^b, 37 CHIRON^b HD 203949 23 HARPS 73 HD 206255 23 HARPS 32 PFS^c 55 26 FEROS d , 35 CHIRON d HD 207229 24 HARPS 85 HD 13445 111 HARPS^e, 54 CORALIE^f, 64 UCLES^g 5 HARPS

Table 6.2 continued from previous page

a: Teng et al. (2023), b: Jones et al. (2014), c: Feng et al. (2019), d: (Jones et al., 2015), e: ESO programmes 0101.C-0232, 097.C-0090, and 0100.C-0414, f: Queloz et al. (2000), g: Butler et al. (2001).

6.4 RV analysis and modelling

We modelled the RV data using the code pyaneti (Barragán et al., 2019, 2022), which has the option to implement Gaussian Processes (GPs) to help account for the impact of stellar activity. The implementation of GPs for this purpose is described in detail in Rajpaul et al. (2015); Aigrain and Foreman-Mackey (2023). We chose to model all of our targets both with and without GPs as a comparison, and with and without the addition of long term trends (both linear and quadratic) meaning a total of 6 different models run for each target.

For all targets we use the published orbital period and 1σ error on this as a Gaussian prior. We took the published value of time of conjunction for each target and set a wider uniform priors on this parameter as the published value \pm 10σ . We also allowed the orbits to be eccentric. We parametrised the eccentricity and argument of periastron as in Chapter 4, Eq. 4.2. For all runs, we performed Markov chain Monte Carlo (MCMC) samplings using the sampler included in pyaneti, which is based on an ensemble sampler (Foreman-Mackey et al., 2013). We sample the parameter space with 200 Markov chains. Each chain is initiated randomly with values within the prior ranges. We create posterior distributions with the last 1000 iterations of converged chains with a thin factor of 10. This generates distributions with 200000 independent points per each sampled parameter.

To determine whether or not a warm Jupiter in our sample has a possible

companion we will first perform model comparison to see whether the models with long term trends are preferred.

6.5 Results

Table 6.3 shows the Akaike information criterion (AIC) for each model of each target, as well as the amplitude of trend found for those models which include long term trend parameters.

Table 6.3: AIC for each model of each target, as well as the amplitude of trend found for those models which include long term trend parameters.

Target	GP	Trend	AIC	Fitted trend amplitude
HD 167768	No	No	-442.3	
	No	Linear	-442.4	0.0059 ^{+0.0051} _{-0.0050} m/s/days
	No	Quadratic	-448.1	$0.0000042^{+0.0000016}_{-0.0000016}$ m/s/days ²
	Yes	No	-482.2	
	Yes	Linear	-472.3	$0.0024^{+0.0049}_{-0.0048}$ m/s/days
	Yes	Quadratic	-480.9	$0.0000024^{+0.0000018}_{-0.0000019} \text{ m/s/days}^2$
HD 203949	No	No	-293.9	
	No	Linear	-296.1	-0.0057 ^{+0.0034} _{-0.0032} m/s/days
	No	Quadratic	-292.4	$0.0000017^{+0.0000009}_{-0.0000009} \text{ m/s/days}^2$
	Yes	No	-327.0	
	Yes	Linear	-324.2	$-0.0027^{+0.0073}_{-0.0066}$ m/s/days
	Yes	Quadratic	-280.9	$0.0000010^{+0.0000017}_{-0.0000018} \text{ m/s/days}^2$
HD 206255	No	No	-476.0	
	No	Linear	-468.6	-0.00058 ^{+0.00062} _{-0.00058} m/s/days
	No	Quadratic	-473.1	$-0.0000001^{+0.0000001}_{-0.0000001}$ m/s/days ²
	Yes	No	-480.1	
	Yes	Linear	-472.3	-0.00034 ^{+0.00088} _{-0.00087} m/s/days
	Yes	Quadratic	-477.1	-0.0000001 ^{+0.0000002} _{-0.0000002} m/s/days ²
HD 207229	No	No	-464.3	
	No	Linear	-499.2	$0.042^{+0.0056}_{-0.0057}$ m/s/days
	No	Quadratic	-462.2	$-0.0000046^{+0.0000132}_{-0.000013}$ m/s/days ²
	Yes	No	-473.1	
	Yes	Linear	-493.3	$0.042^{+0.0068}_{-0.0069}$ m/s/days
	Yes	Quadratic	-471.2	-0.0000033 ^{+0.0000191} _{-0.0000166} m/s/days ²

6.5. *Results* 160

Table 6.3 continued from previous page

Target	GP	Trend	AIC	Fitted trend amplitude
HD 13445	No	No	-813.0	
	No	Linear	-1394	$-0.13^{+0.0016}_{-0.0016}$ m/s/days
	No	Quadratic	-1296	$-0.0000094^{+0.0000001}_{-0.0000001}~\text{m/s/days}^2$
	Yes	No	-1629	
	Yes	Linear	-1703	-0.18 ^{+0.0} _{-0.013} m/s/days
	Yes	Quadratic	-1633	$-0.0000143^{+0.0000044}_{-0.0000023}~\text{m/s/days}^2$

6.5.1 HD 167768

HD 167768 b has a minimum mass of $\sim 0.85~M_{Jupiter}$ and orbital period of $\sim 20~$ days (Teng et al., 2023). The system is not previously known to have any planet companions or stellar binaries. For this target we find that of the 3 models with no GP added give the best AIC value when a long-term quadratic trend is added. However, of the 3 models which include a GP give the no long-term trend model as the best model. It is possible that the GP is 'absorbing' some of the long-term trend in the system and so we do not rule out the possibility of a long-term trend in this system.

In Figure 6.1 we show the results of the model including a long-term quadratic trend in this system (with no GP added). The long time baseline combined with short orbital period mean that the periodic motion of the system is difficult to see in the plot but the long-term trend in RV is visible. Note that the observations from different instruments occur mostly at different observing seasons. This means that it is possible that the trend we see is actually the result of an offset between instruments. We do fit for instrument offsets in our modelling but in the absence of observations with multiple instruments at the same time it is difficult to know for sure if we fully account for this potential impact. This is issue is relevant for almost all our targets and a challenging problem to solve. For now, we assume that modelling the instruments offsets is sufficient to reduce the impact. In Figure 6.2 we show the RV data with this long-term trend subtracted, and phase folded to the orbital period of the known planet. Here the data shows a good fit to the model.

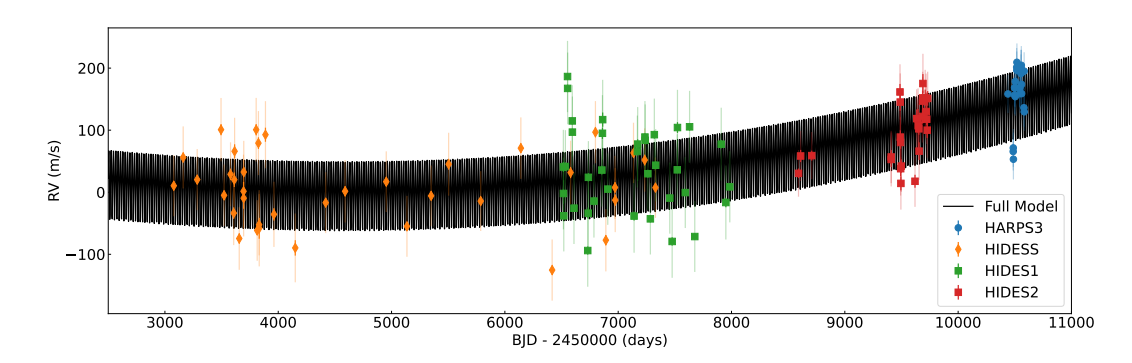


Figure 6.1: Planet model with a long-term quadratic trend included for HD 167768. HARPS data shown by blue circles, the data from the HIDES instrument are modelled as 3 separate instruments due to alterations in the instrument at different times. All as a function of time. The best-fitting model for the planet signals is shown in black. The overall quadratic trend is visible.

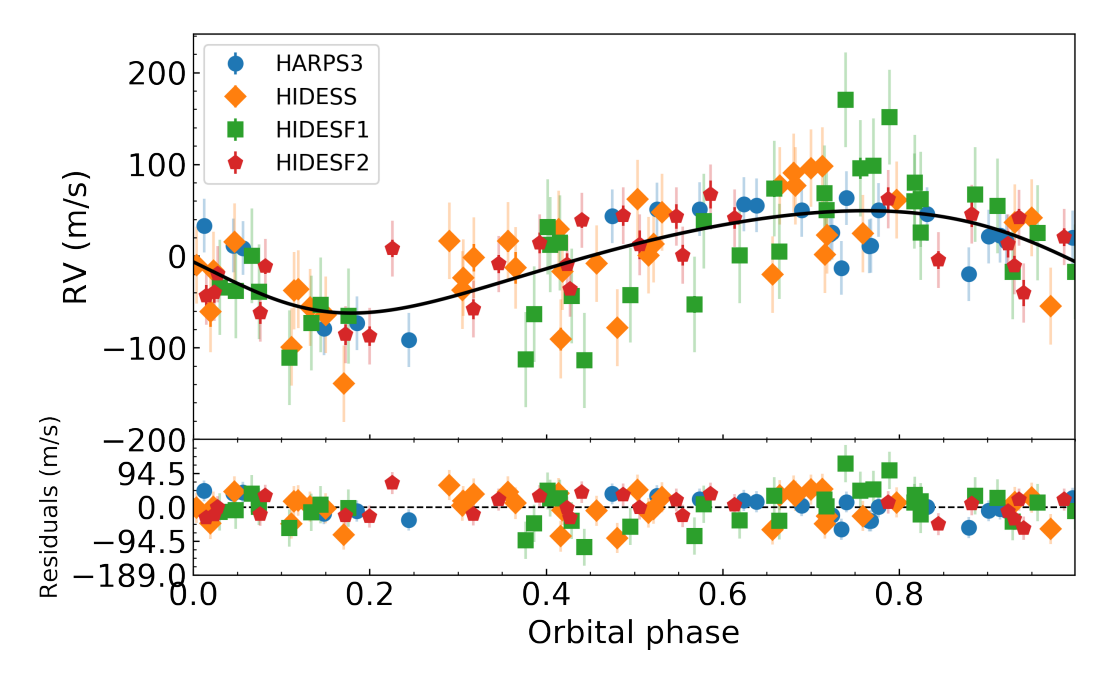


Figure 6.2: Phase-folded RV data from HARPS (blue circles), and HIDES alongside the planet model for HD 167768 b (with the effect of the quadratic trend subtracted).

6.5. *Results* 162

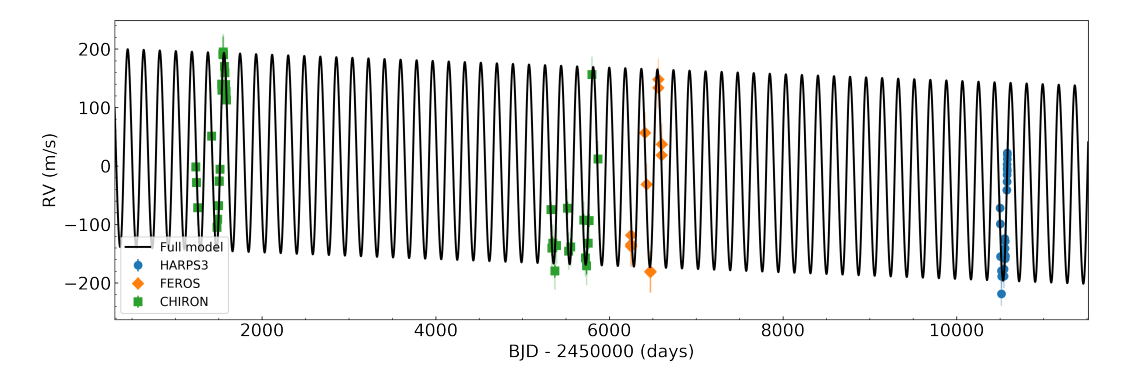


Figure 6.3: Planet model with a long-term linear trend included for HD 203949. HARPS data shown by blue circles, FEROS data in orange diamonds, and CHIRON data in green squares. All as a function of time. The best-fitting model for the planet signals is shown in black. The overall linear trend is visible.

6.5.2 HD 203949

HD 203949 b has a minimum mass of ~ 8 M_{Jupiter} and orbital period of ~ 184 days (Jones et al., 2014), putting it at the outer edge of the warm Jupiter range. The system is not known to have any planet companions or stellar binaries. For this target we find that of the 3 models with no GP added give the best AIC value when a long-term linear trend is added. However, of the 3 models which include a GP give the no long-term trend model as the best model. As with the case of HD 167768, it is possible that the GP is 'absorbing' some of the long-term trend in the system and so we do not rule out the possibility of a long-term trend in this system.

In Figure 6.3 we show the results of the model including a long-term linear trend in this system (with no GP added). The long-term linear trend in RV is visible. In Figure 6.4 we show the RV data with this long-term trend subtracted, and phase folded to the orbital period of the known planet. Here the data shows a good fit to the model.

6.5.3 HD 206255

HD 206255 b has a minimum mass of $\sim 0.11~M_{Jupiter}$ and orbital period of ~ 96 days (Feng et al., 2019), meaning that this planet is only just above the typical cut off for a giant planets of $0.1~M_{Jupiter}$. The system is not known to have any planet companions or stellar binaries. For this target we find that in both the GP and no GP cases, the preferred model is one without the addition of any long-term trend. For

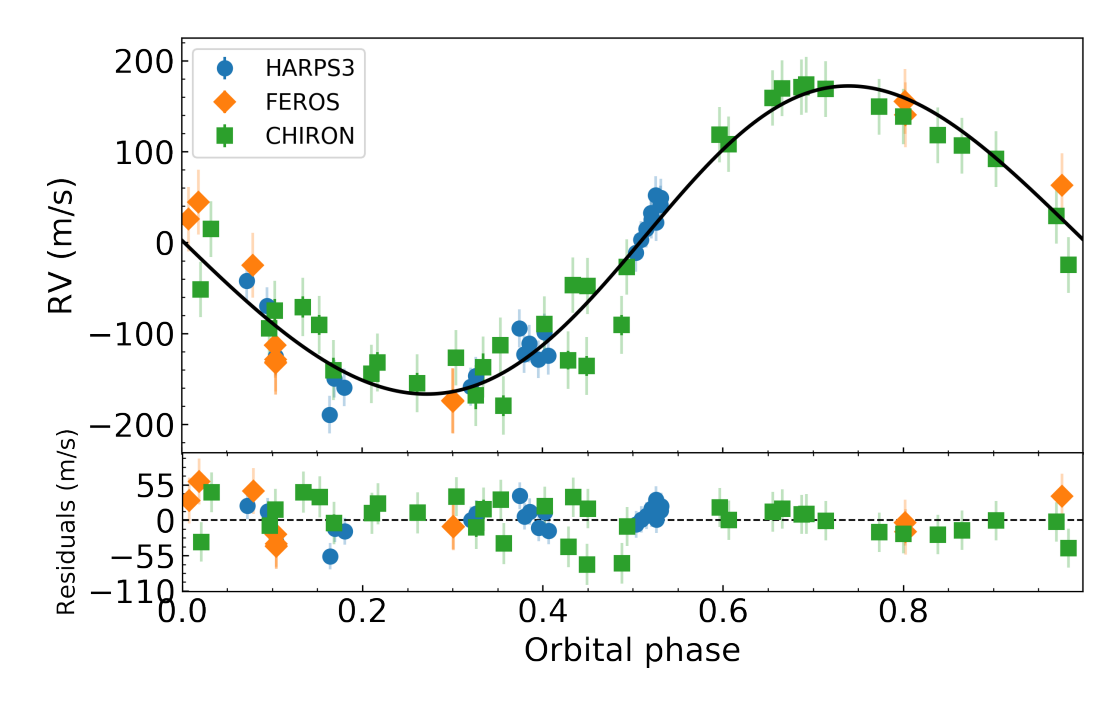


Figure 6.4: Phase-folded RV data from HARPS (blue circles), FEROS (orange diamonds), and CHIRON (green squares), alongside the planet model for HD 203949 b (with the effect of the linear trend subtracted).

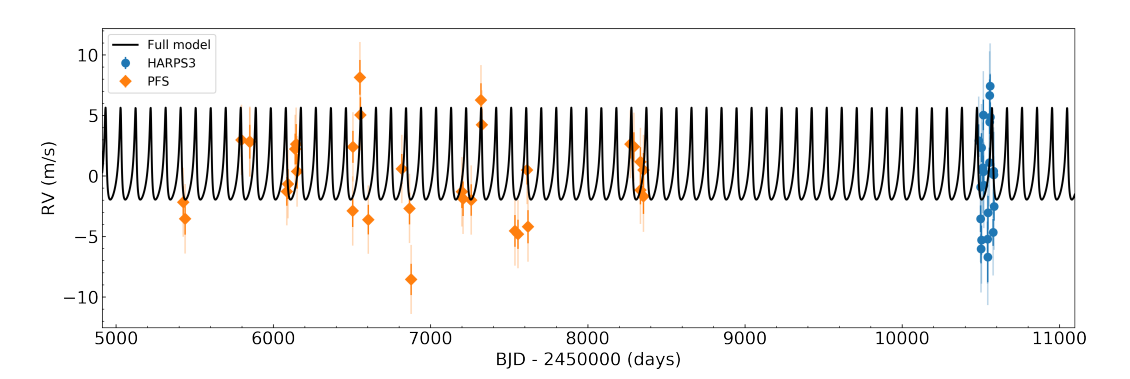


Figure 6.5: Planet model without a long-term trend included for HD 206255. HARPS data shown by blue circles, and PFS data in orange diamonds. All as a function of time. The best-fitting model for the planet signals is shown in black.

the purposes of our study we now designate this target as not having any additional planet companions. We note that it is possible that there are more planets in this system but we would need many more observations to find them as they must be lower mass and/or on longer orbital periods.

In Figure 6.5 we show the results of the model with no GP and no long-term trend. In Figure 6.6 we show the RV data phase folded to the orbital period of the known planet.

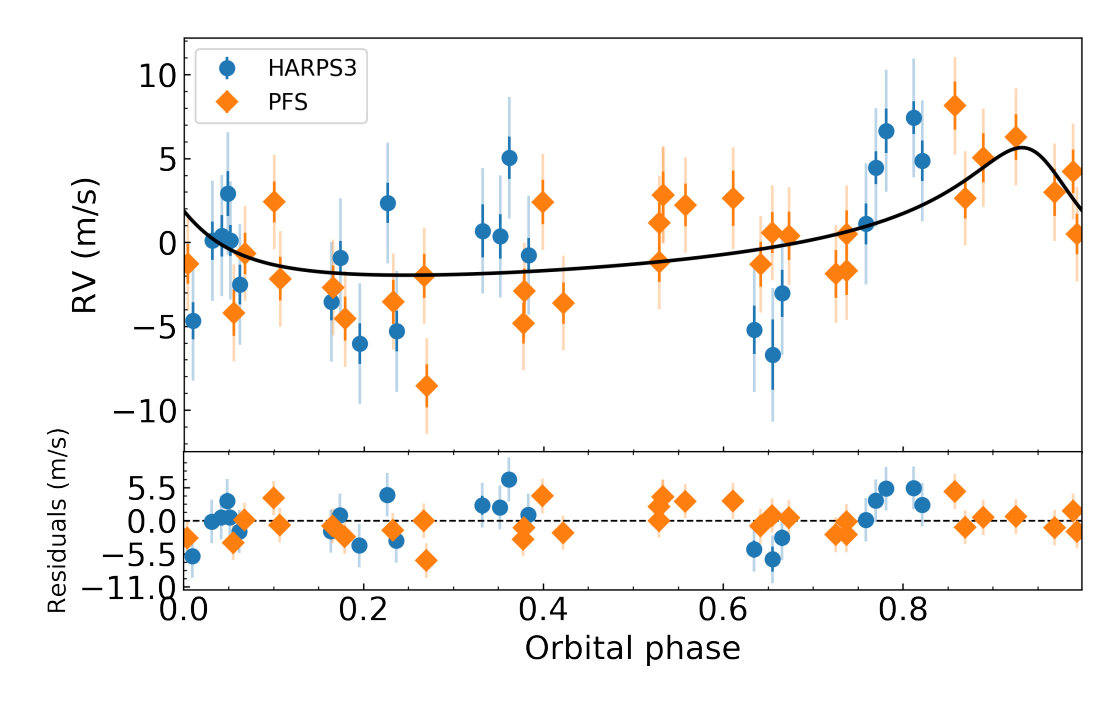


Figure 6.6: Phase-folded RV data from HARPS (blue circles), and PFS (orange diamonds), alongside the planet model for HD 206255 b.

6.5.4 HD 207229

HD 207229 b has a minimum mass of ~ 2 M_{Jupiter} and orbital period of ~ 144 days (Jones et al., 2015). The system is not known to have any planet companions or stellar binaries. For this target we find that in both the GP and no GP cases, the preferred model is one that includes a long-term linear trend. Therefore, for this target we are confident that the long term trend is real.

In Figure 6.7 we show the results of the model with no GP and a long-term linear trend. The linear trend is clearly visible in the data. In Figure 6.8 we show the RV data phase folded to the orbital period of the known planet. Here the data shows a good fit to the model.

6.5.5 HD 13445

HD 13445 b has a minimum mass of ~ 4 M_{Jupiter} and orbital period of 15 days (Butler et al., 2006), putting it just within the warm Jupiter range. This star is thought to have a binary companion which is either a brown dwarf (Els et al., 2001) or a white dwarf (Mugrauer and Neuhäuser, 2005). This means that we do expect to see evidence of a trend in our data as this companion (whatever it's nature may be) will impact the RV

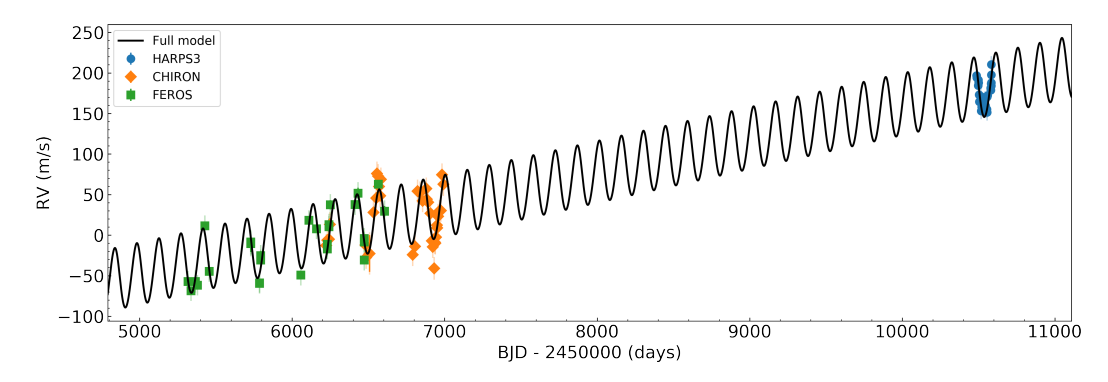


Figure 6.7: Planet model with a long-term linear trend included for HD 207229. HARPS data shown by blue circles, CHIRON data in orange diamonds, and FEROS in green squares. All as a function of time. The best-fitting model for the planet signals is shown in black. The overall linear trend is visible.

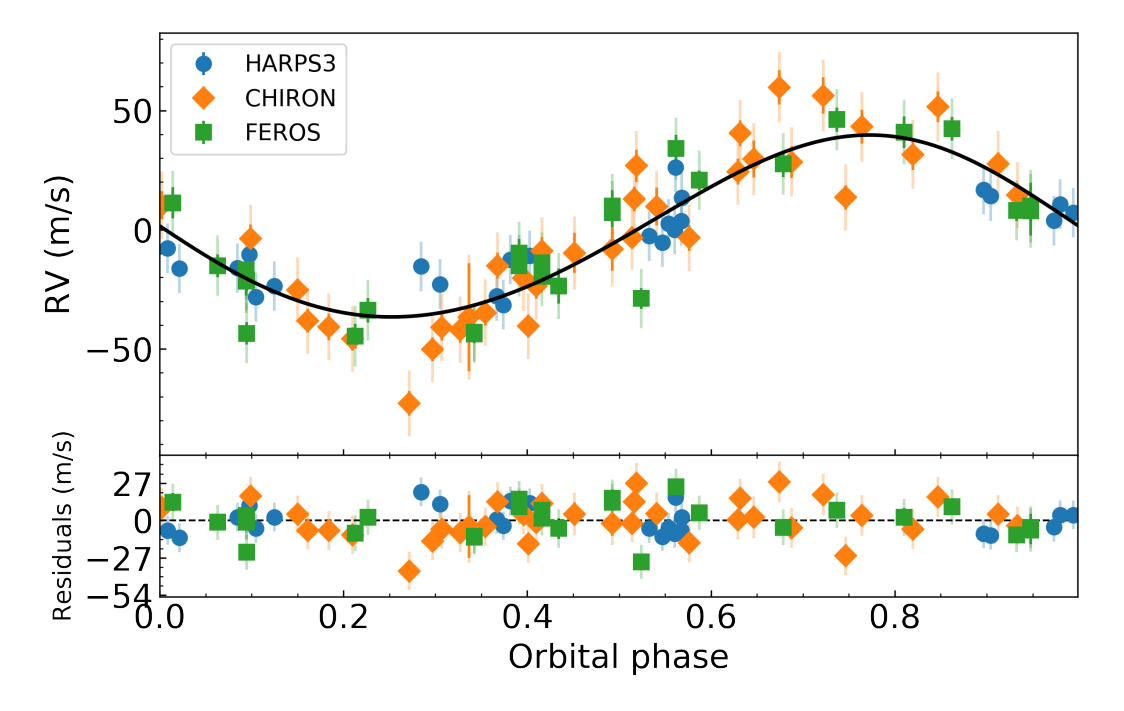


Figure 6.8: Phase-folded RV data from HARPS (blue circles), CHIRON (orange diamonds), and FEROS (green squares), alongside the planet model for HD 207229 b (with the effect of the linear trend subtracted).

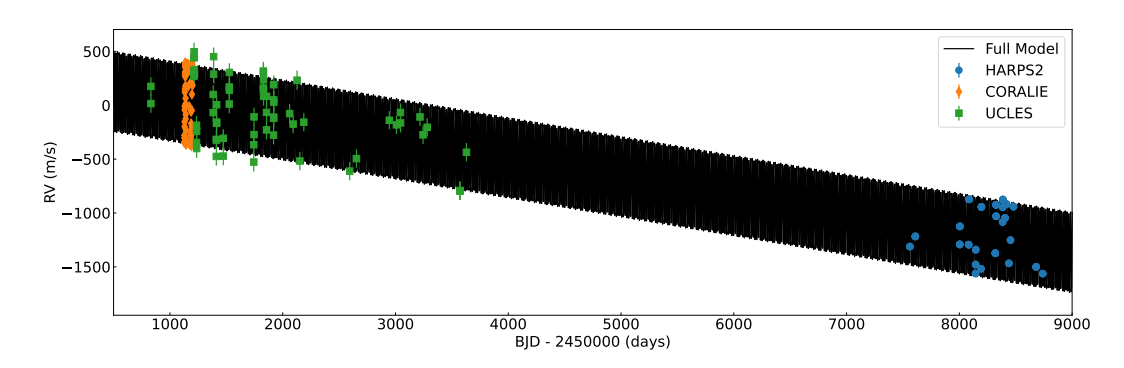


Figure 6.9: Planet model with a long-term linear trend included for HD 13445. HARPS data shown by blue circles, CORALIE as orange diamonds and UCLES as green squares. All as a function of time. The best-fitting model for the planet signals is shown in black. The short orbital period and long observing baseline mean it is difficult to see orbital motion, but the overall trend is clear.

motion of the star. The aim for this target is to then two-fold: to confirm the nature of this known companion, and to search for additional planetary mass companions.

Of all 6 models run on this target, the AIC gives the chosen model as the one with a linear long-term trend and a GP added. We note that the AIC for the no GP case with a linear trend is closely ranked in terms of AIC. In Figure 6.9 we show the results of the model including a long-term linear trend in this system (with no GP added). Here the long time baseline combined with short orbital period mean that the periodic motion of the system is difficult to see in the plot. However the long-term trend in RV is visible quite clearly. In Figure 6.10 we show the RV data with this long-term trend subtracted, and phase folded to the orbital period of the known planet. Here the data shows a very good fit to the model. For HD 13445 it seems clear that there is a long-term trend but the nature of this trend is still uncertain.

6.6 Discussion

Out of the 5 targets presented here, we find that 1 has no evidence for a long term trend (HD 206255), 2 targets have clear signs of trends (HD 207229 and HD 13445), and 2 targets have potential long term trends (HD 203949 and HD 167768).

It is important to note that there is a possibility that any trend observed is not due to the presence of a companion but due to a systematic offsets between observing

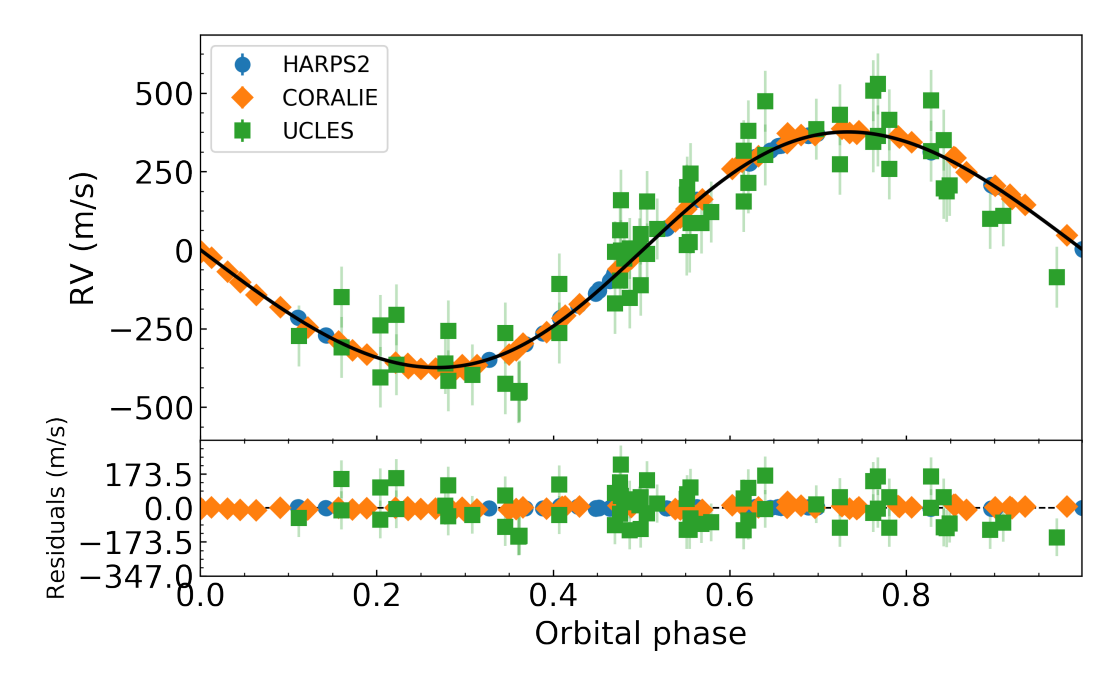


Figure 6.10: Phase-folded RV data from HARPS (blue circles), CORALIE (orange diamonds) and UCLES (green squares) alongside the planet model for HD 13445 b (with the effect of the linear trend subtracted).

instruments. For most of our targets, the observation data for each instrument or telescope does not overlap in time. This means that the shift in RVs seen over time could actually be due to the different instruments having offsets between one another. In our model we do fit for offsets between instruments but there may still be an impact unaccounted for. Very little is understood about potential offsets between RV instruments, particularly over long time baselines, and so this would be an important area of future research. An alternative approach would be to use the same instrument for observing each target, however this can be challenging over long baseline as observing programme periods typically last for, at most, a few years.

For the targets with likely/potential trends the next step is to determine the parameters of the object causing the trend. One way to do this would be to include a second Keplerian signal in the RV modelling for each system. However, in all but one of our targets the long term trend observed is linear in nature, rather than quadratic. This means that the periodic motion has yet to turn over within our baseline of observations i.e. the motion *appears* linear as we are only observing a small fraction of the actual sinusoidal motion. Because of this it would be uninformative to attempt

to model these as sinusoids. It is possible that continuing RV observations of these targets would enable a turn over in the motion to be observed, however it is not possible to predict how long it would take for this to occur. In the case of HD 13445, the baseline of observations already covers nearly 20 years with no sign of a turn over, it is possible that we would need to continue observations for many more years to see this. This highlights the importance of considering alternative observation methods for studying very long orbital periods; RVs are effective for modelling orbits only as long as your baseline of observations.

Additionally, even if we were able to fit the RV orbits of the long term trends we would not be able to reliably find the masses of these companions. This is because these potential companions are non-transiting so we find only the mass $\sin i$ and not the true mass of the companion. One method to combat both the very long orbital period and the degeneracy from unknown inclination is to combine RVs with other observing methods to find true, dynamical masses. A proven method for doing this for substellar companions is presented in Rickman et al. (2022) where they combine long-term CORALIE RVs with astrometric observations. Rickman et al. (2022) first use the absolute astrometry from the HIPPARCOS-Gaia Catalog of Accelerations (HGCS Brandt, 2018, 2021) and combine this with the relative astrometry from their direct imaging observations, and the long term RVs from CORALIE. With this method they are able to complete full orbit fitting and provide precise dynamical masses for their companions. This method has also been shown to be successful in (e.g. Brandt et al., 2019; Rickman et al., 2024) where the HGCS accelerations were combined with archival RVs to find masses for stellar companions.

To confirm the long term trends presented in this work and to determine if they are planetary in nature, and capable of perturbing the warm Jupiters into high-eccentricity migration, we will need to carry out full orbit fitting with combined astrometry and RVs. All of our targets are included in the HGCS and so the absolute astrometry is already known. By combining this with the constraints from the RVs it will hopefully enable the full orbital solutions to be found. Additionally, we may be able to complete direct imaging observations of some of these companions.

If we are able to confirm all 4 long-term trends as planetary companions to our warm Jupiters then this would be a significant contribution to occurrence rate studies of multiplanet systems. Additionally, if we find that these companions have masses and orbital periods suitable for perturbation of the warm Jupiters then it would be strong evidence for the perturber-coupled high-eccentricity migration scenario for these systems. Alternatively, if we find that none of these trends represent companions capable of perturbation then an alternative mechanism, such as disk migration, must have been responsible for these warm Jupiters. For HD 206255 we find no evidence of a long-term trend and so it is likely this warm Jupiter did not reach its current location as a result of perturber-coupled high-eccentricity migration.

Similar studies have been conducted for hot Jupiter planets – closer to their host stars – this includes Knutson et al. (2014) where they conduct a radial velocity survey to search for companions to known hot Jupiters, and Zink and Howard (2023) who use a large archival survey to argue that hot Jupiters do have companions. As well as Wu et al. (2023) who use transit-timing variations to search for companions. Some individual warm Jupiter systems have also been searched for companions, such as the K2-139 system, where observations ruled-out potential companions up to periods of 150 days (Smith and Csizmadia, 2022).

6.7 Conclusion

In this work we present new RV observations of 5 warm Jupiter systems. By combining these new observations with publicly available archival RVs from other instruments we are able to search for long term trends in the data. In HD 206255 we find no evidence of a long-term trend. In HD 203949 and HD 167768 we find tentative evidence of long term trends. And in HD 207229 and HD 13445 we find strong evidence of long term trends. To determine whether these trends are caused by planetary companions, and whether these companions themselves are capable of perturbing the warm Jupiters, we will need to complete full orbit fitting. This will require combining the RV observations with absolute astrometry and relative astrometry observations. For future surveys of this nature, we make the suggestion

that the combination of observing methods is likely necessary due to the very long orbital periods of potential companions. Additionally, a future investigation into the offsets between different RV instruments would be a significant contribution to this area of research.

Chapter 7

Conclusions

7.1 Small planet compositions

Some of the biggest open questions in astrophysics are what are the physical and chemical properties of the planets which exist? How many exoplanets are like our own Earth? And how many are of a completely different nature? More than 3000 small planets have been discovered in the past ten years, however their composition remains unknown in most cases. Finding the composition of even just one more planet in an important region of parameter space can provide important insights for understanding small planet demographics.

One big area of contention is whether the radius valley is a result of atmospheric loss processes or due to a variation in composition at formation. Both theories have been shown to be plausible explanation for this bi-modality in radii but there is still no overall consensus within the community. In Chapter 3, I presented the results of newly-characterised small planet, TOI-544 b, which is inside the radius valley, a region where very few planets are found. By modelling the RVs from an extensive observing programme, we were able to confirm the planet TOI-544 b and derive a precise mass of $M_b = 2.89 \pm 0.48$ M_{\oplus} which, combined with the planetary radius of $R_b = 2.018 \pm 0.076$ R_{\oplus} gives a bulk density of $\rho_b = 1.93^{+0.30}_{-0.25}$ g cm⁻³. TOI-544 b has an unusual density for a planet of its size, occupying a region of the mass-radius diagram where very few planets are found. The density of the planet means it most likely has either a significant fraction of ice within its composition (around

30% by mass) or is composed of an Earth-like rocky core surrounded by a layer of atmospheric H-He (around 0.5 - 1 % by mass).

Additionally, the very high TSM and ESM values mean it is an ideal candidate for atmospheric characterisation (see Section 3.6.4). In fact, TOI-544 b is one of the top small planet candidates for further investigation, see Chapter 5. By carrying out atmospheric observations with, for example, JWST, future researchers will be able to determine one of two likely scenarios for this planet:

- A water-rich composition: By fully characterising the bulk composition of the atmosphere of TOI-544b we may find that this is a water-world planet meaning that it is the result of a distinct formation pathway (separate to the rocky super-Earth and sub-Neptune regime) therefore explaining its location inside the radius valley. This would be the first detection of water-world orbiting an FGK-type star.
- Escaping He atmosphere: If observations show an escaping H-He atmosphere then TOI-544 b is undergoing atmospheric loss and transitioning from a sub-Neptune to a super-Earth planet. This would be the first detection of a planet *inside* the radius valley undergoing atmospheric loss (see, e.g. Masson et al., 2024, for other studies of He escape in planets), confirming that this observational feature really is a transition zone between the two types of small planets. This result would also imply that TOI-544 b would have migrated to its current orbital location very recently and could provide more insight into how these small planet systems evolve following their formation.

To confirm either of the possible scenarios for this planet would allow confirmation of the existence of water-world planets or provide direct evidence of the nature of the radius valley. For the astronomy community more generally, the results will impact our understanding of small planet formation and evolution. In particular, if TOI-544 b is found to be a water-world we will have the opportunity to conduct a full investigation into how these types of planets form. As well as this, we would be able to investigate how the atmosphere and solid surface of the planet interact with

each other, providing essential constraints for the planetary science and astrobiology community. Alternatively, if we detect that TOI-544 is not a water-world but is a sub-Neptune undergoing atmospheric loss, we will be able to investigate the evolution of this planet (and planetary system), impacting our understanding of planetary system dynamics.

7.2 The importance of consistency

With increasingly precise and stable spectrographs coming into operation over the past decades and the advent of communities such as the EPRV research coordination network (see Section 2.4.2), more and more small planet masses are being found. However there is still on ongoing discussion within the RV community on the 'best' way to find planet masses: from the scheduling of observations (Lam et al., 2024); the extraction of RVs from the spectra (Cretignier et al., 2023); the modelling toolkit used; and even the priors on the parameters in the model (Stevenson et al., 2025). Different teams have taken different approaches to finding the most *precise* masses possible for a given dataset. This, though, can lead to an issue of the published mass for a planet not necessarily being *accurate*. Specifically, if we go to the NASA Exoplanet Archive page for a single planet, we may see several published masses, some significantly different from one another. This then presents a dilemma to researchers studying population demographics: which published mass do I use? And does it really make a difference?

In Chapters 4 and 5 I present the results of a homogeneous analysis of small planet masses from archival HARPS observations. I refitted publicly available RV observations in a consistent way for a sample of 87 small planets. This is the first time such a large sample of archival RV observations was modelled homogeneously to find planet masses. The resulting masses, and other orbital parameters, for each of these planets is now available as a resource to the community for use in demographics studies.

In addition, I wanted to investigate how much of a difference homogeneity (or in-homogeneity) actually makes to the planet mass found. To do this, I modelled

every planet with 12 different models to investigate how model choice impacts the planet mass found. The models varied in whether they assumed the planets were on circular orbits or eccentric (and what kind of prior was put on the eccentricity parameter), whether long term trends were added to the model or not, and whether a GP was included – and if so, whether it used additional activity indicators or just the RVs themselves. It is important to note that for each planet we used an identical set of RV data each time so the differences are really only due to the modelling choices; if we changed the number of data points, baseline of observations, or choice of instrument or telescope, we may find additional changes in the planet masses derived. Despite this identical data, we found that the planet mass can vary by up to factor of 4 depending on model choices. In particular we found that the assumptions on orbital eccentricity had the largest impact on planet mass. As a result, we recommend that teams modelling large sets of RV data use an informed prior on the eccentricity distribution to ensure that realistic eccentricities are found. We also noted that when using GPs for stellar activity mitigation, the most consistent results were found using multi-dimensional GPs which incorporate additional data in the form of activity indicators. Overall, these results show how crucial a homogenous analysis is for determining planet masses. We recommend that moving forward, researchers are very clear in the modelling choices when publishing RV masses – even if they choose to make difference choices it is important to be aware of the differences this may cause in planet mass found.

Whilst this work was a significant step in the right direction, there are still a lot of difficulties with trying to conduct such a large homogeneous study. The first step in the study, to actually collate all the archival data, was a significant one. We were lucky that the HARPS archive has recently been published in Barbieri (2023) and so we were able to use their catalogue of observations rather than individually querying and downloading the data from the ESO archive portal. However, given some historical inconsistencies in the naming of objects in the archive it is likely that we missed some data and/or targets altogether. As well as this, the choice of binary mask (a stellar template of absorption lines used for cross correlation) varies

(sometimes seemingly randomly) between observations of the same target, and the version of the data reduction software pipeline also changes. All of these things will have an impact on the extracted RVs. In future it would be very beneficial to the entire community to ensure that archival data is maintained in an easily-accessible format and that the raw spectra are treated consistently in the data reduction process. Although I note that this is not a problem unique to HARPS data, in fact the ESO archive is one of the easiest to navigate and most open-access of all ground-based observatories. If other observatories were to replicate this level of access it would enable a larger study of archival RVs to be conducted on data from multiple telescopes.

This is without even considering the impact of using data from multiple instruments within the same analysis: how can we be sure that there aren't offsets between the instruments? One way to investigate this would be to compare how the sample from HARPS to that of ESPRESSO: firstly, in the general case, how does the improvement in precision of ESPRESSO change the overall population statistics? Then more specifically for targets which have both HARPS and ESPRESSO data, do we see a difference in derived planet mass (and composition) for these? This would enable a quantitative overview of the instrument performance of ESPRESSO, which will be beneficial for the design of similar instruments in future – potentially including the ArmazoNes high Dispersion Echelle Spectrograph (ANDES) Roederer et al., 2024), a second-generation instrument on the Extremely Large Telescope (ELT).

Another potential area of investigation is the inclusion of photometric data with the RV observations. Including a joint fit to data from, e.g. the Transiting Exoplanet Survey Satellite (TESS), would potentially provide additional constraints on the planet system parameters (Beard et al., 2025). In particular, the orbital eccentricity which was shown in Chapter 4 to be very challenging to constrain with RV observations alone. Additionally, increasing the sample of small planets which have precise masses (found in a consistent method) would be beneficial for the many areas of exoplanet science. An ideal goal for the RV community then would

be to create a database of homogenously characterized exoplanet masses which other groups can contribute to. This would be of huge benefit to the wider exoplanet community as a resource for population studies and to plan future observations. Most upcoming exoplanet-specific missions (e.g. Ariel and ELT-ANDES) are focused on the atmospheric characterization of small planets. To complete this characterization, it is essential to have precise mass measurements. This community database would provide accurate and precise planet masses to be used directly in these missions.

7.3 When RVs alone are insufficient

Sometimes in science the best-laid plans go awry. In Chapter 6, I present the results of an observing programme which aimed to search for companions to warm Jupiter planets which could have caused their migration. This survey was motivated by a theory paper which predicted that, if these companions exist, we should be able to detect reasonably-easily with a modest RV survey. After collecting our new, high-precision, RV data for 11 systems we were able to combine this with archival observations from other instruments. For the first 5 systems which we analysed we were able to model the RVs with a series of 6 models (some including long term trends, and some including GPs to mitigate stellar activity) to assess whether the addition of a trend was preferred over models without trends. For 4 of the systems we found that the models with trends included seem to be preferred. However, we did run into a problem.

The baseline of observations was not sufficient for the long period motion we were seeing. The presence of a long period companions is expected to show up as a sinusoidal trend in the data – or quadratic motion if we see part of the sinusoid. However, the trends in this case appeared linear, meaning we only observed a short part of the motion. This means that we cannot fully model these companions to confirm that they exist and characterise their masses and orbital periods. It also means we cannot be completely sure that this trend is due to a companion; it could be caused by instrumental offsets or stellar activity variations. Thankfully, there is a way forward with the targets: combining RVs with astrometry. By using this

combined method, it will be possible in the future to complete full orbital fits of these systems and find dynamical masses of both the warm Jupiter and any candidate companion.

This highlights several important points. Firstly, using theory to predict how well RV observations will characterise an orbit is extremely challenging. There are so many unknowns in the scheduling of observations, particularly for a telescope like the 3.6m (where HARPS is mounted) which uses a pool of visiting astronomers to plan observing runs. There are also increasingly difficult to predict weather events – including sudden snow storms which close the observatory entirely. In future, any studies in how observation scheduling and number and cadence of observations required to model RV signals will be hugely beneficial.

Secondly, it is important to consider how we can combine observation techniques to best reach our science goals. For many years, the transit and RV communities have been collaborating on the characterisation of close-in planets but now we can start to combine RVs and astrometric methods to better model further-out planets (or other stellar and substellar objects). This will be of increasing importance as we move towards future missions like the Habitable Worlds Observatory (HWO, Stark et al., 2024) which will focus primarily on trying to detect Earth-like planets on Earth-like orbits – i.e. on long orbital periods which may require the combination of RV and astrometry.

7.4 Looking to the future of exoplanet characterisation

The field of exoplanet science has grown almost exponentially over the past 3 decades, with new detections and discoveries seemingly constant. It is a topic of both scientific interest and public curiosity to search for an 'Earth 2.0' – an Earth-like planet in orbit around a Sun-like star. The advent of new observational techniques as well as improvements in engineering and data analysis have garnered a new era in our understanding of planetary systems, one not offered by studies of the solar system alone. Before 1995 our understanding of planetary systems came solely

from our own solar system and it seems that this is not a good model for what we see elsewhere. The existence of hot Jupiters, super-Earths and sub-Neptune planets came as something of a surprise, as well as the huge variations in bulk density and orbital parameters – finding planets orbiting binary star systems would not have been thought possible in the days when *Tatooine* was first dreamt up. Certainly, it is clear now that planets are ubiquitous in our galaxy – on average every star is likely to host at least one exoplanet and many are in multi-planet systems.

The focus of the exoplanet community has begun to broaden in multiple directions: some focus on dramatically increasing the number of detected planets (particularly in under-observed regions of parameter space) to enable large scale statistics and demographics studies; some focus on the composition characterisation of individual planets and planetary systems to investigate theories of planet formation and evolution; the era of JWST has welcomed huge new programmes aimed at characterising the atmospheres of exoplanets; and increasingly impressive instrumentation has enabled the direct imaging community to take images of ever small and closer-in planets. So where do we, as a community, go from here? What are the big next steps in exoplanet characterisation? And what can we look forward to in the coming decade?

Within the RV observers community the path forward will likely focus on overcoming the challenges of extreme precision RV observations. Investigations into stellar activity mitigation methods, new ways to design large surveys, and the reliability of planet masses found with differing methods will likely feature heavily in upcoming research. The continued community interest in collaboration through large networks also promises to improve the science being done in this area.

In terms of upcoming missions, the Terra Hunting Experiment (THE, Hall et al., 2018) on the newly-installed HARPS3 instrument (Thompson et al., 2016) will observe Sun-like stars every night for at least 10 years to search for Earthtwins. This kind of long-term study will be beneficial not just in the search for Earth analogues, but in understanding the long-term evolution of stellar activity on Sun-like stars, the performance of instruments over long baseline, and the impact of

observation cadence and scheduling in the characterisation of planetary signals.

In exoplanet studies more generally, one area of increasing interest is in the ages of planetary systems. By finding and characterising planets at a range of ages we are able to see a full 'life-cycle' of planets. Stellar ages are notoriously challenging to find reliably but new missions like PLATO, due to launch in 2026, will hopefully open-up this realm of temporal exoplanet studies.

Of course, the 2020s may be seen as the space-telescope age of exoplanets. JWST launched in 2021 with a major goal of charactering exoplanet atmospheres and enabling direct imaging of exoplanets and brown dwarfs. Ariel is set to launch before the end of 2029 with a specific goal to characterise the atmospheres of up to 1000 exoplanets (Tinetti et al., 2018). Outside of atmospheres, there is also the Nancy Grace Roman Telescope set for launch in 2027. Some predictions put the number of planets to be found by Roman in the tens or hundreds of thousands (Wilson et al., 2023), a massive boost for demographics studies of exoplanet populations.

But here on Earth we also have the highly-anticipated ELT first light to look forward to before the end of this decade. The world's biggest eye on the sky has many scientific goals covering most areas of astronomy, including exoplanet studies. The ELT will enable significant improvements in direct imaging, atmospheric characterisation, and studies of planet-forming disks. For the first time, it may be possible to directly image a planet in the habitable zone around another star (Bowens et al., 2021; Quanz et al., 2015).

So far, huge progress has been made in exoplanet science. In a relatively short space of time we have, as a community, gone from detecting a handful of planets, to being able to characterise the nature of planets and complete population-level statistics. With many questions still unanswered on how planets form and evolve over time, the golden era of exoplanet science looks set to last at least a little while longer. The upcoming missions, both ground- and space-based, coupled with the increasing public interest in finding another Earth-like planet give exoplanetologists much to look forward to in the coming decade and beyond.

Appendix A

Appendix material for Chapter 3

Table A.1: Absolute radial velocities and spectral activity indicators measured from the HARPS spectra with the DRS.

$\mathrm{BJD}_{\mathrm{TBD}}$	RV	$\sigma_{ m RV}$	FWHM	BIS	Contrast	T _{exp}	SNR
-2450000	$(km s^{-1})$	$(km s^{-1})$	$(km s^{-1})$	$(\mathrm{km}\mathrm{s}^{-1})$	(%)	(s)	@550nn
8578.51514	8.3561	0.0035	6.5993	0.0833	38.785	1800	35.5
8579.53150	8.3449	0.0030	6.6112	0.0635	38.743	1500	40.8
9205.63053	8.3640	0.0026	6.4372	0.0499	39.787	1800	43.0
9206.63247	8.3729	0.0018	6.4598	0.0446	39.642	1800	58.6
9207.57568	8.3665	0.0022	6.4685	0.0398	39.526	1800	48.5
9207.66046	8.3655	0.0018	6.4766	0.0470	39.529	1800	58.1
9214.71815	8.3418	0.0019	6.4361	0.0721	39.454	2400	57.0
9215.64475	8.3462	0.0017	6.4391	0.0708	39.640	2400	62.0
9217.68640	8.3486	0.0019	6.4223	0.0515	39.845	1800	55.1
9218.68225	8.3483	0.0017	6.4289	0.0527	39.817	1800	61.0
9219.65704	8.3470	0.0016	6.4178	0.0542	39.848	1800	64.6
9221.60896	8.3482	0.0017	6.4250	0.0660	39.860	1800	60.8
9222.61015	8.3382	0.0016	6.4123	0.0583	39.892	1800	64.0
9223.56895	8.3505	0.0017	6.4189	0.0525	39.943	1800	60.7
9224.66129	8.3476	0.0018	6.4348	0.0403	39.820	1800	58.5
9226.65544	8.3572	0.0019	6.4612	0.0390	39.638	1800	56.1
9227.66789	8.3493	0.0023	6.4623	0.0571	39.592	1800	46.5
9228.64010	8.3423	0.0028	6.4661	0.0659	39.562	1800	40.5
9230.63045	8.3425	0.0017	6.4496	0.0663	39.652	1800	61.3
9231.63611	8.3439	0.0025	6.4623	0.0673	39.691	1800	44.2
9232.63467	8.3486	0.0016	6.4501	0.0619	39.705	1800	64.8
9233.67770	8.3443	0.0018	6.4614	0.0573	39.736	1800	59.0
9242.62501	8.3451	0.0016	6.4328	0.0650	39.495	2400	67.8
9243.56834	8.3522	0.0017	6.4395	0.0521	39.540	1800	62.0
9244.54494	8.3552	0.0019	6.4387	0.0528	39.538	1800	55.9
9244.62785	8.3553	0.0017	6.4513	0.0519	39.516	1800	63.9
9245.60955	8.3526	0.0027	6.4711	0.0454	39.245	1800	41.7
9246.63208	8.3594	0.0020	6.4711	0.0625	39.388	1800	53.8
9247.59527	8.3478	0.0021	6.4614	0.0628	39.417	1800	50.9
9248.61373	8.3503	0.0032	6.4636	0.0792	39.252	2700	36.4

Continued on next page

Table A.1 – continued from previous page.

BJD _{TBD}	RV	$\sigma_{ m RV}$	FWHM	BIS	Contrast	T _{exp}	SNR
-2450000	$(km s^{-1})$	$(km s^{-1})$	$(km s^{-1})$	$(km s^{-1})$	(%)	(s)	@550nm
9249.62657	8.3502	0.0022	6.4572	0.0698	39.648	2100	49.9
9250.57953	8.3420	0.0027	6.4415	0.0538	39.744	1860	42.2
9251.59236	8.3586	0.0026	6.4425	0.0492	39.694	1800	43.7
9256.62889	8.3508	0.0021	6.4400	0.0542	39.724	1800	53.8
9257.58116	8.3564	0.0017	6.4369	0.0595	39.724	1800	64.6
9261.63836	8.3525	0.0031	6.4272	0.0582	39.488	1800	38.4
9262.59334	8.3549	0.0028	6.4447	0.0652	39.466	1800	41.8
9264.60899	8.3479	0.0019	6.4604	0.0502	39.435	1800	59.2
9265.56638	8.3532	0.0019	6.4639	0.0633	39.396	1800	57.8
9266.55658	8.3535	0.0022	6.4603	0.0633	39.334	1800	50.4
9267.55362	8.3425	0.0020	6.4707	0.0640	39.352	1800	55.6
9269.57020	8.3487	0.0024	6.4821	0.0541	39.077	1800	47.9
9272.57672	8.3419	0.0021	6.4640	0.0555	39.208	1800	55.5
9273.59284	8.3397	0.0034	6.4738	0.0650	38.892	1800	37.2
9274.58962	8.3417	0.0022	6.5579	0.0610	38.735	1800	52.0
9275.56486	8.3413	0.0023	6.5514	0.0540	38.866	1800	49.6
9276.59246	8.3501	0.0026	6.5467	0.0656	38.799	1800	45.8
9277.57256	8.3518	0.0024	6.5421	0.0557	38.822	1800	48.9
9284.57306	8.3475	0.0024	6.5636	0.0653	38.916	1800	48.1
9287.53172	8.3509	0.0021	6.5785	0.0534	38.835	1800	54.6
9288.53857	8.3512	0.0022	6.5767	0.0612	38.844	1800	51.3
9290.53613	8.3509	0.0024	6.5842	0.0594	38.662	1800	48.7
9291.52201	8.3473	0.0019	6.6084	0.0724	38.602	1800	58.6
9294.53123	8.3411	0.0042	6.4445	0.0656	39.689	1800	31.0
9295.53344	8.3511	0.0021	6.5290	0.0583	39.035	2100	52.6
9296.51173	8.3565	0.0018	6.5513	0.0555	38.968	1800	61.4
9297.52848	8.3549	0.0019	6.5676	0.0610	38.844	1800	60.2
9490.84461	8.3381	0.0031	6.4877	0.0455	39.551	2100	35.6
9491.81716	8.3320	0.0034	6.4756	0.0611	39.570	2100	33.3
9497.84874	8.3623	0.0024	6.5573	0.0357	39.088	2100	45.0
9501.84420	8.3521	0.0028	6.6205	0.0841	38.682	2100	41.3
9502.76982	8.3440	0.0021	6.5560	0.0797	38.988	2100	50.3
		Cor	ntinued on 1	next nage			

Continued on next page

Table A.1 – continued from previous page.

				om previou		т	CNID
BJD _{TBD}	RV	$\sigma_{\rm RV}$	FWHM	BIS	Contrast	T_{exp}	SNR
-2450000 	(km s ⁻¹)	(km s ⁻¹)	$(km s^{-1})$	$(km s^{-1})$	(%)	(s)	@550nm
9503.79777	8.3469	0.0033	6.5105	0.0817	39.296	2100	34.5
9504.76620	8.3426	0.0019	6.5036	0.0798	39.304	2100	52.6
9505.77836	8.3443	0.0020	6.4825	0.0727	39.424	2100	51.7
9506.76111	8.3513	0.0019	6.4833	0.0532	39.397	2100	51.5
9515.84526	8.3553	0.0020	6.4251	0.0505	39.651	2100	51.8
9520.79982	8.3479	0.0022	6.5727	0.0768	38.986	2100	47.8
9521.83149	8.3351	0.0027	6.5614	0.0698	39.099	1800	40.8
9528.73056	8.3472	0.0016	6.4964	0.0595	39.430	2100	61.4
9529.73908	8.3359	0.0015	6.3965	0.0611	40.033	2100	66.8
9530.74356	8.3309	0.0017	6.4914	0.0694	39.560	2100	57.6
9531.71638	8.3378	0.0016	6.3912	0.0595	40.061	2100	63.7
9543.61494	8.3315	0.0034	6.4788	0.0713	39.594	2100	33.3
9545.68951	8.3502	0.0027	6.4897	0.0612	39.545	2100	39.4
9546.72099	8.3539	0.0022	6.4835	0.0458	39.584	2100	47.8
9547.69656	8.3478	0.0016	6.5002	0.0518	39.420	2100	61.0
9548.80186	8.3506	0.0016	6.5131	0.0586	39.395	2100	62.6
9550.71766	8.3409	0.0039	6.5141	0.0607	39.461	1800	30.9
9560.66602	8.3452	0.0017	6.5592	0.0726	39.081	2100	59.0
9561.67646	8.3432	0.0029	6.5259	0.0777	39.188	2100	38.7
9563.68304	8.3437	0.0018	6.5071	0.0648	39.222	2100	57.8
9564.66694	8.3414	0.0021	6.5121	0.0508	39.162	2100	50.6
9577.74753	8.3495	0.0016	6.6025	0.0607	38.779	2100	62.9
9579.75033	8.3417	0.0019	6.5518	0.0774	39.066	2100	53.9
9581.72990	8.3445	0.0017	6.5317	0.0701	39.188	2100	59.1
9583.70601	8.3418	0.0019	6.5170	0.0536	39.369	2100	53.7
9584.59477	8.3422	0.0015	6.4280	0.0693	39.868	2100	67.8
9584.72285	8.3367	0.0017	6.5352	0.0527	39.275	2100	60.9
9585.58600	8.3453	0.0019	6.5261	0.0634	39.290	2100	54.7
9585.72824	8.3452	0.0018	6.5310	0.0657	39.298	2100	57.8
9586.72537	8.3349	0.0020	6.5147	0.0628	39.340	2100	52.4
9587.72124	8.3372	0.0020	6.5399	0.0621	39.176	1800	52.8
9588.56786	8.3388	0.0017	6.4888	0.0641	39.473	2100	59.8
			ntinued on 1	ovt nego			

Continued on next page

Table A.1 – continued from previous page.

BJD_{TBD}	RV	$\sigma_{ m RV}$	FWHM	BIS	Contrast	T _{exp}	SNR
-2450000	$(\mathrm{km}\mathrm{s}^{-1})$	$(\mathrm{km}\mathrm{s}^{-1})$	(kms^{-1})	$(\mathrm{km}\mathrm{s}^{-1})$	(%)	(s)	@550nm
9588.71681	8.3391	0.0020	6.5125	0.0550	39.362	1800	52.0
9589.71870	8.3407	0.0027	6.5096	0.0609	39.411	1808	41.6
9590.59269	8.3467	0.0025	6.5111	0.0596	39.275	2100	44.3
9591.58055	8.3421	0.0014	6.5012	0.0467	39.353	2100	71.9
9591.73732	8.3422	0.0030	6.5125	0.0577	39.195	2100	38.8
9592.59389	8.3501	0.0014	6.5164	0.0463	39.230	2100	69.1
9592.72732	8.3519	0.0021	6.5372	0.0396	38.925	2100	51.1
9606.67799	8.3471	0.0023	6.4959	0.0590	39.498	2100	46.8
9609.64815	8.3498	0.0015	6.5043	0.0614	39.329	2100	68.4
9610.65838	8.3519	0.0017	6.5121	0.0556	39.229	2100	62.5
9626.55046	8.3360	0.0019	6.5169	0.0653	39.220	2100	54.6
9627.55019	8.3415	0.0021	6.4967	0.0683	39.226	2100	49.5
9628.54583	8.3358	0.0017	6.4972	0.0659	39.329	2100	58.1
9629.56926	8.3376	0.0016	6.5055	0.0595	39.418	2100	59.9

Table A.2: Relative radial velocities and spectral activity indicators measured from the HARPS spectra with SERVAL and TERRA.

$\mathrm{BJD}_{\mathrm{TBD}}$	RV	σ_{RV}	dlW	$\sigma_{ m dlW}$	CRX	$\sigma_{ m CRX}$	S-index	$\sigma_{ ext{S-index}}$	H_{a}	NaD_1	NaD_2
-2450000	$(km s^{-1})$ $(km s$	(kms^{-1})	$(kms^{-1}Np^{-1})$	$(kms^{-1}Np^{-1})$	$(m^2 s^{-2})$	$(m^2 s^{-2})$			1	I	
8578.51514	0.0032	0.0026	34.208	3.675	8.059	23.737	1.287	0.018	0.432	1.219	0.968
8579.53150	-0.0034	0.0021	32.141	2.956	3.908	19.040	1.202	0.016	0.473	1.220	0.965
9205.63053	0.0194	0.0017	1.408	2.658	1.540	14.505	1.172	0.013	0.480	1.244	1.004
9206.63247	0.0304	0.0014	7.962	1.862	-1.187	12.339	1.126	0.010	0.501	1.239	0.988
9207.57568	0.0215	0.0019	14.317	2.154	11.742	16.447	1.150	0.012	0.477	1.241	0.978
9207.66046	0.0227	0.0013	18.549	1.854	-6.042	11.509	1.157	0.011	0.477	1.241	0.979
9214.71815	-0.0021	0.0014	16.143	1.665	7.481	11.826	1.098	0.011	0.496	1.240	0.990
9215.64475	0.0003	0.0012	7.563	1.671	3.814	10.529	1.094	0.009	0.505	1.243	0.990
9217.68640	0.0025	0.0013	-6.021	1.627	-3.028	11.113	1.119	0.011	0.497	1.243	0.996
9218.68225	0.0052	0.0016	-0.511	1.910	-16.867	13.649	1.117	0.010	0.505	1.248	0.995
9219.65704	0.0017	0.0011	-2.072	1.314	-7.816	9.266	1.178	0.010	0.511	1.245	0.994
9221.60896	0.0009	0.0021	-9.785	1.701	-11.633	18.359	1.061	0.010	0.524	1.247	0.998
9222.61015	-0.0022	0.0012	-9.937	1.485	1.309	10.524	1.078	0.009	0.513	1.255	0.997
9223.56895	0.0063	0.0016	-13.314	1.676	5.411	13.658	1.067	0.009	0.513	1.247	0.993
9224.66129	0.0076	0.0015	-8.005	1.551	8.850	12.633	1.125	0.011	0.496	1.248	1.001
9226.65544	0.0177	0.0018	15.761	1.684	-6.285	15.531	1.202	0.012	0.462	1.245	0.995
				Continued on next page	n next page						

Table A.2 – Continued from previous page.

					man bran	can Laga.					
BJD _{TBD}	RV	ORV	MID	ОДІМ	CRX	JCRX	S-index	<i>o</i> S-index	H_{α}	NaD_1	NaD_2
-2450000	$(km s^{-1})$	(kms^{-1})	$({\rm km}{\rm s}^{-1}{\rm Np}^{-1})$	$({\rm kms^{-1}Np^{-1}})$	$(m^2 s^{-2})$	$(m^2 s^{-2})$		I		1	I
9227.66789	0.0076	0.0016	16.473	2.468	13.923	14.013	1.158	0.013	0.485	1.232	0.989
9228.64010	-0.0037	0.0018	21.783	2.357	14.554	15.479	1.222	0.014	0.460	1.232	0.999
9230.63045	-0.0030	0.0015	11.931	1.842	1.778	13.448	1.205	0.010	0.463	1.237	966.0
9231.63611	-0.0016	0.0018	5.839	2.627	4.030	15.996	1.227	0.013	0.437	1.241	0.983
9232.63467	0.0054	0.0014	6.978	1.499	2.628	12.142	1.148	0.009	0.508	1.246	0.979
9233.67770	-0.0010	0.0012	6.140	1.694	-5.641	10.425	1.227	0.011	0.499	1.248	0.980
9242.62501	0.0035	0.0011	1.181	1.876	1.219	009.6	1.110	0.009	0.473	1.248	0.988
9243.56834	0.0084	0.0016	2.409	1.752	24.240	13.777	1.042	0.009	0.500	1.249	0.997
9244.54494	0.0136	0.0014	5.752	1.937	-17.013	12.236	1.167	0.010	0.463	1.242	0.988
9244.62785	0.0105	0.0013	6.332	1.635	-17.780	11.490	1.130	0.010	0.481	1.245	0.993
9245.60955	0.0101	0.0022	17.823	2.499	-8.225	19.301	1.085	0.012	0.481	1.241	0.985
9246.63208	0.0176	0.0011	17.052	2.235	14.530	9.895	1.151	0.011	0.476	1.241	986.0
9247.59527	0.0067	0.0014	11.328	2.117	4.072	12.566	1.266	0.012	0.428	1.241	0.660
9248.61373	0.0059	0.0021	16.507	3.031	2.775	18.452	1.107	0.013	0.472	1.241	1.006
9249.62657	0.0061	0.0014	5.621	2.045	-0.665	12.126	1.225	0.012	0.434	1.237	0.989
9250.57953	0.0032	0.0020	2.527	2.567	-29.112	17.551	1.175	0.014	0.486	1.248	986.0
9251.59236	0.0169	0.0018	6.505	2.333	32.852	15.445	1.122	0.013	0.483	1.242	0.987
				Continued on next page	n next page						

Table A.2 – Continued from previous page.

					1	2					
BJD _{TBD}	RV	ORV	MID	Jaiw	CRX	$\sigma_{ m CRX}$	S-index	$\sigma_{ ext{S-index}}$	H_{α}	NaD_1	NaD_2
-2450000	$(\mathrm{km}\mathrm{s}^{-1})$	(kms^{-1})	$({\rm km}{\rm s}^{-1}{\rm Np}^{-1})$	$({\rm kms^{-1}Np^{-1}})$	$(m^2 s^{-2})$	$(m^2 s^{-2})$	1	1		1	I
9256.62889	0.0116	0.0015	-1.067	1.991	20.526	13.127	1.126	0.012	0.510	1.254	0.989
9257.58116	0.0108	0.0012	-0.888	1.812	-3.710	10.565	1.080	0.010	0.514	1.249	0.997
9261.63836	0.0108	0.0020	1.164	2.689	-5.115	17.970	1.179	0.014	0.468	1.242	0.994
9262.59334	0.0086	0.0019	5.578	2.697	-1.354	16.608	1.136	0.013	0.484	1.245	0.991
9264.60899	0.0085	0.0015	12.321	1.688	23.788	13.227	1.141	0.011	0.475	1.243	0.989
9265.56638	0.0105	0.0014	16.936	1.789	13.431	12.501	1.144	0.010	0.479	1.240	966.0
9266.55658	0.0061	0.0016	21.902	2.065	-15.066	14.264	1.058	0.011	0.479	1.227	0.988
9267.55362	-0.0023	0.0017	19.330	2.024	-23.256	14.982	1.128	0.010	0.466	1.236	0.992
9269.57020	0.0036	0.0021	26.274	2.322	-13.285	18.773	1.109	0.012	0.469	1.233	966.0
9272.57672	-0.0034	0.0017	20.085	2.112	-25.857	14.051	1.023	0.011	0.481	1.245	0.988
9273.59284	-0.0062	0.0023	21.943	3.283	28.042	19.846	1.157	0.015	0.479	1.233	0.991
9274.58962	-0.0029	0.0018	14.123	1.905	4.171	15.381	1.048	0.012	0.482	1.246	0.987
9275.56486	-0.0019	0.0019	5.611	2.094	-9.529	16.267	1.098	0.012	0.509	1.248	966.0
9276.59246	0.0045	0.0020	8.596	2.098	-36.640	16.241	1.099	0.013	0.507	1.238	0.991
9277.57256	0.0101	0.0018	5.113	2.221	8.146	14.986	1.077	0.013	0.522	1.255	0.987
9284.57306	0.0012	0.0016	6.835	2.262	16.514	13.827	1.122	0.014	0.490	1.243	0.983
9287.53172	0.0040	0.0016	8.554	2.338	-11.277	13.664	1.219	0.013	0.451	1.240	0.980
				Continued on next page	n next page						

Table A.2 – Continued from previous page.

					mand man	can Lage.					
$\mathrm{BJD}_{\mathrm{TBD}}$	RV	ORV	MID	Odiw	CRX	OCRX	S-index	<i>O</i> S-index	H_{α}	NaD_1	NaD_2
-2450000	$(km s^{-1})$	(kms^{-1})	$({\rm km}{\rm s}^{-1}{\rm Np}^{-1})$	$({\rm km}{\rm s}^{-1}{\rm Np}^{-1})$	$(m^2 s^{-2})$	$(m^2 s^{-2})$		I		1	
9288.53857	0.0059	0.0019	7.805	2.324	23.854	16.430	1.196	0.014	0.465	1.237	0.980
9290.53613	0.0044	0.0021	13.845	2.513	3.938	18.318	1.137	0.013	0.471	1.236	0.982
9291.52201	-0.0008	0.0017	15.065	1.888	-11.754	14.296	1.106	0.012	0.463	1.233	0.984
9294.53123	0.0016	0.0028	5.710	3.835	-40.164	23.510	1.086	0.019	0.489	1.226	0.989
9295.53344	0.0084	0.0016	-3.504	2.134	-18.821	13.893	1.085	0.012	0.489	1.236	986.0
9296.51173	0.0115	0.0014	-5.641	1.553	-25.846	11.635	1.036	0.011	0.491	1.242	0.992
9297.52848	0.0097	0.0015	1.038	1.929	-10.220	12.634	1.080	0.012	0.497	1.241	0.999
9490.84461	-0.0025	0.0021	-10.560	2.627	31.414	17.347	1.017	0.015	0.494	1.239	1.000
9491.81716	-0.0053	0.0024	-9.314	3.564	-1.185	19.828	1.094	0.016	0.504	1.240	0.994
9497.84874	0.0223	0.0018	16.723	2.395	11.851	14.785	1.123	0.013	0.477	1.227	0.991
9501.84420	0.0081	0.0021	35.467	3.039	24.537	17.057	1.212	0.017	0.456	1.232	0.985
9502.76982	-0.0033	0.0018	25.389	2.206	-35.382	14.474	1.137	0.011	0.472	1.236	0.992
9503.79777	0.0049	0.0021	16.456	2.838	12.757	17.890	1.167	0.015	0.482	1.226	0.997
9504.76620	-0.0028	0.0015	1.115	2.058	-5.004	12.200	1.124	0.011	0.510	1.237	0.995
9505.77836	0.0011	0.0013	-8.146	2.128	-3.565	10.689	1.085	0.011	0.500	1.240	966.0
9506.76111	0.0124	0.0015	-7.221	2.400	-4.195	12.763	1.036	0.010	0.505	1.243	966.0
9515.84526	0.0169	0.0012	4.103	1.865	15.499	9.970	1.200	0.011	0.465	1.239	966.0
				Continued on next page	n next page						

Table A.2 – Continued from previous page.

NaD_2	I	0.982	0.995	1.006	1.000	1.006	1.009	0.995	0.997	0.999	1.005	1.002	1.008	0.990	0.983	0.995	1.004	0.982	
Na D ₁	I	1.224	1.233	1.248	1.246	1.247	1.253	1.242	1.233	1.249	1.254	1.247	1.250	1.232	1.239	1.243	1.245	1.231	
H_{α}	I	0.457	0.476	0.510	0.500	0.528	0.506	0.494	0.507	0.501	0.513	0.511	0.503	0.461	0.454	0.503	0.498	0.452	
∂S-index		0.013	0.014	0.010	0.009	0.010	0.009	0.017	0.013	0.012	0.010	0.010	0.019	0.010	0.015	0.010	0.011	0.012	
S-index	1	1.218	1.140	1.063	1.087	0.985	1.051	1.194	1.038	1.119	1.056	1.074	0.987	1.198	1.247	1.116	1.086	1.255	
JCRX	$(m^2 s^{-2})$	15.120	18.976	12.269	10.958	13.925	11.465	18.773	14.722	17.166	10.477	10.365	17.984	12.644	16.595	14.258	12.000	968.6	
CRX	$(m^2 s^{-2})$	12.793	-35.168	9.057	10.040	12.450	2.905	60.551	-0.357	-3.592	18.692	-3.601	44.748	-9.347	24.920	7.718	-14.148	8.929	next page
$\sigma_{ m dlW}$	$(kms^{-1}Np^{-1})$	2.408	2.396	1.675	1.503	1.694	1.857	2.915	2.894	2.055	1.600	1.677	3.639	1.898	2.569	1.830	2.391	1.986	Continued on next page
MID	$({\rm kms^{-1}Np^{-1}})$	26.476	20.910	-16.502	-15.958	-19.460	-22.994	-11.499	-20.699	-15.993	-12.159	-13.524	-15.334	15.928	10.411	-1.442	-4.118	27.385	
$\sigma_{ m RV}$	$(km s^{-1})$	0.0018	0.0023	0.0015	0.0013	0.0017	0.0014	0.0024	0.0018	0.0021	0.0013	0.0012	0.0022	0.0015	0.0020	0.0017	0.0015	0.0012	
RV	$(km s^{-1})$	0.0049	-0.0106	0.0038	-0.0047	-0.0128	-0.0043	-0.0062	0.0055	0.0115	0.0048	0.0075	0.0012	0.0024	-0.0012	-0.0004	0.0001	0.0035	
BJD _{TBD}	-2450000	9520.79982	9521.83149	9528.73056	9529.73908	9530.74356	9531.71638	9543.61494	9545.68951	9546.72099	9547.69656	9548.80186	9550.71766	9560.66602	9561.67646	9563.68304	9564.66694	9577.74753	

Table A.2 – Continued from previous page.

			Table	Table A.2 – Continued from previous page.	from previ	ious page.					
BJD _{TBD}	RV	JRV	MID	ОДШ	CRX	$\sigma_{ m CRX}$	S-index	\(\sigma\)-index	H_{α}	NaD_1	NaD_2
-2450000	$(km s^{-1})$	$(km s^{-1})$ $(km s^{-1})$	$({\rm km}{\rm s}^{-1}{\rm Np}^{-1})$	$(km s^{-1} N p^{-1})$	$(m^2 s^{-2})$	$(m^2 s^{-2})$			I	I	
9579.75033	-0.0033	0.0016	11.216	1.902	13.664	13.375	1.227	0.012	0.476	1.238	0.993
9581.72990	0.0017	0.0015	-5.253	1.439	-4.690	12.474	1.125	0.011	0.514	1.246	0.989
9583.70601	-0.0013	0.0016	-6.852	1.771	5.427	13.540	1.108	0.011	0.500	1.247	966.0
9584.59477	0.0000	0.0010	-7.261	1.347	-3.137	8.676	1.123	0.009	0.498	1.246	0.997
9584.72285	-0.0048	0.0014	-8.671	1.472	-3.113	11.580	1.119	0.010	0.503	1.245	0.993
9585.58600	0.0011	0.0018	-8.802	1.801	-27.674	14.346	1.117	0.011	0.509	1.242	966.0
9585.72824	-0.0002	0.0014	-8.467	1.504	20.429	11.416	1.060	0.011	0.519	1.247	0.991
9586.72537	-0.0066	0.0014	-9.467	2.168	-16.669	11.553	1.087	0.012	0.502	1.243	0.993
9587.72124	-0.0044	0.0019	-15.800	1.706	19.157	15.762	1.036	0.013	0.532	1.252	0.997
9588.56786	-0.0024	0.0012	-15.175	1.775	-10.650	9.543	1.043	0.009	0.526	1.251	0.995
9588.71681	-0.0035	0.0013	-18.477	1.962	-9.275	10.962	1.024	0.012	0.546	1.254	0.995
9589.71870	-0.0024	0.0020	-22.861	3.204	9.360	17.309	0.963	0.015	0.556	1.259	0.980
9590.59269	0.0045	0.0018	-16.850	2.585	-20.246	15.141	1.009	0.014	0.553	1.254	0.980
9591.58055	-0.0001	0.0012	-17.048	1.674	-10.154	688.6	1.052	0.009	0.545	1.257	0.968
9591.73732	0.0042	0.0021	-19.114	3.110	20.262	17.930	1.027	0.017	0.558	1.259	0.957
9592.59389	0.0097	0.0014	-9.301	1.424	12.005	11.847	1.055	0.009	0.540	1.255	0.971
9592.72732	0.0102	0.0017	-1.401	2.003	13.551	14.051	1.091	0.013	0.554	1.259	0.962
				Continued on next page	n next page						

Table A.2 – Continued from previous page.

					in and more	Lagad Case					
BJD _{TBD}	RV	∂RV	MID	Odiw	CRX	σ_{CRX}	S-index \(\sigma_{\text{S-index}}\)	∂S-index	H_{α}	NaDı	NaD_2
-2450000	$(km s^{-1})$	-2450000 (km s ⁻¹) (km s ⁻¹)	$(km s^{-1} N p^{-1})$	$(km s^{-1} Np^{-1})$ $(m^2 s^{-2})$	$(m^2 s^{-2})$	$(m^2 s^{-2})$	1	1	I		
66129.9096	0.0067	0.0021	-20.079	2.204	-9.169	17.897	1.074	0.013	0.013 0.514 1.250	1.250	0.994
9609.64815	0.0041	0.0011	-21.853	1.758	4.793	8.854	1.100	0.009	0.489	1.251	1.005
9610.65838	0.0077	0.0015	-19.701	2.086	1.889	12.824	1.070	0.010	0.521	1.257	0.994
9626.55046	-0.0051	0.0014	-4.369	1.641	4.147	11.515	1.048	0.011	0.515	1.248	1.001
9627.55019	-0.0022	0.0017	-1.363	2.395	31.082	13.849	1.091	0.011	0.495	1.249	0.999
9628.54583	-0.0063	0.0014	-12.073	1.657	-24.609	11.074	1.065	0.010	0.518	1.246	1.005
9629.56926	-0.0043	0.0015	-17.272	1.985	-17.906	12.741	1.092	0.010	0.512	1.253	1.002

Table A.3: Absolute radial velocities and spectral activity indicators measured from the HARPS-N spectra with the DRS.

BJD _{TBD}	RV	$\sigma_{ m RV}$	FWHM	BIS	Contrast	T _{exp}	SNR
-2450000	$(km s^{-1})$	$(\mathrm{km}\mathrm{s}^{-1})$	$(\mathrm{km}\mathrm{s}^{-1})$	$(\mathrm{km}\mathrm{s}^{-1})$	(%)	(s)	@550nm
8578.35923	8.3519	0.0019	6.5098	0.0696	39.407	2400	51.6
8579.35283	8.3376	0.0048	6.4946	0.0508	39.360	1230	25.1
8732.71766	8.3678	0.0052	6.4912	0.0487	39.276	1800	23.1
8732.74144	8.3591	0.0064	6.5139	0.0486	39.264	1800	19.8
8752.68369	8.3692	0.0017	6.4828	0.0564	39.660	1800	57.7
8752.70581	8.3665	0.0014	6.4835	0.0600	39.669	1800	67.4
8753.70744	8.3513	0.0021	6.4844	0.0657	39.616	1800	47.3
8754.71549	8.3551	0.0017	6.4857	0.0632	39.663	1800	55.7
9204.51620	8.3541	0.0023	6.4273	0.0419	39.997	1800	42.4
9204.65656	8.3560	0.0018	6.4217	0.0470	40.037	1800	52.0
9205.54599	8.3619	0.0015	6.4309	0.0386	40.037	1500	60.1
9205.63930	8.3590	0.0014	6.4366	0.0510	40.001	1500	65.9
9206.47971	8.3674	0.0018	6.4567	0.0291	39.875	1800	52.3
9206.65731	8.3705	0.0019	6.4491	0.0362	39.874	2400	51.4

Table A.4: Relative radial velocities and spectral activity indicators measured from the HARPS-N spectra with SERVAL and TERRA.

$\mathrm{BJD}_{\mathrm{TBD}}$	RV	σ_{RV}	dlW	$\sigma_{ m dlw}$	CRX	$\sigma_{ m CRX}$	S-index	$\sigma_{ ext{S-index}}$	H_{lpha}	NaD_1	$\mathrm{Na}\mathrm{D}_2$
-2450000 (km s ⁻¹) (km s ⁻¹)	$(\mathrm{km}\mathrm{s}^{-1})$	$(km s^{-1})$	$({\rm kms^{-1}Np^{-1}})$	$({\rm kms^{-1}Np^{-1}})$	$(m^2 s^{-2})$	$(m^2 s^{-2})$				I	I
8578.35923	-0.0153	0.0012	-10.331	3.298	-14.213	10.557	1.289	0.010	0.382	1.2058	0.9705
8579.35283	-0.0189	0.0023	-2.017	4.584	-4.860	20.180	1.099	0.018	0.407	1.2022	0.9588
8732.71766	0.0062	0.0025	-0.417	5.610	-35.894	20.131	1.477	0.022	0.368	1.1750	0.9311
8732.74144	-0.0029	0.0033	-6.190	5.519	-23.484	28.098	1.482	0.025	0.374	1.1705	0.9313
8752.68369	0.0004	0.0010	-24.896	2.236	1.003	8.720	1.216	0.009	0.416	1.2200	0.9864
8752.70581	0.0001	0.0009	-27.621	2.072	9.871	7.201	1.208	0.007	0.412	1.2189	0.9840
8753.70744	-0.0153	0.0012	-22.886	2.317	-4.919	10.278	1.217	0.010	0.411	1.2071	0.9789
8754.71549	-0.0119	0.0011	-31.619	2.284	-11.948	9.137	1.264	0.009	0.396	1.2214	0.9830
9204.51620	-0.0115	0.0016	-57.931	2.722	30.076	13.728	1.144	0.011	0.461	1.2207	0.9819
9204.65656	-0.0069	0.0011	-62.660	2.495	-8.303	9.456	1.153	0.009	0.451	1.2261	9966.0
9205.54599	-0.0019	0.0011	-58.627	2.216	13.321	9.308	1.159	0.007	0.434	1.2321	0.9950
9205.63930	-0.0044	0.0010	-58.836	1.951	4.622	8.335	1.167	0.007	0.442	1.2318	0.9930
9206.47971	0.0017	0.0012	-47.854	2.351	-2.439	11.255	1.144	0.008	0.451	1.2231	0.9867
9206.65731	0.0022	0.0012	-44.826	2.328	-11.085	9886	1.133	0.009	0.446	1.2166	0.9821

Table A.5: Comparison of all RV fitting models used, all results are within 1-sigma.

Toolkit	GP Kernel	Activity Indicator	Number of planets	Eccentricity	K_b [m/s]	$M_b \ [M_{\oplus}]$
RadVel	No GP	1	2	Circular	$2.77^{+0.81}_{-0.82}$	3.69+1.19
RadVel	Celerite Quasi-Periodic	1	1	Circular	2.61 ± 0.49	$3.48^{+0.73}_{0.70}$
RadVel	Celerite Quasi-Periodic		2	Circular	$2.59^{+0.49}_{-0.48}$	$3.45^{+0.73}_{0.71}$
RadVel	Celerite Quasi-Periodic	1	2	Both eccentric	$3.22^{+1.9}_{-0.69}$	$4.29^{+2.66}_{0.98}$
RadVel	Celerite Quasi-Periodic	1	3	Circular	2.60 ± 0.50	$3.46^{+0.74}_{0.72}$
RadVel HARPS only	Celerite Quasi-Periodic		2	Circular	2.83 ± 0.53	$3.77_{0.76}^{+0.79}$
RadVel	Square Exponential		2	Circular	2.70 ± 0.40	$3.59^{+0.61}_{0.59}$
RadVel	Square Exponential		2	Outer planet eccentric	$2.69^{+0.37}_{-0.36}$	3.58+0.57
RadVel	Square Exponential	1	3	Circular	2.67 + 0.39	$3.55^{+0.61}_{0.50}$
Pyaneti multi-dimensional	Quasi-Periodic	S-index	2	Circular	2.07 ± 0.39	2.75 ± 0.52
Pyaneti multi-dimensional	Quasi-Periodic	S-index	2	Both eccentric	$2.66^{+0.44}_{-0.41}$	3.28 ± 0.48
Pyaneti multi-dimensional	Quasi-Periodic	S-index	2	Outer planet eccentric	2.17 ± 0.36	2.89 ± 0.48
Pyaneti multi-dimensional	Quasi-Periodic	Contrast	2		$2.47^{+0.41}_{-0.40}$	3.13 ± 0.49
Pyaneti multi-dimensional	Quasi-Periodic	FWHM	2	Both eccentric	$2.48^{+0.38}_{-0.37}$	3.16 ± 0.47
Pyaneti multi-dimensional	Quasi-Periodic	S-index & FWHM	2	Both eccentric	$2.56^{+0.43}_{-0.39}$	$3.20^{+0.48}_{-0.47}$
Pyaneti multi-dimensional	Quasi-Periodic	S-index & Contrast	2	Both eccentric	$2.59^{+0.42}_{-0.40}$	3.22 ± 0.48
Pyaneti multi-dimensional	Quasi-Periodic	FWHM & Contrast	2	Both eccentric	$2.55 \stackrel{+0.46}{-0.43}$	$3.26^{+0.57}_{-0.55}$
Pyaneti RV only	Quasi-Periodic	1	2	Both eccentric	$2.52 \stackrel{+0.40}{-0.38}$	$3.16_{-0.47}^{+0.46}$
Pyaneti RV only	Quasi-Periodic	1	2	Outer planet eccentric	2.12 ± 0.35	$2.82^{+0.48}_{-0.47}$
Pyaneti Joint Model	Quasi-Periodic	S-index	2	Both eccentric	2.58 ± 0.38	$3.28^{+0.47}_{-0.48}$

Table A.6: Priors used for the RV fitting for each parameter. $\mathcal{U}[a,b]$ refers to uniform priors in the range a - b, $\mathcal{N}[a,b]$ refers to a Gaussian prior with mean a and width b, and $\mathcal{F}[a,b]$ is a fixed parameter at value a.

Fitted Parameter	Prior
Planet Parameters	
Orbital Period, P _b [days]	N[1.5484,0.000002]
Time of Inf. Conjunction, $T_{\text{conj,b}}$ [BJD _{TDB}]	$\mathcal{N}[2459199.0314, 0.0007]$
RV Amplitude, K_b [km s ⁻¹]	$\mathcal{U}[0.0000, 0.0500]$
$ew1_{\rm b}, \sqrt{e_{\rm b}}\sin\omega_{\rm b}$	$\mathcal{F}[0.0000, 0.0000]$
$ew2_{\rm b}, \sqrt{e_{\rm b}}\cos\omega_{\rm b}$	$\mathcal{F}[0.0000, 0.0000]$
Orbital Period, P _c [days]	$\mathcal{U}[49.0000, 52.0000]$
Time of Inf. Conjunction, $T_{\text{conj,c}}$ [BJD _{TDB}]	$\mathcal{U}[2459205.0000, 2459225.0000]$
RV Amplitude, K_c [km s ⁻¹]	$\mathcal{U}[0.0000, 0.0500]$
$ew1_{\rm c}, \sqrt{e_{\rm c}}\sin\omega_{\rm c}$	$\mathcal{U}[-1.0000, 1.0000]$
$ew2_{\rm c}$, $\sqrt{e_{\rm c}}\cos\omega_{\rm c}$	$\mathcal{U}[-1.0000, 1.0000]$
Other Parameters	
GP Hyperparameters	
$\overline{A_0}$	$\mathcal{U}[0.0, 0.05]$
A_1	$\mathcal{U}[0.0, 0.1]$
A_2	$\mathcal{U}[0.,0.25]$
A_3	≡ 0
$\lambda_{\rm e}$ [days]	U[1,500]
$\lambda_{ m p}$	U[0.1, 3.0]
Rotation Period, P _{GP} [days]	$\mathcal{U}[15.0, 25.0]$

Table A.7: Priors used for the transit fitting for each parameter. $\mathcal{U}[a,b]$ refers to uniform priors in the range a - b, $\mathcal{N}[a,b]$ refers to a Gaussian prior with mean a and width b, and $\mathcal{F}[a,b]$ is a fixed parameter at value a.

Fitted Parameter	Prior
Planet Parameters	
Orbital Period, P_b [days] Time of Mid-Transit, T_0 [BJD _{TDB}] R_b/R_{\star} Impact Parameter b	$\mathcal{U}[1.547352, 1.549352]$ $\mathcal{U}[2459199.02185, 2459199.041850]$ $\mathcal{U}[0.023699, 0.039530]$ $\mathcal{U}[0, 1]$
Other Parameters	
$M_{\star} [M_{\odot}]$ $R_{\star} [R_{\odot}]$ u_1 u_2	N[0.630,0.018] N[0.624,0.013] N[0.436,0.202] N[0.217,0.155]
Noise Model Parameters	
$ ho_{ ext{GP}}$ [days] $\sigma_{ ext{GP}}$ [ppt] $\log \sigma_{ ext{S6}}$ [ppt] $\log \sigma_{ ext{S32}}$ [ppt]	$\mathcal{N}[10.0, 5.0]$ $\mathcal{N}[1.0, 0.5]$ $\mathcal{N}[-0.614, 10]$ $\mathcal{N}[-0.684, 10]$

Appendix B

Appendix material for Chapter 4

B.1 Individual systems

We aimed in all cases to treat the data homogeneously for every target so that the same steps could be applied to everything automatically. However, in a few cases we noticed some issues with individual systems which required us to make manual changes to the input files for those. We tried to keep everything else homogeneous in our analysis, and in most cases it just involved excluding some of the RV data points. These specific cases are detailed below.

B.1.1 Removal of RV data

For the system TIC 173103335, we noticed that quite a bit of RV data was largely offset (more than 30km/s) from the rest of the RVs. If we include this data in the fit then the model struggles to find a solution, particularly in the cases including a GP where the additional GP hyperparameters allow for possible over fitting. For this reason, we removed the largely outlying data from this system (we cut out all data with RV values < 10km/s. As this is archival data it is difficult to know why in some cases there would be such a large offset; we believe it is likely due to the incorrect stellar mask being applied for the CCF data reduction in the HARPS pipeline.

For TIC 220479565, we again see that this system appears to have some largely offset RV data which makes the modelling very challenging. We choose to cut all data where the RV is negative (i.e. we cut at RV = 0 km/s). In the case of TIC 260004324 we also cut the outlying data points at the threshold of 42.5 km/s.

TIC ID T_c (-2450000) Reference 307210830 8439.40 ± 0.37 Demangeon et al. (2021) e 388804061 7264.55 ± 0.46 Cloutier et al. (2017) 101955023 c 7506.02 ± 0.34 Bonfils et al. (2018) 413248763 8314.30 ± 0.42 Luque et al. (2019) c Luque et al. (2019) 413248763 d 8326.10 ± 3.9 Otegi et al. (2021) 299799658 9087.61 ± 1.84 8798.17 ± 0.19 Osborn et al. (2021) 73228647 c d^a Queloz et al. (2009) 280304863 4445.00 ± 20

Table B.1: The T_c values added manually for targets where the NASA Exoplanet Archive does not provide these.

a: For this planet no papers provide a T_0 value and so we use the value for planet c, in the listed reference, with a wide uncertainty of ~ 2 times the orbital period.

This successfully removes the largely outlying RV data. TIC 56815340 has a large amount of in-transit RV observations, this means that many exposures are taken over the course of one observing night. Because of this, the fitting with a GP takes much longer and can be confused by the many points over one night. For this reason, we remove any data for this target where there are more than 5 observations in a single date.

B.1.2 Defining priors

For the majority of our targets, the NASA Exoplanet Archive provides details of the orbital period and time of mid-transit, T_c (or time of inferior conjunction for non-transiting companions). However, a few systems do not have T_c listed and so for these we search the published literature for these planets and manually input the values. Table B.1 gives the specific values for these priors and the reference they were taken from. For one system, TIC 280304863, there was no T_c given for planet d, so for this planet we set a wide Gaussian priors on the T_c for planet c.

B.2 Stellar IDs observation summary

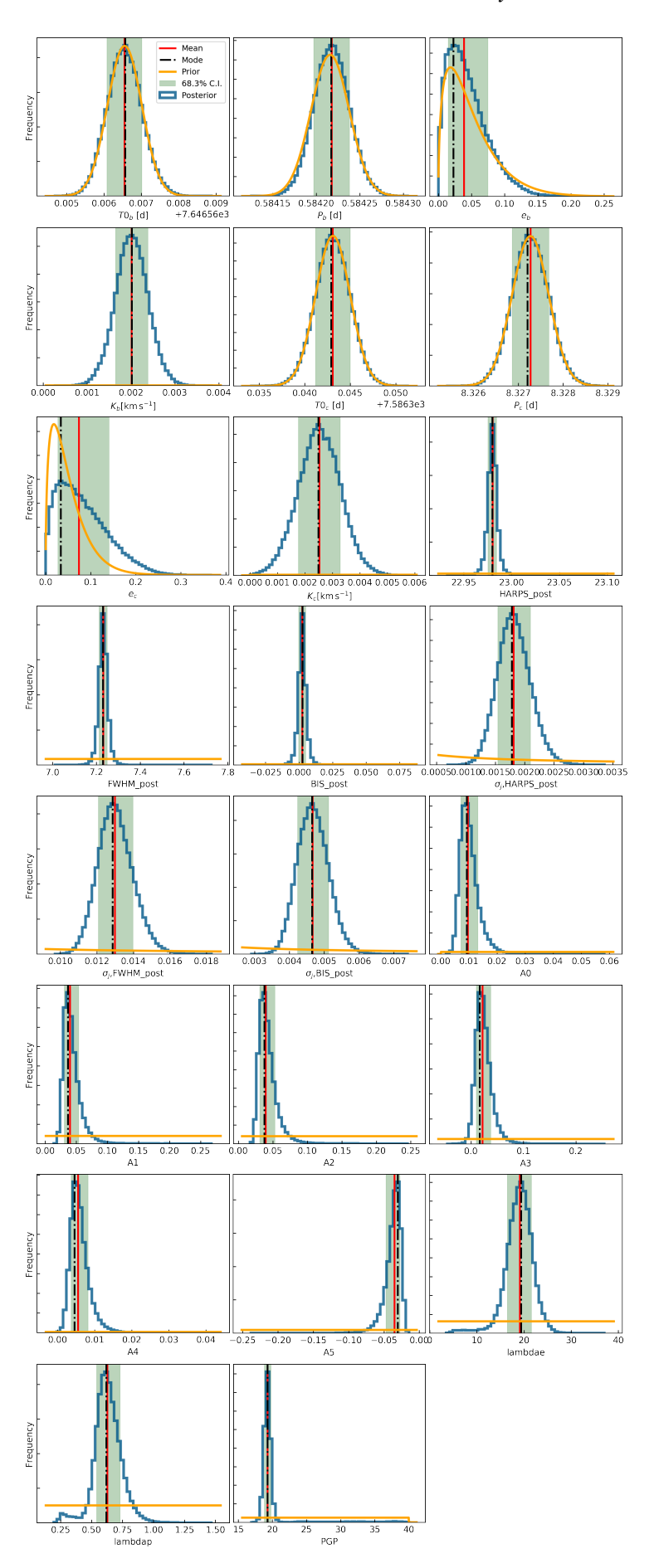


Figure B.1: Full posterior distribution of fitted parameters for TIC 98720809 with the 3D GP beta distribution model.

Table B.2: Priors used for the 3D GP model with beta distribution on eccentricity for TIC 9870809.

Planet b Priors	
T0	= g[7646.5666, 0.0005]
P	= g[0.5842 , 0.0000]
e	= b[1.5200 , 29.0000]
W	= f[0.0000 , 6.2832]
b	$= f[\ 0.0000\ ,\ 0.0000\]$
a	= f[1.5000 , 1000.0000]
rp	= f[0.0000, 0.0000]
K	= u[0.0000, 0.5000]
Planet c Priors	
T0	= g[7586.3431, 0.0019]
P	= g[8.3273, 0.0004]
e	= b[1.5200 , 29.0000]
W	= f[0.0000, 6.2832]
b	= f[0.0000, 0.0000]
a	= f[1.5000 , 1000.0000]
rp	= f[0.0000, 0.0000]
K	= u[0.0000, 0.5000]
Other Parameter Priors	
q1	= f[0.0000 , 1.0000]
q2	$= f[\ 0.0000\ ,\ 1.0000\]$
HARPS_post	= u[22.4567, 23.5048]
FWHM_post	= u[6.6676, 7.7970]
BIS_post	= u[-0.5328, 0.5252]

The priors are given as g, normal distribution, f, fixed value, b, beta distribution, or u, uniform distribution.

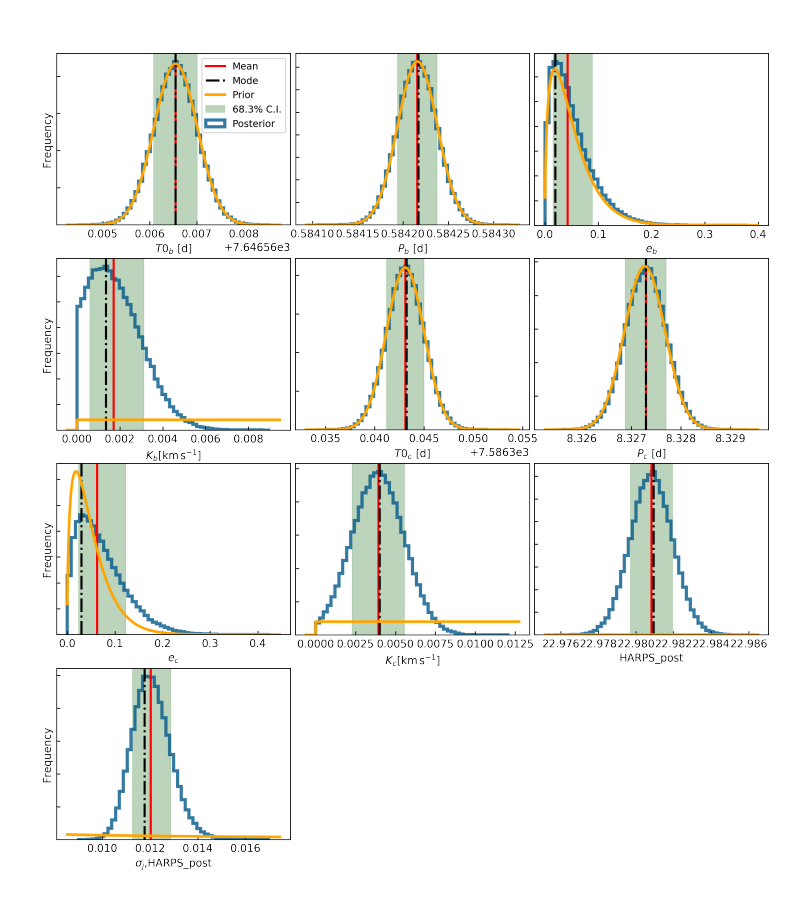


Figure B.2: Full posterior distribution of fitted parameters for TIC 98720809 with the no GP beta distribution model.

Table B.3: Fitted and derived parameters for the 2-planet system TIC 9870809.

Output Summary	
chi2	= 342.0834
dof	= 337
chi2/dof	= 1.0151
ln likelihood	= 1289.9751
BIC	= -2444.5698
AIC	= -2533.9501
Planet b	Fitted
T0	= $7646.5665430^{+0.0004680}_{-0.0004630}$ days
P	$= 0.5842176^{+0.0000206}_{-0.0000205} \text{ days}$
e	$= 0.0387125^{+0.0360824}_{-0.0238209}$
W	$= 0.0000000_{-0.0000000}^{+0.023020} \text{ deg}$
K	$= 2.0147679^{+0.3688024}_{-0.3621305} \text{ m/s}$
	Derived
Mp	= 2.2259962 ^{+0.4080294} _{-0.3999928} M_earth
Tperi	$= 7646.4276887^{+0.0067113}_{-0.0044212} \text{ days}$
Planet c	Fitted
T0	$= 7586.3430800^{+0.0019140}_{-0.0018820} \text{ days}$
P	$= 8.3272693^{+0.0004133}_{-0.0004023} \text{ days}$
e	$= 0.0734197^{+0.0672700}_{-0.0459481}$
W	$= 0.0000000_{-0.0000000}^{+0.0000000} \text{ deg}$
K	$= 2.5267559^{+0.7617282}_{-0.7660638} \text{ m/s}$
	Derived
Mp	= $6.7427960^{+2.0289184}_{-2.0410651}$ M_earth
Tperi	$= 7584.4557591^{+0.1772512}_{-0.1217128} \text{ days}$
Other parameters	0.1217120
Sys. vel. HARPS_post	= $22.9800205^{+0.0044317}_{-0.0045698}$ km/s
Sys. vel. FWHM_post	$= 7.2315287^{+0.0185481}_{-0.0189790} \text{ km/s}$
Sys. vel. BIS_post	$= 0.0023307^{+0.0026301}_{-0.0026849} \text{ km/s}$
HARPS_post jitter	$= 1.8102796^{+0.2901762}_{-0.2667877} \text{ m/s}$
FWHM_post jitter	= 12.9766515 + 1.0032974 m/s
BIS_post jitter	- 4 6680670+0.4590220 m/s
$\frac{1}{A0}$	$= 0.0096250^{+0.0035341}$
A1	$= 0.0398090^{+0.0142108}$
A2	$= 0.0396643^{+0.0133253}$
A3	$= 0.0219536^{+0.0156001}$
A4	= 0.0055228+0.0026643
A5	$= -0.0350163^{+0.0076725}$
lambdae	= 19 1165742+2.4364964
lambdap	$= 0.6272393^{+0.1037217}$
PGP	-0.0863693 - 10.2001787+0.5123584
	= 17.2701707 _{-0.4651249}

 Table B.3: The different identifiers of all stars in our sample.

NASA Host Name	TIC ID	Gaia DR2 ID	Simbad ID	#RVs
HD 136352	136916387	Gaia DR2 5902750168276592256	* nu.02 Lup	674
HR 858	178155732	Gaia DR2 5064574720469473792	HD 17926	75
GJ 143	279741379	Gaia DR2 4673947174316727040	HD 21749	58
HD 183579	320004517	Gaia DR2 6641996571978861440	HD 183579	71
HD 106315	56815340	Gaia DR2 3698307419878650240	HD 106315	92
HD 18599	207141131	Gaia DR2 4728513943538448512	HD 18599	106
HD 15337	120896927	Gaia DR2 5068777809824976256	HD 15337	118
TOI-431	31374837	Gaia DR2 2908664557091200768	CD-26 2288	174
HD 108236	260647166	Gaia DR2 6125644402384918784	HD 108236	157
HD 73583	101011575	Gaia DR2 5746824674801810816	HD 73583	98
TOI-421	94986319	Gaia DR2 2984582227215748864	BD-14 1137	103
TOI-836	440887364	Gaia DR2 6230733559097425152	CD-23 12010	53
GJ 367	34068865	Gaia DR2 5412250540681250560	CD-45 5378	398
HD 137496	346250894	Gaia DR2 6258810550587404672	HD 137496	142
HD 110113	73228647	Gaia DR2 6133384959942131968	HD 110113	115
TOI-1062	299799658	Gaia DR2 4632865331094140928	CD-78 83	87
TOI-763	178819686	Gaia DR2 6140553127216043648	CD-39 7945	77
TOI-220	150098860	Gaia DR2 5481210874877547904	CD-61 1276	99
TOI-500	134200185	Gaia DR2 5509620021956148736	CD-47 2804	198
TOI-544	50618703	Gaia DR2 3220926542276901888	HD 290498	70
K2-233	428820090	Gaia DR2 6253186686054822784	BD-19 4086	126
GJ 357	413248763	Gaia DR2 5664814198431308288	L 678-39	49
K2-229	98720809	Gaia DR2 3583630929786305280	BD-05 3504	120
TOI-125	52368076	Gaia DR2 4698692744355471616	TOI-125	124
K2-265	146364192	Gaia DR2 2597119620985658496	BD-15 6276	149
GJ 3090	262530407	Gaia DR2 4933912198893332224	CD-47 399	57
TOI-776	306996324	Gaia DR2 3460438662009633408	LP 961-53	64
EPIC 249893012	432254760	Gaia DR2 6259263137059042048	K2-314	77
TOI-1130	254113311	Gaia DR2 6715688452614516736	TOI-1130	76
L 98-59	307210830	Gaia DR2 5271055243163629056	L 98-59	158
LHS 1815	260004324	Gaia DR2 5500061456275483776	L 181-1	72
K2-3	173103335	Gaia DR2 3796690380302214272	K2-3	110
K2-138	4610830	Gaia DR2 2413596935442139520	K2-138	204
K2-32	437444661	Gaia DR2 4130539180358512768	K2-32	245
TOI-270	259377017	Gaia DR2 4781196115469953024	L 231-32	50
TOI-700	150428135	Gaia DR2 5284517766615492736	TOI-700	61
K2-18	388804061	Gaia DR2 3910747531814692736	K2-18	99
LHS 1140	92226327	Gaia DR2 2371032916186181760	G 268-38	291
TOI-269	220479565	Gaia DR2 4770828304936109056	TOI-269	65
GJ 1214	467929202	Gaia DR2 4393265392167891712	G 139-21	165
HD 3167	318707987	Gaia DR2 2554032474712538880	HD 3167	50
K2-266	374180079	Gaia DR2 3855246074629979264	K2-266	63
GJ 1132	101955023	Gaia DR2 5413438219396893568	L 320-124	122
AU Mic	441420236	Gaia DR2 6794047652729201024	HD 197481	153
HD 39091	261136679	Gaia DR2 4623036865373793408	* pi. Men	555
CoRoT-7	280304863	Gaia DR2 3107267177757848576	CoRoT-7	173
HIP 41378	366443426	Gaia DR2 600698184764497664	BD+10 1799	362
TOI-1052	317060587	Gaia DR2 6357524189130820992	HD 212729	53
HIP 94235	464646604	Gaia DR2 6632318361397624960	HD 212729 HD 178085	58
1117 94233	404040004	Gaia DK2 003231830139/024900	כפטפ/ו עם	20

Appendix C

Appendix material for Chapter 6

Table C.1: RV data used for modelling of HD 13445.

RV (km/s)	RV error (km/s)	Instrument
55.3225833	0.00084745	HARPS2
55.3226517	0.00085175	HARPS2
55.3239791	0.00088161	HARPS2
55.3238363	0.00089161	HARPS2
55.3240088	0.00086659	HARPS2
55.4161429	0.00082809	HARPS2
55.416682	0.00084003	HARPS2
55.4173693	0.00084153	HARPS2
55.4188226	0.00082837	HARPS2
55.4185331	0.00082645	HARPS2
55.4191665	0.00083164	HARPS2
55.3427803	0.00096969	HARPS2
55.3441131	0.00099844	HARPS2
55.3434294	0.00093804	HARPS2
55.3426064	0.00090485	HARPS2
55.34457	0.00090536	HARPS2
55.3450584	0.00088426	HARPS2
55.5098094	0.00088984	HARPS2
	55.3225833 55.3226517 55.3239791 55.3238363 55.3240088 55.4161429 55.416682 55.4173693 55.4185331 55.4191665 55.3427803 55.3441131 55.3434294 55.3426064 55.34457 55.3450584	55.3225833 0.00084745 55.3226517 0.00085175 55.3239791 0.00088161 55.3238363 0.00089161 55.3240088 0.00086659 55.4161429 0.00082809 55.416682 0.00084003 55.4173693 0.00084153 55.4188226 0.00082837 55.4185331 0.00082645 55.3427803 0.000983164 55.3427803 0.000996969 55.3434294 0.00093804 55.3426064 0.00090485 55.3450584 0.00088426

Table C.1 continued from previous page

Time (BJD - 2450000)	RV (km/s)	RV error (km/s)	Instrument
8004.84717	55.5095496	0.00087712	HARPS2
8004.85036	55.5104336	0.00087591	HARPS2
8004.85361	55.5116354	0.00086697	HARPS2
8004.85683	55.5121423	0.00086992	HARPS2
8004.86014	55.5120854	0.00086775	HARPS2
8082.6988	55.3416028	0.00115079	HARPS2
8082.69995	55.3419265	0.00113118	HARPS2
8082.70112	55.3407421	0.00121018	HARPS2
8082.70229	55.3408386	0.00117272	HARPS2
8082.70346	55.3412228	0.00117564	HARPS2
8082.70462	55.3428852	0.001186	HARPS2
8085.71364	55.7622139	0.00114057	HARPS2
8085.7148	55.7619434	0.00114953	HARPS2
8085.71596	55.7621238	0.00115599	HARPS2
8085.71713	55.7622321	0.00111741	HARPS2
8085.71831	55.7630665	0.00121576	HARPS2
8085.71947	55.7621036	0.00108424	HARPS2
8143.55958	55.0738253	0.00086948	HARPS2
8143.56296	55.0737342	0.00086496	HARPS2
8143.56622	55.0737069	0.00086431	HARPS2
8144.52181	5.52E+01	0.00083601	HARPS2
8144.52504	55.1574497	0.000838	HARPS2
8144.52838	55.1577459	0.00084079	HARPS2
8145.52261	55.292441	0.00095191	HARPS2
8145.52593	55.2932749	0.00100877	HARPS2
8145.52885	55.297999	0.00184435	HARPS2
8191.50075	55.1174596	0.00092932	HARPS2
8191.5042	55.1169017	0.00092006	HARPS2

Table C.1 continued from previous page

Time (BJD - 2450000)	RV (km/s)	RV error (km/s)	Instrument
8191.50725	55.1174582	0.00090421	HARPS2
8195.5006	55.6915096	0.00108682	HARPS2
8195.50368	55.6908194	0.00098296	HARPS2
8195.50672	55.691585	0.00101024	HARPS2
8195.51	55.6910946	0.00103205	HARPS2
8195.51311	55.6923572	0.00100884	HARPS2
8195.51627	55.6928121	0.00096717	HARPS2
8318.87561	55.259875	0.00109677	HARPS2
8318.87883	55.2618927	0.0012154	HARPS2
8318.8821	55.2602396	0.00116046	HARPS2
8318.88536	55.2639894	0.00116173	HARPS2
8318.88865	55.2620456	0.00106057	HARPS2
8318.89188	55.2642792	0.00102428	HARPS2
8324.85687	55.7107814	0.00095113	HARPS2
8324.86012	55.7121947	0.00094185	HARPS2
8324.86338	55.7107229	0.00099753	HARPS2
8324.86669	55.7116013	0.00093826	HARPS2
8324.86988	55.7119154	0.0009282	HARPS2
8324.87312	55.7100761	0.00091975	HARPS2
8325.93959	55.6064237	0.0008768	HARPS2
8325.94281	55.6053983	0.00085696	HARPS2
8325.94611	55.606223	0.00086978	HARPS2
8325.94933	55.6052199	0.00087037	HARPS2
8325.95261	55.6041714	0.00086192	HARPS2
8325.95583	55.6044207	0.00085921	HARPS2
8383.74292	55.5508533	0.00102655	HARPS2
8383.74452	55.55154	0.00101954	HARPS2
8383.746	55.5529357	0.00098677	HARPS2

Table C.1 continued from previous page

Time (BJD - 2450000)	RV (km/s)	RV error (km/s)	Instrument
8384.79104	55.6877119	0.00091442	HARPS2
8384.79244	55.6876814	0.00098773	HARPS2
8384.79393	55.6883991	0.00091877	HARPS2
8385.73456	55.7538481	0.00095836	HARPS2
8385.73609	55.7534942	0.00095219	HARPS2
8385.73761	55.7570011	0.00093725	HARPS2
8385.89393	55.7621346	0.00091581	HARPS2
8385.89549	55.7606588	0.00090658	HARPS2
8385.89701	55.7607158	0.00089961	HARPS2
8404.83207	55.5896942	0.00096451	HARPS2
8404.83511	55.5893813	0.00101266	HARPS2
8404.83851	55.588778	0.00101	HARPS2
8404.84169	55.5897085	0.00100174	HARPS2
8404.84509	55.5886928	0.00098696	HARPS2
8404.84833	55.5881748	0.00099074	HARPS2
8416.72029	55.717768	0.00082006	HARPS2
8416.72354	55.7179811	0.00081735	HARPS2
8416.72682	55.71825	0.00081781	HARPS2
8416.72999	55.7184584	0.00082263	HARPS2
8416.7333	55.7178303	0.00083148	HARPS2
8416.73652	55.7191463	0.00083287	HARPS2
8439.6738	55.1688392	0.0007894	HARPS2
8439.67982	55.1678031	0.00079695	HARPS2
8439.68596	55.1676987	0.00079406	HARPS2
8453.69074	55.3849514	0.00081867	HARPS2
8453.69403	55.3837104	0.00081896	HARPS2
8453.69726	55.3835115	0.00081242	HARPS2
8479.64029	55.6945486	0.00085043	HARPS2

Table C.1 continued from previous page

Time (BJD - 2450000)	RV (km/s)	RV error (km/s)	Instrument
8479.64351	55.6949819	0.0008427	HARPS2
8479.64679	55.6950044	0.00084663	HARPS2
8479.65006	55.6953752	0.00085337	HARPS2
8479.65331	55.6957142	0.00084583	HARPS2
8479.6566	55.6964837	0.00084877	HARPS2
8680.82544	55.1343842	0.00082518	HARPS2
8680.82876	55.1346065	0.00083337	HARPS2
8680.83203	55.1352914	0.00081905	HARPS2
8680.83527	55.1361803	0.00082092	HARPS2
8680.83852	55.1363502	0.00081816	HARPS2
8680.84181	55.1370898	0.00081762	HARPS2
8739.70606	55.0733453	0.00084615	HARPS2
8739.71128	55.0728509	0.00082278	HARPS2
8739.71801	55.071922	0.00083416	HARPS2
1126.75682	56.4374152	0.00243536	CORALIE
1127.7333	56.4326526	0.00173413	CORALIE
1128.69465	56.4805423	0.00337503	CORALIE
1128.81505	56.5015762	0.00445389	CORALIE
1129.51938	56.5821752	0.00481053	CORALIE
1129.83	56.6272893	0.00287704	CORALIE
1130.51646	56.7388288	0.00584513	CORALIE
1130.7533	56.771489	0.0044525	CORALIE
1131.62603	56.9021468	0.00361708	CORALIE
1131.73769	56.9298733	0.00480603	CORALIE
1132.55499	57.0575428	0.00344089	CORALIE
1132.72995	57.0799077	0.00565427	CORALIE
1133.53718	57.1393859	0.006968	CORALIE
1133.78805	57.1648523	0.00477026	CORALIE

Table C.1 continued from previous page

Time (BJD - 2450000)	RV (km/s)	RV error (km/s)	Instrument
1134.64849	57.1716503	0.00614572	CORALIE
1134.82021	57.1761233	0.00653678	CORALIE
1135.53888	57.1561053	0.00413072	CORALIE
1135.76058	57.1411669	0.00451733	CORALIE
1136.54728	57.0911118	0.00506504	CORALIE
1136.74189	57.0453254	0.00495075	CORALIE
1137.55515	56.9614819	0.00457668	CORALIE
1137.78526	56.9422116	0.00506167	CORALIE
1138.53589	56.8449078	0.00360264	CORALIE
1138.83334	56.7926446	0.00486271	CORALIE
1139.52592	56.6948491	0.0041218	CORALIE
1139.81522	56.6556173	0.0053882	CORALIE
1140.73865	56.5510449	0.00338018	CORALIE
1141.53717	56.4783384	0.00427433	CORALIE
1141.7893	56.4646206	0.00481479	CORALIE
1142.53307	56.4217594	0.00498699	CORALIE
1142.75986	56.4194333	0.0041465	CORALIE
1143.52902	56.4174269	0.00452984	CORALIE
1143.76178	56.430851	0.00514004	CORALIE
1150.54742	57.1662274	0.00455391	CORALIE
1163.54739	56.9559671	0.00260888	CORALIE
1164.54985	57.0936487	0.00295511	CORALIE
1165.56001	57.1609345	0.00301936	CORALIE
1170.54442	56.7700541	0.00263526	CORALIE
1174.5468	56.4156	0.00273501	CORALIE
1176.53372	56.5321979	0.00237803	CORALIE
1184.54784	56.9959694	0.00599952	CORALIE
1186.60055	56.7226595	0.0031465	CORALIE

Table C.1 continued from previous page

Time (BJD - 2450000)	RV (km/s)	RV error (km/s)	Instrument	
1187.5416	56.6096573	0.00368685	CORALIE	
1188.5784	56.499861	0.00327025	CORALIE	
1189.59515	56.4331771	0.00376346	CORALIE	
1190.62386	56.4023373	0.00397238	CORALIE	
1191.62924	56.45831	0.00470414	CORALIE	
1192.62631	56.582589	0.00436622	CORALIE	
1193.62162	56.7323058	0.00338998	CORALIE	
1194.59506	56.8816419	0.00395928	CORALIE	
1196.60195	57.1618914	0.00585013	CORALIE	
1197.57843	57.176625	0.00469198	CORALIE	
1198.57524	57.1525355	0.00610641	CORALIE	
1199.57651	57.0859228	0.00542893	CORALIE	
1200.57716	56.965736	0.00469846	CORALIE	
831.035	0.0835	0.004	UCLES	
1211.9651	0.3382	0.0057	UCLES	
1213.9815	0.3985	0.0053	UCLES	
1214.9298	0.3499	0.0047	UCLES	
1235.9312	-0.2772	0.0052	UCLES	
1236.9078	-0.3335	0.0055	UCLES	
1383.2736	0	0.0048	UCLES	
1387.3139	0.3566	0.004	UCLES	
1411.2467	-0.4067	0.0049	UCLES	
1413.2313	-0.2553	0.004	UCLES	
1414.3164	-0.0881	0.0042	UCLES	
1473.0974	-0.4038	0.0043	UCLES	
1525.932	0.0796	0.0049	UCLES	
1526.9613	0.2076	0.0048	UCLES	
1743.3292	-0.4594	0.0065	UCLES	

Table C.1 continued from previous page

Time (BJD - 2450000)	RV (km/s)	RV error (km/s)	Instrument
1745.2853	-0.2045	0.0053	UCLES
1828.1337	0.2282	0.0052	UCLES
1829.0121	0.2132	0.0054	UCLES
1829.988	0.1505	0.0063	UCLES
1856.1052	-0.1609	0.0062	UCLES
1918.966	-0.2093	0.0046	UCLES
1919.9811	-0.0417	0.0048	UCLES
1921.0019	0.097	0.005	UCLES
831.034977	0.2437	0.0037	UCLES
1211.96513	0.5096	0.0045	UCLES
1213.98147	0.5646	0.0048	UCLES
1214.92978	0.5113	0.0039	UCLES
1235.9312	-0.1175	0.0042	UCLES
1236.9078	-0.174	0.0045	UCLES
1383.27361	0.1681	0.0042	UCLES
1387.31387	0.5194	0.0034	UCLES
1411.24665	-0.2485	0.0042	UCLES
1413.23122	-0.0994	0.0036	UCLES
1414.31635	0.0724	0.0039	UCLES
1473.09736	-0.2389	0.0039	UCLES
1525.93201	0.2374	0.0047	UCLES
1526.9613	0.373	0.004	UCLES
1743.32924	-0.2981	0.0057	UCLES
1745.28527	-0.0399	0.0049	UCLES
1828.13369	0.3853	0.0047	UCLES
1829.01214	0.3687	0.0046	UCLES
1829.98801	0.304	0.005	UCLES
1856.10521	0.0017	0.0058	UCLES

Table C.1 continued from previous page

Time (BJD - 2450000)	RV (km/s)	RV error (km/s)	Instrument
1856.93135	0.151	0.013	UCLES
1918.96598	-0.0522	0.0043	UCLES
1919.9811	0.118	0.0038	UCLES
1921.00191	0.2589	0.0043	UCLES
2061.34131	-0.0093	0.0071	UCLES
2092.27897	-0.1067	0.004	UCLES
2127.24163	0.3007	0.0076	UCLES
2152.1424	-0.4496	0.0046	UCLES
2187.14068	-0.089	0.0035	UCLES
2594.03865	-0.5433	0.004	UCLES
2654.00484	-0.4269	0.004	UCLES
2945.13811	-0.0711	0.0038	UCLES
3008.02186	-0.1137	0.0037	UCLES
3043.98671	0.0014	0.0039	UCLES
3044.94298	-0.0958	0.0069	UCLES
3217.34251	-0.0402	0.0036	UCLES
3244.28447	-0.2063	0.005	UCLES
3281.18382	-0.1359	0.0035	UCLES
3572.28482	-0.7285	0.003	UCLES
3572.29837	-0.7257	0.0029	UCLES
3572.30818	-0.7232	0.0042	UCLES
3629.19478	-0.3682	0.0045	UCLES

Table C.2: RV data used for modelling of HD 167768.

Time (BJD - 2450000)	RV (km/s)	RV error (km/s)	Instrument
10436.8341	1.66600396	0.00133077	HARPS3
10439.8337	1.63207819	0.00133788	HARPS3
10485.8214	1.5393255	0.001246	HARPS3

Table C.2 continued from previous page

Time (BJD - 2450000)	RV (km/s)	RV error (km/s)	Instrument
10486.5882	1.54511395	0.00121973	HARPS3
10487.81	1.52687295	0.00310209	HARPS3
10497.6683	1.64231901	0.00107934	HARPS3
10498.6242	1.63011865	0.00113402	HARPS3
10501.6496	1.64134276	0.00130781	HARPS3
10503.6711	1.65211796	0.0013455	HARPS3
10504.5762	1.62779239	0.00148011	HARPS3
10516.607	1.67502805	0.00170519	HARPS3
10517.6573	1.6700008	0.00122593	HARPS3
10518.7028	1.68306778	0.00112003	HARPS3
10542.6906	1.64229138	0.00170712	HARPS3
10544.6575	1.64132253	0.0021079	HARPS3
10545.6585	1.63248762	0.00162783	HARPS3
10554.5309	1.66499835	0.00144616	HARPS3
10555.5785	1.67249261	0.00118742	HARPS3
10556.5786	1.67280024	0.00124458	HARPS3
10557.6132	1.6782616	0.00166836	HARPS3
10559.677	1.64737068	0.00127593	HARPS3
10560.5451	1.63263263	0.00159743	HARPS3
10580.5551	1.60982804	0.00122713	HARPS3
10582.5541	1.66878877	0.00116307	HARPS3
10583.5347	1.60328061	0.0012815	HARPS3
3078.326	0.00238865	0.00739035	HIDESS
3161.264	0.04799941	0.00803718	HIDESS
3284.994	0.01223185	0.00742293	HIDESS
3495.224	0.09272069	0.00892885	HIDESS
3522.151	-0.0130297	0.00770633	HIDESS
3579.063	0.02075172	0.00933821	HIDESS

Table C.2 continued from previous page

Time (BJD - 2450000)	RV (km/s)	RV error (km/s)	Instrument
3607.06	-0.0416886	0.00932924	HIDESS
3612.062	0.01208708	0.01167686	HIDESS
3615.097	0.05791492	0.01125325	HIDESS
3655.929	-0.0826384	0.00836454	HIDESS
3693.883	-0.0065132	0.01511216	HIDESS
3694.863	-0.0176187	0.01707949	HIDESS
3695.868	0.0244948	0.00821211	HIDESS
3805.316	9.26E-02	0.00909948	HIDESS
3814.345	-0.0697427	0.0070222	HIDESS
3825.341	0.07106694	0.00936216	HIDESS
3831.318	-0.0604309	0.00750563	HIDESS
3832.302	-0.0661499	0.01686918	HIDESS
3887.261	0.08459462	0.01133804	HIDESS
3962.126	-0.0437094	0.01008534	HIDESS
4150.328	-0.0977827	0.01239667	HIDESS
4418.874	-0.024903	0.00722859	HIDESS
4590.265	-0.0065077	0.00833602	HIDESS
4953.26	0.00889796	0.00709503	HIDESS
5135.894	-0.0629962	0.00726386	HIDESS
5349.149	-0.0138975	0.00710164	HIDESS
5503.91	0.03706792	0.00859323	HIDESS
5787.019	-0.0223379	0.00648092	HIDESS
6141.054	0.06295572	0.00765267	HIDESS
6417.277	-0.1334789	0.00742682	HIDESS
6516.141	0.00593974	0.0078542	HIDESF1
6517.018	-0.0367521	0.00612168	HIDESF1
6520.013	-0.0727273	0.00569878	HIDESF1
6534.059	0.00665769	0.00676336	HIDESF1

Table C.2 continued from previous page

Time (BJD - 2450000)	RV (km/s)	RV error (km/s)	Instrument
6552.958	0.15168802	0.00571689	HIDESF1
6553.987	0.13257588	0.00603042	HIDESF1
6579.965	0.02366234	0.00911319	HIDESS
6594.914	0.08015416	0.00585273	HIDESF1
6595.886	0.06210602	0.00561771	HIDESF1
6609.887	-0.0604138	0.0060223	HIDESF1
6731.364	-0.1286931	0.00655789	HIDESF1
6735.311	-0.0684915	0.00918571	HIDESF1
6737.301	-0.0107217	0.00654917	HIDESF1
6786.162	-0.0490031	0.00694556	HIDESF1
6799.271	0.08869239	0.00809602	HIDESS
6856.089	0.00097405	0.00714308	HIDESF1
6861.109	0.06024817	0.00919232	HIDESF1
6863.128	0.08221951	0.01150254	HIDESF1
6891.118	-0.0853255	0.00827863	HIDESS
6908.003	-0.0297445	0.00578209	HIDESF1
6971.907	-0.0003795	0.00873984	HIDESS
6973.894	-0.0207945	0.0093263	HIDESS
7135.251	0.05522746	0.0069145	HIDESS
7140.312	-0.0731329	0.00722716	HIDESF1
7169.28	0.03086178	0.00615052	HIDESF1
7172.161	0.04280554	0.00769619	HIDESF1
7234.128	0.04380308	0.00886011	HIDESS
7236.175	0.05416906	0.00621684	HIDESF1
7238.118	0.04893675	0.00607839	HIDESF1
7261.973	-0.0049183	0.00639722	HIDESF1
7284.021	-0.0776151	0.00573931	HIDESF1
7318.941	0.05801655	0.00635791	HIDESF1

Table C.2 continued from previous page

Time (BJD - 2450000)	RV (km/s)	RV error (km/s)	Instrument
7328.894	-0.000674	0.00690781	HIDESS
7330.928	0.00874168	0.00654568	HIDESF1
7455.359	-0.0441493	0.00568307	HIDESF1
7476.305	-0.1140414	0.00674576	HIDESF1
7521.257	0.00136131	0.00556675	HIDESF1
7523.24	0.06950894	0.00864776	HIDESF1
7592.079	-0.0353052	0.00546115	HIDESF1
7630.038	0.07066448	0.00616718	HIDESF1
7675.956	-0.1061633	0.00542286	HIDESF1
7909.197	0.04270276	0.00688529	HIDESF1
7950.192	-0.0513115	0.00764724	HIDESF1
7985.06	-0.0260266	0.00565122	HIDESF1
8591.332	-0.0679007	0.00774586	HIDESF2
8610.317	-0.0399666	0.00987604	HIDESF2
8708.129	-0.0393633	0.00801921	HIDESF2
9409.014	-0.0455348	0.01213669	HIDESF2
9409.198	-0.0415501	0.01118333	HIDESF2
9486.942	0.06320276	0.01292537	HIDESF2
9488.898	0.04690734	0.01404772	HIDESF2
9489.897	-0.0095203	0.01091608	HIDESF2
9491.901	-0.0182182	0.01015576	HIDESF2
9492.894	-0.0604312	0.01198091	HIDESF2
9494.897	-0.0841115	0.01123637	HIDESF2
9497.889	-0.0561948	0.01084016	HIDESF2
9619.385	-0.0806837	0.01046566	HIDESF2
9634.336	0.02029098	0.01469762	HIDESF2
9646.358	0.02010495	0.01587215	HIDESF2
9647.367	0.00881316	0.01148427	HIDESF2

Table C.2 continued from previous page

Time (BJD - 2450000)	RV (km/s)	RV error (km/s)	Instrument
9653.361	0.00380313	0.00955485	HIDESF2
9655.352	-0.0321272	0.01422419	HIDESF2
9685.332	0.02381072	0.01116777	HIDESF2
9686.321	0.04854569	0.00844587	HIDESF2
9687.284	0.05361224	0.01113129	HIDESF2
9689.336	0.0768139	0.01523014	HIDESF2
9709.19	0.05365822	0.01335388	HIDESF2
9717.208	0.05265796	0.00961014	HIDESF2
9718.265	0.03161999	0.00970302	HIDESF2
9723.198	0.01934796	0.00957303	HIDESF2
9727.28	0.00166451	0.01272825	HIDESF2
9731.209	0.0528045	0.01180418	HIDESF2

Table C.3: RV data used for modelling of HD 203949.

Time (BJD - 2450000)	RV (km/s)	RV error (km/s)	Instrument
10498.7111	-83.652239	0.00082688	HARPS3
10502.868	-83.67973	0.00099748	HARPS3
10504.6922	-83.73548	0.00085756	HARPS3
10515.6885	-83.799371	0.00089592	HARPS3
10516.6677	-83.75979	0.0008921	HARPS3
10518.7534	-83.769479	0.00081505	HARPS3
10544.6655	-83.768776	0.00120955	HARPS3
10545.6854	-83.756846	0.00093074	HARPS3
10554.6065	-83.70464	0.00087331	HARPS3
10555.6217	-83.733052	0.00080839	HARPS3
10556.7033	-83.721364	0.00088547	HARPS3
10558.5295	-83.738872	0.00081858	HARPS3
10559.7553	-83.709152	0.00081323	HARPS3

Table C.3 continued from previous page

Time (BJD - 2450000)	RV (km/s)	RV error (km/s)	Instrument
10560.569	-83.734759	0.00089951	HARPS3
10578.5621	-83.621738	0.00086052	HARPS3
10579.6123	-83.607549	0.00083296	HARPS3
10580.6329	-83.595412	0.00083117	HARPS3
10581.6135	-83.578005	0.00085571	HARPS3
10581.7333	-83.585218	0.00086814	HARPS3
10582.5626	-83.558263	0.00079204	HARPS3
10582.6893	-83.588182	0.00083979	HARPS3
10583.5432	-83.568683	0.00087442	HARPS3
10583.6736	-83.561081	0.00086027	HARPS3
6251.54	-0.0641	0.005	FEROS
6251.597	-0.0824	0.0017	FEROS
6251.6	-0.0796	0.0019	FEROS
6251.602	-0.0834	0.0016	FEROS
6412.805	0.111	0.0046	FEROS
6431.821	0.0229	0.0067	FEROS
6472.822	-0.1261	0.0066	FEROS
6472.853	-0.127	0.0072	FEROS
6472.89	-0.1261	0.0068	FEROS
6565.558	0.2025	0.0057	FEROS
6565.615	0.1878	0.0054	FEROS
6603.591	0.0728	0.0052	FEROS
6605.623	0.0916	0.0057	FEROS
5326.9	-0.0681	0.0126	CHIRON
5338.851	-0.1338	0.0137	CHIRON
5347.865	-0.1254	0.0113	CHIRON
5373.746	-0.173	0.0115	CHIRON
5390.762	-0.1295	0.0111	CHIRON

Table C.3 continued from previous page

Time (BJD - 2450000)	RV (km/s)	RV error (km/s)	Instrument
5517.551	-0.0654	0.0116	CHIRON
5531.553	-0.139	0.0112	CHIRON
5554.519	-0.1317	0.0151	CHIRON
5705.838	-0.086	0.011	CHIRON
5725.866	-0.1504	0.0112	CHIRON
5737.903	-0.1639	0.0149	CHIRON
5756.807	-0.1252	0.0101	CHIRON
5767.798	-0.0866	0.0111	CHIRON
5798.755	0.163	0.0064	CHIRON
5868.494	0.0185	0.0066	CHIRON
1236.531	0.0051	0.0059	CHIRON
1243.537	-0.0218	0.0057	CHIRON
1257.551	-0.0648	0.0051	CHIRON
1418.928	0.0578	0.0048	CHIRON
1480.818	-0.0984	0.0054	CHIRON
1489.911	-0.0844	0.0056	CHIRON
1498.898	-0.0613	0.0056	CHIRON
1504.699	-0.0188	0.0053	CHIRON
1507.754	-0.0196	0.007	CHIRON
1515.805	0.0012	0.0054	CHIRON
1534.849	0.1466	0.0059	CHIRON
1536.687	0.1362	0.0057	CHIRON
1547.655	0.1977	0.0058	CHIRON
1551.601	0.199	0.0051	CHIRON
1552.541	0.2016	0.0071	CHIRON
1556.527	0.1968	0.0059	CHIRON
1567.496	0.1772	0.0069	CHIRON
1572.499	0.1664	0.0059	CHIRON

Table C.3 continued from previous page

Time (BJD - 2450000)	RV (km/s)	RV error (km/s)	Instrument
1579.517	0.1459	0.0066	CHIRON
1584.53	0.1343	0.0063	CHIRON
1591.523	0.1196	0.0071	CHIRON

Table C.4: RV data used for modelling of HD 206255.

Time (BJD - 2450000)	RV (km/s)	RV error (km/s)	Instrument
10486.7201	-3.6533846	0.00134467	HARPS3
10497.7319	-3.6598375	0.00109397	HARPS3
10498.7181	-3.6572147	0.00100087	HARPS3
10500.7725	-3.6623296	0.00119982	HARPS3
10503.7523	-3.6539521	0.00119385	HARPS3
10504.7067	-3.661596	0.00120742	HARPS3
10513.8543	-3.6556139	0.00157699	HARPS3
10515.7094	-3.6559376	0.00131948	HARPS3
10516.6739	-3.6512554	0.00125841	HARPS3
10518.7465	-3.6570612	0.00102041	HARPS3
10542.6988	-3.6615181	0.00144325	HARPS3
10544.6797	-3.6629931	0.00208971	HARPS3
10545.6775	-3.6593362	0.00139201	HARPS3
10554.6202	-3.6551907	0.00122341	HARPS3
10555.6357	-3.6518402	0.00097362	HARPS3
10556.7273	-3.6496496	0.00132516	HARPS3
10559.6863	-3.6488753	0.00097672	HARPS3
10560.5749	-3.6514253	0.00120474	HARPS3
10578.5771	-3.6609612	0.0011071	HARPS3
10580.6473	-3.6562021	0.00114354	HARPS3
10581.6325	-3.6559	0.00123297	HARPS3
10582.5767	-3.6561941	0.00093117	HARPS3

Table C.4 continued from previous page

Time (BJD - 2450000)	RV (km/s)	RV error (km/s)	Instrument
10583.5579	-3.6588106	0.00118906	HARPS3
5427.71742	-0.00266	0.0013	PFS
5439.73885	-0.00403	0.00132	PFS
5796.7401	0.00249	0.0014	PFS
5850.65044	0.00232	0.00126	PFS
5850.65416	0.00234	0.0014	PFS
6086.81919	-0.00177	0.00118	PFS
6092.85872	-0.00116	0.00123	PFS
6139.70543	0.00173	0.00127	PFS
6144.7747	0.00214	0.00165	PFS
6150.7277	-0.00011	0.00144	PFS
6504.83089	-0.00338	0.00132	PFS
6506.78512	0.00191	0.00132	PFS
6550.62471	0.00766	0.00143	PFS
6553.6186	0.00455	0.00147	PFS
6604.54902	-0.0041	0.00123	PFS
6817.86837	9.00E-05	0.00123	PFS
6866.69534	-0.00318	0.00131	PFS
6876.68366	-0.00905	0.00129	PFS
7198.86731	-0.0018	0.00134	PFS
7206.83583	-0.00237	0.00143	PFS
7258.61859	-0.00248	0.00131	PFS
7321.57596	0.00579	0.00137	PFS
7327.61917	0.00374	0.0013	PFS
7536.90929	-0.00504	0.00131	PFS
7555.86064	-0.00531	0.00121	PFS
7614.71064	0	0.0012	PFS
7620.63101	-0.00469	0.00137	PFS

Table C.4 continued from previous page

Time (BJD - 2450000)	RV (km/s)	RV error (km/s)	Instrument
8271.77631	0.00213	0.00119	PFS
8293.81535	0.00192	0.00121	PFS
8334.76763	-0.00166	0.00118	PFS
8334.77142	0.00067	0.00121	PFS
8354.67918	-0.00219	0.00144	PFS
8354.68676	0	0.00141	PFS

Table C.5: RV data used for modelling of HD 207229.

RV (km/s)	RV error (km/s)	Instrument
55.3225833	0.00084745	HARPS2
55.3226517	0.00085175	HARPS2
55.3239791	0.00088161	HARPS2
55.3238363	0.00089161	HARPS2
55.3240088	0.00086659	HARPS2
55.4161429	0.00082809	HARPS2
55.416682	0.00084003	HARPS2
55.4173693	0.00084153	HARPS2
55.4188226	0.00082837	HARPS2
55.4185331	0.00082645	HARPS2
55.4191665	0.00083164	HARPS2
55.3427803	0.00096969	HARPS2
55.3441131	0.00099844	HARPS2
55.3434294	0.00093804	HARPS2
55.3426064	0.00090485	HARPS2
55.34457	0.00090536	HARPS2
55.3450584	0.00088426	HARPS2
55.5098094	0.00088984	HARPS2
55.5095496	0.00087712	HARPS2
	55.3225833 55.3226517 55.3239791 55.3238363 55.3240088 55.4161429 55.416682 55.4173693 55.4185331 55.4191665 55.3427803 55.3427803 55.3441131 55.3434294 55.3426064 55.3450584 55.5098094	55.3225833 0.00084745 55.3226517 0.00085175 55.3239791 0.00088161 55.3238363 0.00089161 55.3240088 0.00086659 55.4161429 0.00082809 55.416682 0.00084003 55.4173693 0.00084153 55.4188226 0.00082837 55.4191665 0.00083164 55.3427803 0.00096969 55.3441131 0.00099844 55.3426064 0.00090485 55.34457 0.00090536 55.3450584 0.00088984

Table C.5 continued from previous page

Time (BJD - 2450000)	RV (km/s)	RV error (km/s)	Instrument
8004.85036	55.5104336	0.00087591	HARPS2
8004.85361	55.5116354	0.00086697	HARPS2
8004.85683	55.5121423	0.00086992	HARPS2
8004.86014	55.5120854	0.00086775	HARPS2
8082.6988	55.3416028	0.00115079	HARPS2
8082.69995	55.3419265	0.00113118	HARPS2
8082.70112	55.3407421	0.00121018	HARPS2
8082.70229	55.3408386	0.00117272	HARPS2
8082.70346	55.3412228	0.00117564	HARPS2
8082.70462	55.3428852	0.001186	HARPS2
8085.71364	55.7622139	0.00114057	HARPS2
8085.7148	55.7619434	0.00114953	HARPS2
8085.71596	55.7621238	0.00115599	HARPS2
8085.71713	55.7622321	0.00111741	HARPS2
8085.71831	55.7630665	0.00121576	HARPS2
8085.71947	55.7621036	0.00108424	HARPS2
8143.55958	55.0738253	0.00086948	HARPS2
8143.56296	55.0737342	0.00086496	HARPS2
8143.56622	55.0737069	0.00086431	HARPS2
8144.52181	5.52E+01	0.00083601	HARPS2
8144.52504	55.1574497	0.000838	HARPS2
8144.52838	55.1577459	0.00084079	HARPS2
8145.52261	55.292441	0.00095191	HARPS2
8145.52593	55.2932749	0.00100877	HARPS2
8145.52885	55.297999	0.00184435	HARPS2
8191.50075	55.1174596	0.00092932	HARPS2
8191.5042	55.1169017	0.00092006	HARPS2
8191.50725	55.1174582	0.00090421	HARPS2

Table C.5 continued from previous page

Time (BJD - 2450000)	RV (km/s)	RV error (km/s)	Instrument
8195.5006	55.6915096	0.00108682	HARPS2
8195.50368	55.6908194	0.00098296	HARPS2
8195.50672	55.691585	0.00101024	HARPS2
8195.51	55.6910946	0.00103205	HARPS2
8195.51311	55.6923572	0.00100884	HARPS2
8195.51627	55.6928121	0.00096717	HARPS2
8318.87561	55.259875	0.00109677	HARPS2
8318.87883	55.2618927	0.0012154	HARPS2
8318.8821	55.2602396	0.00116046	HARPS2
8318.88536	55.2639894	0.00116173	HARPS2
8318.88865	55.2620456	0.00106057	HARPS2
8318.89188	55.2642792	0.00102428	HARPS2
8324.85687	55.7107814	0.00095113	HARPS2
8324.86012	55.7121947	0.00094185	HARPS2
8324.86338	55.7107229	0.00099753	HARPS2
8324.86669	55.7116013	0.00093826	HARPS2
8324.86988	55.7119154	0.0009282	HARPS2
8324.87312	55.7100761	0.00091975	HARPS2
8325.93959	55.6064237	0.0008768	HARPS2
8325.94281	55.6053983	0.00085696	HARPS2
8325.94611	55.606223	0.00086978	HARPS2
8325.94933	55.6052199	0.00087037	HARPS2
8325.95261	55.6041714	0.00086192	HARPS2
8325.95583	55.6044207	0.00085921	HARPS2
8383.74292	55.5508533	0.00102655	HARPS2
8383.74452	55.55154	0.00101954	HARPS2
8383.746	55.5529357	0.00098677	HARPS2
8384.79104	55.6877119	0.00091442	HARPS2

Table C.5 continued from previous page

Time (BJD - 2450000)	RV (km/s)	RV error (km/s)	Instrument
8384.79244	55.6876814	0.00098773	HARPS2
8384.79393	55.6883991	0.00091877	HARPS2
8385.73456	55.7538481	0.00095836	HARPS2
8385.73609	55.7534942	0.00095219	HARPS2
8385.73761	55.7570011	0.00093725	HARPS2
8385.89393	55.7621346	0.00091581	HARPS2
8385.89549	55.7606588	0.00090658	HARPS2
8385.89701	55.7607158	0.00089961	HARPS2
8404.83207	55.5896942	0.00096451	HARPS2
8404.83511	55.5893813	0.00101266	HARPS2
8404.83851	55.588778	0.00101	HARPS2
8404.84169	55.5897085	0.00100174	HARPS2
8404.84509	55.5886928	0.00098696	HARPS2
8404.84833	55.5881748	0.00099074	HARPS2
8416.72029	55.717768	0.00082006	HARPS2
8416.72354	55.7179811	0.00081735	HARPS2
8416.72682	55.71825	0.00081781	HARPS2
8416.72999	55.7184584	0.00082263	HARPS2
8416.7333	55.7178303	0.00083148	HARPS2
8416.73652	55.7191463	0.00083287	HARPS2
8439.6738	55.1688392	0.0007894	HARPS2
8439.67982	55.1678031	0.00079695	HARPS2
8439.68596	55.1676987	0.00079406	HARPS2
8453.69074	55.3849514	0.00081867	HARPS2
8453.69403	55.3837104	0.00081896	HARPS2
8453.69726	55.3835115	0.00081242	HARPS2
8479.64029	55.6945486	0.00085043	HARPS2
8479.64351	55.6949819	0.0008427	HARPS2

Table C.5 continued from previous page

Time (BJD - 2450000)	RV (km/s)	RV error (km/s)	Instrument
8479.64679	55.6950044	0.00084663	HARPS2
8479.65006	55.6953752	0.00085337	HARPS2
8479.65331	55.6957142	0.00084583	HARPS2
8479.6566	55.6964837	0.00084877	HARPS2
8680.82544	55.1343842	0.00082518	HARPS2
8680.82876	55.1346065	0.00083337	HARPS2
8680.83203	55.1352914	0.00081905	HARPS2
8680.83527	55.1361803	0.00082092	HARPS2
8680.83852	55.1363502	0.00081816	HARPS2
8680.84181	55.1370898	0.00081762	HARPS2
8739.70606	55.0733453	0.00084615	HARPS2
8739.71128	55.0728509	0.00082278	HARPS2
8739.71801	55.071922	0.00083416	HARPS2
1126.75682	56.4374152	0.00243536	CORALIE
1127.7333	56.4326526	0.00173413	CORALIE
1128.69465	56.4805423	0.00337503	CORALIE
1128.81505	56.5015762	0.00445389	CORALIE
1129.51938	56.5821752	0.00481053	CORALIE
1129.83	56.6272893	0.00287704	CORALIE
1130.51646	56.7388288	0.00584513	CORALIE
1130.7533	56.771489	0.0044525	CORALIE
1131.62603	56.9021468	0.00361708	CORALIE
1131.73769	56.9298733	0.00480603	CORALIE
1132.55499	57.0575428	0.00344089	CORALIE
1132.72995	57.0799077	0.00565427	CORALIE
1133.53718	57.1393859	0.006968	CORALIE
1133.78805	57.1648523	0.00477026	CORALIE
1134.64849	57.1716503	0.00614572	CORALIE

Table C.5 continued from previous page

Time (BJD - 2450000)	RV (km/s)	RV error (km/s)	Instrument
1134.82021	57.1761233	0.00653678	CORALIE
1135.53888	57.1561053	0.00413072	CORALIE
1135.76058	57.1411669	0.00451733	CORALIE
1136.54728	57.0911118	0.00506504	CORALIE
1136.74189	57.0453254	0.00495075	CORALIE
1137.55515	56.9614819	0.00457668	CORALIE
1137.78526	56.9422116	0.00506167	CORALIE
1138.53589	56.8449078	0.00360264	CORALIE
1138.83334	56.7926446	0.00486271	CORALIE
1139.52592	56.6948491	0.0041218	CORALIE
1139.81522	56.6556173	0.0053882	CORALIE
1140.73865	56.5510449	0.00338018	CORALIE
1141.53717	56.4783384	0.00427433	CORALIE
1141.7893	56.4646206	0.00481479	CORALIE
1142.53307	56.4217594	0.00498699	CORALIE
1142.75986	56.4194333	0.0041465	CORALIE
1143.52902	56.4174269	0.00452984	CORALIE
1143.76178	56.430851	0.00514004	CORALIE
1150.54742	57.1662274	0.00455391	CORALIE
1163.54739	56.9559671	0.00260888	CORALIE
1164.54985	57.0936487	0.00295511	CORALIE
1165.56001	57.1609345	0.00301936	CORALIE
1170.54442	56.7700541	0.00263526	CORALIE
1174.5468	56.4156	0.00273501	CORALIE
1176.53372	56.5321979	0.00237803	CORALIE
1184.54784	56.9959694	0.00599952	CORALIE
1186.60055	56.7226595	0.0031465	CORALIE
1187.5416	56.6096573	0.00368685	CORALIE

Table C.5 continued from previous page

Time (BJD - 2450000)	RV (km/s)	RV error (km/s)	Instrument
1188.5784	56.499861	0.00327025	CORALIE
1189.59515	56.4331771	0.00376346	CORALIE
1190.62386	56.4023373	0.00397238	CORALIE
1191.62924	56.45831	0.00470414	CORALIE
1192.62631	56.582589	0.00436622	CORALIE
1193.62162	56.7323058	0.00338998	CORALIE
1194.59506	56.8816419	0.00395928	CORALIE
1196.60195	57.1618914	0.00585013	CORALIE
1197.57843	57.176625	0.00469198	CORALIE
1198.57524	57.1525355	0.00610641	CORALIE
1199.57651	57.0859228	0.00542893	CORALIE
1200.57716	56.965736	0.00469846	CORALIE
831.035	0.0835	0.004	UCLES
1211.9651	0.3382	0.0057	UCLES
1213.9815	0.3985	0.0053	UCLES
1214.9298	0.3499	0.0047	UCLES
1235.9312	-0.2772	0.0052	UCLES
1236.9078	-0.3335	0.0055	UCLES
1383.2736	0	0.0048	UCLES
1387.3139	0.3566	0.004	UCLES
1411.2467	-0.4067	0.0049	UCLES
1413.2313	-0.2553	0.004	UCLES
1414.3164	-0.0881	0.0042	UCLES
1473.0974	-0.4038	0.0043	UCLES
1525.932	0.0796	0.0049	UCLES
1526.9613	0.2076	0.0048	UCLES
1743.3292	-0.4594	0.0065	UCLES
1745.2853	-0.2045	0.0053	UCLES

Table C.5 continued from previous page

Time (BJD - 2450000)	RV (km/s)	RV error (km/s)	Instrument
1828.1337	0.2282	0.0052	UCLES
1829.0121	0.2132	0.0054	UCLES
1829.988	0.1505	0.0063	UCLES
1856.1052	-0.1609	0.0062	UCLES
1918.966	-0.2093	0.0046	UCLES
1919.9811	-0.0417	0.0048	UCLES
1921.0019	0.097	0.005	UCLES
831.034977	0.2437	0.0037	UCLES
1211.96513	0.5096	0.0045	UCLES
1213.98147	0.5646	0.0048	UCLES
1214.92978	0.5113	0.0039	UCLES
1235.9312	-0.1175	0.0042	UCLES
1236.9078	-0.174	0.0045	UCLES
1383.27361	0.1681	0.0042	UCLES
1387.31387	0.5194	0.0034	UCLES
1411.24665	-0.2485	0.0042	UCLES
1413.23122	-0.0994	0.0036	UCLES
1414.31635	0.0724	0.0039	UCLES
1473.09736	-0.2389	0.0039	UCLES
1525.93201	0.2374	0.0047	UCLES
1526.9613	0.373	0.004	UCLES
1743.32924	-0.2981	0.0057	UCLES
1745.28527	-0.0399	0.0049	UCLES
1828.13369	0.3853	0.0047	UCLES
1829.01214	0.3687	0.0046	UCLES
1829.98801	0.304	0.005	UCLES
1856.10521	0.0017	0.0058	UCLES
1856.93135	0.151	0.013	UCLES

Table C.5 continued from previous page

Time (BJD - 2450000)	RV (km/s)	RV error (km/s)	Instrument
1918.96598	-0.0522	0.0043	UCLES
1919.9811	0.118	0.0038	UCLES
1921.00191	0.2589	0.0043	UCLES
2061.34131	-0.0093	0.0071	UCLES
2092.27897	-0.1067	0.004	UCLES
2127.24163	0.3007	0.0076	UCLES
2152.1424	-0.4496	0.0046	UCLES
2187.14068	-0.089	0.0035	UCLES
2594.03865	-0.5433	0.004	UCLES
2654.00484	-0.4269	0.004	UCLES
2945.13811	-0.0711	0.0038	UCLES
3008.02186	-0.1137	0.0037	UCLES
3043.98671	0.0014	0.0039	UCLES
3044.94298	-0.0958	0.0069	UCLES
3217.34251	-0.0402	0.0036	UCLES
3244.28447	-0.2063	0.005	UCLES
3281.18382	-0.1359	0.0035	UCLES
3572.28482	-0.7285	0.003	UCLES
3572.29837	-0.7257	0.0029	UCLES
3572.30818	-0.7232	0.0042	UCLES
3629.19478	-0.3682	0.0045	UCLES

Bibliography

- Adibekyan, V., Deal, M., Dorn, C., Dittrich, I., Soares, B. M. T. B., Sousa, S. G., Santos, N. C., Bitsch, B., Mordasini, C., Barros, S. C. C., Bossini, D., Campante, T. L., Delgado Mena, E., Demangeon, O. D. S., Figueira, P., Moedas, N., Martirosyan, Z., Israelian, G., and Hakobyan, A. A. (2024). Linking the primordial composition of planet building disks to the present-day composition of rocky exoplanets. , 692:A67.
- Aguichine, A., Mousis, O., Deleuil, M., and Marcq, E. (2021). Mass-Radius Relationships for Irradiated Ocean Planets. , 914(2):84.
- Aguirre Børsen-Koch, V., Rørsted, J. L., Justesen, A. B., Stokholm, A., Verma, K., Winther, M. L., Knudstrup, E., Nielsen, K. B., Sahlholdt, C., Larsen, J. R., Cassisi, S., Serenelli, A. M., Casagrande, L., Christensen-Dalsgaard, J., Davies, G. R., Ferguson, J. W., Lund, M. N., Weiss, A., and White, T. R. (2022). The BAyesian STellar algorithm (BASTA): a fitting tool for stellar studies, asteroseismology, exoplanets, and Galactic archaeology. , 509(3):4344–4364.
- Aigrain, S. and Foreman-Mackey, D. (2023). Gaussian Process Regression for Astronomical Time Series., 61:329–371.
- Al Moulla, K., Dumusque, X., and Cretignier, M. (2024). Measuring precise radial velocities on individual spectral lines. IV. Stellar activity correlation with line formation temperature. , 683:A106.
- Alibert, Y., Mordasini, C., Benz, W., and Winisdoerffer, C. (2005). Models of giant planet formation with migration and disc evolution. , 434(1):343–353.

- Allard, F., Homeier, D., and Freytag, B. (2012). Models of very-low-mass stars, brown dwarfs and exoplanets. *Philosophical Transactions of the Royal Society of London Series A*, 370(1968):2765–2777.
- Anglada-Escudé, G. and Butler, R. P. (2012). The HARPS-TERRA Project. I. Description of the Algorithms, Performance, and New Measurements on a Few Remarkable Stars Observed by HARPS., 200(2):15.
- Bahng, J. and Schwarzschild, M. (1961). Lifetime of Solar Granules. , 134:312.
- Balmer, W. O., Kammerer, J., Pueyo, L., Perrin, M. D., Girard, J. H., Leisenring,
 J. M., Lawson, K., Dennen, H., van der Marel, R. P., Beichman, C. A., Bryden,
 G., Llop-Sayson, J., Valenti, J. A., Lothringer, J. D., Lewis, N. K., Mâlin, M.,
 Rebollido, I., Rickman, E., Hoch, K. K. W., Soummer, R., Clampin, M., and
 Mountain, C. M. (2025). JWST-TST High Contrast: Living on the Wedge, or,
 NIRCam Bar Coronagraphy Reveals CO₂ in the HR 8799 and 51 Eri Exoplanets'
 Atmospheres., 169(4):209.
- Baranne, A., Queloz, D., Mayor, M., Adrianzyk, G., Knispel, G., Kohler, D., Lacroix, D., Meunier, J. P., Rimbaud, G., and Vin, A. (1996). ELODIE: A spectrograph for accurate radial velocity measurements., 119:373–390.
- Barbieri, M. (2023). Eso/harps radial velocities catalog.
- Barclay, T., Sheppard, K. B., Latouf, N., Mandell, A. M., Quintana, E. V., Gilbert,
 E. A., Liuzzi, G., Villanueva, G. L., Arney, G., Brande, J., Colón, K. D., Covone,
 G., Crossfield, I. J. M., Damiano, M., Domagal-Goldman, S. D., Fauchez, T. J.,
 Fiscale, S., Gallo, F., Hedges, C. L., Hu, R., Kite, E. S., Koll, D., Kopparapu, R. K.,
 Kostov, V. B., Kreidberg, L., Lopez, E. D., Mang, J., Morley, C. V., Mullally, F.,
 Mullally, S. E., Pidhorodetska, D., Schlieder, J. E., Vega, L. D., Youngblood, A.,
 and Zieba, S. (2025). The Transmission Spectrum of the Potentially Rocky Planet
 L 98-59 c., 169(5):241.
- Barragán, O., Aigrain, S., Rajpaul, V. M., and Zicher, N. (2022). PYANETI -

- II. A multidimensional Gaussian process approach to analysing spectroscopic time-series. , 509(1):866–883.
- Barragán, O., Gandolfi, D., and Antoniciello, G. (2019). PYANETI: a fast and powerful software suite for multiplanet radial velocity and transit fitting., 482(1):1017–1030.
- Barragán, O., Gillen, E., Aigrain, S., Meech, A., Klein, B., Nielsen, L. D., Yu, H., O'Sullivan, N. K., Nicholson, B. A., and Lillo-Box, J. (2023). Revisiting K2-233 spectroscopic time-series with multidimensional Gaussian processes. , 522(3):3458–3471.
- Bashi, D., Helled, R., Zucker, S., and Mordasini, C. (2017). Two empirical regimes of the planetary mass-radius relation., 604:A83.
- Batalha, N. E., Lewis, T., Fortney, J. J., Batalha, N. M., Kempton, E., Lewis, N. K., and Line, M. R. (2019). The Precision of Mass Measurements Required for Robust Atmospheric Characterization of Transiting Exoplanets. , 885(1):L25.
- Bean, J. L., Raymond, S. N., and Owen, J. E. (2020). The nature and origins of sub-Neptune size planets. *arXiv:2010.11867 [astro-ph]*. arXiv: 2010.11867.
- Beard, C., Robertson, P., Lubin, J., Han, T., Holcomb, R., Premnath, P., Butler,
 R. P., Dalba, P. A., Holden, B., Blake, C. H., Diddams, S. A., Gupta, A. F.,
 Halverson, S., Krolikowski, D. M., Li, D., Lin, A. S. J., Logsdon, S. E., Lubar, E.,
 Mahadevan, S., McElwain, M. W., Ninan, J. P., Paredes, L. A., Roy, A., Schwab,
 C., Stefansson, G., Terrien, R. C., and Wright, J. T. (2025). Jitter Across 15
 yr: Leveraging Precise Photometry from Kepler and TESS to Extract Exoplanets
 from Radial Velocity Time Series. , 169(2):92.
- Bedding, T. R., Butler, R. P., Kjeldsen, H., Baldry, I. K., O'Toole, S. J., Tinney,
 C. G., Marcy, G. W., Kienzle, F., and Carrier, F. (2001). Evidence for Solar-like
 Oscillations in β Hydri., 549(1):L105–L108.

- Bedding, T. R., Huber, D., Stello, D., Elsworth, Y. P., Hekker, S., Kallinger, T., Mathur, S., Mosser, B., Preston, H. L., Ballot, J., Barban, C., Broomhall, A. M., Buzasi, D. L., Chaplin, W. J., García, R. A., Gruberbauer, M., Hale, S. J., De Ridder, J., Frandsen, S., Borucki, W. J., Brown, T., Christensen-Dalsgaard, J., Gilliland, R. L., Jenkins, J. M., Kjeldsen, H., Koch, D., Belkacem, K., Bildsten, L., Bruntt, H., Campante, T. L., Deheuvels, S., Derekas, A., Dupret, M.-A., Goupil, M.-J., Hatzes, A., Houdek, G., Ireland, M. J., Jiang, C., Karoff, C., Kiss, L. L., Lebreton, Y., Miglio, A., Montalbán, J., Noels, A., Roxburgh, I. W., Sangaralingam, V., Stevens, I. R., Suran, M. D., Tarrant, N. J., and Weiss, A. (2010). Solar-like Oscillations in Low-luminosity Red Giants: First Results from Kepler., 713:L176–L181.
- Bello-Arufe, A., Damiano, M., Bennett, K. A., Hu, R., Welbanks, L., MacDonald,R. J., Seligman, D. Z., Sing, D. K., Tokadjian, A., Oza, A. V., and Yang, J. (2025).Evidence for a Volcanic Atmosphere on the Sub-Earth L 98-59 b. , 980(2):L26.
- Bergsten, G. J., Pascucci, I., Hardegree-Ullman, K. K., Fernandes, R. B., Christiansen, J. L., and Mulders, G. D. (2023). No Evidence for More Earth-sized Planets in the Habitable Zone of Kepler's M versus FGK Stars., 166(6):234.
- Bitsch, B., Raymond, S. N., and Izidoro, A. (2019). Rocky super-Earths or waterworlds: the interplay of planet migration, pebble accretion, and disc evolution., 624:A109.
- Bonfils, X., Almenara, J. M., Cloutier, R., Wünsche, A., Astudillo-Defru, N., Berta-Thompson, Z., Bouchy, F., Charbonneau, D., Delfosse, X., Díaz, R. F., Dittmann, J., Doyon, R., Forveille, T., Irwin, J., Lovis, C., Mayor, M., Menou, K., Murgas, F., Newton, E., Pepe, F., Santos, N. C., and Udry, S. (2018). Radial velocity follow-up of GJ1132 with HARPS. A precise mass for planet b and the discovery of a second planet. , 618:A142.
- Bordé, P., Rouan, D., and Léger, A. (2003). Exoplanet detection capability of the COROT space mission. , 405:1137–1144.

- Borucki, W. J., Koch, D., Basri, G., Batalha, N., Brown, T., Caldwell, D., Caldwell, J., Christensen-Dalsgaard, J., Cochran, W. D., DeVore, E., Dunham, E. W., Dupree, A. K., Gautier, T. N., Geary, J. C., Gilliland, R., Gould, A., Howell, S. B., Jenkins, J. M., Kondo, Y., Latham, D. W., Marcy, G. W., Meibom, S., Kjeldsen, H., Lissauer, J. J., Monet, D. G., Morrison, D., Sasselov, D., Tarter, J., Boss, A., Brownlee, D., Owen, T., Buzasi, D., Charbonneau, D., Doyle, L., Fortney, J., Ford, E. B., Holman, M. J., Seager, S., Steffen, J. H., Welsh, W. F., Rowe, J., Anderson, H., Buchhave, L., Ciardi, D., Walkowicz, L., Sherry, W., Horch, E., Isaacson, H., Everett, M. E., Fischer, D., Torres, G., Johnson, J. A., Endl, M., MacQueen, P., Bryson, S. T., Dotson, J., Haas, M., Kolodziejczak, J., Van Cleve, J., Chandrasekaran, H., Twicken, J. D., Quintana, E. V., Clarke, B. D., Allen, C., Li, J., Wu, H., Tenenbaum, P., Verner, E., Bruhweiler, F., Barnes, J., and Prsa, A. (2010). Kepler Planet-Detection Mission: Introduction and First Results. *Science*, 327(5968):977–980.
- Borucki, W. J. and Summers, A. L. (1984). The photometric method of detecting other planetary systems. , 58(1):121–134.
- Boss, A. P. (1997). Giant planet formation by gravitational instability. *Science*, 276:1836–1839.
- Bowens, R., Meyer, M. R., Delacroix, C., Absil, O., van Boekel, R., Quanz, S. P., Shinde, M., Kenworthy, M., Carlomagno, B., Orban de Xivry, G., Cantalloube, F., and Pathak, P. (2021). Exoplanets with ELT-METIS. I. Estimating the direct imaging exoplanet yield around stars within 6.5 parsecs. , 653:A8.
- Brandt, T. D. (2018). The Hipparcos-Gaia Catalog of Accelerations. , 239(2):31.
- Brandt, T. D. (2021). The Hipparcos-Gaia Catalog of Accelerations: Gaia EDR3 Edition. , 254(2):42.
- Brandt, T. D., Dupuy, T. J., and Bowler, B. P. (2019). Precise Dynamical Masses of Directly Imaged Companions from Relative Astrometry, Radial Velocities, and Hipparcos-Gaia DR2 Accelerations., 158(4):140.

- Burn, R., Mordasini, C., Mishra, L., Haldemann, J., Venturini, J., Emsenhuber, A., and Henning, T. (2024). A radius valley between migrated steam worlds and evaporated rocky cores. *Nature Astronomy*, 8:463–471.
- Burrows, A., Halverson, S., Siegel, J. C., Gilbertson, C., Luhn, J., Burt, J., Bender,
 C. F., Roy, A., Terrien, R. C., Vangstein, S., Mahadevan, S., Wright, J. T.,
 Robertson, P., Ford, E. B., Stefánsson, G., Ninan, J. P., Blake, C. H., McElwain,
 M. W., Schwab, C., and Zhao, J. (2024). The Death of Vulcan: NEID Reveals
 That the Planet Candidate Orbiting HD 26965 Is Stellar Activity., 167(5):243.
- Butler, R. P., Tinney, C. G., Marcy, G. W., Jones, H. R. A., Penny, A. J., and Apps, K. (2001). Two New Planets from the Anglo-Australian Planet Search., 555(1):410–417.
- Butler, R. P., Wright, J. T., Marcy, G. W., Fischer, D. A., Vogt, S. S., Tinney, C. G., Jones, H. R. A., Carter, B. D., Johnson, J. A., McCarthy, C., and Penny, A. J. (2006). Catalog of Nearby Exoplanets. , 646(1):505–522.
- Cadieux, C., Doyon, R., Plotnykov, M., Hébrard, G., Jahandar, F., Artigau, , Valencia, D., Cook, N. J., Martioli, E., Vandal, T., Donati, J.-F., Cloutier, R., Narita, N., Fukui, A., Hirano, T., Bouchy, F., Cowan, N. B., Gonzales, E. J., Ciardi, D. R., Stassun, K. G., Arnold, L., Benneke, B., Boisse, I., Bonfils, X., Carmona, A., Cortés-Zuleta, P., Delfosse, X., Forveille, T., Fouqué, P., da Silva, J. G., Jenkins, J. M., Kiefer, F., Kóspál, , Lafrenière, D., Martins, J. H. C., Moutou, C., Nascimento Jr., J.-D. d., Ould-Elhkim, M., Pelletier, S., Twicken, J. D., Bouma, L. G., Cartwright, S., Darveau-Bernier, A., Grankin, K., Ikoma, M., Kagetani, T., Kawauchi, K., Kodama, T., Kotani, T., Latham, D. W., Menou, K., Ricker, G., Seager, S., Tamura, M., Vanderspek, R., and Watanabe, N. (2022). TOI-1452 b: SPIRou and TESS reveal a super-Earth in a temperate orbit transiting an M4 dwarf. *The Astronomical Journal*, 164(3):96. arXiv:2208.06333 [astro-ph].
- Cadieux, C., Plotnykov, M., Doyon, R., Valencia, D., Jahandar, F., Dang, L., Turbet, M., Fauchez, T. J., Cloutier, R., Cherubim, C., Artigau, É., Cook, N. J., Edwards,

- B., Hallatt, T., Charnay, B., Bouchy, F., Allart, R., Mignon, L., Baron, F., Barros, S. C. C., Benneke, B., Canto Martins, B. L., Cowan, N. B., De Medeiros, J. R., Delfosse, X., Delgado-Mena, E., Dumusque, X., Ehrenreich, D., Frensch, Y. G. C., González Hernández, J. I., Hara, N. C., Lafrenière, D., Lo Curto, G., Malo, L., Melo, C., Mounzer, D., Passeger, V. M., Pepe, F., Poulin-Girard, A.-S., Santos, N. C., Sosnowska, D., Suárez Mascareño, A., Thibault, S., Vaulato, V., Wade, G. A., and Wildi, F. (2024). New Mass and Radius Constraints on the LHS 1140 Planets: LHS 1140 b Is either a Temperate Mini-Neptune or a Water World. , 960(1):L3.
- Cegla, H. M., Watson, C. A., Shelyag, S., Mathioudakis, M., and Moutari, S. (2019). Stellar Surface Magnetoconvection as a Source of Astrophysical Noise. III. Sun-as-a-Star Simulations and Optimal Noise Diagnostics. , 879(1):55.
- Chabrier, G., Johansen, A., Janson, M., and Rafikov, R. (2014). Giant Planet and Brown Dwarf Formation. *Protostars and Planets VI*, pages 619–642.
- Chakrabarty, A. and Mulders, G. D. (2024). Where Are the Water Worlds? Identifying Exo-water-worlds Using Models of Planet Formation and Atmospheric Evolution., 966(2):185.
- Chen, J. and Kipping, D. (2017). Probabilistic Forecasting of the Masses and Radii of Other Worlds., 834(1):17.
- Choi, J., Dotter, A., Conroy, C., Cantiello, M., Paxton, B., and Johnson, B. D. (2016). Mesa Isochrones and Stellar Tracks (MIST). I. Solar-scaled Models., 823(2):102.
- Claret, A. (2017). Limb and gravity-darkening coefficients for the TESS satellite at several metallicities, surface gravities, and microturbulent velocities. , 600:A30.
- Claret, A., Hauschildt, P. H., and Witte, S. (2012). VizieR Online Data Catalog: Limb-darkening for CoRoT, Kepler, Spitzer (Claret+, 2012). *VizieR Online Data Catalog*, 354.

- Cloutier, R., Astudillo-Defru, N., Doyon, R., Bonfils, X., Almenara, J. M., Benneke,
 B., Bouchy, F., Delfosse, X., Ehrenreich, D., Forveille, T., Lovis, C., Mayor, M.,
 Menou, K., Murgas, F., Pepe, F., Rowe, J., Santos, N. C., Udry, S., and Wünsche,
 A. (2017). Characterization of the K2-18 multi-planetary system with HARPS.
 A habitable zone super-Earth and discovery of a second, warm super-Earth on a non-coplanar orbit. , 608:A35.
- Cloutier, R. and Menou, K. (2020). Evolution of the Radius Valley around Low-mass Stars from Kepler and K2., 159(5):211.
- Cointepas, M., Almenara, J. M., Bonfils, X., Bouchy, F., Astudillo-Defru, N., Murgas, F., Otegi, J. F., Wyttenbach, A., Anderson, D. R., Artigau, É., Canto Martins, B. L., Charbonneau, D., Collins, K. A., Collins, K. I., Correia, J. J., Curaba, S., Delboulbé, A., Delfosse, X., Díaz, R. F., Dorn, C., Doyon, R., Feautrier, P., Figueira, P., Forveille, T., Gaisne, G., Gan, T., Gluck, L., Helled, R., Hellier, C., Jocou, L., Kern, P., Lafrasse, S., Law, N., Leão, I. C., Lovis, C., Magnard, Y., Mann, A. W., Maurel, D., de Medeiros, J. R., Melo, C., Moulin, T., Pepe, F., Rabou, P., Rochat, S., Rodriguez, D. R., Roux, A., Santos, N. C., Ségransan, D., Stadler, E., Ting, E. B., Twicken, J. D., Udry, S., Waalkes, W. C., West, R. G., Wünsche, A., Ziegler, C., Ricker, G., Vanderspek, R., Latham, D. W., Seager, S., Winn, J., and Jenkins, J. M. (2021). TOI-269 b: an eccentric sub-Neptune transiting a M2 dwarf revisited with ExTrA., 650:A145.
- Collier Cameron, A. and Jardine, M. (2018). Hierarchical Bayesian calibration of tidal orbit decay rates among hot Jupiters. , 476:2542–2555.
- Colwell, I., Timmaraju, V., Venkataram, H. S., and Wise, A. (2025). Deep Learning–based Measurement of Planetary Radial Velocities in the Presence of Stellar Variability., 169(1):24.
- Cosentino, R., Lovis, C., Pepe, F., Collier Cameron, A., Latham, D. W., Molinari, E., Udry, S., Bezawada, N., Black, M., Born, A., Buchschacher, N., Charbonneau, D., Figueira, P., Fleury, M., Galli, A., Gallie, A., Gao, X., Ghedina, A., Gonzalez,

- C., Gonzalez, M., Guerra, J., Henry, D., Horne, K., Hughes, I., Kelly, D., Lodi, M., Lunney, D., Maire, C., Mayor, M., Micela, G., Ordway, M. P., Peacock, J., Phillips, D., Piotto, G., Pollacco, D., Queloz, D., Rice, K., Riverol, C., Riverol, L., San Juan, J., Sasselov, D., Segransan, D., Sozzetti, A., Sosnowska, D., Stobie, B., Szentgyorgyi, A., Vick, A., and Weber, L. (2012). Harps-N: the new planet hunter at TNG. In *Ground-based and Airborne Instrumentation for Astronomy IV*, volume 8446 of , page 84461V.
- Crane, J. D., Shectman, S. A., Butler, R. P., Thompson, I. B., Birk, C., Jones, P., and Burley, G. S. (2010). The Carnegie Planet Finder Spectrograph: integration and commissioning. In McLean, I. S., Ramsay, S. K., and Takami, H., editors, *Ground-based and Airborne Instrumentation for Astronomy III*, volume 7735 of *Society of Photo-Optical Instrumentation Engineers (SPIE) Conference Series*, page 773553.
- Cretignier, M., Dumusque, X., Aigrain, S., and Pepe, F. (2023). YARARA V2: Reaching sub-m s⁻¹ precision over a decade using PCA on line-by-line radial velocities., 678:A2.
- Dai, F., Masuda, K., Winn, J. N., and Zeng, L. (2019). Homogeneous Analysis of Hot Earths: Masses, Sizes, and Compositions. *The Astrophysical Journal*, 883(1):79. arXiv: 1908.06299.
- Dainese, S. and Albrecht, S. H. (2025). No Robust Statistical Evidence for a Population of Water Worlds in a 2025 Sample of Planets Orbiting M Stars. *arXiv e-prints*, page arXiv:2503.02451.
- Dalal, S., Haywood, R. D., Mortier, A., Chaplin, W. J., and Meunier, N. (2023).
 Predicting convective blueshift and radial-velocity dispersion due to granulation for FGK stars., 525(3):3344–3353.
- Damiano, M., Hu, R., Bello-Arufe, A., Tokadjian, A., and Yang, J. (2025). LHS 1140 b is a potentially habitable water world. In *American Astronomical Society Meeting*

- Abstracts, volume 245 of American Astronomical Society Meeting Abstracts, page 232.06.
- Dawson, R. I. and Johnson, J. A. (2018). Origins of Hot Jupiters. *Annual Review of Astronomy and Astrophysics*, 56(1):175–221. arXiv: 1801.06117.
- de Beurs, Z. L., Vanderburg, A., Shallue, C. J., Dumusque, X., Cameron, A. C., Leet, C., Buchhave, L. A., Cosentino, R., Ghedina, A., Haywood, R. D., Langellier, N., Latham, D. W., López-Morales, M., Mayor, M., Micela, G., Milbourne, T. W., Mortier, A., Molinari, E., Pepe, F., Phillips, D. F., Pinamonti, M., Piotto, G., Rice, K., Sasselov, D., Sozzetti, A., Udry, S., and Watson, C. A. (2022). Identifying Exoplanets with Deep Learning. IV. Removing Stellar Activity Signals from Radial Velocity Measurements Using Neural Networks., 164(2):49.
- Del Moro, D., Berrilli, F., Duvall, Jr., T. L., and Kosovichev, A. G. (2004). Dynamics and Structure of Supergranulation. , 221(1):23–32.
- Delisle, J. B., Unger, N., Hara, N. C., and Ségransan, D. (2022). Efficient modeling of correlated noise. III. Scalable methods for jointly modeling several observables' time series with Gaussian processes. , 659:A182.
- Demangeon, O. D. S., Zapatero Osorio, M. R., Alibert, Y., Barros, S. C. C., Adibekyan, V., Tabernero, H. M., Antoniadis-Karnavas, A., Camacho, J. D., Suárez Mascareño, A., Oshagh, M., Micela, G., Sousa, S. G., Lovis, C., Pepe, F. A., Rebolo, R., Cristiani, S., Santos, N. C., Allart, R., Allende Prieto, C., Bossini, D., Bouchy, F., Cabral, A., Damasso, M., Di Marcantonio, P., D'Odorico, V., Ehrenreich, D., Faria, J., Figueira, P., Génova Santos, R., Haldemann, J., Hara, N., González Hernández, J. I., Lavie, B., Lillo-Box, J., Lo Curto, G., Martins, C. J. A. P., Mégevand, D., Mehner, A., Molaro, P., Nunes, N. J., Pallé, E., Pasquini, L., Poretti, E., Sozzetti, A., and Udry, S. (2021). Warm terrestrial planet with half the mass of Venus transiting a nearby star., 653:A41.
- Desort, M., Lagrange, A. M., Galland, F., Udry, S., and Mayor, M. (2007). Search for

- exoplanets with the radial-velocity technique: quantitative diagnostics of stellar activity., 473(3):983–993.
- Di Maio, C., Changeat, Q., Benatti, S., and Micela, G. (2023). Analysis of the planetary mass uncertainties on the accuracy of atmospherical retrieval. , 669:A150.
- Diamond-Lowe, H., Kreidberg, L., Harman, C. E., Kempton, E. M. R., Rogers, L. A., Joyce, S. R. G., Eastman, J. D., King, G. W., Kopparapu, R., Youngblood, A., Kosiarek, M. R., Livingston, J. H., Hardegree-Ullman, K. K., and Crossfield, I. J. M. (2022). The K2-3 System Revisited: Testing Photoevaporation and Corepowered Mass Loss with Three Small Planets Spanning the Radius Valley. , 164(5):172.
- Diego, F., Charalambous, A., Fish, A. C., and Walker, D. D. (1990). Final tests and commissioning of the UCL echelle spectrograph. In Crawford, D. L., editor, *Instrumentation in Astronomy VII*, volume 1235 of *Society of Photo-Optical Instrumentation Engineers (SPIE) Conference Series*, pages 562–576.
- Dong, S., Katz, B., and Socrates, A. (2013). Warm Jupiters Need Close "Friends" for High-Eccentricity Migration A Stringent Upper Limit on the Perturber's Separation. *The Astrophysical Journal*, 781(1):L5. arXiv: 1309.0011.
- Dumusque, X. (2018). Measuring precise radial velocities on individual spectral lines. I. Validation of the method and application to mitigate stellar activity., 620:A47.
- Dumusque, X., Udry, S., Lovis, C., Santos, N. C., and Monteiro, M. J. P. F. G. (2011). Planetary detection limits taking into account stellar noise. I. Observational strategies to reduce stellar oscillation and granulation effects. , 525:A140.
- Durisen, R. H., Boss, A. P., Mayer, L., Nelson, A. F., Quinn, T., and Rice, W. K. M. (2007). Gravitational Instabilities in Gaseous Protoplanetary Disks and Implications for Giant Planet Formation. In Reipurth, B., Jewitt, D., and Keil, K., editors, *Protostars and Planets V*, page 607.

- Els, S. G., Sterzik, M. F., Marchis, F., Pantin, E., Endl, M., and Kürster, M. (2001). A second substellar companion in the Gliese 86 system. A brown dwarf in an extrasolar planetary system. , 370:L1–L4.
- Espinoza, N., Hartman, J. D., Bakos, G. Á., Henning, T., Bayliss, D., Bento, J., Bhatti, W., Brahm, R., Csubry, Z., Suc, V., Jordán, A., Mancini, L., Tan, T. G., Penev, K., Rabus, M., Sarkis, P., de Val-Borro, M., Durkan, S., Lázár, J., Papp, I., and Sári, P. (2019). HATS-54b-HATS-58Ab: Five New Transiting Hot Jupiters Including One with a Possible Temperate Companion. , 158(2):63.
- Estrela, R., Swain, M., Gupta, A., Sotin, C., and Valio, A. (2020). The evolutionary track of H/He envelope in the observed population of sub-Neptunes and Super-Earths planets. *The Astrophysical Journal*, 898(2):104. arXiv: 2001.01299.
- Feng, F., Crane, J. D., Xuesong Wang, S., Teske, J. K., Shectman, S. A., Díaz, M. R., Thompson, I. B., Jones, H. R. A., and Butler, R. P. (2019). Search for Nearby Earth Analogs. I. 15 Planet Candidates Found in PFS Data. , 242(2):25.
- Ford, E. B., Bender, C. F., Blake, C. H., Gupta, A. F., Kanodia, S., Lin, A. S. J., Logsdon, S. E., Luhn, J. K., Mahadevan, S., Palumbo, III, M. L., Terrien, R. C., Wright, J. T., Zhao, J., Halverson, S., Hunting, E., Robertson, P., Roy, A., and Stefansson, G. (2024). Earths within Reach: Evaluation of Strategies for Mitigating Solar Variability using 3.5 years of NEID Sun-as-a-Star Observations. *arXiv e-prints*, page arXiv:2408.13318.
- Foreman-Mackey, D. (2018). Scalable Backpropagation for Gaussian Processes using Celerite. *Research Notes of the American Astronomical Society*, 2(1):31.
- Foreman-Mackey, D., Agol, E., Ambikasaran, S., and Angus, R. (2017). Fast and Scalable Gaussian Process Modeling with Applications to Astronomical Time Series., 154:220.
- Foreman-Mackey, D., Barentsen, G., and Barclay, T. (2019). dfm/exoplanet: exoplanet v0.1.5.

- Foreman-Mackey, D., Hogg, D. W., Lang, D., and Goodman, J. (2013). emcee: The MCMC Hammer., 125:306.
- Fortney, J. J., Dawson, R. I., and Komacek, T. D. (2021). Hot Jupiters: Origins, Structure, Atmospheres. *Journal of Geophysical Research (Planets)*, 126(3):e06629.
- Fridlund, M., Gaidos, E., Barragán, O., Persson, C. M., Gandolfi, D., Cabrera,
 J., Hirano, T., Kuzuhara, M., Csizmadia, S., Nowak, G., Endl, M., Grziwa, S.,
 Korth, J., Pfaff, J., Bitsch, B., Johansen, A., Mustill, A. J., Davies, M. B., Deeg,
 H. J., Palle, E., Cochran, W. D., Eigmüller, P., Erikson, A., Guenther, E., Hatzes,
 A. P., Kiilerich, A., Kudo, T., MacQueen, P., Narita, N., Nespral, D., Pätzold, M.,
 Prieto-Arranz, J., Rauer, H., and Van Eylen, V. (2017). K2-111 b a short period
 super-Earth transiting a metal poor, evolved old star., 604:A16.
- Fulton, B. J., Petigura, E. A., Blunt, S., and Sinukoff, E. (2018). RadVel: The Radial Velocity Modeling Toolkit. *Publications of the Astronomical Society of* the Pacific, 130(986):044504. arXiv: 1801.01947.
- Fulton, B. J., Petigura, E. A., Howard, A. W., Isaacson, H., Marcy, G. W., Cargile,
 P. A., Hebb, L., Weiss, L. M., Johnson, J. A., Morton, T. D., Sinukoff, E.,
 Crossfield, I. J. M., and Hirsch, L. A. (2017). The California- *Kepler* Survey. III.
 A Gap in the Radius Distribution of Small Planets. *The Astronomical Journal*,
 154(3):109.
- Gaia Collaboration, Brown, A. G. A., Vallenari, A., Prusti, T., de Bruijne, J. H. J.,
 Babusiaux, C., Biermann, M., Creevey, O. L., Evans, D. W., Eyer, L., Hutton,
 A., Jansen, F., Jordi, C., Klioner, S. A., Lammers, U., Lindegren, L., Luri, X.,
 Mignard, F., Panem, C., Pourbaix, D., Randich, S., Sartoretti, P., Soubiran, C.,
 Walton, N. A., Arenou, F., Bailer-Jones, C. A. L., Bastian, U., Cropper, M.,
 Drimmel, R., Katz, D., Lattanzi, M. G., van Leeuwen, F., Bakker, J., Cacciari, C.,
 Castañeda, J., De Angeli, F., Ducourant, C., Fabricius, C., Fouesneau, M., Frémat,
 Y., Guerra, R., Guerrier, A., Guiraud, J., Jean-Antoine Piccolo, A., Masana, E.,

Messineo, R., Mowlavi, N., Nicolas, C., Nienartowicz, K., Pailler, F., Panuzzo, P., Riclet, F., Roux, W., Seabroke, G. M., Sordo, R., Tanga, P., Thévenin, F., Gracia-Abril, G., Portell, J., Teyssier, D., Altmann, M., Andrae, R., Bellas-Velidis, I., Benson, K., Berthier, J., Blomme, R., Brugaletta, E., Burgess, P. W., Busso, G., Carry, B., Cellino, A., Cheek, N., Clementini, G., Damerdji, Y., Davidson, M., Delchambre, L., Dell'Oro, A., Fernández-Hernández, J., Galluccio, L., García-Lario, P., Garcia-Reinaldos, M., González-Núñez, J., Gosset, E., Haigron, R., Halbwachs, J. L., Hambly, N. C., Harrison, D. L., Hatzidimitriou, D., Heiter, U., Hernández, J., Hestroffer, D., Hodgkin, S. T., Holl, B., Janßen, K., Jevardat de Fombelle, G., Jordan, S., Krone-Martins, A., Lanzafame, A. C., Löffler, W., Lorca, A., Manteiga, M., Marchal, O., Marrese, P. M., Moitinho, A., Mora, A., Muinonen, K., Osborne, P., Pancino, E., Pauwels, T., Petit, J. M., Recio-Blanco, A., Richards, P. J., Riello, M., Rimoldini, L., Robin, A. C., Roegiers, T., Rybizki, J., Sarro, L. M., Siopis, C., Smith, M., Sozzetti, A., Ulla, A., Utrilla, E., van Leeuwen, M., van Reeven, W., Abbas, U., Abreu Aramburu, A., Accart, S., Aerts, C., Aguado, J. J., Ajaj, M., Altavilla, G., Álvarez, M. A., Álvarez Cid-Fuentes, J., Alves, J., Anderson, R. I., Anglada Varela, E., Antoja, T., Audard, M., Baines, D., Baker, S. G., Balaguer-Núñez, L., Balbinot, E., Balog, Z., Barache, C., Barbato, D., Barros, M., Barstow, M. A., Bartolomé, S., Bassilana, J. L., Bauchet, N., Baudesson-Stella, A., Becciani, U., Bellazzini, M., Bernet, M., Bertone, S., Bianchi, L., Blanco-Cuaresma, S., Boch, T., Bombrun, A., Bossini, D., Bouquillon, S., Bragaglia, A., Bramante, L., Breedt, E., Bressan, A., Brouillet, N., Bucciarelli, B., Burlacu, A., Busonero, D., Butkevich, A. G., Buzzi, R., Caffau, E., Cancelliere, R., Cánovas, H., Cantat-Gaudin, T., Carballo, R., Carlucci, T., Carnerero, M. I., Carrasco, J. M., Casamiquela, L., Castellani, M., Castro-Ginard, A., Castro Sampol, P., Chaoul, L., Charlot, P., Chemin, L., Chiavassa, A., Cioni, M. R. L., Comoretto, G., Cooper, W. J., Cornez, T., Cowell, S., Crifo, F., Crosta, M., Crowley, C., Dafonte, C., Dapergolas, A., David, M., David, P., de Laverny, P., De Luise, F., De March, R., De Ridder, J., de Souza, R., de Teodoro, P., de Torres, A., del Peloso, E. F., del Pozo, E., Delbo, M., Delgado,

A., Delgado, H. E., Delisle, J. B., Di Matteo, P., Diakite, S., Diener, C., Distefano, E., Dolding, C., Eappachen, D., Edvardsson, B., Enke, H., Esquej, P., Fabre, C., Fabrizio, M., Faigler, S., Fedorets, G., Fernique, P., Fienga, A., Figueras, F., Fouron, C., Fragkoudi, F., Fraile, E., Franke, F., Gai, M., Garabato, D., Garcia-Gutierrez, A., García-Torres, M., Garofalo, A., Gavras, P., Gerlach, E., Geyer, R., Giacobbe, P., Gilmore, G., Girona, S., Giuffrida, G., Gomel, R., Gomez, A., Gonzalez-Santamaria, I., González-Vidal, J. J., Granvik, M., Gutiérrez-Sánchez, R., Guy, L. P., Hauser, M., Haywood, M., Helmi, A., Hidalgo, S. L., Hilger, T., H ladczuk, N., Hobbs, D., Holland, G., Huckle, H. E., Jasniewicz, G., Jonker, P. G., Juaristi Campillo, J., Julbe, F., Karbevska, L., Kervella, P., Khanna, S., Kochoska, A., Kontizas, M., Kordopatis, G., Korn, A. J., Kostrzewa-Rutkowska, Z., Kruszyńska, K., Lambert, S., Lanza, A. F., Lasne, Y., Le Campion, J. F., Le Fustec, Y., Lebreton, Y., Lebzelter, T., Leccia, S., Leclerc, N., Lecoeur-Taibi, I., Liao, S., Licata, E., Lindstrøm, E. P., Lister, T. A., Livanou, E., Lobel, A., Madrero Pardo, P., Managau, S., Mann, R. G., Marchant, J. M., Marconi, M., Marcos Santos, M. M. S., Marinoni, S., Marocco, F., Marshall, D. J., Martin Polo, L., Martín-Fleitas, J. M., Masip, A., Massari, D., Mastrobuono-Battisti, A., Mazeh, T., McMillan, P. J., Messina, S., Michalik, D., Millar, N. R., Mints, A., Molina, D., Molinaro, R., Molnár, L., Montegriffo, P., Mor, R., Morbidelli, R., Morel, T., Morris, D., Mulone, A. F., Munoz, D., Muraveva, T., Murphy, C. P., Musella, I., Noval, L., Ordénovic, C., Orrù, G., Osinde, J., Pagani, C., Pagano, I., Palaversa, L., Palicio, P. A., Panahi, A., Pawlak, M., Peñalosa Esteller, X., Penttilä, A., Piersimoni, A. M., Pineau, F. X., Plachy, E., Plum, G., Poggio, E., Poretti, E., Poujoulet, E., Prša, A., Pulone, L., Racero, E., Ragaini, S., Rainer, M., Raiteri, C. M., Rambaux, N., Ramos, P., Ramos-Lerate, M., Re Fiorentin, P., Regibo, S., Reylé, C., Ripepi, V., Riva, A., Rixon, G., Robichon, N., Robin, C., Roelens, M., Rohrbasser, L., Romero-Gómez, M., Rowell, N., Royer, F., Rybicki, K. A., Sadowski, G., Sagristà Sellés, A., Sahlmann, J., Salgado, J., Salguero, E., Samaras, N., Sanchez Gimenez, V., Sanna, N., Santoveña, R., Sarasso, M., Schultheis, M., Sciacca, E., Segol, M., Segovia, J. C., Ségransan, D., Semeux,

- D., Shahaf, S., Siddiqui, H. I., Siebert, A., Siltala, L., Slezak, E., Smart, R. L., Solano, E., Solitro, F., Souami, D., Souchay, J., Spagna, A., Spoto, F., Steele, I. A., Steidelmüller, H., Stephenson, C. A., Süveges, M., Szabados, L., Szegedi-Elek, E., Taris, F., Tauran, G., Taylor, M. B., Teixeira, R., Thuillot, W., Tonello, N., Torra, F., Torra, J., Turon, C., Unger, N., Vaillant, M., van Dillen, E., Vanel, O., Vecchiato, A., Viala, Y., Vicente, D., Voutsinas, S., Weiler, M., Wevers, T., Wyrzykowski, L., Yoldas, A., Yvard, P., Zhao, H., Zorec, J., Zucker, S., Zurbach, C., and Zwitter, T. (2021). Gaia Early Data Release 3. Summary of the contents and survey properties., 649:A1.
- Gao, P., Piette, A. A. A., Steinrueck, M. E., Nixon, M. C., Zhang, M., Kempton,
 E. M. R., Bean, J. L., Rauscher, E., Parmentier, V., Batalha, N. E., Savel, A. B.,
 Arnold, K. E., Roman, M. T., Malsky, I., and Taylor, J. (2023). The Hazy and
 Metal-rich Atmosphere of GJ 1214 b Constrained by Near- and Mid-infrared
 Transmission Spectroscopy. , 951(2):96.
- Gelman, A. and Rubin, D. B. (1992). Inference from Iterative Simulation Using Multiple Sequences. *Statistical Science*, 7:457–472.
- Giacalone, S., Dressing, C. D., Hedges, C., Kostov, V. B., Collins, K. A., Jensen, E. L. N., Yahalomi, D. A., Bieryla, A., Ciardi, D. R., Howell, S. B., Lillo-Box, J., Barkaoui, K., Winters, J. G., Matthews, E., Livingston, J. H., Quinn, S. N., Safonov, B. S., Cadieux, C., Furlan, E., Crossfield, I. J. M., Mandell, A. M., Gilbert, E. A., Kruse, E., Quintana, E. V., Ricker, G. R., Seager, S., Winn, J. N., Jenkins, J. M., Duffy Adkins, B., Baker, D., Barclay, T., Barrado, D., Batalha, N. M., Belinski, A. A., Benkhaldoun, Z., Buchhave, L. A., Cacciapuoti, L., Charbonneau, D., Chontos, A., Christiansen, J. L., Cloutier, R., Collins, K. I., Conti, D. M., Cutting, N., Dixon, S., Doyon, R., Mufti, M. E., Esparza-Borges, E., Essack, Z., Fukui, A., Gan, T., Gary, K., Ghachoui, M., Gillon, M., Girardin, E., Glidden, A., Gonzales, E. J., Guerra, P., Horch, E. P., He lminiak, K. G., Howard, A. W., Huber, D., Irwin, J. M., Isopi, G., Jehin, E., Kagetani, T., Kane, S. R., Kawauchi, K., Kielkopf, J. F., Lewin, P., Luker, L., Lund, M. B., Mallia, F.,

- Mao, S., Massey, B., Matson, R. A., Mireles, I., Mori, M., Murgas, F., Narita, N., O'Dwyer, T., Petigura, E. A., Polanski, A. S., Pozuelos, F. J., Palle, E., Parviainen, H., Plavchan, P. P., Relles, H. M., Robertson, P., Rose, M. E., Rowden, P., Roy, A., Savel, A. B., Schlieder, J. E., Schnaible, C., Schwarz, R. P., Sefako, R., Selezneva, A., Skinner, B., Stockdale, C., Strakhov, I. A., Tan, T.-G., Torres, G., Tronsgaard, R., Twicken, J. D., Vermilion, D., Waite, I. A., Walter, B., Wang, G., Ziegler, C., and Zou, Y. (2022). Validation of 13 Hot and Potentially Terrestrial TESS Planets., 163(2):99.
- Gilbertson, C., Ford, E. B., Jones, D. E., and Stenning, D. C. (2020). Toward Extremely Precise Radial Velocities. II. A Tool for Using Multivariate Gaussian Processes to Model Stellar Activity., 905(2):155.
- Ginzburg, S., Schlichting, H. E., and Sari, R. (2016). Super-Earth Atmospheres: Self-consistent Gas Accretion and Retention., 825(1):29.
- Ginzburg, S., Schlichting, H. E., and Sari, R. (2018). Core-powered mass-loss and the radius distribution of small exoplanets. , 476(1):759–765.
- Goffo, E., Gandolfi, D., Egger, J. A., Mustill, A. J., Albrecht, S. H., Hirano, T., Kochukhov, O., Astudillo-Defru, N., Barragan, O., Serrano, L. M., Hatzes, A. P., Alibert, Y., Guenther, E., Dai, F., Lam, K. W. F., Csizmadia, S., Smith, A. M. S., Fossati, L., Luque, R., Rodler, F., Winther, M. L., Rørsted, J. L., Alarcon, J., Bonfils, X., Cochran, W. D., Deeg, H. J., Jenkins, J. M., Korth, J., Livingston, J. H., Meech, A., Murgas, F., Orell-Miquel, J., Osborne, H. L. M., Palle, E., Persson, C. M., Redfield, S., Ricker, G. R., Seager, S., Vanderspek, R., Van Eylen, V., and Winn, J. N. (2023). Company for the Ultra-high Density, Ultra-short Period Sub-Earth GJ 367 b: Discovery of Two Additional Low-mass Planets at 11.5 and 34 Days., 955(1):L3.
- Goldreich, P. and Tremaine, S. (1980). Disk-satellite interactions. , 241:425–441.
- González, D. P., Astudillo-Defru, N., and Mennickent, R. E. (2024). Stellar Activity

- or a Planet? Revisiting dubious planetary signals in M-dwarf systems. *Boletin de la Asociacion Argentina de Astronomia La Plata Argentina*, 65:36–39.
- Gray, D. F. (2008). *The Observation and Analysis of Stellar Photospheres*. Cambridge University Press.
- Green, G. M., Schlafly, E., Zucker, C., Speagle, J. S., and Finkbeiner, D. (2019). A 3D Dust Map Based on Gaia, Pan-STARRS 1, and 2MASS., 887(1):93.
- Gupta, A., Nicholson, L., and Schlichting, H. E. (2022). Properties of the radius valley around low mass stars: predictions from the core-powered mass-loss mechanism. *Monthly Notices of the Royal Astronomical Society*, 516(3):4585–4593.
- Gupta, A. and Schlichting, H. E. (2019). Sculpting the valley in the radius distribution of small exoplanets as a by-product of planet formation: the core-powered massloss mechanism. *Monthly Notices of the Royal Astronomical Society*, 487(1):24–33.
- Gupta, A. and Schlichting, H. E. (2021). Caught in the Act: Core-powered Mass-loss Predictions for Observing Atmospheric Escape. *arXiv:2103.08785 [astro-ph]*. arXiv: 2103.08785.
- Gupta, A. F. and Bedell, M. (2024). Fishing for Planets: A Comparative Analysis of EPRV Survey Performance in the Presence of Correlated Noise., 168(1):29.
- Hale, A. and Doyle, L. R. (1994). The Photometric Method of Extrasolar Planet Detection Revisited. , 212(1-2):335–348.
- Hall, R. D., Thompson, S. J., Handley, W., and Queloz, D. (2018). On the Feasibility of Intense Radial Velocity Surveys for Earth-Twin Discoveries. , 479(3):2968–2987.
- Hara, N. C., Boué, G., Laskar, J., Delisle, J. B., and Unger, N. (2019). Bias and robustness of eccentricity estimates from radial velocity data. , 489(1):738–762.
- Hatzes, A. P. (2019). The Doppler Method for the Detection of Exoplanets.

- Hatzes, A. P., Dvorak, R., Wuchterl, G., Guterman, P., Hartmann, M., Fridlund, M., Gandolfi, D., Guenther, E., and Pätzold, M. (2010). An investigation into the radial velocity variations of CoRoT-7., 520:A93.
- Hatzes, A. P. and Rauer, H. (2015). A Definition for Giant Planets Based on the Mass-Density Relationship. , 810(2):L25.
- Haywood, R. D., Collier Cameron, A., Queloz, D., Barros, S. C. C., Deleuil, M., Fares, R., Gillon, M., Lanza, A. F., Lovis, C., Moutou, C., Pepe, F., Pollacco, D., Santerne, A., Ségransan, D., and Unruh, Y. C. (2014). Planets and stellar activity: hide and seek in the CoRoT-7 system. *Monthly Notices of the Royal Astronomical Society*, 443(3):2517–2531.
- Hidalgo, S. L., Pietrinferni, A., Cassisi, S., Salaris, M., Mucciarelli, A., Savino, A., Aparicio, A., Silva Aguirre, V., and Verma, K. (2018). The Updated BaSTI Stellar Evolution Models and Isochrones. I. Solar-scaled Calculations. , 856(2):125.
- Ho, C. S. K., Rogers, J. G., Van Eylen, V., Owen, J. E., and Schlichting, H. E. (2024). Shallower radius valley around low-mass hosts: evidence for icy planets, collisions, or high-energy radiation scatter. , 531(3):3698–3714.
- Ho, C. S. K. and Van Eylen, V. (2023). A deep radius valley revealed by Kepler short cadence observations. *Monthly Notices of the Royal Astronomical Society*, 519(3):4056–4073. _eprint: https://academic.oup.com/mnras/article-pdf/519/3/4056/48617644/stac3802.pdf.
- Hoffman, M. D. and Gelman, A. (2014). The no-u-turn sampler: adaptively setting path lengths in hamiltonian monte carlo. *Journal of Machine Learning Research*, 15(1):1593–1623.
- Husser, T. O., Wende-von Berg, S., Dreizler, S., Homeier, D., Reiners, A., Barman,T., and Hauschildt, P. H. (2013). A new extensive library of PHOENIX stellar atmospheres and synthetic spectra. , 553:A6.

- Izumiura, H. (1999). HIDES: a high dispersion echelle spectrograph. *Publications* of the Yunnan Observatory, pages 77–81.
- Jackson, J. M., Dawson, R. I., Shannon, A., and Petrovich, C. (2021). Observable Predictions from Perturber-coupled High-eccentricity Tidal Migration of Warm Jupiters. arXiv:2102.03427 [astro-ph]. arXiv: 2102.03427.
- Jenkins, J. M., Twicken, J. D., McCauliff, S., Campbell, J., Sanderfer, D., Lung,
 D., Mansouri-Samani, M., Girouard, F., Tenenbaum, P., Klaus, T., Smith, J. C.,
 Caldwell, D. A., Chacon, A. D., Henze, C., Heiges, C., Latham, D. W., Morgan, E.,
 Swade, D., Rinehart, S., and Vanderspek, R. (2016). The TESS science processing
 operations center. In , volume 9913 of *Society of Photo-Optical Instrumentation*Engineers (SPIE) Conference Series, page 99133E.
- Jones, D. E., Stenning, D. C., Ford, E. B., Wolpert, R. L., Loredo, T. J., Gilbertson, C., and Dumusque, X. (2017). Improving Exoplanet Detection Power: Multivariate Gaussian Process Models for Stellar Activity. arXiv e-prints, page arXiv:1711.01318.
- Jones, M. I., Jenkins, J. S., Bluhm, P., Rojo, P., and Melo, C. H. F. (2014). The properties of planets around giant stars. , 566:A113.
- Jones, M. I., Jenkins, J. S., Rojo, P., Olivares, F., and Melo, C. H. F. (2015). Giant planets around two intermediate-mass evolved stars and confirmation of the planetary nature of HIP 67851c., 580:A14.
- Kaufer, A. and Pasquini, L. (1998). FEROS: the new fiber-linked echelle spectrograph for the ESO 1.52-m telescope. In D'Odorico, S., editor, *Optical Astronomical Instrumentation*, volume 3355 of *Society of Photo-Optical Instrumentation Engineers (SPIE) Conference Series*, pages 844–854.
- Kaushik, M., Mattoo, A., and Rastogi, R. (2024). Exoplanet detection: A detailed analysis.

- Kempton, E. M. R., Bean, J. L., Louie, D. R., Deming, D., Koll, D. D. B., Mansfield, M., Christiansen, J. L., López-Morales, M., Swain, M. R., Zellem, R. T., Ballard, S., Barclay, T., Barstow, J. K., Batalha, N. E., Beatty, T. G., Berta-Thompson, Z., Birkby, J., Buchhave, L. A., Charbonneau, D., Cowan, N. B., Crossfield, I., de Val-Borro, M., Doyon, R., Dragomir, D., Gaidos, E., Heng, K., Hu, R., Kane, S. R., Kreidberg, L., Mallonn, M., Morley, C. V., Narita, N., Nascimbeni, V., Pallé, E., Quintana, E. V., Rauscher, E., Seager, S., Shkolnik, E. L., Sing, D. K., Sozzetti, A., Stassun, K. G., Valenti, J. A., and von Essen, C. (2018). A Framework for Prioritizing the TESS Planetary Candidates Most Amenable to Atmospheric Characterization., 130(993):114401.
- Kempton, E. M. R., Lessard, M., Malik, M., Rogers, L. A., Futrowsky, K. E., Ih, J., Marounina, N., and Romero-Mirza, C. E. (2023). Where are the Water Worlds?: Self-consistent Models of Water-rich Exoplanet Atmospheres. , 953(1):57.
- Klein, B., Aigrain, S., Cretignier, M., Al Moulla, K., Dumusque, X., Barragán, O.,
 Yu, H., Mortier, A., Rescigno, F., Cameron, A. C., López-Morales, M., Meunier,
 N., Sozzetti, A., and O'Sullivan, N. K. (2024). Investigating stellar activity
 through eight years of Sun-as-a-star observations. , 531(4):4238–4262.
- Knudstrup, E., Albrecht, S. H., Winn, J. N., Gandolfi, D., Zanazzi, J. J., Persson,
 C. M., Fridlund, M., Marcussen, M. L., Chontos, A., Keniger, M. A. F., Eisner,
 N. L., Bieryla, A., Isaacson, H., Howard, A. W., Hirsch, L. A., Murgas, F., Narita,
 N., Palle, E., Kawai, Y., and Baker, D. (2024). Obliquities of exoplanet host
 stars: Nineteen new and updated measurements, and trends in the sample of 205
 measurements., 690:A379.
- Knutson, H. A., Fulton, B. J., Montet, B. T., Kao, M., Ngo, H., Howard, A. W.,
 Crepp, J. R., Hinkley, S., Bakos, G. Á., Batygin, K., Johnson, J. A., Morton,
 T. D., and Muirhead, P. S. (2014). Friends of Hot Jupiters. I. A Radial Velocity
 Search for Massive, Long-period Companions to Close-in Gas Giant Planets.,
 785(2):126.

- Korth, J., Gandolfi, D., Šubjak, J., Howard, S., Ataiee, S., Collins, K. A., Quinn, S. N., Mustill, A. J., Guillot, T., Lodieu, N., Smith, A. M. S., Esposito, M., Rodler, F., Muresan, A., Abe, L., Albrecht, S. H., Alqasim, A., Barkaoui, K., Beck, P. G., Burke, C. J., Butler, R. P., Conti, D. M., Collins, K. I., Crane, J. D., Dai, F., Deeg, H. J., Evans, P., Grziwa, S., Hatzes, A. P., Hirano, T., Horne, K., Huang, C. X., Jenkins, J. M., Kabáth, P., Kielkopf, J. F., Knudstrup, E., Latham, D. W., Livingston, J., Luque, R., Mathur, S., Murgas, F., Osborne, H. L. M., Palle, E., Persson, C. M., Rodriguez, J. E., Rose, M., Rowden, P., Schwarz, R. P., Seager, S., Serrano, L. M., Sha, L., Shectman, S. A., Shporer, A., Srdoc, G., Stockdale, C., Tan, T. G., Teske, J. K., Van Eylen, V., Vanderburg, A., Vanderspek, R., Wang, S. X., and Winn, J. N. (2023). TOI-1130: A photodynamical analysis of a hot Jupiter in resonance with an inner low-mass planet., 675:A115.
- Kosiarek, M. R. and Crossfield, I. J. M. (2020). Photometry as a Proxy for Stellar Activity in Radial Velocity Analyses., 159(6):271.
- Kuchner, M. J. (2003). Volatile-rich Earth-Mass Planets in the Habitable Zone. , 596(1):L105–L108.
- Kuerster, M., Schmitt, J. H. M. M., Cutispoto, G., and Dennerl, K. (1997). ROSAT and AB Doradus: the first five years., 320:831–839.
- Kurucz, R. L. (2013). ATLAS12: Opacity sampling model atmosphere program. Astrophysics Source Code Library.
- Lam, C., Bedell, M., Zhao, L. L., Gupta, A. F., and Ballard, S. A. (2024). Gaspery: Optimized Scheduling of Radial Velocity Follow-up Observations for Active Host Stars., 168(5):200.
- Lee, C.-H. (2018). Exoplanets: past, present, and future. *arXiv:1804.08907* [astro-ph]. arXiv: 1804.08907.
- Léger, A., Selsis, F., Sotin, C., Guillot, T., Despois, D., Mawet, D., Ollivier, M., Labèque, A., Valette, C., Brachet, F., Chazelas, B., and Lammer, H. (2004). A new family of planets? "Ocean-Planets". , 169(2):499–504.

- Liang, Y., Winn, J. N., and Melchior, P. (2024). AESTRA: Deep Learning for Precise Radial Velocity Estimation in the Presence of Stellar Activity., 167(1):23.
- Lin, D. N. C. and Papaloizou, J. (1986). On the Tidal Interaction between Protoplanets and the Protoplanetary Disk. III. Orbital Migration of Protoplanets., 309:846.
- Lisogorskyi, M., Boro Saikia, S., Jeffers, S. V., Jones, H. R. A., Morin, J., Mengel, M., Reiners, A., Vidotto, A. A., and Petit, P. (2020). The impact of unresolved magnetic spots on high-precision radial velocity measurements. , 497(3):4009–4021.
- Lopez, E. D. and Fortney, J. J. (2013). The Role of Core Mass in Controlling Evaporation: The Kepler Radius Distribution and the Kepler-36 Density Dichotomy., 776(1):2.
- Lopez, E. D. and Fortney, J. J. (2014). Understanding the Mass-Radius Relation for Sub-neptunes: Radius as a Proxy for Composition., 792:1.
- Lopez, E. D. and Rice, K. (2018). How formation time-scales affect the period dependence of the transition between rocky super-earths and gaseous subneptunesand implications for $\eta \oplus$. *Monthly Notices of the Royal Astronomical Society*, 479(4):5303–5311.
- Lovis, C. and Fischer, D. (2010). *Radial Velocity Techniques for Exoplanets*, pages 27–53.
- Lovis, C. and Pepe, F. (2007). A new list of thorium and argon spectral lines in the visible. , 468(3):1115–1121.
- Lovis, C., Pepe, F., Bouchy, F., Lo Curto, G., Mayor, M., Pasquini, L., Queloz, D., Rupprecht, G., Udry, S., and Zucker, S. (2006). The exoplanet hunter HARPS: unequalled accuracy and perspectives toward 1 cm s⁻¹ precision. In McLean, I. S. and Iye, M., editors, *Ground-based and Airborne Instrumentation for Astron-*

- omy, volume 6269 of Society of Photo-Optical Instrumentation Engineers (SPIE) Conference Series, page 62690P.
- Lubin, J., Van Zandt, J., Holcomb, R., Weiss, L. M., Petigura, E. A., Robertson, P., Akana Murphy, J. M., Scarsdale, N., Batygin, K., Polanski, A. S., Batalha, N. M., Crossfield, I. J. M., Dressing, C., Fulton, B., Howard, A. W., Huber, D., Isaacson, H., Kane, S. R., Roy, A., Beard, C., Blunt, S., Chontos, A., Dai, F., Dalba, P. A., Gary, K., Giacalone, S., Hill, M. L., Mayo, A., Močnik, T., Kosiarek, M. R., Rice, M., Rubenzahl, R. A., Latham, D. W., Seager, S., Winn, J. N., and Gary, K. (2022). TESS-Keck Survey. IX. Masses of Three Sub-Neptunes Orbiting HD 191939 and the Discovery of a Warm Jovian plus a Distant Substellar Companion. , 163(2):101.
- Lucy, L. B. and Sweeney, M. A. (1971). Spectroscopic binaries with circular orbits. , 76:544–556.
- Luger, R., Agol, E., Foreman-Mackey, D., Fleming, D. P., Lustig-Yaeger, J., and Deitrick, R. (2019). starry: Analytic Occultation Light Curves., 157:64.
- Luo, H., Dorn, C., and Deng, J. (2024). The interior as the dominant water reservoir in super-Earths and sub-Neptunes. *Nature Astronomy*, 8:1399–1407.
- Luque, R., Pallé, E., Kossakowski, D., Dreizler, S., Kemmer, J., Espinoza, N.,
 Burt, J., Anglada-Escudé, G., Béjar, V. J. S., Caballero, J. A., Collins, K. A.,
 Collins, K. I., Cortés-Contreras, M., Díez-Alonso, E., Feng, F., Hatzes, A.,
 Hellier, C., Henning, T., Jeffers, S. V., Kaltenegger, L., Kürster, M., Madden,
 J., Molaverdikhani, K., Montes, D., Narita, N., Nowak, G., Ofir, A., Oshagh,
 M., Parviainen, H., Quirrenbach, A., Reffert, S., Reiners, A., Rodríguez-López,
 C., Schlecker, M., Stock, S., Trifonov, T., Winn, J. N., Zapatero Osorio, M. R.,
 Zechmeister, M., Amado, P. J., Anderson, D. R., Batalha, N. E., Bauer, F. F.,
 Bluhm, P., Burke, C. J., Butler, R. P., Caldwell, D. A., Chen, G., Crane, J. D.,
 Dragomir, D., Dressing, C. D., Dynes, S., Jenkins, J. M., Kaminski, A., Klahr,
 H., Kotani, T., Lafarga, M., Latham, D. W., Lewin, P., McDermott, S., Montañés-

- Rodríguez, P., Morales, J. C., Murgas, F., Nagel, E., Pedraz, S., Ribas, I., Ricker, G. R., Rowden, P., Seager, S., Shectman, S. A., Tamura, M., Teske, J., Twicken, J. D., Vanderspeck, R., Wang, S. X., and Wohler, B. (2019). Planetary system around the nearby M dwarf GJ 357 including a transiting, hot, Earth-sized planet optimal for atmospheric characterization. , 628:A39.
- Luque, R. and Pallé, E. (2022). Density, not radius, separates rocky and water-rich small planets orbiting M dwarf stars. *Science*, 377(6611):1211–1214. Publisher: American Association for the Advancement of Science.
- Luque, R., Serrano, L. M., Molaverdikhani, K., Nixon, M. C., Livingston, J. H., Guenther, E. W., Pallé, E., Madhusudhan, N., Nowak, G., Korth, J., Cochran, W. D., Hirano, T., Chaturvedi, P., Goffo, E., Albrecht, S., Barragán, O., Briceño, C., Cabrera, J., Charbonneau, D., Cloutier, R., Collins, K. A., Collins, K. I., Colón, K. D., Crossfield, I. J. M., Csizmadia, S., Dai, F., Deeg, H. J., Esposito, M., Fridlund, M., Gandolfi, D., Georgieva, I., Glidden, A., Goeke, R. F., Grziwa, S., Hatzes, A. P., Henze, C. E., Howell, S. B., Irwin, J., Jenkins, J. M., Jensen, E. L. N., Kábath, P., Kidwell, R. C., Kielkopf, J. F., Knudstrup, E., Lam, K. W. F., Latham, D. W., Lissauer, J. J., Mann, A. W., Matthews, E. C., Mireles, I., Narita, N., Paegert, M., Persson, C. M., Redfield, S., Ricker, G. R., Rodler, F., Schlieder, J. E., Scott, N. J., Seager, S., Šubjak, J., Tan, T. G., Ting, E. B., Vanderspek, R., Van Eylen, V., Winn, J. N., and Ziegler, C. (2021). A planetary system with two transiting mini-Neptunes near the radius valley transition around the bright M dwarf TOI-776., 645:A41.
- Madhusudhan, N., Sarkar, S., Constantinou, S., Holmberg, M., Piette, A. A. A., and Moses, J. I. (2023). Carbon-bearing Molecules in a Possible Hycean Atmosphere. , 956(1):L13.
- Malavolta, L., Mayo, A. W., Louden, T., Rajpaul, V. M., Bonomo, A. S., Buchhave, L. A., Kreidberg, L., Kristiansen, M. H., Lopez-Morales, M., Mortier, A., Vanderburg, A., Coffinet, A., Ehrenreich, D., Lovis, C., Bouchy, F., Charbonneau, D., Ciardi, D. R., Collier Cameron, A., Cosentino, R., Crossfield, I. J. M., Damasso,

- M., Dressing, C. D., Dumusque, X., Everett, M. E., Figueira, P., Fiorenzano, A. F. M., Gonzales, E. J., Haywood, R. D., Harutyunyan, A., Hirsch, L., Howell, S. B., Johnson, J. A., Latham, D. W., Lopez, E., Mayor, M., Micela, G., Molinari, E., Nascimbeni, V., Pepe, F., Phillips, D. F., Piotto, G., Rice, K., Sasselov, D., Ségransan, D., Sozzetti, A., Udry, S., and Watson, C. (2018). An Ultra-short Period Rocky Super-Earth with a Secondary Eclipse and a Neptune-like Companion around K2-141., 155(3):107.
- Malavolta, L., Nascimbeni, V., Piotto, G., Quinn, S. N., Borsato, L., Granata, V., Bonomo, A. S., Marzari, F., Bedin, L. R., Rainer, M., Desidera, S., Lanza, A. F., Poretti, E., Sozzetti, A., White, R. J., Latham, D. W., Cunial, A., Libralato, M., Nardiello, D., Boccato, C., Claudi, R. U., Cosentino, R., Covino, E., Gratton, R., Maggio, A., Micela, G., Molinari, E., Pagano, I., Smareglia, R., Affer, L., Andreuzzi, G., Aparicio, A., Benatti, S., Bignamini, A., Borsa, F., Damasso, M., Di Fabrizio, L., Harutyunyan, A., Esposito, M., Fiorenzano, A. F. M., Gandolfi, D., Giacobbe, P., González Hernández, J. I., Maldonado, J., Masiero, S., Molinaro, M., Pedani, M., and Scandariato, G. (2016). The GAPS programme with HARPS-N at TNG. XI. Pr 0211 in M 44: the first multi-planet system in an open cluster., 588:A118.
- Malsky, I., Rauscher, E., Stevenson, K., Savel, A. B., Steinrueck, M. E., Gao, P.,
 Kempton, E. M. R., Roman, M. T., Bean, J. L., Zhang, M., Parmentier, V., Piette,
 A. A. A., and Kataria, T. (2025). Clouds and Hazes in GJ 1214 b's Metal-rich
 Atmosphere., 169(4):221.
- Mamajek, E. E. and Hillenbrand, L. A. (2008). Improved Age Estimation for Solar-Type Dwarfs Using Activity-Rotation Diagnostics. , 687(2):1264–1293.
- Masson, A., Vinatier, S., Bézard, B., López-Puertas, M., Lampón, M., Debras, F.,
 Carmona, A., Klein, B., Artigau, E., Dethier, W., Pelletier, S., Hood, T., Allart,
 R., Bourrier, V., Cadieux, C., Charnay, B., Cowan, N. B., Cook, N. J., Delfosse,
 X., Donati, J. F., Gu, P. G., Hébrard, G., Martioli, E., Moutou, C., Venot, O.,

- and Wyttenbach, A. (2024). Probing atmospheric escape through metastable He I triplet lines in 15 exoplanets observed with SPIRou., 688:A179.
- Maxted, P. F. L., Anderson, D. R., Burleigh, M. R., Cameron, A. C., Heber, U., Gänsicke, B. T., Geier, S., Kupfer, T., Marsh, T. R., Nelemans, G., O'Toole, S. J., Østensen, R. H., Smalley, B., and West, R. G. (2011). Discovery of a stripped red giant core in a bright eclipsing binary system72. *Monthly Notices of the Royal Astronomical Society*, 418(2):1156–1164.
- Maxted, P. F. L., Anderson, D. R., Collier Cameron, A., Hellier, C., Queloz, D.,
 Smalley, B., Street, R. A., Triaud, A. H. M. J., West, R. G., Gillon, M., Lister,
 T. A., Pepe, F., Pollacco, D., Ségransan, D., Smith, A. M. S., and Udry, S. (2011).
 WASP-41b: A Transiting Hot Jupiter Planet Orbiting a Magnetically Active G8V
 Star., 123(903):547.
- Mayor, M., Pepe, F., Queloz, D., Bouchy, F., Rupprecht, G., Lo Curto, G., Avila, G.,
 Benz, W., Bertaux, J. L., Bonfils, X., Dall, T., Dekker, H., Delabre, B., Eckert,
 W., Fleury, M., Gilliotte, A., Gojak, D., Guzman, J. C., Kohler, D., Lizon, J. L.,
 Longinotti, A., Lovis, C., Megevand, D., Pasquini, L., Reyes, J., Sivan, J. P.,
 Sosnowska, D., Soto, R., Udry, S., van Kesteren, A., Weber, L., and Weilenmann,
 U. (2003). Setting New Standards with HARPS. *The Messenger*, 114:20–24.
- Mayor, M. and Queloz, D. (1995). A Jupiter-mass companion to a solar-type star., 378:355–359.
- McLaughlin, D. B. (1924). Some results of a spectrographic study of the Algol system., 60:22–31.
- Meunier, N. (2021). Stellar variability in radial velocity. *arXiv:2104.06072* [astro-ph]. arXiv: 2104.06072.
- Meunier, N. (2024). Impact of stellar variability on exoplanet detectability and characterisation. *Comptes Rendus Physique*, 24(S2):140.

- Meunier, N. and Lagrange, A. M. (2013). Using the Sun to estimate Earth-like planets detection capabilities. IV. Correcting for the convective component., 551:A101.
- Meunier, N. and Lagrange, A. M. (2020). The effects of granulation and supergranulation on Earth-mass planet detectability in the habitable zone around F6-K4 stars., 642:A157.
- Meunier, N., Lagrange, A. M., and Borgniet, S. (2017). A new method of correcting radial velocity time series for inhomogeneous convection. , 607:A6.
- Mikal-Evans, T., Madhusudhan, N., Dittmann, J., Guenther, M. N., Welbanks, L., Van Eylen, V., Crossfield, I. J. M., Daylan, T., and Kreidberg, L. (2022). Hubble Space Telescope transmission spectroscopy for the temperate sub-Neptune TOI-270d: a possible hydrogen-rich atmosphere containing water vapour. *arXiv e-prints*, page arXiv:2211.15576.
- Mills, S. M. and Mazeh, T. (2017). The Planetary Mass-Radius Relation and Its Dependence on Orbital Period as Measured by Transit Timing Variations and Radial Velocities., 839(1):L8.
- Mitchell, E. G. and Madhusudhan, N. (2025). Prospects for biological evolution on Hycean worlds. , 538(3):1653–1662.
- Mizuno, H. (1980). Formation of the Giant Planets. *Progress of Theoretical Physics*, 64(2):544–557.
- Montet, B. T. (2018). Unbiased Inference of the Masses of Transiting Planets from Radial Velocity Follow-up. *Research Notes of the American Astronomical Society*, 2(2):28.
- Mordasini, C. and Burn, R. (2024). Planet Formation—Observational Constraints, Physical Processes, and Compositional Patterns. *Reviews in Mineralogy and Geochemistry*, 90(1):55–112.
- Morton, T. D. (2015). isochrones: Stellar model grid package.

- Mousavi-Sadr, M., Jassur, D. M., and Gozaliasl, G. (2023). Revisiting mass-radius relationships for exoplanet populations: a machine learning insight., 525(3):3469–3485.
- Mugrauer, M. and Neuhäuser, R. (2005). Gl86B: a white dwarf orbits an exoplanet host star., 361(1):L15–L19.
- Müller, S. and Helled, R. (2023). Warm giant exoplanet characterisation: current state, challenges and outlook. *Frontiers in Astronomy and Space Sciences*, 10:1179000.
- Murdoch, K. A., Hearnshaw, J. B., and Clark, M. (1993). A Search for Substellar Companions to Southern Solar-Type Stars. , 413:349.
- Nava, C., López-Morales, M., Haywood, R. D., and Giles, H. A. C. (2019). Exoplanet Imitators: A Test of Stellar Activity Behavior in Radial Velocity Signals. *The Astronomical Journal*, 159(1):23.
- Neil, A. R. and Rogers, L. A. (2018). Host Star Dependence of Small Planet Mass-Radius Distributions., 858(1):58.
- Neil, A. R. and Rogers, L. A. (2020). A Joint Mass-Radius-Period Distribution of Exoplanets., 891(1):12.
- Newman, P. D., Plavchan, P., Burt, J. A., Teske, J., Mamajek, E. E., Leifer, S., Gaudi, B. S., Blackwood, G., and Morgan, R. (2023). Simulations for Planning Next-generation Exoplanet Radial Velocity Surveys., 165(4):151.
- Nicholson, B. A. and Aigrain, S. (2022). Quasi-periodic Gaussian processes for stellar activity: From physical to kernel parameters. , 515(4):5251–5266.
- Nielsen, J., Johansen, A., Bali, K., and Dorn, C. (2025). A primordial radius valley as a consequence of planet formation. , 695:A184.
- Niraula, P., Redfield, S., Dai, F., Barragán, O., Gandolfi, D., Cauley, P. W., Hirano, T., Korth, J., Smith, A. M. S., Prieto-Arranz, J., Grziwa, S., Fridlund, M., Persson,

- C. M., Justesen, A. B., Winn, J. N., Albrecht, S., Cochran, W. D., Csizmadia, S., Duvvuri, G. M., Endl, M., Hatzes, A. P., Livingston, J. H., Narita, N., Nespral, D., Nowak, G., Pätzold, M., Palle, E., and Van Eylen, V. (2017). Three Super-Earths Transiting the Nearby Star GJ 9827., 154(6):266.
- Nixon, M. C., Piette, A. A. A., Kempton, E. M. R., Gao, P., Bean, J. L., Steinrueck, M. E., Mahajan, A. S., Eastman, J. D., Zhang, M., and Rogers, L. A. (2024). New Insights into the Internal Structure of GJ 1214 b Informed by JWST., 970(2):L28.
- Nocedal, J. and Wright, S. J. (2006). *Numerical Optimization*. Springer, New York, NY, USA, second edition.
- Ohno, K., Schlawin, E., Bell, T. J., Murphy, M. M., Beatty, T. G., Welbanks, L., Greene, T. P., Fortney, J. J., Parmentier, V., Edelman, I. R., Mehta, N., and Rieke, M. J. (2025). A Possible Metal-dominated Atmosphere below the Thick Aerosols of GJ 1214 b Suggested by Its JWST Panchromatic Transmission Spectrum. , 979(1):L7.
- Osborn, H. P., Armstrong, D. J., Adibekyan, V., Collins, K. A., Delgado-Mena, E., Howell, S. B., Hellier, C., King, G. W., Lillo-Box, J., Nielsen, L. D., Otegi, J. F., Santos, N. C., Ziegler, C., Anderson, D. R., Briceño, C., Burke, C., Bayliss, D., Barrado, D., Bryant, E. M., Brown, D. J. A., Barros, S. C. C., Bouchy, F., Caldwell, D. A., Conti, D. M., Díaz, R. F., Dragomir, D., Deleuil, M., Demangeon, O. D. S., Dorn, C., Daylan, T., Figueira, P., Helled, R., Hoyer, S., Jenkins, J. M., Jensen, E. L. N., Latham, D. W., Law, N., Louie, D. R., Mann, A. W., Osborn, A., Pollacco, D. L., Rodriguez, D. R., Rackham, B. V., Ricker, G., Scott, N. J., Sousa, S. G., Seager, S., Stassun, K. G., Smith, J. C., Strøm, P., Udry, S., Villaseñor, J., Vanderspek, R., West, R., Wheatley, P. J., and Winn, J. N. (2021). A hot mini-Neptune in the radius valley orbiting solar analogue HD 110113., 502(4):4842–4857.
- Osborne, H. L. M., Nielsen, L. D., Van Eylen, V., and Barragán, O. (2025). Ho-

- mogeneous planet masses: I. Reanalysis of archival HARPS radial velocities. , 693:A4.
- Osborne, H. L. M., Van Eylen, V., Goffo, E., Gandolfi, D., Nowak, G., Persson, C. M., Livingston, J., Weeks, A., Pallé, E., Luque, R., Hellier, C., Carleo, I., Redfield, S., Hirano, T., Garbaccio Gili, M., Alarcon, J., Barragán, O., Casasayas-Barris, N., Díaz, M. R., Esposito, M., Knudstrup, E., Jenkins, J. S., Murgas, F., Orell-Miquel, J., Rodler, F., Serrano, L., Stangret, M., Albrecht, S. H., Alqasim, A., Cochran, W. D., Deeg, H. J., Fridlund, M., Hatzes, A. P., Korth, J., and Lam, K. W. F. (2024). TOI-544 b: a potential water-world inside the radius valley in a two-planet system. , 527(4):11138–11157.
- Otegi, J. F., Bouchy, F., and Helled, R. (2020). Revisited mass-radius relations for exoplanets below 120 M_{\oplus} ., 634:A43.
- Otegi, J. F., Bouchy, F., Helled, R., Armstrong, D. J., Stalport, M., Psaridi, A., Delisle, J. B., Stassun, K. G., Delgado-Mena, E., Santos, N. C., Hara, N. C., Collins, K., Gandhi, S., Dorn, C., Brogi, M., Fridlund, M., Osborn, H. P., Hoyer, S., Udry, S., Hojjatpanah, S., Nielsen, L. D., Dumusque, X., Adibekyan, V., Conti, D., Schwarz, R., Wang, G., Figueira, P., Lillo-Box, J., Hadjigeorghiou, A., Bayliss, D., Strøm, P. A., Sousa, S. G., Barrado, D., Osborn, A., Barros, S. C. C., Brown, D. J. A., Eastman, J. D., Ciardi, D. R., Vanderburg, A., Goeke, R. F., Guerrero, N. M., Boyd, P. T., Caldwell, D. A., Henze, C. E., McLean, B., Ricker, G., Vanderspek, R., Latham, D. W., Seager, S., Winn, J., and Jenkins, J. M. (2021). TESS and HARPS reveal two sub-Neptunes around TOI 1062., 653:A105.
- Owen, J. E. and Wu, Y. (2013). Kepler Planets: A Tale of Evaporation. , 775(2):105.
- Owen, J. E. and Wu, Y. (2017). The Evaporation Valley in the Kepler Planets. *The Astrophysical Journal*, 847(1):29.
- Palumbo, III, M. L., Ford, E. B., Wright, J. T., Mahadevan, S., Wise, A. W.,

- and Löhner-Böttcher, J. (2022). GRASS: Distinguishing Planet-induced Doppler Signatures from Granulation with a Synthetic Spectra Generator. , 163(1):11.
- Parc, L., Bouchy, F., Venturini, J., Dorn, C., and Helled, R. (2024). From super-Earths to sub-Neptunes: Observational constraints and connections to theoretical models., 688:A59.
- Parviainen, H., Luque, R., and Palle, E. (2024). SPRIGHT: a probabilistic mass-density-radius relation for small planets. , 527(3):5693–5716.
- Pepe, F., Cristiani, S., Rebolo, R., Santos, N., Amorim, A., Avila, G., Benz, W.,
 Bonifacio, P., Cabral, A., Carvas, P., Cirami, R., Coelho, J., Comari, M., Coretti,
 I., Caprio, V., Dekker, H., Delabre, B., Di Marcantonio, P., D'Odorico, V., and
 Zerbi, F. (2010). Espresso: the echelle spectrograph for rocky exoplanets and
 stable spectroscopic observations. *Proc SPIE*, 7735:77350F.
- Pepe, F., Mayor, M., Rupprecht, G., Avila, G., Ballester, P., Beckers, J.-L., Benz, W., Bertaux, J.-L., Bouchy, F., Buzzoni, B., Cavadore, C., Deiries, S., Dekker, H., Delabre, B., D'Odorico, S., Eckert, W., Fischer, J., Fleury, M., George, M., Gilliotte, A., Gojak, D., Guzman, J.-C., Koch, F., Kohler, D., Kotzlowski, H., Lacroix, D., Le Merrer, J., Lizon, J.-L., Lo Curto, G., Longinotti, A., Megevand, D., Pasquini, L., Petitpas, P., Pichard, M., Queloz, D., Reyes, J., Richaud, P., Sivan, J.-P., Sosnowska, D., Soto, R., Udry, S., Ureta, E., van Kesteren, A., Weber, L., Weilenmann, U., Wicenec, A., Wieland, G., Christensen-Dalsgaard, J., Dravins, D., Hatzes, A., Kürster, M., Paresce, F., and Penny, A. (2002). HARPS: ESO's coming planet searcher. Chasing exoplanets with the La Silla 3.6-m telescope. *The Messenger*, 110:9–14.
- Perger, M., Anglada-Escudé, G., Baroch, D., Lafarga, M., Ribas, I., Morales, J. C., Herrero, E., Amado, P. J., Barnes, J. R., Caballero, J. A., Jeffers, S. V., Quirrenbach, A., and Reiners, A. (2023). A machine learning approach for correcting radial velocities using physical observables. , 672:A118.

Perruchot, S., Kohler, D., Bouchy, F., Richaud, Y., Richaud, P., Moreaux, G., Merzougui, M., Sottile, R., Hill, L., Knispel, G., Regal, X., Meunier, J.-P., Ilovaisky, S., Le Coroller, H., Gillet, D., Schmitt, J., Pepe, F., Fleury, M., Sosnowska, D., Vors, P., Mégevand, D., Blanc, P. E., Carol, C., Point, A., Laloge, A., and Brunel, J.-C. (2008). The SOPHIE spectrograph: design and technical key-points for high throughput and high stability. In *Society of Photo-Optical Instrumentation Engineers (SPIE) Conference Series*, volume 7014 of *Society of Photo-Optical Instrumentation Engineers (SPIE) Conference Series*.

Perryman, M. (2011). The Exoplanet Handbook. Cambridge University Press.

Perryman, M. (2018). The Exoplanet Handbook.

- Persson, C. M., Fridlund, M., Barragán, O., Dai, F., Gandolfi, D., Hatzes, A. P., Hirano, T., Grziwa, S., Korth, J., Prieto-Arranz, J., Fossati, L., Van Eylen, V., Justesen, A. B., Livingston, J., Kubyshkina, D., Deeg, H. J., Guenther, E. W., Nowak, G., Cabrera, J., Eigmüller, P., Csizmadia, S., Smith, A. M. S., Erikson, A., Albrecht, S., Sobrino, A., Cochran, W. D., Endl, M., Esposito, M., Fukui, A., Heeren, P., Hidalgo, D., Hjorth, M., Kuzuhara, M., Narita, N., Nespral, D., Palle, E., Pätzold, M., Rauer, H., Rodler, F., and Winn, J. N. (2018). Super-Earth of 8 M₂ in a 2.2-day orbit around the K5V star K2-216., 618:A33.
- Petigura, E. A., Rogers, J. G., Isaacson, H., Owen, J. E., Kraus, A. L., Winn, J. N., MacDougall, M. G., Howard, A. W., Fulton, B., Kosiarek, M. R., Weiss, L. M., Behmard, A., and Blunt, S. (2022). The California-Kepler Survey. X. The Radius Gap as a Function of Stellar Mass, Metallicity, and Age. *The Astronomical Journal*, 163(4):179.
- Petrovich, C. (2015). Steady-state planet migration by the Kozai-Lidov mechanism in stellar binaries. *The Astrophysical Journal*, 799(1):27. arXiv: 1405.0280.
- Petrovich, C. and Tremaine, S. (2016). WARM JUPITERS FROM SECULAR PLANET-PLANET INTERACTIONS. *The Astrophysical Journal*, 829(2):132.

- Piaulet, C., Benneke, B., Almenara, J. M., Dragomir, D., Knutson, H. A., Thorngren,
 D., Peterson, M. S., Crossfield, I. J. M., Kempton, E. M.-R., Kubyshkina, D.,
 Howard, A. W., Angus, R., Isaacson, H., Weiss, L. M., Beichman, C. A., Fortney,
 J. J., Fossati, L., Lammer, H., McCullough, P. R., Morley, C. V., and Wong, I.
 (2022). Evidence for the volatile-rich composition of a 1.5-earth-radius planet.
 Nature Astronomy.
- Pietrinferni, A., Hidalgo, S., Cassisi, S., Salaris, M., Savino, A., Mucciarelli, A., Verma, K., Silva Aguirre, V., Aparicio, A., and Ferguson, J. W. (2021). Updated BaSTI Stellar Evolution Models and Isochrones. II. α -enhanced Calculations. , 908(1):102.
- Piskunov, N. and Valenti, J. A. (2017). Spectroscopy Made Easy: Evolution. , 597:A16.
- Polanski, A. S., Lubin, J., Beard, C., Akana Murphy, J. M., Rubenzahl, R., Hill, M. L., Crossfield, I. J. M., Chontos, A., Robertson, P., Isaacson, H., Kane, S. R., Ciardi, D. R., Batalha, N. M., Dressing, C., Fulton, B., Howard, A. W., Huber, D., Petigura, E. A., Weiss, L. M., Angelo, I., Behmard, A., Blunt, S., Brinkman, C. L., Dai, F., Dalba, P. A., Fetherolf, T., Giacalone, S., Hirsch, L. A., Holcomb, R., Kosiarek, M. R., Mayo, A. W., MacDougall, M. G., Močnik, T., Pidhorodetska, D., Rice, M., Rosenthal, L. J., Scarsdale, N., Turtelboom, E. V., Tyler, D., Van Zandt, J., Yee, S. W., Coria, D. R., Dulz, S. D., Hartman, J. D., Householder, A., Lange, S., Langford, A., Louden, E. M., Siegel, J. C., Gilbert, E. A., Gonzales, E. J., Schlieder, J. E., Boyle, A. W., Christiansen, J. L., Clark, C. A., Fernandes, R. B., Lund, M. B., Savel, A. B., Gill, H., Beichman, C., Matson, R., Matthews, E. C., Furlan, E., Howell, S. B., Scott, N. J., Everett, M. E., Livingston, J. H., Ershova, I. O., Cheryasov, D. V., Safonov, B., Lillo-Box, J., Barrado, D., and Morales-Calderón, M. (2024). The TESS-Keck Survey. XX. 15 New TESS Planets and a Uniform RV Analysis of All Survey Targets., 272(2):32.
- Pollacco, D. L., Skillen, I., Collier Cameron, A., Christian, D. J., Hellier, C., Irwin, J., Lister, T. A., Street, R. A., West, R. G., Anderson, D. R., Clarkson, W. I.,

- Deeg, H., Enoch, B., Evans, A., Fitzsimmons, A., Haswell, C. A., Hodgkin, S., Horne, K., Kane, S. R., Keenan, F. P., Maxted, P. F. L., Norton, A. J., Osborne, J., Parley, N. R., Ryans, R. S. I., Smalley, B., Wheatley, P. J., and Wilson, D. M. (2006). The WASP Project and the SuperWASP Cameras., 118:1407–1418.
- Pollack, J. B., Hubickyj, O., Bodenheimer, P., Lissauer, J. J., Podolak, M., and Greenzweig, Y. (1996). Formation of the Giant Planets by Concurrent Accretion of Solids and Gas., 124(1):62–85.
- Quanz, S. P., Crossfield, I., Meyer, M. R., Schmalzl, E., and Held, J. (2015). Direct detection of exoplanets in the 3-10 μm range with E-ELT/METIS. *International Journal of Astrobiology*, 14(2):279–289.
- Queloz, D., Bouchy, F., Moutou, C., Hatzes, A., Hébrard, G., Alonso, R., Auvergne, M., Baglin, A., Barbieri, M., Barge, P., Benz, W., Bordé, P., Deeg, H. J., Deleuil, M., Dvorak, R., Erikson, A., Ferraz Mello, S., Fridlund, M., Gandolfi, D., Gillon, M., Guenther, E., Guillot, T., Jorda, L., Hartmann, M., Lammer, H., Léger, A., Llebaria, A., Lovis, C., Magain, P., Mayor, M., Mazeh, T., Ollivier, M., Pätzold, M., Pepe, F., Rauer, H., Rouan, D., Schneider, J., Segransan, D., Udry, S., and Wuchterl, G. (2009). The CoRoT-7 planetary system: two orbiting super-Earths., 506(1):303–319.
- Queloz, D., Henry, G. W., Sivan, J. P., Baliunas, S. L., Beuzit, J. L., Donahue, R. A., Mayor, M., Naef, D., Perrier, C., and Udry, S. (2001). No planet for HD 166435. , 379:279–287.
- Queloz, D., Mayor, M., Weber, L., Blécha, A., Burnet, M., Confino, B., Naef, D., Pepe, F., Santos, N., and Udry, S. (2000). The CORALIE survey for southern extra-solar planets. I. A planet orbiting the star Gliese 86., 354:99–102.
- Rafikov, R. R. (2005). Can Giant Planets Form by Direct Gravitational Instability? , 621(1):L69–L72.
- Rajpaul, V., Aigrain, S., Osborne, M. A., Reece, S., and Roberts, S. (2015). A

Gaussian process framework for modelling stellar activity signals in radial velocity data. , 452(3):2269–2291.

- Rasio, F. A. and Ford, E. B. (1996). Dynamical instabilities and the formation of extrasolar planetary systems. *Science*, 274:954–956.
- Rasmussen, C. E. and Williams, C. K. I. (2005). *Gaussian Processes for Machine Learning (Adaptive Computation and Machine Learning)*. The MIT Press.
- Rauer, H., Catala, C., Aerts, C., Appourchaux, T., Benz, W., Brandeker, A., Christensen-Dalsgaard, J., Deleuil, M., Gizon, L., Goupil, M.-J., Güdel, M., Janot-Pacheco, E., Mas-Hesse, M., Pagano, I., Piotto, G., Pollacco, D., Santos, C., Smith, A., Suárez, J.-C., Szabó, R., Udry, S., Adibekyan, V., Alibert, Y., Almenara, J.-M., Amaro-Seoane, P., Eiff, M. A.-v., Asplund, M., Antonello, E., Barnes, S., Baudin, F., Belkacem, K., Bergemann, M., Bihain, G., Birch, A. C., Bonfils, X., Boisse, I., Bonomo, A. S., Borsa, F., Brandão, I. M., Brocato, E., Brun, S., Burleigh, M., Burston, R., Cabrera, J., Cassisi, S., Chaplin, W., Charpinet, S., Chiappini, C., Church, R. P., Csizmadia, S., Cunha, M., Damasso, M., Davies, M. B., Deeg, H. J., Díaz, R. F., Dreizler, S., Dreyer, C., Eggenberger, P., Ehrenreich, D., Eigmüller, P., Erikson, A., Farmer, R., Feltzing, S., de Oliveira Fialho, F., Figueira, P., Forveille, T., Fridlund, M., García, R. A., Giommi, P., Giuffrida, G., Godolt, M., Gomes da Silva, J., Granzer, T., Grenfell, J. L., Grotsch-Noels, A., Günther, E., Haswell, C. A., Hatzes, A. P., Hébrard, G., Hekker, S., Helled, R., Heng, K., Jenkins, J. M., Johansen, A., Khodachenko, M. L., Kislyakova, K. G., Kley, W., Kolb, U., Krivova, N., Kupka, F., Lammer, H., Lanza, A. F., Lebreton, Y., Magrin, D., Marcos-Arenal, P., Marrese, P. M., Marques, J. P., Martins, J., Mathis, S., Mathur, S., Messina, S., Miglio, A., Montalban, J., Montalto, M., Monteiro, M. J. P. F. G., Moradi, H., Moravveji, E., Mordasini, C., Morel, T., Mortier, A., Nascimbeni, V., Nelson, R. P., Nielsen, M. B., Noack, L., Norton, A. J., Ofir, A., Oshagh, M., Ouazzani, R.-M., Pápics, P., Parro, V. C., Petit, P., Plez, B., Poretti, E., Quirrenbach, A., Ragazzoni, R., Raimondo, G., Rainer, M., Reese, D. R., Redmer, R., Reffert, S., Rojas-Ayala, B., Roxburgh, I. W., Salmon,

- S., Santerne, A., Schneider, J., Schou, J., Schuh, S., Schunker, H., Silva-Valio, A., Silvotti, R., Skillen, I., Snellen, I., Sohl, F., Sousa, S. G., Sozzetti, A., Stello, D., Strassmeier, K. G., Švanda, M., Szabó, G. M., Tkachenko, A., Valencia, D., Van Grootel, V., Vauclair, S. D., Ventura, P., Wagner, F. W., Walton, N. A., Weingrill, J., Werner, S. C., Wheatley, P. J., and Zwintz, K. (2014). The PLATO 2.0 mission. *Experimental Astronomy*, 38:249–330.
- Rice, K. (2014). The Detection and Characterization of Extrasolar Planets. *Challenges*, 5:296–323.
- Ricker, G. R., Winn, J. N., Vanderspek, R., Latham, D. W., Bakos, G. A., Bean, J. L., Berta-Thompson, Z. K., Brown, T. M., Buchhave, L., Butler, N. R., Butler, R. P., Chaplin, W. J., Charbonneau, D., Christensen-Dalsgaard, J., Clampin, M., Deming, D., Doty, J., De Lee, N., Dressing, C., Dunham, E. W., Endl, M., Fressin, F., Ge, J., Henning, T., Holman, M. J., Howard, A. W., Ida, S., Jenkins, J., Jernigan, G., Johnson, J. A., Kaltenegger, L., Kawai, N., Kjeldsen, H., Laughlin, G., Levine, A. M., Lin, D., Lissauer, J. J., MacQueen, P., Marcy, G., McCullough, P. R., Morton, T. D., Narita, N., Paegert, M., Palle, E., Pepe, F., Pepper, J., Quirrenbach, A., Rinehart, S. A., Sasselov, D., Sato, B., Seager, S., Sozzetti, A., Stassun, K. G., Sullivan, P., Szentgyorgyi, A., Torres, G., Udry, S., and Villasenor, J. (2014). The Transiting Exoplanet Survey Satellite. *Journal of Astronomical Telescopes, Instruments, and Systems*, 1(1):014003. arXiv: 1406.0151.
- Rickman, E. L., Ceva, W., Matthews, E. C., Ségransan, D., Bowler, B. P., Forveille, T., Franson, K., Hagelberg, J., Udry, S., and Vigan, A. (2024). The discovery of two new benchmark brown dwarfs with precise dynamical masses at the stellar-substellar boundary. , 684:A88.
- Rickman, E. L., Matthews, E., Ceva, W., Ségransan, D., Brandt, G. M., Zhang, H., Brandt, T. D., Forveille, T., Hagelberg, J., and Udry, S. (2022). Precise dynamical masses of new directly imaged companions from combining relative astrometry, radial velocities, and HIPPARCOS-Gaia eDR3 accelerations., 668:A140.

- Roberts, S., Osborne, M., Ebden, M., Reece, S., Gibson, N., and Aigrain, S. (2013). Gaussian processes for time-series modelling. *Philosophical Transactions of the Royal Society A: Mathematical, Physical and Engineering Sciences*, 371(1984):20110550.
- Roederer, I. U., Alvarado-Gómez, J. D., Allende Prieto, C., Adibekyan, V., Aguado,
 D. S., Amado, P. J., Amazo-Gómez, E. M., Baratella, M., Barnes, S. A., Bensby,
 T., Bigot, L., Chiavassa, A., Domiciano de Souza, A., González Hernández, J. I.,
 Hansen, C. J., Järvinen, S. P., Korn, A. J., Lucatello, S., Magrini, L., Maiolino, R.,
 Di Marcantonio, P., Marconi, A., De Medeiros, J. R., Mucciarelli, A., Nardetto,
 N., Origlia, L., Peroux, C., Poppenhäger, K., Reiners, A., Rodríguez-López, C.,
 Romano, D., Salvadori, S., Tisserand, P., Venn, K., Wade, G. A., and Zanutta,
 A. (2024). The discovery space of ELT-ANDES. Stars and stellar populations.
 Experimental Astronomy, 57(2):17.
- Rogers, J. G., Gupta, A., Owen, J. E., and Schlichting, H. E. (2021). Photoevaporation versus core-powered mass-loss: model comparison with the 3D radius gap., 508(4):5886–5902.
- Rogers, J. G., Schlichting, H. E., and Owen, J. E. (2023). Conclusive evidence for a population of water-worlds around m-dwarfs remains elusive.
- Rossiter, R. A. (1924). On the detection of an effect of rotation during eclipse in the velocity of the brigher component of beta Lyrae, and on the constancy of velocity of this system., 60:15–21.
- Ryabchikova, T., Piskunov, N., Kurucz, R. L., Stempels, H. C., Heiter, U., Pakhomov, Y., and Barklem, P. S. (2015). A major upgrade of the VALD database., 90(5):054005.
- Salvatier, J., Wiecki, T. V., and Fonnesbeck, C. (2016). Probabilistic programming in python using pymc3. *PeerJ Computer Science*, 2:e55.
- Scarsdale, N., Wogan, N., Wakeford, H. R., Wallack, N. L., Batalha, N. E., Alderson, L., Aguichine, A., Wolfgang, A., Teske, J., Moran, S. E., López-Morales, M., Kirk,

- J., Gordon, T., Gao, P., Batalha, N. M., Alam, M. K., and Adams Redai, J. (2024). JWST COMPASS: The 3–5 μ m Transmission Spectrum of the Super-Earth L 98-59 c. , 168(6):276.
- Schlawin, E., Ohno, K., Bell, T. J., Murphy, M. M., Welbanks, L., Beatty, T. G.,
 Greene, T. P., Fortney, J. J., Parmentier, V., Edelman, I. R., Gill, S., Anderson,
 D. R., Wheatley, P. J., Henry, G. W., Mehta, N., Kreidberg, L., and Rieke, M. J.
 (2024). Possible Carbon Dioxide above the Thick Aerosols of GJ 1214 b. ,
 974(2):L33.
- Schrijver, C. J. (2002). Solar spots as prototypes for stellar spots. *Astronomische Nachrichten*, 323:157–164.
- Schwab, C., Spronck, J. F. P., Tokovinin, A., Szymkowiak, A., Giguere, M., and Fischer, D. A. (2012). Performance of the CHIRON high-resolution Echelle spectrograph. In McLean, I. S., Ramsay, S. K., and Takami, H., editors, *Ground-based and Airborne Instrumentation for Astronomy IV*, volume 8446 of *Society of Photo-Optical Instrumentation Engineers (SPIE) Conference Series*, page 84460B.
- Seager, S., Kuchner, M., Hier-Majumder, C., and Militzer, B. (2007). Mass-Radius Relationships for Solid Exoplanets. *The Astrophysical Journal*, 669(2):1279–1297. arXiv: 0707.2895.
- Seidel, J. V., Prinoth, B., Knudstrup, E., Hoeijmakers, H. J., Zanazzi, J. J., and Albrecht, S. (2023). Detection of atmospheric species and dynamics in the bloated hot Jupiter WASP-172 b with ESPRESSO., 678:A150.
- Serenelli, A. M., Bergemann, M., Ruchti, G., and Casagrande, L. (2013). Bayesian analysis of ages, masses and distances to cool stars with non-LTE spectroscopic parameters. , 429(4):3645–3657.
- Serrano, L. M., Gandolfi, D., Mustill, A. J., Barragán, O., Korth, J., Dai, F., Redfield, S., Fridlund, M., Lam, K. W. F., Díaz, M. R., Grziwa, S., Collins, K. A., Livingston, J. H., Cochran, W. D., Hellier, C., Bellomo, S. E., Trifonov,

- T., Rodler, F., Alarcon, J., Jenkins, J. M., Latham, D. W., Ricker, G., Seager, S., Vanderspeck, R., Winn, J. N., Albrecht, S., Collins, K. I., Csizmadia, S., Daylan, T., Deeg, H. J., Esposito, M., Fausnaugh, M., Georgieva, I., Goffo, E., Guenther, E., Hatzes, A. P., Howell, S. B., Jensen, E. L. N., Luque, R., Mann, A. W., Murgas, F., Osborne, H. L. M., Palle, E., Persson, C. M., Rowden, P., Rudat, A., Smith, A. M. S., Twicken, J. D., Van Eylen, V., and Ziegler, C. (2022). A low-eccentricity migration pathway for a 13-h-period Earth analogue in a four-planet system. *Nature Astronomy*, 6:736–750.
- Siegel, J. C., Halverson, S., Luhn, J. K., Zhao, L. L., Al Moulla, K., Robertson,
 P., Bender, C. F., Terrien, R. C., Roy, A., Mahadevan, S., Hearty, F., Ninan,
 J. P., Wright, J. T., Ford, E. B., Schwab, C., Stefánsson, G., Blake, C. H., and
 McElwain, M. W. (2024). Quiet Please: Detrending Radial Velocity Variations
 from Stellar Activity with a Physically Motivated Spot Model., 168(4):158.
- Siegel, J. C., Rubenzahl, R. A., Halverson, S., and Howard, A. W. (2022). Into the Depths: A New Activity Metric for High-precision Radial Velocity Measurements Based on Line Depth Variations., 163(6):260.
- Silva Aguirre, V., Davies, G. R., Basu, S., Christensen-Dalsgaard, J., Creevey, O., Metcalfe, T. S., Bedding, T. R., Casagrande, L., Handberg, R., Lund, M. N., Nissen, P. E., Chaplin, W. J., Huber, D., Serenelli, A. M., Stello, D., Van Eylen, V., Campante, T. L., Elsworth, Y., Gilliland, R. L., Hekker, S., Karoff, C., Kawaler, S. D., Kjeldsen, H., and Lundkvist, M. S. (2015). Ages and fundamental properties of Kepler exoplanet host stars from asteroseismology. , 452(2):2127–2148.
- Smith, A. M. S. and Csizmadia, S. (2022). A CHEOPS Search for Massive, Long-period Companions to the Warm Jupiter K2-139 b., 164(1):21.
- Sousa, S. G., Adibekyan, V., Delgado-Mena, E., Santos, N. C., Rojas-Ayala, B., Barros, S. C. C., Demangeon, O. D. S., Hoyer, S., Israelian, G., Mortier, A., Soares, B. M. T. B., and Tsantaki, M. (2024). SWEET-Cat: A view on the planetary mass-radius relation., 691:A53.

- Sousa, S. G., Adibekyan, V., Delgado-Mena, E., Santos, N. C., Rojas-Ayala, B.,
 Soares, B. M. T. B., Legoinha, H., Ulmer-Moll, S., Camacho, J. D., Barros,
 S. C. C., Demangeon, O. D. S., Hoyer, S., Israelian, G., Mortier, A., Tsantaki,
 M., and Monteiro, M. A. (2021). SWEET-Cat 2.0: The Cat just got SWEETer.
 Higher quality spectra and precise parallaxes from Gaia eDR3., 656:A53.
- Stark, C. C., Mennesson, B., Bryson, S., Ford, E. B., Robinson, T. D., Belikov, R.,
 Bolcar, M. R., Feinberg, L. D., Guyon, O., Latouf, N., Mandell, A. M., Rauscher,
 B. J., Sirbu, D., and Tuchow, N. W. (2024). Paths to robust exoplanet science
 yield margin for the Habitable Worlds Observatory. *Journal of Astronomical Telescopes, Instruments, and Systems*, 10:034006.
- Stassun, K. G., Oelkers, R. J., Paegert, M., Torres, G., Pepper, J., De Lee, N., Collins, K., Latham, D. W., Muirhead, P. S., Chittidi, J., Rojas-Ayala, B., Fleming, S. W., Rose, M. E., Tenenbaum, P., Ting, E. B., Kane, S. R., Barclay, T., Bean, J. L., Brassuer, C. E., Charbonneau, D., Ge, J., Lissauer, J. J., Mann, A. W., McLean, B., Mullally, S., Narita, N., Plavchan, P., Ricker, G. R., Sasselov, D., Seager, S., Sharma, S., Shiao, B., Sozzetti, A., Stello, D., Vanderspek, R., Wallace, G., and Winn, J. N. (2019). The Revised TESS Input Catalog and Candidate Target List., 158(4):138.
- Steffen, J. H. (2016). Sensitivity bias in the mass–radius distribution from transit timing variations and radial velocity measurements. *Monthly Notices of the Royal Astronomical Society*, 457(4):4384–4392. _eprint: https://academic.oup.com/mnras/article-pdf/457/4/4384/18515010/stw241.pdf.
- Stevenson, A. T., Haswell, C. A., Faria, J. P., Barnes, J. R., Barstow, J. K., Dickinson, H., and Standing, M. R. (2025). RV-exoplanet eccentricities: Good, Beta, and Best., 539(2):727–754.
- Swift, D. C., Eggert, J. H., Hicks, D. G., Hamel, S., Caspersen, K., Schwegler,E., Collins, G. W., Nettelmann, N., and Ackland, G. J. (2012). Mass-RadiusRelationships for Exoplanets., 744(1):59.

- Takarada, T., Sato, B., Omiya, M., Hori, Y., and Fujii, M. S. (2020). Radial-velocity search and statistical studies for short-period planets in the Pleiades open cluster. *arXiv:2010.11577 [astro-ph]*. arXiv: 2010.11577.
- Takeda, G. and Rasio, F. A. (2005). High Orbital Eccentricities of Extrasolar Planets Induced by the Kozai Mechanism. *The Astrophysical Journal*, 627(2):1001–1010.
- Teng, H.-Y., Sato, B., Kunitomo, M., Takarada, T., Omiya, M., Harakawa, H., Xiao, G.-Y., Liu, Y.-J., Izumiura, H., Kambe, E., Yoshida, M., Itoh, Y., Ando, H., Kokubo, E., and Ida, S. (2023). A close-in planet orbiting giant star HD 167768. , 75(1):169–176.
- Teske, J., Wang, S. X., Wolfgang, A., Gan, T., Plotnykov, M., Armstrong, D. J., Butler, R. P., Cale, B., Crane, J. D., Howard, W., Jensen, E. L. N., Law, N., Shectman, S. A., Plavchan, P., Valencia, D., Vanderburg, A., Ricker, G. R., Vanderspek, R., Latham, D. W., Seager, S., Winn, J. N., Jenkins, J. M., Adibekyan, V., Barrado, D., Barros, S. C. C., Benkhaldoun, Z., Brown, D. J. A., Bryant, E. M., Burt, J., Caldwell, D. A., Charbonneau, D., Cloutier, R., Collins, K. A., Collins, K. I., Colon, K. D., Conti, D. M., Demangeon, O. D. S., Eastman, J. D., Elmufti, M., Feng, F., Flowers, E., Guerrero, N. M., Hojjatpanah, S., Irwin, J. M., Isopi, G., Lillo-Box, J., Mallia, F., Massey, B., Mori, M., Mullally, S. E., Narita, N., Nishiumi, T., Osborn, A., Paegert, M., de Leon, J. P., Quinn, S. N., Reefe, M., Schwarz, R. P., Shporer, A., Soubkiou, A., Sousa, S. G., Stockdale, C., Strøm, P. A., Tan, T.-G., Tang, J., Tenenbaum, P., Wheatley, P. J., Wittrock, J., Yahalomi, D. A., and Zohrabi, F. (2021). The Magellan-TESS Survey. I. Survey Description and Midsurvey Results. , 256(2):33.
- Thompson, S. J., Queloz, D., Baraffe, I., Brake, M., Dolgopolov, A., Fisher, M.,
 Fleury, M., Geelhoed, J., Hall, R., González Hernández, J. I., ter Horst, R.,
 Kragt, J., Navarro, R., Naylor, T., Pepe, F., Piskunov, N., Rebolo, R., Sander, L.,
 Ségransan, D., Seneta, E., Sing, D., Snellen, I., Snik, F., Spronck, J., Stempels,
 E., Sun, X., Santana Tschudi, S., and Young, J. (2016). HARPS3 for a roboticized
 Isaac Newton Telescope. In Evans, C. J., Simard, L., and Takami, H., editors,

Ground-based and Airborne Instrumentation for Astronomy VI, volume 9908 of Society of Photo-Optical Instrumentation Engineers (SPIE) Conference Series, page 99086F.

Tinetti, G., Drossart, P., Eccleston, P., Hartogh, P., Heske, A., Leconte, J., Micela, G., Ollivier, M., Pilbratt, G., Puig, L., Turrini, D., Vandenbussche, B., Wolkenberg, P., Beaulieu, J.-P., Buchave, L. A., Ferus, M., Griffin, M., Guedel, M., Justtanont, K., Lagage, P.-O., Machado, P., Malaguti, G., Min, M., Nørgaard-Nielsen, H. U., Rataj, M., Ray, T., Ribas, I., Swain, M., Szabo, R., Werner, S., Barstow, J., Burleigh, M., Cho, J., Coudé du Foresto, V., Coustenis, A., Decin, L., Encrenaz, T., Galand, M., Gillon, M., Helled, R., Morales, J. C., García Muñoz, A., Moneti, A., Pagano, I., Pascale, E., Piccioni, G., Pinfield, D., Sarkar, S., Selsis, F., Tennyson, J., Triaud, A., Venot, O., Waldmann, I., Waltham, D., Wright, G., Amiaux, J., Auguères, J.-L., Berthé, M., Bezawada, N., Bishop, G., Bowles, N., Coffey, D., Colomé, J., Crook, M., Crouzet, P.-E., Da Peppo, V., Sanz, I. E., Focardi, M., Frericks, M., Hunt, T., Kohley, R., Middleton, K., Morgante, G., Ottensamer, R., Pace, E., Pearson, C., Stamper, R., Symonds, K., Rengel, M., Renotte, E., Ade, P., Affer, L., Alard, C., Allard, N., Altieri, F., André, Y., Arena, C., Argyriou, I., Aylward, A., Baccani, C., Bakos, G., Banaszkiewicz, M., Barlow, M., Batista, V., Bellucci, G., Benatti, S., Bernardi, P., Bézard, B., Blecka, M., Bolmont, E., Bonfond, B., Bonito, R., Bonomo, A. S., Brucato, J. R., Brun, A. S., Bryson, I., Bujwan, W., Casewell, S., Charnay, B., Pestellini, C. C., Chen, G., Ciaravella, A., Claudi, R., Clédassou, R., Damasso, M., Damiano, M., Danielski, C., Deroo, P., Di Giorgio, A. M., Dominik, C., Doublier, V., Doyle, S., Doyon, R., Drummond, B., Duong, B., Eales, S., Edwards, B., Farina, M., Flaccomio, E., Fletcher, L., Forget, F., Fossey, S., Fränz, M., Fujii, Y., García-Piquer, Á., Gear, W., Geoffray, H., Gérard, J. C., Gesa, L., Gomez, H., Graczyk, R., Griffith, C., Grodent, D., Guarcello, M. G., Gustin, J., Hamano, K., Hargrave, P., Hello, Y., Heng, K., Herrero, E., Hornstrup, A., Hubert, B., Ida, S., Ikoma, M., Iro, N., Irwin, P., Jarchow, C., Jaubert, J., Jones, H., Julien, Q., Kameda, S., Kerschbaum, F., Kervella, P., Koskinen, T., Krijger, M., Krupp, N., Lafarga, M.,

- Landini, F., Lellouch, E., Leto, G., Luntzer, A., Rank-Lüftinger, T., Maggio, A., Maldonado, J., Maillard, J.-P., Mall, U., Marquette, J.-B., Mathis, S., Maxted, P., Matsuo, T., Medvedev, A., Miguel, Y., Minier, V., Morello, G., Mura, A., Narita, N., Nascimbeni, V., Nguyen Tong, N., Noce, V., Oliva, F., Palle, E., Palmer, P., Pancrazzi, M., Papageorgiou, A., Parmentier, V., Perger, M., Petralia, A., Pezzuto, S., Pierrehumbert, R., Pillitteri, I., Piotto, G., Pisano, G., Prisinzano, L., Radioti, A., Réess, J.-M., Rezac, L., Rocchetto, M., Rosich, A., Sanna, N., Santerne, A., Savini, G., Scandariato, G., Sicardy, B., Sierra, C., Sindoni, G., Skup, K., Snellen, I., Sobiecki, M., Soret, L., Sozzetti, A., Stiepen, A., Strugarek, A., Taylor, J., Taylor, W., Terenzi, L., Tessenyi, M., Tsiaras, A., Tucker, C., Valencia, D., Vasisht, G., Vazan, A., Vilardell, F., Vinatier, S., Viti, S., Waters, R., Wawer, P., Wawrzaszek, A., Whitworth, A., Yung, Y. L., Yurchenko, S. N., Zapatero Osorio, M. R., Zellem, R., Zingales, T., and Zwart, F. (2018). A chemical survey of exoplanets with ARIEL. *Experimental Astronomy*, 46(1):135–209.
- Tran, Q. H., Bedell, M., Foreman-Mackey, D., and Luger, R. (2023). Joint Modeling of Radial Velocities and Photometry with a Gaussian Process Framework., 950(2):162.
- Twicken, J., Caldwell, D. A., Davies, M. D., Jenkins, J. M., Li, J., Morris, R. L., Rose, M. E., Smith, J. C., Tenenbaum, P., Ting, E. B., and Wohler, B. (2019). TESS SPOC Pipeline Data Validation Products: Now Available at MAST. In American Astronomical Society Meeting Abstracts #233, volume 233 of American Astronomical Society Meeting Abstracts, page 140.03.
- Ulmer-Moll, S., Santos, N. C., Figueira, P., Brinchmann, J., and Faria, J. P. (2019). Beyond the exoplanet mass-radius relation., 630:A135.
- Valenti, J. A. and Piskunov, N. (1996). Spectroscopy made easy: A new tool for fitting observations with synthetic spectra., 118:595–603.
- Van Eylen, V., Agentoft, C., Lundkvist, M. S., Kjeldsen, H., Owen, J. E., Fulton, B. J., Petigura, E., and Snellen, I. (2018). An asteroseismic view of the radius

- valley: stripped cores, not born rocky. *arXiv:1710.05398 [astro-ph]*. arXiv: 1710.05398.
- Van Eylen, V., Albrecht, S., Huang, X., MacDonald, M. G., Dawson, R. I., Cai, M. X., Foreman-Mackey, D., Lundkvist, M. S., Silva Aguirre, V., Snellen, I., and Winn, J. N. (2019). The Orbital Eccentricity of Small Planet Systems., 157(2):61.
- Van Eylen, V., Astudillo-Defru, N., Bonfils, X., Livingston, J., Hirano, T., Luque, R., Lam, K. W. F., Justesen, A. B., Winn, J. N., Gandolfi, D., Nowak, G., Palle, E., Albrecht, S., Dai, F., Campos Estrada, B., Owen, J. E., Foreman-Mackey, D., Fridlund, M., Korth, J., Mathur, S., Forveille, T., Mikal-Evans, T., Osborne, H. L. M., Ho, C. S. K., Almenara, J. M., Artigau, E., Barragán, O., Bouchy, F., Cabrera, J., Caldwell, D. A., Charbonneau, D., Chaturvedi, P., Cochran, W. D., Csizmadia, S., Damasso, M., Delfosse, X., De Medeiros, J. R., Díaz, R. F., Doyon, R., Esposito, M., Fűrész, G., Figueira, P., Georgieva, I., Goffo, E., Grziwa, S., Guenther, E., Hatzes, A. P., Jenkins, J. M., Kabath, P., Knudstrup, E., Latham, D. W., Lavie, B., Lovis, C., Mennickent, R. E., Mullally, S. E., Murgas, F., Narita, N., Pepe, F. A., Persson, C. M., Redfield, S., Ricker, G. R., Santos, N. C., Seager, S., Serrano, L. M., Smith, A. M. S., Suárez Mascareño, A., Subjak, J., Twicken, J. D., Udry, S., Vanderspek, R., and Zapatero Osorio, M. R. (2021). Masses and compositions of three small planets orbiting the nearby M dwarf L231-32 (TOI-270) and the M dwarf radius valley. arXiv e-prints, page arXiv:2101.01593.
- Vines, J. I. and Jenkins, J. S. (2022). ARIADNE: Measuring accurate and precise stellar parameters through SED fitting. *arXiv e-prints*, page arXiv:2204.03769.
- Weeks, A., Van Eylen, V., Huber, D., Kawata, D., Stokholm, A., Aguirre Børsen-Koch, V., Pinilla, P., Rørsted, J. L., Winther, M. L., and Berger, T. (2025). A link between rocky planet composition and stellar age., 539(1):405–421.
- Weiss, L. M. and Marcy, G. W. (2014). THE MASS-RADIUS RELATION FOR 65 EXOPLANETS SMALLER THAN 4 EARTH RADII. *The Astrophysical Journal*, 783(1):L6.

- Weiss, L. M., Marcy, G. W., Rowe, J. F., Howard, A. W., Isaacson, H., Fortney, J. J., Miller, N., Demory, B.-O., Fischer, D. A., Adams, E. R., Dupree, A. K., Howell, S. B., Kolbl, R., Johnson, J. A., Horch, E. P., Everett, M. E., Fabrycky, D. C., and Seager, S. (2013). The Mass of KOI-94d and a Relation for Planet Radius, Mass, and Incident Flux., 768(1):14.
- Wilson, R. F., Barclay, T., Powell, B. P., Schlieder, J., Hedges, C., Montet, B. T.,
 Quintana, E., Mcdonald, I., Penny, M. T., Espinoza, N., and Kerins, E. (2023).
 Transiting Exoplanet Yields for the Roman Galactic Bulge Time Domain Survey
 Predicted from Pixel-level Simulations., 269(1):5.
- Winn, J. N. and Fabrycky, D. C. (2015). The Occurrence and Architecture of Exoplanetary Systems. *Annual Review of Astronomy and Astrophysics*, 53(1):409–447. arXiv: 1410.4199.
- Wu, D.-H., Rice, M., and Wang, S. (2023). Evidence for Hidden Nearby Companions to Hot Jupiters., 165(4):171.
- Wu, Y. and Murray, N. (2003). Planet Migration and Binary Companions: The Case of HD 80606b., 589(1):605–614.
- Yang, J. and Hu, R. (2024). Chemical Mapping of Temperate Sub-Neptune Atmospheres: Constraining the Deep Interior H₂O/H₂ Ratio from the Atmospheric CO₂/CH₄ Ratio. , 971(2):L48.
- Yee, S. W., Petigura, E. A., and von Braun, K. (2017). Precision Stellar Characterization of FGKM Stars using an Empirical Spectral Library. , 836(1):77.
- Yu, H., Aigrain, S., Klein, B., Cretignier, M., Lienhard, F., and Roberts, S. J. (2024).
 A Gaussian process model for stellar activity in 2D line profile time-series.
 535(1):634–646.
- Zechmeister, M. and Kürster, M. (2009). The generalised Lomb-Scargle periodogram. A new formalism for the floating-mean and Keplerian periodograms., 496(2):577–584.

- Zechmeister, M., Reiners, A., Amado, P. J., Azzaro, M., Bauer, F. F., Béjar, V. J. S., Caballero, J. A., Guenther, E. W., Hagen, H. J., Jeffers, S. V., Kaminski, A., Kürster, M., Launhardt, R., Montes, D., Morales, J. C., Quirrenbach, A., Reffert, S., Ribas, I., Seifert, W., Tal-Or, L., and Wolthoff, V. (2018). Spectrum radial velocity analyser (SERVAL). High-precision radial velocities and two alternative spectral indicators., 609:A12.
- Zeng, L., Jacobsen, S. B., Hyung, E., Levi, A., Nava, C., Kirk, J., Piaulet, C., Lacedelli, G., Sasselov, D. D., Petaev, M. I., Stewart, S. T., Alam, M. K., López-Morales, M., Damasso, M., and Latham, D. W. (2021). New Perspectives on the Exoplanet Radius Gap from a Mathematica Tool and Visualized Water Equation of State. , 923(2):247.
- Zeng, L., Jacobsen, S. B., Sasselov, D. D., Petaev, M. I., Vanderburg, A., Lopez-Morales, M., Perez-Mercader, J., Mattsson, T. R., Li, G., Heising, M. Z., Bonomo, A. S., Damasso, M., Berger, T. A., Cao, H., Levi, A., and Wordsworth, R. D. (2019). Growth model interpretation of planet size distribution. *Proceedings of the National Academy of Science*, 116(20):9723–9728.
- Zhao, L. L., Bedell, M., Hogg, D. W., and Luger, R. (2024a). A Compact, Coherent Representation of Stellar Surface Variation in the Spectral Domain. , 977(2):140.
- Zhao, L. L., Dumusque, X., Ford, E. B., Llama, J., Mortier, A., Bedell, M., Al Moulla, K., Bender, C. F., Blake, C. H., Brewer, J. M., Collier Cameron, A., Cosentino, R., Figueira, P., Fischer, D. A., Ghedina, A., Gonzalez, M., Halverson, S., Kanodia, S., Latham, D. W., Lin, A. S. J., Lo Curto, G., Lodi, M., Logsdon, S. E., Lovis, C., Mahadevan, S., Monson, A., Ninan, J. P., Pepe, F., Roettenbacher, R. M., Roy, A., Santos, N. C., Schwab, C., Stefánsson, G., Szymkowiak, A. E., Terrien, R. C., Udry, S., Weiss, S. A., Wildi, F., Wildi, T., and Wright, J. T. (2023). The Extreme Stellar-signals Project. III. Combining Solar Data from HARPS, HARPS-N, EXPRES, and NEID., 166(4):173.
- Zhao, L. L., Fischer, D. A., Ford, E. B., Wise, A., Cretignier, M., Aigrain, S.,

- Barragan, O., Bedell, M., Buchhave, L. A., Camacho, J. D., Cegla, H. M., Cisewski-Kehe, J., Collier Cameron, A., de Beurs, Z. L., Dodson-Robinson, S., Dumusque, X., Faria, J. P., Gilbertson, C., Haley, C., Harrell, J., Hogg, D. W., Holzer, P., John, A. A., Klein, B., Lafarga, M., Lienhard, F., Maguire-Rajpaul, V., Mortier, A., Nicholson, B., Palumbo, M. L., Ramirez Delgado, V., Shallue, C. J., Vanderburg, A., Viana, P. T. P., Zhao, J., Zicher, N., Cabot, S. H. C., Henry, G. W., Roettenbacher, R. M., Brewer, J. M., Llama, J., Petersburg, R. R., and Szymkowiak, A. E. (2022). The EXPRES Stellar Signals Project II. State of the Field in Disentangling Photospheric Velocities. , 163(4):171.
- Zhao, Y., Dumusque, X., Cretignier, M., Cameron, A. C., Latham, D. W., López-Morales, M., Mayor, M., Sozzetti, A., Cosentino, R., Gómez-Vargas, I., Pepe, F., and Udry, S. (2024b). Improving Earth-like planet detection in radial velocity using deep learning., 687:A281.
- Zhou, G., Wirth, C. P., Huang, C. X., Venner, A., Franson, K., Quinn, S. N., Bouma, L. G., Kraus, A. L., Mann, A. W., Newton, E. R., Dragomir, D., Heitzmann, A., Lowson, N., Douglas, S. T., Battley, M., Gillen, E., Triaud, A., Latham, D. W., Howell, S. B., Hartman, J. D., Tofflemire, B. M., Wittenmyer, R. A., Bowler, B. P., Horner, J., Kane, S. R., Kielkopf, J., Plavchan, P., Wright, D. J., Addison, B. C., Mengel, M. W., Okumura, J., Ricker, G., Vanderspek, R., Seager, S., Jenkins, J. M., Winn, J. N., Daylan, T., Fausnaugh, M., and Kunimoto, M. (2022).
 A Mini-Neptune from TESS and CHEOPS Around the 120 Myr Old AB Dor Member HIP 94235., 163(6):289.
- Zhu, W. and Dong, S. (2021). Exoplanet Statistics and Theoretical Implications. arXiv:2103.02127 [astro-ph]. arXiv: 2103.02127.
- Zink, J. K. and Howard, A. W. (2023). Hot Jupiters Have Giant Companions: Evidence for Coplanar High-eccentricity Migration., 956(1):L29.